Fluid and Structural Analysis of Pipes Under Water Hammer Effects

Huade Cao

Thesis submitted to the University of Ottawa

in partial fulfillment of the requirements for the degree of

DOCTOR OF PHILOSOPHY

in Civil Engineering

Department of Civil Engineering

Faculty of Engineering

University of Ottawa

Acknowledgments

The author would like to express his deepest gratitude and appreciation to his supervisors, Prof. Magdi Mohareb and Prof. Ioan Nistor, for their continuous encouragement, assistance, valuable suggestions and advice throughout his study and research work. Especially, the author would like to thank Dr. Mohareb for his patience to assist the author from catching up on the foundation knowledge of structural engineering, as well as English writing skills.

The author would like to thank Prof. Jianxin Xia for his financial support and valuable suggestions to conduct experiments at the Minzu University of China, Beijing China.

The author also would like to thank the China Scholarship Council and the University of Ottawa for their financial support toward his Ph.D. program in the Department of Civil Engineering.

The author wishes to express his highest appreciation to his parents, family members of his brother and sister for their support and encouragement, as well as strong support among them, that the author could focus on his academic research abroad.

Abstract

The present study contributes to the analysis of pipes under water hammer by developing a hydraulic model, a structural model, and a fluid-pipe interaction model.

Under the conventional hydraulic water hammer models based on the classical boundary conditions, the energy is dissipated along the pipe only through friction at the pipe-fluid interface. As a result, the predicted water hammer pressure waves are observed to dissipate in a pattern that differs from that observed in experimental studies. This is particularly the case for water hammer models with unsteady friction based on weighting-functions, in which the predicted pressure wave front keeps its original shape during propagation, as opposed to smoothen and widen as observed in experiments. In a bid to improve the predicted pressure wave front smoothing, the first contribution of the study postulates the presence of a water jet at the pipe inlet throughout water hammer, resulting in a newly proposed boundary expression. The boundary expression introduces an additional source of energy dissipation due to the reflection of the pressure wave at the pipe inlet. The boundary expression was applied in conjunction to three friction models in order to predict the pressure wave history. The model was calibrated based on published experimental data. The proposed boundary expression was shown to improve the predictive capability of the classical water hammer model in replicating of experimentally observed damping patterns in pressure history with respect to peak pressure values, wave front smoothing and phase shifting.

While the classical water hammer model omits all inertial effects in the pipe wall, the extended water hammer model captures longitudinal inertial effects. Neither models, however, capture the bending stiffness of the pipe wall, thus predicting an unrealistic discontinuity in the radial displacement of the pipe wall in neighbourhood of the wave front. In order to remedy this limitation, the second contribution of the study develops a finite element formulation for the dynamic structural analysis of pipes subjected to general axisymmetric loading based on thin shell analysis. The validity of the formulation is demonstrated through comparisons with predictions of shell models based on the commercial software ABAQUS for static, natural vibration, and transient dynamic problems. The model is subsequently used to conduct a one-way coupled water hammer analysis, in which the transient pressure histories as predicted from the classical water hammer model is used as input into the structural model. The results suggest that the radial inertial effects in the pipe wall influence the predicted pipe response for fast valve closure scenarios, but

the effect becomes negligible when the valve closure time is over eight times larger than the radial period of vibration.

Water hammer models based on one-way coupling omit the fluid-pipe interaction effects. In order to capture such effects, the structural finite element model developed herein, was coupled to several hydraulic water hammer models, in a partitioned algorithm. The coupling was based on the Block Gauss-Seidel Algorithm, in which the hydraulic and structural models were iterated sequentially until convergence was attained within a specified tolerance before advancing to a new time step. A linear interpolation technique was adopted to exchange information between the non-matched fluid and structure interfaces. The number of iterations needed for convergence were accelerated by adopting either constant or dynamic relaxation factors. In order to assess the correctness of the implementation of the partitioned approach scheme, the classical and extended water hammer models were solved using the implemented Block Gauss-Seidel Algorithm and the results were compared to those based on the monolithic approach. The close agreement between both predictions demonstrated the validity of the Block Gauss-Seidel Algorithm implementation. The Algorithm was then extended to couple the structural shell finite element model developed herein with the hydraulic water hammer model. The effect of the specified convergence tolerance, the Courant number, the type of relaxation factor and fluid-structure interfaces, were investigated on the stability and computational efficiency for the partitioned models. The results indicate that the Aitken relaxation technique is recommended to accelerate the convergence rate of the two-way coupled analyses.

Table of Contents

List of Figures

List of Tables

Chapter 1 INTRODUCTION

1.1. Background

Pipelines are widely used to transport water in hydropower plants and to convey oil and gas from centers of production to costumes. In these applications, sudden closures of gates or valves typically lead to pressure waves traveling within the pipe. Under extremely circumstantial, the traveling pressure waves may lead to pipe rupture or collapse, resulting in economic lose and/or environmental pollution. Some accidents due to water hammer in hydropower plants and pipeline transportation systems are presented.

1.1.1. Hydropower plants

Hydroelectric power is clean and renewable energy. It's harmless to the environment comparing to the energy generated by fossil fuels, such as oil and coal. Hydroelectric power contributed 67.1% of Canada's renewable energy (e.g., wind and solar energy) in 2017 (Natural Resources Canada, 2019). Figure 1.1 depicts a schematic of the hydropower station that a turbine is turned by flowing water to generate power. The high-level reservoir locates at the penstock upstream inlet. At the downstream end of the penstock, a turbine connects to a power generator using the turbine to convert kinetic energy into electric power. Pipes with large dimeters are normally used for penstocks to maintain large discharge that make them vulnerable to water hammer. For example, each penstock of Sir Adam Beck II power station (Ontario, Canada) has a diameter of 5 m and a maximum discharge of 158.6 m^3/s (Ontario power generation, 2012).

Bonin (1960) reported an accident in Oigawa power station, Japan, which occurred in 1950. The accident caused three fatalities and seriously injured one, alongside economic losses of over half a million dollars. This accident was due to the incorrect operation and malfunctioning of equipment. Water hammer occurred in the penstock after a valve was closed in 0.3sec instead of 28sec as designed. The extremely high pressure ruptured the penstock (Figure 1.2a). In consequence, the water freely discharged at the pipe rupture that water column separation occurred, and the negative pressure collapsed 53 m pipe segment (Figure 1.2b).

During regular operation, the transient pressure fluctuations normally will not induce pipe failure. However, high pressure induced by transient pressure radially expands the pipe while low pressures radially contract the pipe. This type of loading and unloading can result in gaps between

penstocks and surrounding rock, that make penstocks more vulnerable to water hammer. For example, on December 12, 2000, the Cleuson-Dixence penstock of the Bieudron Hydroelectric Power Station ruptured at the location of low strength soil surrounding the penstock (tunnelintelligence,2008). Massive water quantities flowed through the rupture at a discharge of over 150 m^3/s. The downstream flood destroyed over $1km^2$ of landscape and caused three fatalities. In other accidents, water hammer effects may not be large enough to induce rupture in the pipeline. However, it could induce vibrations that could loosen connection bolts leading to fluid leakage (Keller 2014).

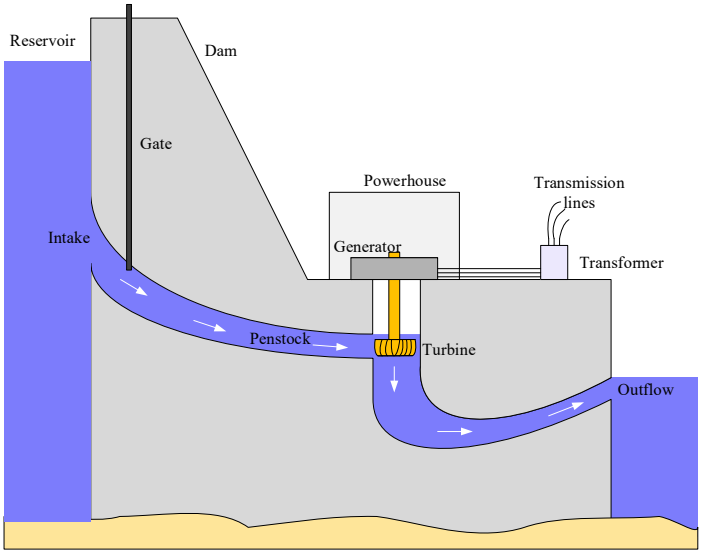

Figure 1.1 Schematic of hydropower station

(adapted from the website: https://science.howstuffworks.com/environmental/ energy/hydropower-plant1.htm)

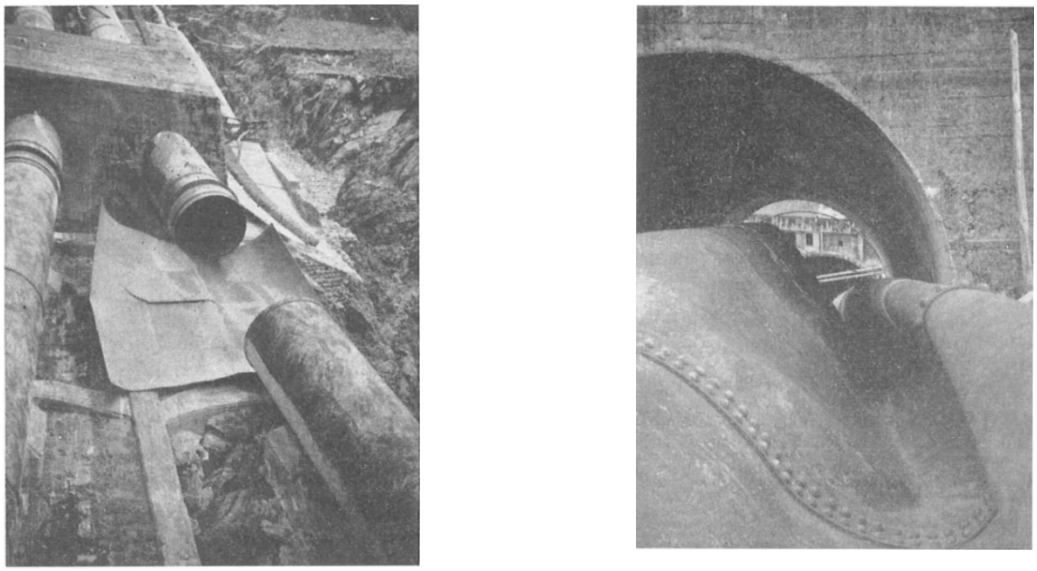

(a) (b)

Figure 1.2 Damage caused by water hammer to Oigawa power station in June 1950. (a) Split and flattened penstock; and (b) collapsed penstock. Reprint from Bonin (1960) with permission.

1.1.2. Pipeline transportation systems

Pipelines are commonly used to transport fluids (oil, gas, etc.) from the centers of production to costumes. Compared to other transportation systems (e.g., water carriers and railroads, etc.), pipelines are the least expensive and the most effective means to transport fluids. Pipelines also possess the additional advantage of being adaptable to complicated topographies. As such, pipelines are the preferred option to transport crude oil and petroleum products (Figure 1.3). After a long service life, soil erosion, corrosion, and environmental conditions will typically weaken the strength of the pipe wall. In some cases, small cracks may exist in the pipe wall. These cracks may propagate under water hammer effects. Released oil or gas from pipe ruptures pollute environment and risks the healthy of surrounding biosystem.

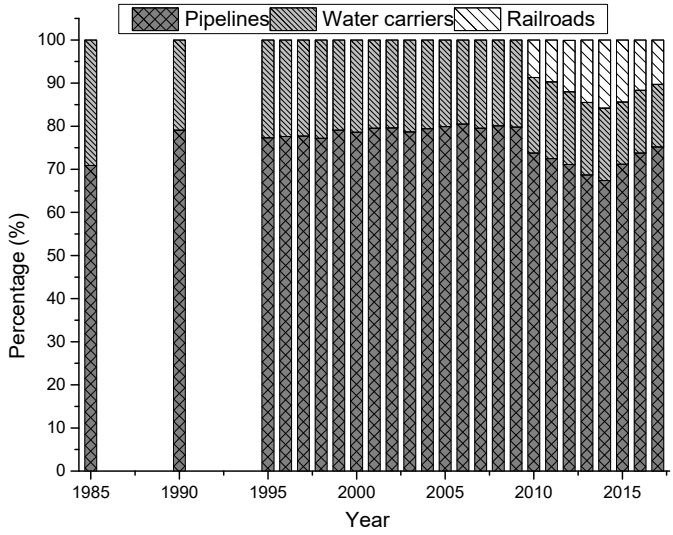

Figure 1.3 Crude oil and petroleum products transported in the United States by modes: data for the railroads before 2010 is unavailable.

(Source: United States Department of Transportation, https://www.bts.gov /content/crude-oil-and-petroleum-products-transported-united-states-mode)

On July 25, 2010, an accident was induced by water hammer phenomenon in the pipeline owned and operated by Enbridge Inc. (Enbridge), starting in Edmonton, Alberta, Canada, and ending in Sarnia, Ontario, Canada (NTSB, 2012). A pipe segment (Figure 1.4) ruptured one kilometer downstream of the Marshall pump station during the pump shut down for scheduled maintenance. The ruptured pipe was part of the Lakehead system in the USA. A total of 3192 m^3 of crude oil were released to the surrounding wetlands (Figure 1.5) and flowed into a nearby river. After pipe rupture, the operators tried to start the line twice. This pipe rupture incident cost Enbridge 1.21 billion U.S. dollars and resulted in the largest inland oil spill in USA history (Ellison 2019). The environmental damage of this disaster is reported to persist until today (Reisterer 2019).

Figure 1.4 The ruptured pipe segment of Line 6 in the oil spilled accident at Marshall, Michigan on July 25, 2010.

(Photo from pipeline accident report published by NTSB, 2012)

Figure 1.5 Cleanup efforts in an oil-soaked wetland near the rupture site.

(Photo from pipeline accident report by NTSB, 2012)

1.2. Research objectives

Water hammer can happen in a wide variety of pipeline systems and are typically induced by start-up or shut down a pump, or sudden opening or closure of valves. In some case, after pipe failure caused by water hammer, column separation may occur due to the freely release of water from the pressured pipe and cause secondary damage in the pipe. Practical pipe networks include

multiple branches, valves, pumps, and are surrounded by various environment (e.g., rock and soil). These complexities challenge the analyses of water hammer. However, conventional water hammer theories have many limitations that prevent them from tackling complex practical situations. Within this context, the present work will focus on developing and extending conventional water hammer models to more accurately characterize the pressure wave, investigate the dynamic response of the pipes under pressure waves induced by water hammer, and characterize the fluid-pipe interaction effects. More specifically, the objectives of this work include:

1) Improving the classical water hammer models in the replication of wave damping pattern.

a) Developing a boundary expression for the upstream reservoir that accounts for the effects of the waterjet during water hammer.

b) Assessing the improvement introduced by the newly proposed boundary expression in conjunction with various friction models.

c) Evaluating the independence of the newly proposed boundary expression on the number of subdivisions.

2) Challenging the unrealistic assumption of the pipe response in previous water hammer models, which leads to a discontinuity in the pipe radial displacement in the proximity of the sharp wave front.

a) Developing an axisymmetric shell element for pipe subjected to axisymmetric loading.

b) Assessing the stiffness and mass matrices of the developed finite element based on static analysis and natural frequency analysis.

c) Evaluating the influence of the shape of the pressure wave front on the pipe dynamic response.

3) Developing a two-way coupling water hammer model that captures the fluid-structure interaction and its effects

a) Developing a fluid solver that can be used to discretize the fluid domain during water hammer.

b) Developing a stable iterative scheme that couples the fluid solver and the structural solver for the two-way coupling water hammer model

c) Assessing the effects of the introduced parameters on the stability and the efficiency of the proposed two-way coupling water hammer model.

1.3. Scope of research

The primary objective of this thesis is to improve the water hammer models in the replication of the measured pressure history from physical models. While the study remedies some restrictions of the previous models, its fundamental assumptions are still identical to those used by the previous water hammer models. The scope of the present study considers:

(1) the one-dimensional case of the water hammer model with single-phase flow. The reason to adopt the one-dimensional case is that the water hammer pressure wave speed is in the order of acoustic speed and a few orders higher than the fluid velocity.

(2) the water hammer in the steel pipe assumes a linear response of the pipe wall subjected to water hammer pressure.

(3) shell pipes that allow for shear deformation in the pipe wall were not considered.

(4) present models are only verified by experimental results from small scale pipe systems constructed in the lab.

In the first objective to account for the waterjet in the classical water hammer, the proposed boundary expression is only in conjunction with the Method of Characteristics which does not introduce any numerical dissipation.

To remediate the unrealistic assumption of the pipe response in previous water hammer models, the friction between the fluid and structure domain was neglected. Hence, the study focuses on investigating the numerical dissipation and damping introduced by the iterative scheme.

1.4. Contributions and Novelty

The influence of the reservoir on the water hammer pressure wave shape was investigated and analyzed for the first time. In previous models, the boundary condition of the reservoir assumes constant pressure at the pipe inlet connected to the reservoir and that the pressure wave bounces back without any energy dissipation. Only the friction between fluid and structure interfaces was considered for the energy dissipation during water hammer. Including the effect of the waterjet,

the water hammer model is more realistic and demonstrated to lead to a more accurate simulation of the pressure wave damping.

The axisymmetric shell element is first-time tailored for the response analysis of the pipe subjected to water hammer pressure. It's also the first time to investigate the influence of the shape of the water hammer pressure wave front on the radial dynamic response in the pipe wall.

Unlike conventional water hammer models, which use a monolithic approach, the strong coupling partitioned algorithm was developed in this work allowed the development of a two-way coupling water hammer model. Using the partitioned approach, both the fluid and structural domains are discretized and solved separately. In this way, further water hammer models only require updating the designated solver to account for more features for the respective domains. For example, further two-way water hammer models can reuse the present fluid solver to simulate the analysis of one-phase water hammer in other types of pipes by updating structural solver, or the present structural solver for other types of flow in steel pipe by updating fluid solver.

1.5. Overview of thesis

To address the objectives stated in section 1.2, the thesis outlines the relative works of water hammer models and details the derivation of newly proposed boundary expression for the upstream reservoir, as well as the development of the finite element and two-way coupling water hammer models. These works are detailed in the following chapters:

Chapter 2: The state-of-the-art of the classical and extended water hammer is reviewed for the perspective of the governing equations and the schemes of numerical solvers. Chapter 2 also outlines the elements for the simulation of shell-cylinder and summarizes the limitations of the conservation water hammer models.

Chapter 3: To improve the replication of the observed pressure wave damping pattern using the Instantaneous-acceleration based (IAB) water hammer model, a new boundary expression was proposed for the upstream reservoir that accounts for the water jet occurred at the pipe inlet. The newly proposed boundary expression is applied in conjunction with the quasi-steady friction, the unsteady friction models based the Weight-function based (WFB) and the IAB. Adopting the proposed boundary expression, the water hammer models predict the pressure history near the valve that closely replicates the experimentally observed patterns for various pipe systems. To

illustrate that the proposed boundary is independent of the scheme of the model discretization, the energy dissipated by the friction and waterjet was computed in the model using a various number of subdivisions.

Chapter 4: To capture the pipe response during water hammer, an axisymmetric stress-deformation model was developed that accounts for the shell behavior of the pipe. The model accounted for inertial and damping effects in the dynamic analysis. Compared to the results obtained from ABAQUS models, the developed element was assessed for static analysis, natural frequency analysis, and dynamic analysis. In the assessment for dynamic analysis, the pressure history determined by frictionless classical water hammer model was served as an input exciting pressure to the structural model. The structural model was intended to predict the temporal and spatial variations of pipe deformation and stress histories. The influence of valve closure time and pattern on the pipe dynamic response was investigated using the one-way coupling water hammer model.

Chapter 5: Since the pressure distribution in the classical water hammer solution is based on a crude representation of the pipe deformation compared to the pipe response predicted in Chapter 4, it becomes of interest in Chapter 5 to develop a more accurate coupled model that captures the interaction between the fluid model and stress-deformation model. Thus, a fluid-pipe model that accounts for two-way coupling was developed in this chapter based on a partitioned approach. In this approach, the fluid and structure models were solved separately and coupled at the fluid-structure interface. The structural model developed in Chapter 4 was adopted to characterize the pipe deformation pattern in the partitioned water hammer model. Using the block Gauss-Seidel scheme, the specified convergence tolerance was achieved after multiple iterations at each time step. To assess the iterative algorithm, the classical and extended water hammer models, which were usually solved monolithically, were solved using the partition approach. Four parameters influenced the performance of the partitioned water hammer model were investigated.

Chapter 6: This chapter briefly summarizes the findings given in Chapters 3, 4, 5, and it lists the main conclusions from previous chapters. Based on the limitation of the proposed partitioned water hammer model, a few possible improvements are proposed at the end.

1.6. References

Tunnelintelligence, 2008, https://web.archive.org/web/20110717113025/ http://www.Tunnel intel ligence .com/safety-in-detail-167.html

Bonin, C.C. (1960) "Water-hammer damage to Oigawa Power Station." *Journal of Engineering for Power*, 82:111-119.

Ellison, G. (2019) "New price tag for Kalamazoo River oil spill cleanup: Enbridge says $1.21 billion." https://www.mlive.com/news/grand-rapids/2014/11/2010_oil_spill_cost_ enbridge_1. html

Keller, R. (2014) "Investigation of severe water hammer in a large pump station-case study." *Pipelines 2014: From Underground to the Forefront of Innovation and Sustainability*, ASCE 2014: 1392-1401.

LeChevallier, M.W., Gullick, R.W., Karim, M. "The potential for health risks from intrusion of contaminants into the distribution system from pressure transients', Office of Water, Office of Ground Water and Drinking water, Distribution System Issue Paper, EPA.

Natural Resources Canda (2019) "Renewable energy facts." https://www.nrcan.gc.ca/ science-data/data-analysis/energy-data-analysis/energy-facts/renewable-energy-facts/ 20069#L4

NTSB. (2012) "National transportation safety board -Annual report to congress." https://www.ntsb.gov/about/Documents/2012_Annual_Report.pdf

Riesterer, J. (2019) "The Enduring Legacy of the 2010 Kalamazoo River Oil Spill." https://beltmag .com/kalamazoo-river-line-6b-oil-spill/

Ontario power generation. (2012) "Niagara tunnel project technical facts", http://www.niagarafrontier.com/tunneltechnical.html

Chapter 2 LITERATURE REVIEW

The water hammer phenomenon has been studied for over a century. The history of water hammer development can be found in numerous textbooks (e.g., Wylie and Streeter 1977, Watters 1979, Chaudhry 2014) and papers (e.g., Wiggert and Tijsseling 2001, Ghidaoui et al. 2005, Bergant et al. 2006, Tijsseling and Anderson 2007, Ferras et al. 2018). To improve the numerical models in the replication of water hammer pressure, mostly research focuses are on three aspects: (1) the fluid domain (e.g., single-phase and two-phase flows); and (2) the structural domain (e.g., linearly elastic and viscoelastic pipes); or (3) the energy dissipation mechanisms (e.g., the viscosity of the fluid, friction at the fluid-structure interface, pipe material damping, Coulomb friction)

When simulating water hammer in a linear elastic pipe without column separation, mass and momentum conservation equations are developed to describe the hydraulic behavior. Figure 2.1 shows that the energy dissipation is taken int considered in the momentum conservation equation through the friction stress either through weighting functions-based unsteady friction models, through the instantaneous acceleration-based unsteady friction model or the quasi-steady friction model. As shown in Figure 2.1, the mass conservation equation accounts for the longitudinal movement of the pipe wall at the pipe ends and the radical movements of the pipe wall. The radial displacement of a pipe is related to the circumferential strain which can be determined from the hoop stress and the longitudinal stress. The hoop stresses are assumed proportional to the pressures after neglecting radial inertial effects and bending stiffness (Appendix A). The longitudinal stresses are determined by two different means that two different models were developed in these respects; the classical and extended water hammer models (Figure 2.1). In the classical water hammer model, the longitudinal stress is assumed proportional to the pressure and the pipe ends are assumed static (e.g., Ghidaoui et al.2005). In the extended water hammer model, the longitudinal stress is determined by the pipe axial motion equations and the pipe ends velocities are assigned as the boundary conditions (e.g., Wiggert and Tijsseling 2001). Literature review on all aspects listed in Figure 2.1 will be presented later in this chapter.

Since hydraulic engineers are primarily interested in the fluid dynamic behavior, e.g., the pressure and velocity change with time, the water hammer models are based on over-simplified structural expressions to account for the fluid-structure interaction effects and able to predict acceptable results for simple pipe in the lab. However, the assumed structural response is

unrealistic under some scenario, for example, the pipe wall has discontinuity radial displacement around the discontinuity pressure wave front (Appendix A). Meanwhile, water hammer models, which attempt to embed the pipe structural response into the momentum conservation equation, are difficult to extend for other types of pipelines, e.g., for pipes with viscoelastic materials or layered pipe. The present study thus aims at proposing improvements to (a) the classical water hammer in the prediction of pressure wave damping, (b) a robust structural model for the pipe, and (c) advancing two-way coupling techniques between the fluid and pipe model.

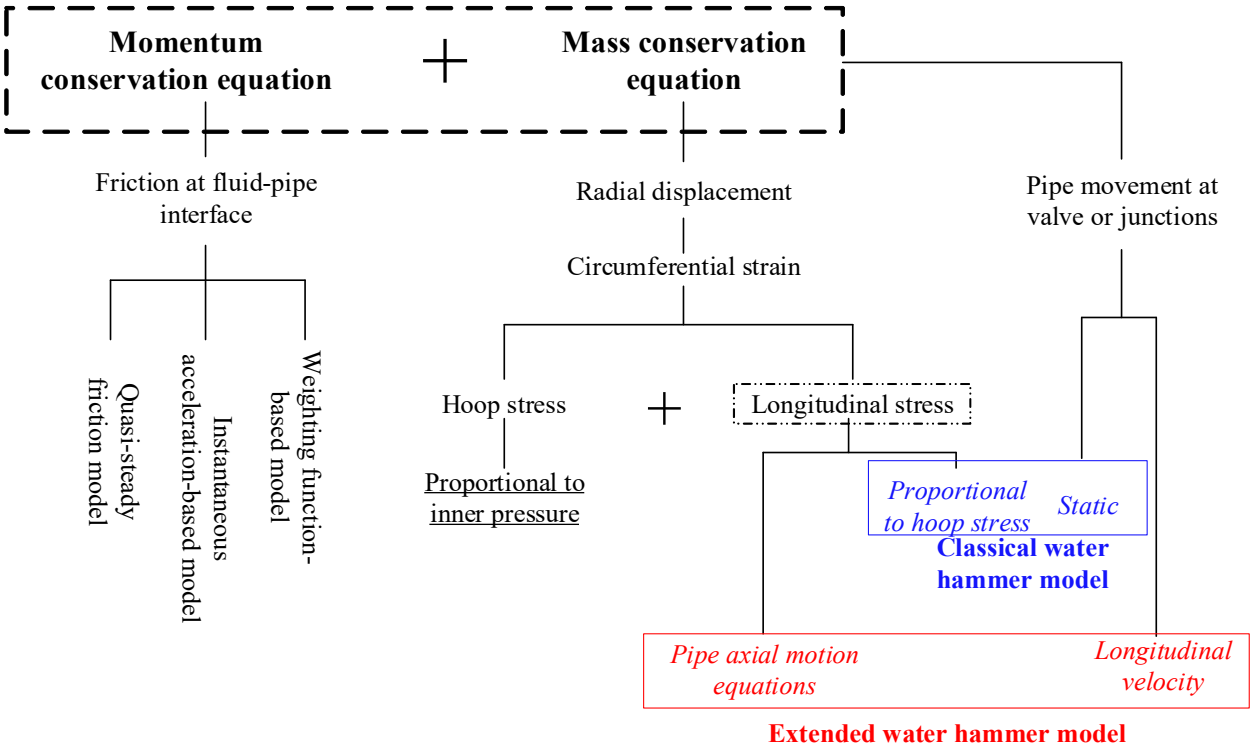

Figure 2.1 Momentum and mass conservation equations for the classical and extended water hammer models.

2.1. Governing equations for the fluid domain

In the investigation of water hammer, the mass and momentum conservation equations are developed to describe the hydraulic dynamic behavior of the fluid.+

2.1.1. Momentum conservation equation

The momentum conservation for the control volume of fluid is given as (e.g., Ghidaoui et al. 2005)

$$\frac{\partial}{\partial t}\int_{CV}\rho_f \mathbf{V} d\Omega + \int_{CS}\rho_f \mathbf{V}\left(\mathbf{V}\cdot\mathbf{n}\right)ds = \mathbf{F} \tag{2.1}$$

where ρ_f is the fluid density, $\mathbf{V}$ is the velocity vector, $\mathbf{n}$ is a vector normal to the surface of the control volume, $\mathbf{F}$ is an external force, t is time, Ω denotes the volume and s is the surface, CV and CS denote the control volume and control surface, respectively. For a horizontal straight pipe with negligible gravitational effects and negligible momentum in the radial direction, the momentum equation along the longitudinal direction for the flow is expressed as

$$\frac{\partial\left(\rho_f A_f V\right)}{\partial t} + \frac{\partial\left(\beta\rho_f A_f V^2\right)}{\partial x} = -\frac{\partial\left(PA_f\right)}{\partial x} - 2\pi R\tau_w \tag{2.2}$$

where x is the longitudinal coordinate, A_f is the pipe cross-sectional area, β is the momentum correction coefficient which is normally set to unity for water hammer problem, V and P are the average fluid longitudinal velocity and fluid pressure along the cross-section, τ_w is the shear stress acting longitudinally at the fluid–pipe interface. By expanding and rearranging, Eq.(2.2) can be expressed as

$$\rho_f A_f\left(\frac{\partial V}{\partial t} + V\frac{\partial V}{\partial x}\right) + P\frac{\partial A_f}{\partial x} + A_f\frac{\partial P}{\partial x} + 2\pi R\tau_w = 0 \tag{2.3}$$

The convective term $V\partial V/\partial x$ and the variation of the cross-sectional area along the longitudinal direction are considered negligible $V\partial V/\partial x = \partial A_f/\partial x = 0$, yielding the following simplification

$$\rho\frac{\partial V}{\partial t} + \frac{\partial P}{\partial x} + \frac{2\tau_w}{R} = 0 \tag{2.4}$$

2.1.2. Mass conservation equation

The mass conservation equation is given by (e.g., Ghidaoui et al. 2005)

$$\frac{\partial}{\partial t}\int_{cv}\rho_f d\Omega + \int_{cs}\rho_f\left(\mathbf{V}\cdot\mathbf{n}\right)ds = 0 \tag{2.5}$$

Assuming the control surface is attached to the pipe wall in the radial direction and the longitudinal velocity V is constant over the cross-section, the mass conservation equations can be simplified to

$$\frac{\partial\left(\rho_f A_f\right)}{\partial t}+\frac{\partial\left(\rho_f A_f V\right)}{\partial x}=0 \tag{2.6}$$

After expanding Eq.(2.6) and rearranging, one obtains

$$A_f\left(\frac{\partial \rho_f}{\partial t}+V\frac{\partial \rho_f}{\partial x}\right)+\rho_f A_f\frac{\partial V}{\partial x}+\rho_f\left(\frac{\partial A_f}{\partial t}+V\frac{\partial A_f}{\partial x}\right)=0 \tag{2.7}$$

According to the definition of the material derivative, e.g., $d(\ )/dt=\partial(\ )/\partial t+V\,\partial(\ )/\partial x$, Eq. (2.7) can be re-written as

$$A_f\frac{d\rho_f}{dP}\frac{\partial P}{\partial t}+\rho_f A_f\frac{\partial V}{\partial x}+\rho_f\frac{dA_f}{dt}=0 \tag{2.8}$$

Based on the definition of the bulk modulus for water K_f, the pressure can be related to the fluid density by

$$\frac{dP}{d\rho_f}=\frac{K_f}{\rho_f} \tag{2.9}$$

The change of the pipe cross-sectional area with respect to time can be related to the pipe wall radial displacement w through

$$\frac{dA_f}{dt}=\frac{d}{dt}\left[\pi\left(R+w\right)^2-\pi R^2\right]=2\pi\left(R+w\right)\frac{dw}{dt} \tag{2.10}$$

where R is the radius of pipe cross-section. In pipes, the radius R is much larger than the radial displacement w occurring throughout water hammer, e.g., $R+w\approx R$. From Eqs.(2.9) and (2.10), by substituting into Eq.(2.8), one obtains

$$\frac{1}{K_f}\frac{\partial P}{\partial t}+\frac{\partial V}{\partial x}+\frac{2}{R}\frac{\partial w}{\partial t}=0 \tag{2.11}$$

Equations (2.11) and (2.4) are the governing equations for one-dimensional water hammer models. The wall shear stress τ_w and the pipe wall radial velocity dw/dt must be determined prior to solve the governing equations for unknown velocities and pressures.

2.2. Wall shear stress

In addition to the quasi-steady friction model, there are other two commonly used unsteady friction models to determine the wall shear stress τ_w, the weighting function based (WFB) and the instantaneous-acceleration based (IAB) unsteady friction models.

2.2.1. Weighting function based unsteady shear stress

From the equation of motion for incompressible laminar axisymmetric flow, Zielke (1968) derived the expression for the wall shear stress τ_w depending on weighted passed velocity changes $\partial v/\partial t$. The wall shear stress τ_w can be thought of as comprising of a quasi-steady component and an unsteady component as follows:

$$\tau_w(t) = \frac{4\rho_f \upsilon}{R} V(t) + \frac{2\rho_f \upsilon}{R} \int_0^t \frac{\partial V}{\partial t}(\psi) W(t-\psi)\, d\psi \tag{2.12}$$

where υ is the kinematic viscosity of the fluid, ψ is a dummy variable of integration, $W = W(\varphi)$ is the weighting function of time given as

$$\begin{aligned} W(\varphi) &= \sum_{i=1}^{5} e^{A_i \varphi}; \varphi > 0.02 \\ W(\varphi) &= \sum_{i=1}^{6} B_i \varphi^{0.5i-1}; \varphi \le 0.02 \end{aligned} \tag{2.13}$$

where $\varphi = \upsilon t/R^2$ is dimensionless time, A_i and B_i are constants (Zielke 1968) given by

$$\begin{aligned} A_i &= [-26.3744, -70.8493, -135.0198, -218.9216, -322.5544] \\ B_i &= [0.232095, -1.25, 1.05855, 0.9375, 0.396696, -0.351563] \end{aligned} \tag{2.14}$$

The first term on the right-hand side of Eq.(2.12) is the steady part determined by the Darcy–Weisbach friction coefficients (Streeter 1963) for steady flow. The second term on the right-hand side of Eq.(2.12) is the unsteady part and is dependent on the weighted rate of change of velocity history. Vardy and Hwang (1993) theoretically derived new weighting functions to extend the

WFB friction models from laminar flows to turbulent flows and approximate weighting functions were presented for practical purposes. These weighting functions were limited to low Reynolds number (Re) turbulent flows in a short time after valve closure. Later on, the WFB friction models were extended for smooth pipes (Vardy and Brown 1995, 2003) and rough pipes (Vardy and Brown 2004). Vardy and Brown (2007) developed a general expression of the weighting functions for all flows in smooth and rough pipes. Integrating the Zielke model with weighting function Eq.(2.13), Shuy (1995) presented a non-dimensional discretizing equation for the wall shear stress. From the non-dimensional wall shear stress equation, by neglecting the initial transient terms and the velocity derivatives, it was reduced to the wall shear stresses in laminar steady flows. After neglecting the terms of velocity derivatives higher than the first order, it was reduced to the wall shear stress in constant acceleration or deceleration flows.

Numerical solution for the unsteady part in the Zielke model requires the storage of all the computed velocities which is time-consuming and computationally expensive. To increase the computational efficiency of the Zielke model, Trikha (1975) adopted an approximate weighting function to replace the original weighting function. The computed results with the approximate weighting function were in good agreement with the experimental results from Holmboe and Rouleau (1967). Suzuki et al. (1991) reorganized that the Zielke model can be approximated with a few exponential expressions. This approximation related the friction for the present time step to the computed velocities in a few previous time steps that only a few steps of previously computed velocities were required. Vardy and Brown (2010) used an approximate discretization form of the Zielke model in the numerical solver for water hammer to decrease the computational efforts. Johnston (2006) lumped up the frequency-dependent distributed frictions in laminar flows at both ends of the pipe to increase the computational efficiency while sacrificing the accuracy of the results at the inner nodes. Vítkovský et al. (2006) evaluated the numerical errors between the exact weighting functions (Vardy and Brown 1995) with the fitting functions in exponential form.

2.2.2. Instantaneous-acceleration based unsteady shear stress

By introducing an empirical parameter k, Brunone et al. (1991) related the unsteady friction shear stress to the local fluid accelerations $\partial V/\partial t$. Bergant et al. (1999) proposed a more general version of the Brunone model, as

$$\tau_w(t) = h_s \frac{\rho_s g D_0}{4} + \frac{k \rho_s g D_0}{8} \left(\frac{\partial V}{\partial t} + a sign(V) \frac{\partial V}{\partial x} \right) \tag{2.15}$$

where h_s is the head loss for the steady part and k is an empirical parameter. As the authors mentioned, by introducing the $sign(V)$, this model provided the correct sign of the convective term $\partial V/\partial t$ for inversed flows. Conducting a comparative analysis with the Zielke model and Brunone model, Vardy and Brown (1996) presented an expression to analytically determine the value of the empirical parameter, k, used in the Brunone model. Using the ratio of the maximum pressures for two consecutive periods near the valve, Brunone et al. (2000) determined the value of k to predict pressure time-histories near the valve which were in good agreement with the experimental results. Pezzinga (2000) proposed a two-parameter IAB friction model which introduces an additional empirical parameter in the convective term $\partial V/\partial x$ and replaces the sign function to generalize the Brunone model for various flow conditions. Vítkovský et al. (2000) illustrated the empirical parameter used in the Brunone model should be time dependent rather than constant.

Wylie (1997) verified the accuracy of the IAB model for wall shear stress in the water hammer model by comparing the numerical solutions with experimental results of Bergant and Simpson (1994), Budny et al. (1990) and Simpson (1986). Bergant et al. (1999) evaluated the accuracy of the modified Brunone model [Eq.(2.15)] by comparing the numerical solutions with the computed results from Zielke's model and the experimental data. The comparison showed that the modified Brunone model leads to more accurate and efficient solutions than Zielke's model in the prediction of the maximum and minimum pressure peaks. Vítkovský et al. (2006) assessed the validity of the IAB model for various transient flows under different conditions by changing flow direction and valve location. They introduced a sign function to correct the original IAB model for various scenarios.

2.3. Pipe radial velocity

In the classical and extended water hammer theory, the inertial effects and bending effects of the pipe wall are neglected. Based on the force equilibrium condition in the radial direction, the hoop stress σ_θ is proportional to the pressure as

$$\sigma_\theta = \frac{PR}{h} \tag{2.16}$$

where h is the thickness of the pipe wall. The radial displacement is related to the circumferential strain ε_θ through

$$w = R\varepsilon_r \tag{2.17}$$

where $\varepsilon_\theta = \left(\sigma_\theta - \nu\sigma_x\right)/E$ in which σ_x is the longitudinal stress, E is Young's modulus of pipe material. From equation (2.17) and (2.16), by substituting into equation (2.11) and rearranging, one obtains

$$\left(\frac{1}{K_f} + \frac{2R}{Eh}\right)\frac{\partial P}{\partial t} + \frac{\partial V}{\partial x} + \frac{\partial P}{\partial t} - \frac{2\nu}{E}\frac{\partial \sigma_x}{\partial t} = 0 \tag{2.18}$$

Thus, to obtain pressure and velocity, the longitudinal stress needs to be determined. The means of characterizing σ_x is the main difference between the classical and the extended water hammer theories and is discusses in the following sections.

2.3.1. The classical water hammer model

In the classical water hammer theory, the inertial effects in the longitudinal direction are neglected. There are three types of pipe boundary conditions: (1) pipes anchored at both ends, in which case the plane strain condition is assumed for the pipe, e.g., $\varepsilon_x = 0$ and $\sigma_x = \nu\sigma_\theta$, where ε_x is the longitudinal strain of pipe and ν is the Poisson ratio of pipe; (2) pipes connected to expansion joints on both ends, in which case the plane stress condition is assumed for the pipe, e.g., $\sigma_x = 0$; and (3) pipes anchored at the upstream end and connected to an expansion joint. In such a case, the longitudinal stress is induced by the effect of the pressure on the closed-end and given as $\sigma_x = PA_f/2\pi Rh = PR/2h = 0.5\sigma_\theta$ (e.g., Tijsseling 1996). Substituting the expressions of longitudinal stress into Eq.(2.18) and rearranging, one obtains

$$\frac{1}{\rho_f a^2}\frac{\partial P}{\partial t} + \frac{\partial V}{\partial x} = 0 \tag{2.19}$$

where a is the water hammer wave speed given by

$$a^2 = \frac{K_f / \rho_f}{1 + c\dfrac{K_f D}{hE}} \tag{2.20}$$

and $c = 1 - \nu^2$ for pipes anchored at both ends, $c = 1$ for pipes connected to expansion joints at both ends, and $c = 1 - 0.5\nu$ for pipes anchored at one end and connected to an expansion joint at the other end. Equations (2.4) and (2.19) are the governing equations for the classical water hammer model (e.g., Ghidaoui et al. 2005, Duan et al. 2012, 2017, Streeter 1963, Lee et al. 2013, McInnis et al. 1997).

2.3.2. The extended water hammer models

In the extended water hammer models, the longitudinal inertial effects are considered. The force equilibrium equation for the pipe wall along the longitudinal direction is given as (e.g., Wiggert et al. 1986, Tijsseling and Lavooij 1990; Wiggert and Tijsseling 2001)

$$\rho_s A_s \frac{\partial \dot{u}_x}{\partial t} - A_s \frac{\partial \sigma_x}{\partial x} = 2\pi R \tau_w \tag{2.21}$$

where ρ_s is the pipe wall density, A_s is the pipe wall cross-sectional area and $\dot{u}_x$ is the pipe wall longitudinal velocity. The stress-strain relationship is given as

$$\varepsilon_x = \frac{1}{E}\left(\sigma_x - \nu\sigma_\theta\right) = \frac{1}{E}\left(\sigma_x - \nu\frac{PR}{h}\right) \tag{2.22}$$

From Eq.(2.22), by expressing the longitudinal strain ε_x in terms of the longitudinal velocity $\dot{u}_x$ and taking the derivative with respect to time, one obtains

$$\frac{\partial \dot{u}_x}{\partial x} - \frac{1}{E}\frac{\partial \sigma_x}{\partial t} = -\frac{\nu R}{Eh}\frac{\partial P}{\partial t} \tag{2.23}$$

Relations (2.4), (2.18), (2.21) and (2.23) represent the governing equations for the four-equation extended water hammer model, which relates four unknown fields: the fluid pressure P, the fluid velocity V, longitudinal velocity of the pipe wall $\dot{u}_x$ and the longitudinal stress σ_x.

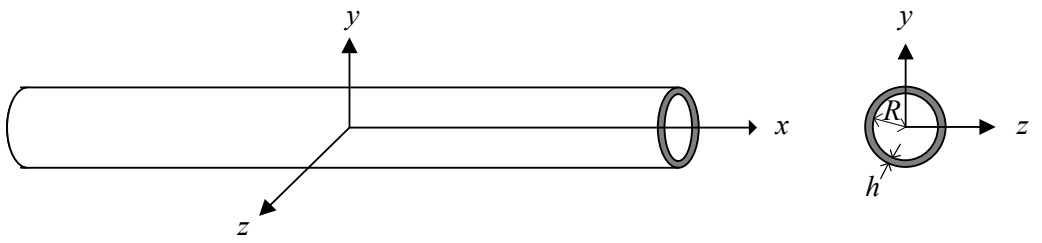

Figure 2.2 Coordinates of the pipe.

In 3-D pipe networks, the pipes are modeled as beams along coordinate x (Figure 2.2) and the additional equations governing the vertical motion of fluid-filled pipe in plane x-y are (e.g., Wiggert et al. 1986; Wiggert and Tijsseling 2001)

$$\begin{aligned}
&\frac{\partial \dot{u}_y}{\partial t}+\frac{1}{\left(\rho_f A+\rho_s A_s\right)}\frac{\partial Q_y}{\partial x}=0\\
&\frac{\partial \dot{u}_y}{\partial x}+\frac{1}{\kappa^2 G A_s}\frac{\partial Q_y}{\partial t}=-\dot{\theta}_z\\
&\frac{\partial \dot{\theta}_z}{\partial t}+\frac{1}{\rho_s I_s}\frac{\partial M_z}{\partial x}=\frac{1}{\rho_s I_s}Q_y\\
&\frac{\partial \dot{\theta}_z}{\partial x}+\frac{1}{EI_s}\frac{\partial M_z}{\partial t}=0
\end{aligned} \qquad (2.24)\text{a-d}$$

where $\dot{u}_y$ is the vertical velocity of pipe, Q_y is the vertical shear force, $\dot{\theta}_z$ is the rotational pipe velocity, M_z is the bending moment, I_s is the moment of inertia of the pipe cross-section, $\kappa^2=2(1+\nu)/(4+3\nu)$ is the shear coefficient for Timoshenko beam theory. The mass term ($\rho_f A_f+\rho_s A_s$) in Eq. (2.24)a reflects the mass of the pipe and the fluid. The four equations for pipe lateral motion can be merged into a single equation in terms of vertical displacement u_y and given as

$$\begin{aligned}
&\left(\rho_f A_f+\rho_s A_s\right)\frac{\partial^2 u_y}{\partial t^2}+EI_s\frac{\partial^4 u_y}{\partial x^4}-EI_s\frac{\rho_f A_f+\rho_s A_s}{\kappa^2 G A_s}\frac{\partial^4 u_y}{\partial t^2\partial y^2}\\
&-\rho_s I_s\frac{\partial^4 u_y}{\partial t^2\partial x^2}+\rho_s I_s\frac{\rho_f A_f+\rho_s A_s}{\kappa^2 G A_s}\frac{\partial^4 u_y}{\partial t^4}=0
\end{aligned} \qquad (2.25)$$

This is the dynamic equation for the Timoshenko beam with adding mass effect. When adopting the Bernoulli-Euler beam theory, the shear deformation term (involving κ) and rotational inertia

($\partial\dot{\theta}_z/\partial t$) are neglected. Similar equations are obtained to describe the lateral motion in the $x-z$ plane.

At an elbow in 3-D pipe networks, the out-plane bending rotation in one of the adjoining straight pipe segment would induce torsional force in the connected straight pipe. The corresponding governing equations of motion are given by (e.g., Wiggert and Tijsseling 2001)

$$\begin{aligned}\frac{\partial\dot{\theta}_x}{\partial t}-\frac{1}{\rho_s J_s}\frac{\partial M_x}{\partial x}=0\\ \frac{\partial\dot{\theta}_x}{\partial x}-\frac{1}{GJ_s}\frac{\partial M_x}{\partial t}=0\end{aligned} \tag{2.26}$$

where G is the shear modulus of the pipe material, and J_s is Saint-Venant torsional constant. Equation (2.26) can be merged into a single equation as

$$\frac{\partial^2\theta_x}{\partial t^2}-\frac{G}{\rho_s}\frac{\partial^2\theta_x}{\partial x^2}=0 \tag{2.27}$$

By combining with Eqs. (2.24) and (2.26), the four-equation extended water hammer model is extended for 3-D pipe network.

In a study on pulse propagation in fluid-filled tubes, Walker and Phillips (1977) accounted for the radial inertial effects into the structural equations based on the thin-walled Kirchhoff hypothesis. Joung and Shin (1987) captured the effect of through thickness shear which was neglected in the Kirchhoff thin-walled hypothesis. Budny et al. (1991) accounted for the structural damping in the four-equation extended water hammer model. Ferràs et al. (2016) added a distributed Coulomb friction term into the structural dynamic equations of motion along the longitudinal direction. To extend the model to account for the effect of flow direction change, Lee et al. (1995) and Lee and Kim (1999) considered the gravitational effect in their structural model. Wang and Tan (1997) accounted for the loading induced by the change in flow direction after the pipe was bent. Ferras et al. (2017a) accounted for the effect of cross-section ovality on the water hammer wave speed in a pipe coil, by introducing a constant to relating the hoop stress to the hydraulic pressure.

2.4. Boundary conditions

2.4.1. Boundary conditions for the classical water hammer model

In the classical water hammer model, the boundary condition at the reservoir is given as

$$P = \rho_f g H_{res} \tag{2.28}$$

where g is the gravitational acceleration, and H_{res} is the hydraulic head at the pipe inlet. At the valve, the velocity V is related to the initial velocity V_0 through

$$V = f(t) V_0 \tag{2.29}$$

where $f(t)$ is a valve closure function that characterizes the velocity at the valve as a function of time and $f(t) = 0$ after complete valve closure. The boundary conditions at the reservoir and at the valve are the ones most commonly used when investigating the classical water hammer model (e.g., Ghidaoui et al.2005). Goldberge and Karr (1987) investigated the influence of valve closure time on the water hammer pressure to optimize the valve closure function $f(t)$ that would minimize the pressure induced by the water hammer. McInnis et al. (1997) accounted for the energy loss at the inline orifice. Ferreira et al. (2018) investigated the influence of the ball valve on hydraulic pressure head both in steady and unsteady flows. Sepehran and Noudeh (2012) considered the energy loss at the pipe entrance on the water hammer pressure. Soares et al. (2013) proposed boundary expressions for pumps, check valves, and variable-level tanks when simulates pumping pipe systems.

2.4.2. Boundary conditions for the extended water hammer model

At a reservoir, the pressure is constant, and the pipe is restrained from moving longitudinally. The boundary expressions at the reservoir are hence expressed as

$$\begin{aligned} &P = \rho_f g H_{res}; \\ &\dot{u}_x = 0; \end{aligned} \tag{2.30}$$

For pipe end with a valve could be either longitudinally restrained or unrestrained. For a pipe with a longitudinally restrained valve, the boundary conditions for a completely closed valve are given by

$$V = 0;$$
$$\dot{u}_x = 0; \tag{2.31}$$

For a pipe with a longitudinally unrestrained valve, the boundary conditions for a completely closed valve is given as

$$V = \dot{u}_x,$$
$$A_s \sigma_x = P_{val} A \tag{2.32}$$

where P_{val} is the pressure acting on the valve. The above boundary conditions are the most commonly investigated boundary expressions within the four-equation extended water hammer model (e.g., Tijsseling and Lavooij 1990, Lavooij and Tijsseling 1991, Ferras et al. 2017a). Lavooij and Tijsseling (1991) proposed boundary expressions for non-instantaneous valve closure with impact loading at closed ends.

Using the four-equation extended water hammer model, Tijsseling et al. (1996) proposed boundary expressions for an elbow connecting two straight pipe segments. While using an eight-equation extended water hammer model, Tijsseling and Vaugrante (2001) extended the boundary expressions for an elbow to account for out-of-plane bending and twisting. Tijsseling and Vardy (1996) accounted for the influence of local Coulomb friction force at a mid-span pipe rack. Ferras et al. (2017b) investigated the influence of various anchoring conditions and various valve masses on the pressure histories. Henclik (2018) adopted a spring model and a Kelvin-Voigt viscoelastic model to represent valves at the end of pipes that were elastically restrained in the longitudinal direction.

2.5. Numerical schemes

2.5.1. Numerical schemes for the classical water hammer model

The method of characteristics is the most commonly used numerical scheme to solve the classical water hammer model. A numerical example of the water hammer pressure wave oscillation in a pipe is described in the Appendix B. There are two types of grids for the classical water hammer model which do not involve interpolation to obtain the characteristic roots, either a rectangular grid (Figure 2.3a) or a staggered grid (Figure 2.3b). Wylie (1997), Bergant et al. (2001), and Afshar and Rohani (2008) adopted a rectangular grid. Using the staggered grid, Wylie (1983) investigated the water hammer in a pipe network. Using the IAB unsteady friction model,

Vítkovský et al. (2000) compared the performance of the rectangular grid and the staggered grid and found that the rectangular gird caused instability in the pressure response that did not occur with the staggered grid.

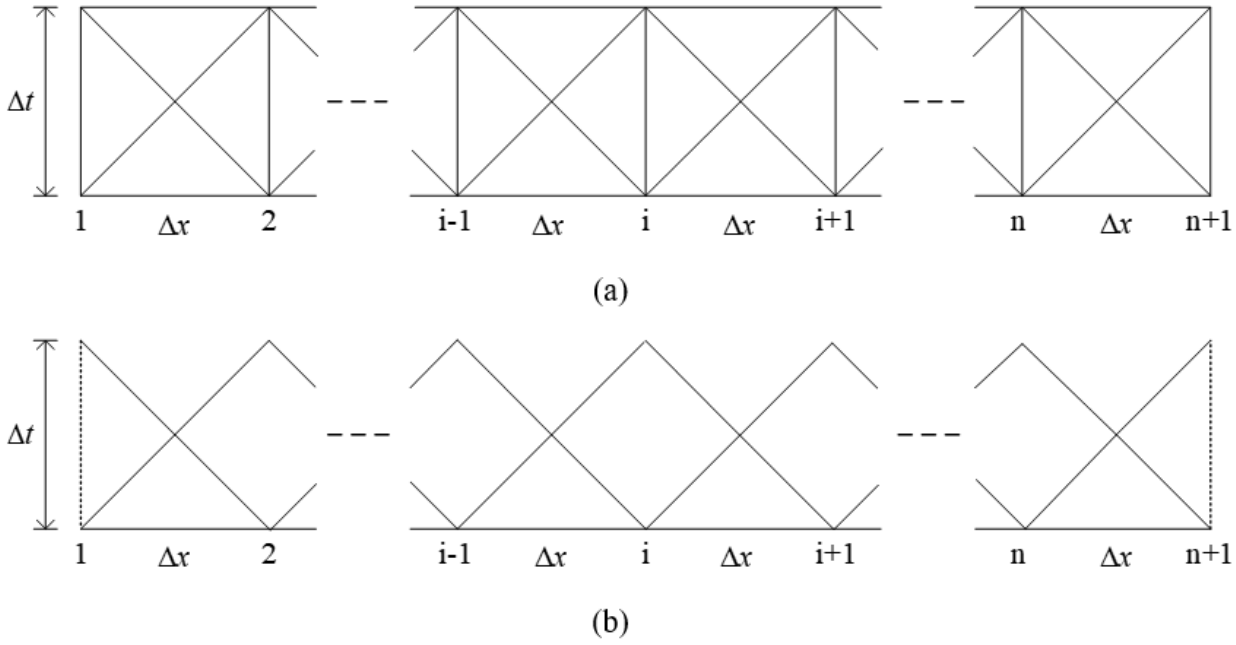

Figure 2.3 Rectangular grid and staggered grid. Horizontal lines are space lines, vertical lines are time lines and inclined lines are the characteristic lines.

When the characteristic roots do not lie on grid nodes for the present time step, interpolation is required to determine the values of the characteristic roots as shown in Figure 2.4 b-h. Lai (1988) proposed a comprehensive expression to represent the space-line interpolation grids (Figure 2.4 b-d) and time-line interpolation grids (Figure 2.4 e-g). Instead of using the points of intersection of the characteristic line with (a) the space-lines or (b) the time-lines, Karney and Ghidaoui (1997) adopted root nodes along the characteristic lines that lie in between (a) and (b). Rather than using linear interpolation for the space interpolation grid, Sibetheros et al. (1991) adopted spline interpolation to determine the values of characteristic roots. Keller and Rastogi (1977) analyzed the error introduced by space-line interpolation. Ghidaoui et al. (1998) computed the energy dissipated in the system by the numerical scheme to estimate the errors introduced by time-line interpolation and space-line interpolation. Using a polynomial transfer matrix technique, Shimada et al. (2006) estimated the errors introduced by time-line interpolation in the simulation of pipe

networks. Shimada et al. (2008) evaluated the numerical errors both in rectangular and staggered grids using either the time-line or space-line interpolations.

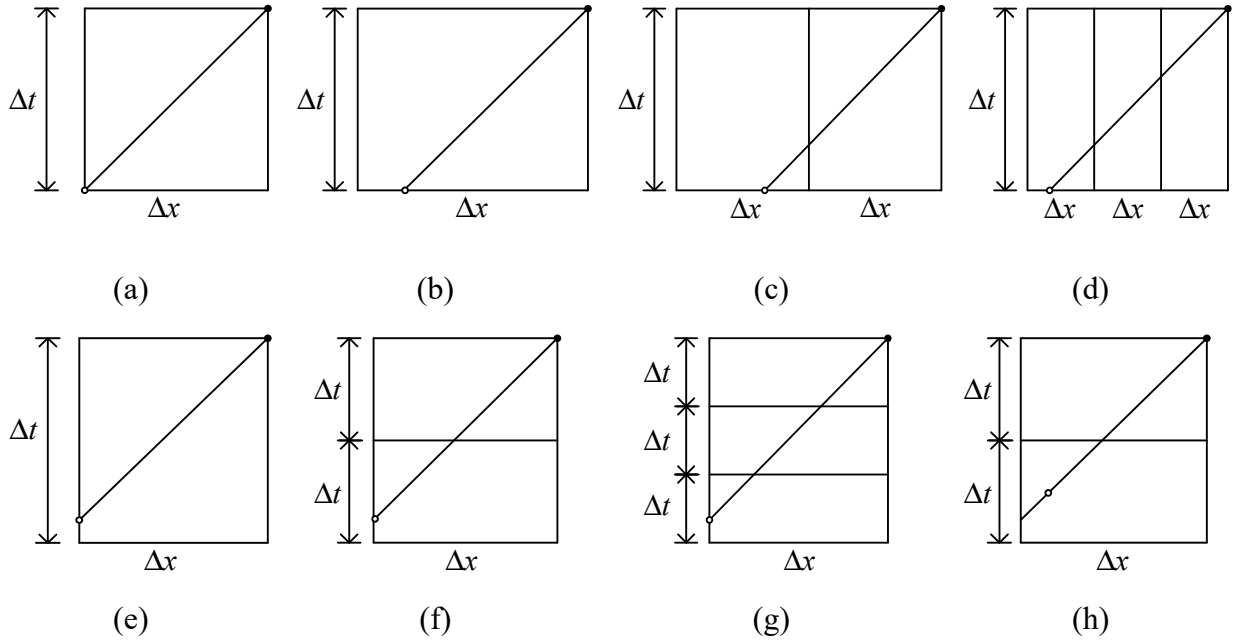

Figure 2.4 Space interpolation and time interpolation grids for the method of characteristic. (a) without interpolation; (b) space interpolation grid for C_r<1; (b) space interpolation grid for 1<C_r<2; (c) space interpolation grid for C_r>2; (d) implicit time interpolation grid for C_r>1; (e) time interpolation grid for 0.5<C_r<1; (f) time interpolation grid for 1/3<C_r<1/2; (g) time interpolation grid for C_r<1/3; (h) Comprehensive grid combining time interpolation and space interpolation. Solid nodes denote unknown nodes at a new time step, opening nodes denote characteristic roots along the positive characteristic lines.

Other numerical schemes have also been adopted to solve the classical water hammer model. Chaudhry and Hussaini (1985) used second-order explicit finite difference schemes (e.g., the MacCormack scheme, the Lambda scheme, and the Gabutti scheme) to solve the classical water hammer model. Szymkiewicz (1995) and Szymkiewicz and Mitosek (2005) adopted the finite element method (FEM) to solve the water hammer model. Wahba (2006) used the Runge-Kutta method for the time-stepping scheme and total variation diminishing (TVD) central differencing for both one- and two-dimensional models. Wang and Yang (2014) proposed an explicit-implicit coupling method to model the water hammer in pipe systems with pumps. Guinot (1998) used the piecewise parabolic method and a higher-order extension of the Godunov scheme to solve the classical water hammer model. Then, Guinot (2000) studied the performance of various Reimann solvers in the Godunov scheme. Zhao and Ghidaoui (2004) noticed that the first order Godunov scheme was identical to the method of characteristics. Using the Chebyshev super spectral

viscosity method, Chen et al. (2013) obtained approximate results compared to those predicted by the finite volume method and by the method of characteristics.

2.5.2. Numerical schemes for the extended water hammer models

Using the method of characteristic, Wiggert et al. (1986) solved the fourteen-equation water hammer model in a pipe system involving elbows. Using the MOC-FEM scheme to solve the four-equation model, Tijsseling and Lavooij (1990) investigated the influence of pipe movement on the pressure history. Based on the four-equation extended water hammer model, Lavooij and Tijessling (1991) compared the pressure history using the MOC (Figure 2.5) to the one obtained using the MOC-FEM scheme. By comparing to experimental results, Krisbrink and Heinsbroek (1993) validated the computer code FLUSTRIN, which is based on MOC-FEM, for large scale pipe system. Using the FLUSTRIN code, Heinsbroek and Tijsseling (1994) investigated the influence of support rigidity on water hammer pressure and pipe stresses. Tijsseling (2007) proposed a four-equation extended water hammer model for a thick pipe which was solved by using the MOC. Using the backtracking technique along the characteristic lines, Tijsseling (2003, 2009) developed an exact computational scheme for the frictionless four-equation extended water hammer model, which directly related any points on the space-time plane to the initial values and boundary conditions. To improve the exact scheme proposed by Tijsseling (2003, 2009), Xu and Jiao (2017) replaced the originally adopted linear interpolation by various interpolation methods, e.g., quadratic or cubic interpolations. Gale and Tiselj (2005) used the Godunov method to solve the four-equation extended water hammer model. Subsequently, Gale and Tiselj (2008) extended the Godunov type solver for the eight-equation extended water hammer model to study the water hammer in a pipe system with an elbow.

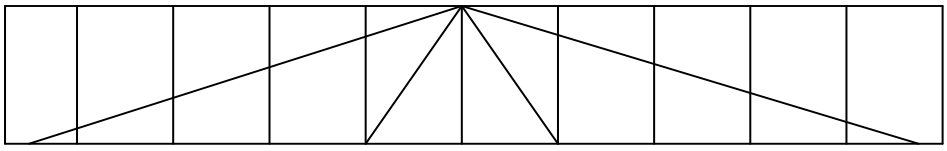

Figure 2.5 Characteristics grid for the four-equation extended water hammer model.

2.6. Shell theory for pipe response

For thin cylindrical shell structures (pipes), the strains are expressed in terms of displacements of pipe middle surface based on the assumptions that 1) the thickness of the shell is small compared to other dimensions; 2) strains and displacements are small so that second-order terms in the strain-

displacement relations are considered negligible; 3) the radial normal stress is small and ignored; 4) points normal to mid-surface before deformation remain normal and without extension (Leissa 1993). Based on these assumptions, either the direct force equilibrium methods or the energy formulations such as the Rayleigh-Ritz method, the Lagrange method, or Hamilton's variational principle, can be applied to obtain the governing equilibrium equations. Analytical methods or numerical methods are then used to determine the response of the pipe for static, free vibration, steady-state, or generally forced vibration, as discussed in the following section.

2.6.1. Analytical methods

Arnold and Warburton (1949) derived the frequency equation for thin cylindrical shells with free ends maintained circular based on the Timoshenko shell theory using the Lagrange method. They provided theoretical predictions for the vibration of cylinders which were compared to experimental results. Based on the Kirchhoff hypothesis, Flugge (1960) derived the equilibrium equations using the direct force equilibrium method and solved it using a series solution. Forsberg (1964) determined the modal characteristics of thin cylindrical shells for 16 sets of homogeneous boundary conditions based on Flugge's theory (1960). Reismann and Pawlik (1968) presented an analytical solution for the dynamic response of circular cylindrical shells subjected to concentrated impulse loads. Using the Laplace transform method, Sagartz and Forrestal (1969) solved the Timoshenko-shell equations of motion to determine the axisymmetric response of a semi-infinite cylinder subjected to a uniform, radial impulse. Using the matrix progression method, Tottenham and Shimizu (1972) conducted a free vibration analysis based on Flugge's theory to determine the eigenvalues and eigenvectors for thin circular cylindrical shells. The results were compared to series solutions, approximate solutions and experimental results by previous authors. Leissa (1973) summarized thin shell theories for natural vibration problems. The equations of motion were developed for shells with various configurations, including cylindrical shells, based on a direct force equilibrium method and energy formulations. Analytical solutions were developed for various boundary conditions. Using the normal mode method, Warburton (1974) provided a series solution for the steady response of simply supported thin cylindrical shells subjected to radial harmonic pressure based on the Novozhilov thin shell theory. The solution considered the effect of hysteretic damping. Using the perturbation method, Chen and Babcock (1975) developed a steady-state solution by solving Donnell's shallow-shell theory for the large amplitude vibration. The results were verified by comparing them to experimental results. Warburton and Soni (1977)

used the modal analysis method to determine the resonant response of simply supported thin and thick orthotropic cylindrical shells, based on the Timoshenko shell theory, with three levels of hysteretic damping. Using the direct force equilibrium method, Soedel (1983) developed the governing equations of motion and obtained the closed form solution for simply supported orthotropic cylindrical shells. Weicker (2008) and Weicker et al. (2010) simplified the strain-displacement relations for pipe elbows from Ohtsubo and Watanabe (1978) to straight pipe. They expanded the displacements into Fourier series and developed a series solution for general loading. Using tensor analysis, Salahifar and Mohareb (2010) and Salahifar (2011) developed a generalized thin-shell theory and provided a series solution for the steady state response of pipes under harmonic forces.

2.6.2. Computational solutions

Using the finite difference method, Forrestal et al. (1972) studied the dynamic response of a clamped cylinder subjected to pressure pulses based on the Timoshenko shell theory. Using the fourth-order Runge Kutta integration method, Radhamohan and Maiti (1977) studied the effect of thickness variation of cylinders on natural frequencies based on Sanders's non-linear shell theory. Using an iterative technique, Leissa and Iyer (1981) determined the resonant frequencies and peak response amplitudes for a pipe subjected to sinusoidal radial pressure. Young's modulus and displacements were expressed as complex variables to incorporate the effect of damping. Based on Love's shell theory, Sivadas and Ganesan (1991) determined the natural frequencies of thin circular cylindrical shells with variable thicknesses using finite element analysis.

Based on a linear thin-shell theory, Bogner et al. (1967) developed a four-node shell element with 12 degrees of freedoms per node. The longitudinal, tangential, and radial displacements were related to the nodal displacements using bilinear interpolation along with the longitudinal and tangential directions. Consistent mass matrices were developed to determine the natural frequency response. Cantin and Clough (1968) developed a four-node curved, cylindrical-shell finite element with 24 degrees of freedom. They used modified bilinear interpolation for longitudinal and tangential displacement and modified bi-cubic interpolation for radial displacement with six rigid-body modes included. Ashwell and Sabir (1972) developed a rectangular cylindrical shell element with 20 degrees of freedom. Based on the Timoshenko shell theory, independent strain functions rather than displacement functions were used to develop the stiffness matrix. In the strain-based

element, the displacement fields were coupled and included six rigid-body modes exactly. Fan and Luah (1995) developed a doubly curved finite element for free vibration analysis of general thin shell structures. The displacements were expanded using spline functions. Ohtsubo and Watanabe (1978) developed an elbow finite element for pipes under general loading. Using the virtual work principle, the authors obtained the discretized equilibrium equations for pipe by interpolating the displacement fields using second-order Hermitian functions along the longitudinal direction and Fourier series around the pipe circumference. Warping was incorporated into the formulation by retaining higher harmonic terms when interpolating the longitudinal displacement. Takeda et al. (1979) developed a finite element based on thin shell theory that incorporates the effects of transverse shear deformation. The pipe circumference was subdivided into several four-node rectangular shell elements with the tangential and radial displacements, rotations about longitudinal and tangential axes. These four displacements were interpolated using two-dimensional Lagrangian bilinear functions. The longitudinal displacement at the center of the section was expanded using Fourier series around the circumference and linearly along the longitudinal direction. Bathe and Almeida (1980) developed a four-node elbow finite element that behaved as a curved beam along the longitudinal direction with sectional ovalization. Longitudinal and transverse displacements, and angle of twist, were interpolated cubically along the longitudinal direction and radial displacements were interpolated with trigonometric functions around the circumference to capture the cross-sectional ovalization effect. Using exact shape functions developed from the series solution of the equilibrium equations in (Weicker 2008; Weicker et al. 2010a), Weicker et al. (2010b) developed a finite element solution for the response of the thin-walled pipe subjected to static general loading. Based on the exact solution for steady response of circular cylindrical shells (Salahifar 2011; Weicker et al. 2010a) , Salahifar and Mohareb (2012) developed a finite element solution for the steady state response for thin circular cylinders subjected to general harmonic forces.

2.6.3. Shell solutions with damping

As mentioned in the previous section, Warburton (1974) and Warburton and Soni (1977) introduced hysteretic damping by assigning to Young's modulus and shear modulus complex values. They investigated the effects of different levels of damping on the harmonic response of cylindrical shells subjected to sinusoidal point loading. In the series solution for vibration of cylindrical shells, Chen and Babcock (1975) introduced a damping factor to replicate the response-

frequency relationships as observed in experimental results. Based on a series solution, Leissa and Iyer (1981) introduced structural damping using complex Young's modulus to determine the response of circular cylindrical shells subjected to sinusoidal radial pressure. In the dynamic analysis of ring-stiffened circular cylindrical shells, Beskos and Oates (1981) introduced viscous damping terms in the equations of equilibrium for external viscous damping and used the Kelvin viscoelastic model to introduce internal damping. Huang and Fuller (1997) studied the effect of dynamic absorbers on reducing the vibration and sound pressure in closed elastic cylindrical shells subjected to external point load and distributed forces. Pellicano and Avramov (2007) introduced Rayleigh damping in the analysis of the dynamic response of a circular cylindrical shell connected to a rigid disk. Using the finite element method with a central difference time integration scheme, Cui et al. (2016) studied the transient response of pipes with different levels of damping subjected to impulse uniform pressure. The pipe was discretized using an axisymmetric element developed by the authors based on Kirchhoff-Love thin shell theory and a Rayleigh damping model. In the above studies, damping has been represented either using a complex Young's modulus, or Rayleigh damping matrix. In addition to energy dissipation due to structural damping, time integration schemes can induce numerical dissipation (or energy dissipation). Little attention was given to this type of damping in cylindrical thin shells and will thus be investigated in the present study.

2.6.4. Elements in ABAQUS for pipe modeling

ABAQUS (2011) is a commercial finite element software with a large library of elements, and analysis types such as static, natural vibration, time history response analysis, etc. This section provides an overview of the ABAQUS elements that are able to model thin pipes subjected to axisymmetric loadings. They are beam-like or shell-theory-based elements. Then, the limitations of adopting these elements in the water hammer models are discussed.

ABAQUS Pipe elements are special beam elements with ring cross-sections that are able to capture the effects of internal pressure. Pipe elements in ABAQUS have either two or three nodes. The displacement fields are interpolated linearly or quadratically along the longitudinal axis respectively. In 2D analysis, pipe elements have three degrees of freedom at each node; longitudinal and transverse displacements and rotation about the axis normal to the plane. In 3D analysis, each node has six degrees of freedom: three displacements and three rotations. Since

these elements are derived based on beam theory, they are unable to capture the shell cross-section deformational behavior.

ABAQUS Elbow elements are beam-like elements with two or three nodes. Like the ABAQUS pipe elements, they capture internal pressure effects. Unlike beam elements, they are able to capture warping and ovalization in a manner akin to shell elements. The displacement fields are interpolated in the circumferential direction using up to seven Fourier modes (zero to six) and are interpolated in the longitudinal direction using polynomial functions (linear or quadratic). Internally, Elbow elements have a large number of degrees of freedom. Externally, the user has access to a limited number of these degrees of freedom, three displacements, and thee rotations. The zero (axisymmetric) mode can be used to model axisymmetric problems and can be considered to model the water hammer problem. The Elbow element implementation in ABAQUS has a few limitations that make it impractical to use for the water hammer problem investigated in the present study: (1) the element cannot model pressure changes along its length, (2) the radial displacement response cannot be output, (3) the time-dependent pressure and friction forces during water hammer require continuous (and impractical) data transfer between the water hammer module and ABAQUS, and (4) the pipe response to water hammer as predicted by the ELBOW model would involve continuous and impractical data transfer between the fluid model and structural model in a two-way coupling water hammer model.

Another types of element in ABAQUS are cylindrical membrane elements that do not have a bending stiffness. Such elements are curved in one direction and have either six or nine nodes. Each node has three displacements. The displacement fields are interpolated in the circumferential direction using trigonometric functions. In the radial or cross-sectional plane, they are interpolated using isoparametric functions. Without capturing the bending effects, cylindrical membrane elements are not suitable for thin pipes subjected to internal pressure with large longitudinal pressure gradients that bending effects are significant.

Axisymmetric shell elements (SAX1, SAX2, etc.) are special shell elements for axisymmetric shells with axisymmetric deformations. These elements have two or three nodes with three degrees of freedom at each node, longitudinal and radial displacement, and rotation about the axis normal to the longitudinal-radial plane. These elements are efficient for thin shells with axisymmetric responses and akin to the proposed element. They can be used to assess the accuracy of the

proposed element. But these elements have limitations similar to the Elbow elements. Except for limitation (2), these limitations make ABAQUS axisymmetric shell elements impractical for solving pipe response during water hammer.

Shell elements are another option for pipe modeling in ABAQUS to capture the shell behaviors. Among general shell elements, the S4R element is a robust and commonly used 4-node shell element with hourglass control for general shell structures. This element has six degrees of freedom for each node, three displacements, and three rotations. A large number of elements would be needed to accurately mesh pipes. As a consequence, the number of DOFs for pipes are large and dynamic analysis such as the one contemplated in the present study would be time-consuming.

2.7. Research needs

Based on the literature review for water hammer without column separation, the following problems are important to advance water hammer models to simulate industry pipe systems.

1) The WFB models require weighting functions that depend on the specifics of the flow (e.g., Vardy et al. 1993; Vardy and Brown 1995, 2003). The use of weighting functions is time-consuming and storage expensive since all velocities computed are needed to be stored (e.g., Zielke 1968). In contrast, the IAB models are computationally efficient and simpler to program for practical applications. Both type models provide accurate predictions for the maximum and minimum pressures near the valve (e.g., Adamkowski and Lewandowski 2006; Vardy and Brown 2010; Vítkovský et al. 2000). However, the pressure wave front as predicted by the IAB models is not as smooth as those observed in experimental studies (e.g., Adamkowski and Lewandowski 2006), which needs to be improved regarding the wave front smoothing.

2) The classical and extended water hammer models are based on Eq. (2.16) which relates the pressure to the hoop stress in the pipe. This assumption neglects the influence of bending stiffness in the pipe wall. It also leads to near-discontinuity of the radial displacement at the discontinuity wave front (Appendix A), which is unattainable based on physical grounds. Meanwhile, the use of Eq. (2.16) relating hoop stress to the pressure leads to a constant wave speed, which simplifies the mass conservation equation, leading to monolithic models, as is the case for the classical and extended water hammer models. In the monolithic models, the shortage of the structural response is embedded in the governing equations for the fluid domain.

3) The water hammer models accounting for the fluid-structural interaction effects are based on a uniform velocity profile through the flow cross-section. In order to simulate the velocity distribution along the cross-section and the corresponding energy dissipation, two- or three-dimensional models should be adopted to discretize the fluid domain.

4) The extended water hammer models have been validated for the simulation of pipe networks, in which straight pipes are connected by elbows. However, there is no model accounting for the centroid force to simulate a water hammer in a curved pipe.

The above problems indicate that the conservation water hammer models are developed on strict assumptions. Water hammer models for general cases are necessary to be proposed to capture more features of practical pipe systems. The present study focuses on the first two problems. Accounting for the energy dissipation at the pipe inlet, the present study is proposed to improve the accuracy of the prediction of the pressure wave front. To remedy the discontinuity of the assumption for pipe response, a displacement-based finite element is tailored for the analysis water hammer phenomenon. A partitioned approach is adopted in the two-way coupling water hammer model to overcome the limitations of the monolithic approach. The partitioned approach also has the potential for the development of advancing water hammer models for the third and fourth perspectives listed above.

2.8. List of symbols

A_f =the pipe cross-sectional area (m^2)

A_i, B_i =Constants in the exact weighting function proposed by Zielke (1968)

A_s =the pipe wall cross-sectional area (m^2)

a =water hammer wave speed (m/s)

c =the constant in the classical water hammer wave speed related to pipe boundary conditions

E =the Young's modulus of pipe material (Pa)

$f(t)$ =valve closure function

G =the shear modulus of the pipe material (Pa)

g =the gravitational acceleration (m/s^2)

H_{res} =the hydraulic head at the pipe inlet (m)

h_s =the head loss for the steady part in the unsteady friction model (m)

h =pipe wall thickness (m)

I_s =the moment of inertia of the pipe cross-section (m^4)

J_s =the Saint-Venant torsional constant (Pa)

K_f =the bulk modulus for water (Pa)

k =empirical parameter in the Instantaneous acceleration-based unsteady friction model

M_z =bending moment (N·m)

P =Average fluid pressure along the cross-section (Pa)

P_{val} =the pressure acting on the valve (Pa)

Q_y =the vertical shear force (N)

R =radius of pipe cross-section (m)

s =surface

t =time (s)

$\dot{u}_x$ =the pipe wall longitudinal velocity (m)

$\dot{u}_y$ =is the vertical velocity of the pipe (m)

V =average fluid longitudinal velocity along cross-section (m)

V_0 =the initial velocity (m)

W =weighting function of time

w =the radial displacement (m)

x =the longitudinal coordinate (m)

β =the momentum correction coefficient

ε_x =longitudinal strain

ε_θ =the circumferential strain

$\dot{\theta}_z$ =the rotational pipe velocity in $x-y$ plane (rad)

κ =the shear coefficient for Timoshenko beam theory

ν =the Poisson ratio of the pipe

ρ_f =fluid density (kg/m^3)

ρ_s =pipe wall density (m)

σ_x =longitudinal stress (Pa)

σ_θ =the hoop stress (Pa)

τ_w =shear stress acting longitudinally at the fluid–pipe interface (Pa)

υ =the Kinematic viscosity of the fluid

Ω =volume (m^3)

F =external force

n =vector normal to the surface of the control volume

V =velocity vector

$sign(\bullet)$ =sign function

CV =the control volume

CS =the control surface

2.9. References

Abani, N., and Ghandhi, J. B. (2012). "Behavior of Unsteady Turbulent Starting Round Jets." *J. Fluids Eng.*, 134(6), 061202.

ABAQUS. (2011). "ABAQUS analysis user's manual." Dassault Systèmes Simulia Corp, Providence, RI,USA.

Adamkowski, A., and Lewandowski, M. (2006). "Experimental Examination of Unsteady Friction Models for Transient Pipe Flow Simulation." *J. Fluids Eng.*, 128(6), 1351.

Afshar, M. H., and Rohani, M. (2008). "Water hammer simulation by implicit method of characteristic." *Int. J. Press. Vessel. Pip.*, 85(12), 851–859.

Arnold, R. N., and Warburton, G. B. (1949). "Flexural vibrations of the walls of thin cylindrical shells having freely supported ends." *Proc. R. Soc. London. Ser. A. Math. Phys. Sci.*, 197(1049), 238–256.

Ashwell, D. G., and Sabir, A. B. (1972). "A new cylindrical shell finite element based on simple independent strain functions." *Int. J. Mech. Sci.*, 14(3), 171–183.

Bathe, K. J., and Almeida, C. A. (1980). "A Simple and Effective Pipe Elbow Element—Linear Analysis." *J. Appl. Mech.*, 47(1), 93–100.

Bergant, A., and Simpson, A. R. (1994). "Estimating unsteady friction in transient cavitating pipe flow." *2nd Int. Conf. Water Pipeline Syst.*, D. S. Miller, ed., BHR Group Conf, Edinburgh, Scotland, 3–15.

Bergant, A., Simpson, A. R., and Vítkovský, J. (2001). "Developments in unsteady pipe flow friction modelling." *J. Hydraul. Res.*, 39(3), 249–257.

Bergant, A., Simpson, A. R., and Vítkovský, J. P. (1999). "Review of unsteady friction models in transient pipe flow." *9th Int. Meet. Behav. Hydraul. Mach. Under Steady Oscil. Cond.*, International Association of Hydraulic Research, Brno, Czech Republic,7-9 Sept.

Beskos, D. E., and Oates, J. B. (1981). "Dynamic analysis of ring-stiffened circular cylindrical shells." *J. Sound Vib.*, 75(1), 1–15.

Bogner, F. K., Fox, R. L., and Schmit, L. A. (1967). "A cylindrical shell discrete element." *AIAA J.*, 5(4), 745–750.

Brunone, B., Golia, U. M., and Greco, M. (1991). "Some remarks on the momentum equation for fast transients." *Hydraul. transients with water column Sep. Work. Grop 1971-1991 Synth. Rep.*, 201–210.

Brunone, B., Karney, B. W., Mecarelli, M., and Ferrante, M. (2000). "Velocity Profiles and Unsteady Pipe Friction in Transient Flow." *J. Water Resour. Plan. Manag.*, 126:4(236), 236–244.

Budny, D. D., Wiggert, D. C., and Hatfield, F. (1990). "Energy Dissipation in the axially-coupled model for transient flow." *Proc. 6th Int. Conf. Press. Surges*, A. R. D. Thorley, ed., BHRA, Cambridge, UK, 15–26.

Budny, D. D., Wiggert, D. C., and Hatfield, F. J. (1991). "The Influence of Structural Damping on Internal Pressure During a Transient Pipe Flow." *J. Fluids Eng.*, 113(3), 424–429.

Cantin, G., and Clough, R. W. (1968). "A curved, cylindrical-shell, finite element." *AIAA J.*, 6(6), 1057–1062.

Chaudhry, M. H., and Hussaini, M. Y. (1985). "Second-Order Accurate Explicit Finite-Difference Schemes for Waterhammer Analysis." *J. Fluids Eng.*, 107(4), 523–529.

Chen, H., Liu, H., Chen, J., and Wu, L. (2013). "Chebyshev super spectral viscosity method for water hammer analysis." *Propuls. Power Res.*, 2(3), 201–207.

Chen, J. C., and Babcock, C. D. (1975). "Nonlinear Vibration of Cylindrical Shells." *AIAA J.*, 13(7), 868–876.

Cui, X. Y., Wang, G., and Li, G. Y. (2016). "A nodal integration axisymmetric thin shell model using linear interpolation." *Appl. Math. Model.*, 40(4), 2720–2742.

Duan, H.-F., Ghidaoui, M. S., Lee, P. J., and Tung, Y. K. (2012). "Relevance of Unsteady Friction to Pipe Size and Length in Pipe Fluid Transients." *J. Hydraul. Eng.*, 138(2), 154–166.

Duan, H. F., Meniconi, S., Lee, P. J., Brunone, B., and Ghidaoui, M. S. (2017). "Local and integral energy-based evaluation for the unsteady friction relevance in transient pipe flows." *J. Hydraul. Eng.*, 143(7), 04017015.

Fan, S. C., and Luah, M. H. (1995). "Free vibration analysis of arbitrary thin shell structures by using spline finite element." *J. Sound Vib.*, 179(5), 763–776.

Ferras, D., Manso, P. A., Covas, D. I. C., and Schleiss, A. J. (2017a). "Fluid–structure interaction in pipe coils during hydraulic transients." *J. Hydraul. Res.*, 55(4), 491–505.

Ferras, D., Manso, P. A., Schleiss, A. J., and Covas, D. I. C. (2017b). "Fluid-structure interaction in straight pipelines with different anchoring conditions." *J. Sound Vib.*, 394, 348–365.

Ferràs, D., Manso, P. A., Schleiss, A. J., and Covas, D. I. C. (2016). "Fluid-structure interaction in straight pipelines: Friction coupling mechanisms." *Comput. Struct.*, 175, 74–90.

Flugge, W. (1960). Stresses in shells. Sprimger, Berlin.

Forrestal, M. J., Sliter, G. E., and Sagartz, M. J. (1972). "Stresses Emanating From the Supports of a Cylindrical Shell Produced by a Lateral Pressure Pulse." *J. Appl. Mech.*, 39(1), 124–128.

Forsberg, K. (1964). "Influence of boundary conditions on the modal characteristics of thin cylindrical shells." *AIAA J.*, 2(12), 2150–2157.

Gale, J., and Tiselj, I. (2005). "Applicability of the Godunov's method for fundamental four-equations FSI model." *Conf. Int. Conf. Nucl. Energy New Eur.* 2005, B. Mavko and I. Kljenak, eds., Bled, Slovenia.

Gale, J., and Tiselj, I. (2008). "Godunov's Method for Simulatinons of Fluid-Structure Interaction in Piping Systems." *J. Press. Vessel Technol.*, 130(3).

Ghidaoui, M. S., Karney, B. W., and McInnis, D. A. (1998). "Energy Estimates for Discretization Errors in Water Hammer Problems." *J. Hydraul. Eng.*, 124(4), 384–393.

Ghidaoui, M. S., Zhao, M., McInnis, D. A., and Axworthy, D. H. (2005). "A review of water hammer theory and practice." *Appl. Mech. Rev.*, 58(1), 49.

Guinot, V. (1998). "Boundary condition treatment in 2×2 systems of propagation equations." *Int. J. Numer. Methods Eng.*, 42(4), 647–666.

Guinot, V. (2000). "Riemann solvers for water hammer simulations by Godunov method." *Int. J. Numer. Methods Eng.*, 49(7), 851–870.

Heinsbroek, A. G. T. J., and Tijsseling, A. S. (1994). "The influence of support rigidity on waterhammer pressures and pipe stresses." BHR Group, *Proc.of Second Int.Conf.on Water Pipeline Syst.*, D. S. Miller, ed., London,UK:Mechanical Engineering Publications, Edinburgh, Scotland.

Henclik, S. (2018). "Numerical modeling of water hammer with fluid–structure interaction in a pipeline with viscoelastic supports." *J. Fluids Struct.*, 76, 469–487.

Holmboe, E. L., and Rouleau, W. T. (1967). "The Effect of Viscous Shear on Transients in Liquid Lines." *J. Basic Eng.*, 89(1), 174–180.

Huang, Y. M., and Fuller, C. R. (1997). "The effects of dynamic absorbers on the forced vibration of a cylindrical shell and its coupled interior sound field." *J. Sound Vib.*, 200(4), 401–418.

Johnston, D. N. (2006). "Efficient methods for numerical modeling of laminar friction in fluid lines." *J. Dyn. Syst. Meas. Control*, 128(4), 829–834.

Joung, I., and Shin, Y. S. (1987). “A New Model on Transient Wave Propagation in Fluid-Filled Tubes.” *J. Press. Vessel Technol.*, 109(1), 88–93.

Karney, B. W., and Ghidaoui, M. S. (1997). “Flexible discretization algorithm for fixed-grid MOC in pipelines.” *J. Hydraul. Eng.*, 123:11(1004), 1004–1011.

Keller, R. J., and Rastogi, A. K. (1977). “Design chart for predicting critical point on spillways.” *J. Hydraul. Div.*, 103(12), 1417–1429.

Kruisbrink, A. C. H., and Heinsbroek, A. G. T. J. (1993). “Fluid-Structure Interaction in Non-Rigid Pipeline Systems — Large Scale Validation Tests — (Eureka Project 274) BT Topics in Applied Mechanics: Integration of Theory and Applications in Applied Mechanics.” J. F. Dijksman and F. T. M. Nieuwstadt, eds., Springer Netherlands, Dordrecht, 57–64.

Lai, C. (1988). “Comprehensive Method of Characteristics Models for Flow Simulation.” *J. Hydraul. Eng.*, 114:9(1074), 1074–1097.

Lavooij, C. S. W., and Tijsseling, A. S. (1991). “Fluid-structure interaction in liquid-filled piping systems.” *J. Fluids Struct.*, 5(5), 573–595.

Lee, P. J., Duan, H. F., Ghidaoui, M., and Karney, B. (2013). “Frequency domain analysis of pipe fluid transient behaviour.” *J. Hydraul. Res.*, 51(6), 609–622.

Lee, U., and Kim, J. (1999). “Dynamics of Branched Pipeline Systems Conveying Internal Unsteady Flow.” *J. Vib. Acoust.*, 121(1), 114–122.

Lee, U., Pak, C. H., and Hong, S. C. (1995). “The dynamics of a piping system with internal unsteady flow.” *J. Sound Vib.*, 180(2), 297–311.

Leissa, A. W. (1993). Vibration of Shells. NASA Report SP-288, 1973. Reprinted in book form by the Acoustical Society of America in 1993.

Leissa, A. W., and Iyer, K. M. (1981). “Modal response of circular cylindrical shells with structural damping.” *J. Sound Vib.*, 77(1), 1–10.

McInnis, D. A., Karney, B. W., and Axworthy, D. H. (1997). “Efficient valve representation in fixed-grid characteritics method.” *J. Hydraul. Eng.*, 123(8), 709–718.

Ohtsubo, H., and Watanabe, O. (1978). “Stress Analysis of Pipe Bends by Ring Elements.” *J. Press. Vessel Technol.*, 100(1), 112–122.

Pellicano, F., and Avramov, K. V. (2007). “Linear and nonlinear dynamics of a circular cylindrical shell connected to a rigid disk.” *Commun. Nonlinear Sci. Numer. Simul.*, 12(4), 496–518.

Pezzinga, G. (2000). “Evaluation of unsteady flow resistances by quasi-2D or 1D models.” *J. Hydraul. Eng.*, 126:10(778), 778–785.

Radhamohan, S. K., and Maiti, M. (1977). “Vibrations of initially stressed cylinders of variable thickness.” *J. Sound Vib.*, 53(2), 267–271.

Reismann, H., and Pawlik, P. S. (1968). “Plane-strain dynamic response of a cylindrical shell—a comparison study of three different shell theories.” *J. Appl. Mech.*, ASME, 35(2), 297–305.

Sagartz, M. J., and Forrestal, M. J. (1969). “Transient stresses at a clamped support of a circular cylindrical shell.” *J. Appl. Mech.*, 36(2), 367–369.

Salahifar, R. (2011). “Analysis of Pipeline Systems under Harmonic Forces.” Ph.D. thesis, University of Ottawa.

Salahifar, R., and Mohareb, M. (2010). “Analysis of circular cylindrical shells under harmonic forces.” *Thin-Walled Struct.*, 48(7), 528–539.

Salahifar, R., and Mohareb, M. (2012). “Finite element for cylindrical thin shells under harmonic forces.” *Finite Elem. Anal. Des.*, 52, 83–92.

Shimada, M., Brown, J., Leslie, D., and Vardy, A. (2006). “Time-Line Interpolation Errors in Pipe Networks.” *J. Hydraul. Eng.*, 132(3), 294–306.

Shimada, M., Brown, J. M., and Vardy, A. E. (2008). “Interpolation Errors in Rectangular and Diamond Characteristic Grids.” *J. Hydraul. Eng.*, 134(10), 1480–1490.

Shuy, E. B. (1995). “Approximate wall shear equation for unsteady laminar pipe flows.” *J. Hydraul. Res.*, 33(4), 457–469.

Sibetheros, A. I., Holley, R. E., and Branski, M. J. (1991). “Spline Interpolations for Water Hammer Analysis.” *J. Hydraul. Eng.*, 117:10(1332), 1332–1351.

Simpson, A. R. (1986). “Large water hammer pressures due to column separation in sloping pipes.” Ph.D. thesis, University of Michigan.

Sivadas, K. R., and Ganesan, N. (1991). “Free vibration of circular cylindrical shells with axially varying thickness.” *J. Sound Vib.*, 147(1), 73–85.

Soedel, W. (1983). “Simplified equations and solutions for the vibration of orthotropic cylindrical shells.” *J. Sound Vib.*, 87(4), 555–566.

Streeter, V. L. (1963). Fluid Mechanics (3rd). McGraw-Hill B. Company,INC., Cambridge University Press.

Suzuki, K., Taketomi, T., and Sato, S. (1991). "Improving Zielke's method of simulating frequency-dependent friction in laminar liquid pipe flow." *J. Fluids Eng.*, 113(4), 569–573.

Szymkiewicz, R. (1995). "Method to solve 1D unsteady transport and flow equations." *J. Hydraul. Eng.*, 121(5), 396–403.

Szymkiewicz, R., and Mitosek, M. (2005). "Analysis of unsteady pipe flow using the modified finite element method." *Commun. Numer. Methods Eng.*, Wiley, 21(4), 183–199.

Takeda, H., Asai, S., and Iwata, K. (1979). "A new finite element for structural analysis of piping systems." *Int. Assoc. Struct. Mech. React. Technol.*, T. A. Jaeger and B. A. Boley, eds., North-Holland Publishing Co, Amsterdam, Netherlands, M5/5:1-8.

Tijsseling, A. S. (1996). "Fluid-structure interaction in liquid-filled pipe system: a review." *J. Fluids Struct.*, 10(2), 109–146.

Tijsseling, A. S. (2003). "Exact solution of linear hyperbolic four-equation system in axial liquid-pipe vibration." *J. Fluids Struct.*, 18(2), 179–196.

Tijsseling, A. S. (2007). "Water hammer with fluid–structure interaction in thick-walled pipes." *Comput. Struct.*, 85(11), 844–851.

Tijsseling, A. S. (2009). "Exact Computation of the Axial Vibration of Two Coupled Liquid-Filled Pipes." *Proceedings 2009 ASME Pressure Vessels and Piping Division Conference*, Prague, Czech Republic, July 26-30, 2009.

Tijsseling, A. S., and Lavooij, C. S. W. (1990). "Waterhammer with fluid-structure interaction." *Appl. Sci. Res.*, 47(3), 273–285.

Tijsseling, A. S., and Vardy, A. E. (1996). "Axial modelling and testing of a pipe rack." *Proc. 7th BHR Gr. Int. Conf. Press. Surges Fluid Transients Pipelines Open Channels*, A. Boldy, ed., Mechanical Engineering Publications, Harrogate, UK, 363–383.

Tijsseling, A. S., Vardy, A. E., and Fan, D. (1996). "Fluid-structure interaction and cavitation in a single-elbow pipe system." *J. Fluids Struct.*, 10(4), 395–420.

Tijsseling, A. S., and Vaugrante, P. (2001). "FSI in L-shaped and T-shapred pipe systems." *10th Int. Meet. Work Gr. Behav. Hydraul. Mach. under steady Oscil. Cond.*, Trondhein, Norway.

Tottenham, H., and Shimizu, K. (1972). "Analysis of the free vibration of cantilever cylindrical thin elastic shells by the matrix progression method." *Int. J. Mech. Sci.*, 14(5), 293–310.

Trikha, A. K. (1975). "An efficient method for simulating frequency-dependent friction in transient liquid flow." *J. Fluids Eng.*, ASME, 97(1), 97–105.

Vardy, A., and Brown, J. (1996). “On Turbulent, unsteady, smooth-pipe friction.” *7th Int. Conf. Press. Surges Fluid Transients Pipelines Open Channals*, A. Boldy, ed., BHR Group, Harrogat, England, 289–312.

Vardy, A., and Brown, J. (2007). “Approximation of turbulent wall shear stresses in highly transient pipe flows.” *J. Hydraul. Eng.*, 133:11(1219), 109.

Vardy, A., and Brown, J. M. B. (2010). “Evaluation of unsteady wall shear stress by Zielke’s method.” *J. Hydraul. Eng.*, 136(7), 453–456.

Vardy, A. E., and Brown, J. M. B. (1995). “Transient, turbulent, smooth pipe friction.” *J. Hydraul. Res.*, 33(4), 435–456.

Vardy, A. E., and Brown, J. M. B. (2003). “Transient turbulent friction in smooth pipe flows.” *J. Sound Vib.*, 259(5), 1011–1036.

Vardy, A. E., and Brown, J. M. B. (2004). “Transient turbulent friction in fully rough pipe flows.” *J. Sound Vib.*, 270(1–2), 233–257.

Vardy, A. E., and Hwang, K.-L. (1993). “A weighting function model of transient turbulent pipe friction.” *J. Hydraul. Res.*, 31(4), 533–548.

Vardy, A. E., Kuo-Lun, H., and Brown, J. M. B. (1993). “A weighting function model of transient turbulent pipe friction.” *J. Hydraul. Res.*, 31(4), 533–548.

Vítkovský, J. P., Lambert, M. F., Simpson, A. R., and Bergant, A. (2000). “Advances in unsteady friction modelling in transient pipe flow.” *8th Int. Conf. Preessure Surges*, BHR, The Hague, The Netherlands.

Vítkovský, J., Stephens, M., Bergant, A., Simpson, A., and Lambert, M. (2006). “Numerical error in weighting function-based unsteady friction models for pipe transients.” *J. Hydraul Eng.*, 132(7), 709–721.

Wahba, E. M. (2006). “Runge–Kutta time-stepping schemes with TVD central differencing for the water hammer equations.” *Int. J. Numer. Methods Fluids*, 52(5), 571–590.

Walker, J. S., and Phillips, J. W. (1977). “Pulse Propagation in Fluid-Filled Tubes.” *J. Appl. Mech.*, 44(1), 31–35.

Wang, C., and Yang, J. (2014). “Water Hammer Simulation Using Explicit – Implicit Coupling Methods.” *J. Hydraul. Eng.*, 141(4), 1–11.

Wang, Z.-M., and Tan, S. K. (1997). “Coupled analysis of fluid transients and structural dynamic responses of a pipeline system.” *J. Hydraul. Res.*, 35(1), 119–131.

Warburton, G. B. (1974). “Harmonic Response of Cylindrical Shells.” *J. Eng. Ind.*, 96(3), 994–999.

Warburton, G. B., and Soni, S. R. (1977). “Resonant response of orthotropic cylindrical shells.” *J. Sound Vib.*, 53(1), 1–23.

Weicker, K. (2008). “Finite element formulation for analysis of pipes based on thin shell theory.” Master thesis, University of Ottawa.

Weicker, K., Salahifar, R., and Mohareb, M. (2010a). “Shell analysis of thin-walled pipes. Part I – Field equations and solution.” *Int. J. Press. Vessel. Pip.*, 87(7), 402–413.

Weicker, K., Salahifar, R., and Mohareb, M. (2010b). “Shell analysis of thin-walled pipes. Part II – Finite element formulation.” *Int. J. Press. Vessel. Pip.*, 87(7), 414–423.

Wiggert, D. C., Hatfield, F. J., and Lesmez, M. W. (1986). “Coupled transient flow and structure motion in liquid-filled piping systems.” *Proc. 5th Internaltional Conf. Press. surges*, Hannover, Gernany, 1–9.

Wiggert, D. C., and Tijsseling, A. S. (2001). “Fluid transients and fluid-structure interaction in flexible liquid-filled piping.” *Appl. Mech. Rev.*, 54(5), 455–481.

Wylie, E. B. (1983). “The Microcomputer and Pipeline Transients.” *J. Hydraul. Eng.*, 109(12), 1723–1739.

Wylie, E. B. (1997). “Frictional Effects in Unsteady Turbulent Pipe Flows.” *Appl. Mech. Rev.*, 50(11), S241–S244.

Xu, Y., and Jiao, Z. (2017). “Exact solution of axial liquid-pipe vibration with time-line interpolation.” *J. Fluids Struct.*, 70, 500–518.

Zhao, M., and Ghidaoui, M. S. (2004). “Godunov-Type Solutions for Water Hammer Flows.” *J. Hydraul. Eng.*, 130(4), 341–348.

Zielke, W. (1968). “Frequency-dependent friction in transient pipe flow.” *J. Basic Eng.*, 90(1), 109–115.

2.10. Appendix

2.10.1. A) Pipe response subjected to static step pressure based on the classical water hammer model and the finite element analysis

A pipe length is 30m with a mid-surface radius 330m and thickness 6mm. Pipe Young's modulus is 210GPa, Poisson's ratio is 0.25. Only one end of the pipe is longitudinal restrained. The pipe is subjected to a static step pressure

$$P(x)=\begin{cases} 0, & 0\le x<15\text{m} \\ 98000\text{Pa}, & 15m\le x<30\text{m} \end{cases} \tag{2.33}$$

The corresponding hoop stresses, hoop strains and radial displacement response, as computed by the finite element analysis, are depicted in Figure 2.6. The pressure, hoop stress, hoop strain, and radial displacements are normalized with respect to their peak values. All three fields computed by the model exhibit a gradual variation, in contrast to the pressure which exhibits a discontinuity at $x=15\text{m}$.

Most published water hammer models are based on the assumption that the circumferential stress is proportional to the fluid pressure, e.g.,

$$\sigma_r(x,t)=P(x,t)(R-0.5h)/h \tag{2.34}$$

Under this assumption, the hypothetical case of discontinuous pressure would inevitably lead to discontinuous stress, strain and radial displacement. This is mathematically demonstrated in the following. Based on Eq. (2.34), the constitutive stress-strain

$$\varepsilon_r(x,t)=\left[\sigma_r(x,t)-\nu\sigma_x(x,t)\right]/E \tag{2.35}$$

would leads to the following expression for ε_r:

$$\varepsilon_r(x,t)=\frac{(R-0.5h)}{Eh}P(x,t)-\frac{\nu}{E}\sigma_x(x,t) \tag{2.36}$$

Given the strain-displacement relation

$$\varepsilon_r(x,t)=w(x,t)/R \tag{2.37}$$

Equation (2.36) would lead to the following expression for the radial displacement

$$w(x,t) = R\varepsilon_r(x,t) = \frac{R}{E}\frac{(R-0.5h)}{h}P(x,t) - \frac{R}{E}\nu\sigma_x(x,t) \tag{2.38}$$

If the pressure is a discontinuous function, Equation (2.34) would indicate that the radial stress must also be discontinuous, Equation (2.36) would also imply a discontinuous hoop strain, and Equation (2.38) would indicate a discontinuous radial displacement. The later condition signifies a rupture in the pipe wall, which is neither consistent with the FEA results in Figure 2.6, nor would in general happen based on physical grounds.

Since the elastic constitutive law Eq.(2.35) for the pipe material and the strain-displacement relation Eq. (2.37) are both founded on established principles of mechanics, one must conclude that the proportionality assumption introduced Eq. (2.34) must involve an approximation. The present formulation avoids this approximation by developing a finite element formulation founded on established principles of mechanics, which leads to a more realistic prediction of the pipe response.

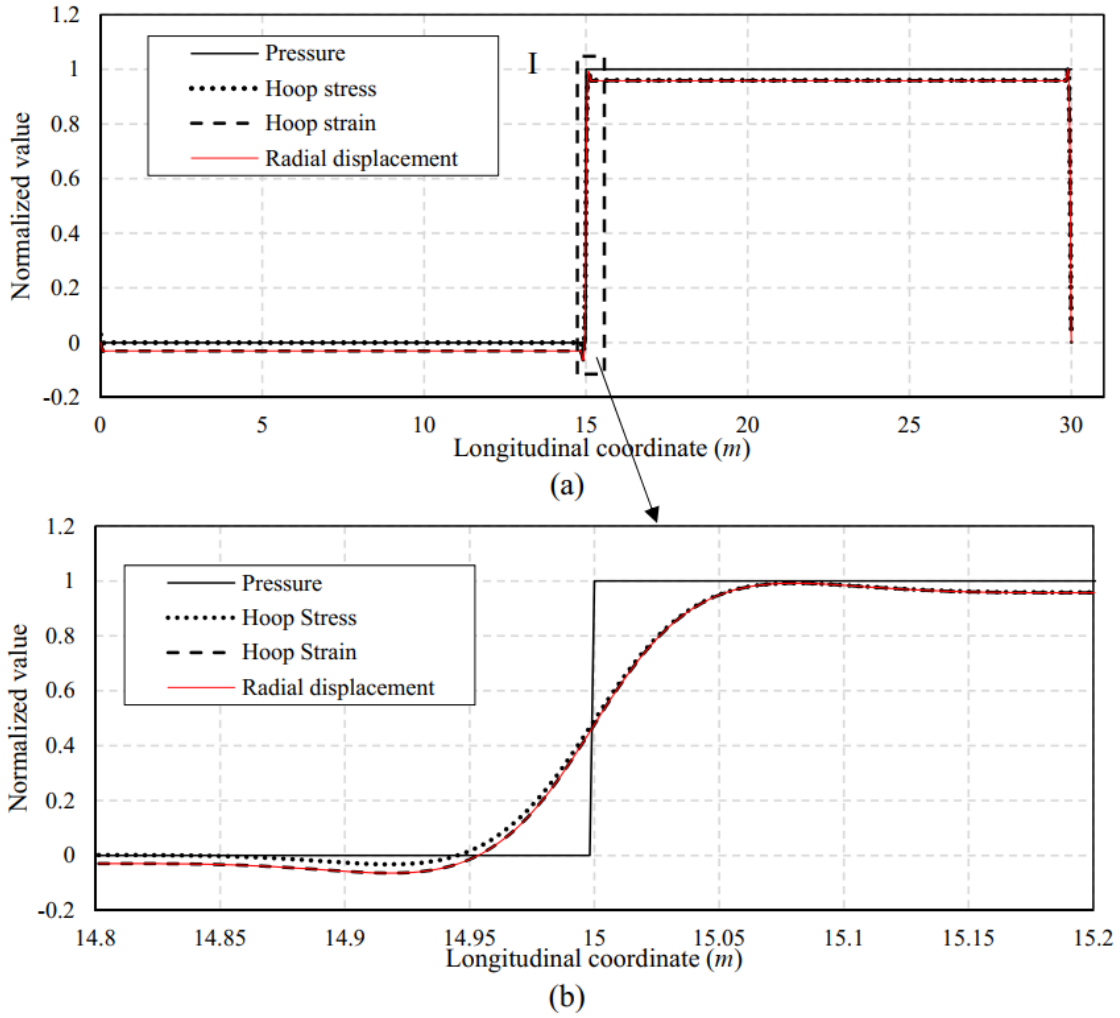

Figure 2.6 Pipe response under static step pressure loading. (a) Normalized values for the whole pipe; (b) Zoom in view of I around the step pressure

2.10.2. B) Example of water hammer pressure propagation based on the classical water hammer theory.

Consider a reservoir-pipe-valve (RPV) system having an upstream reservoir with a head, H_{res}, and a valve located downstream at the end of a uniform cross-section pipe of length L (Figure 2.7).

Prior to valve closure, the flow in the pipe is steady. Due to friction between the fluid and pipe wall, the hydraulic grade line (HGL) slopes uniformly downwards along the pipe length (Figure 2.8a). Immediately after a sudden valve closure, the flowing fluid is suddenly stopped by the valve and the flow decreases to zero in vicinity of the valve, but remains constant along the rest of the pipe (Figure 2.8b). Subsequently, a pressure wave front, H_w, travels upstream at a wave speed a

such that the flow in the pipe between the pressure wave front and the valve is reduced to zero, while the flow in the remaining pipe remains non-zero (Figure 2.8b-c). The pressure wave propagates upstream (Figure 2.8c-d), then travels back (Figure 2.8e-f) and forth between the valve and reservoir for a number of cycles (Figure 2.8b-j) before it dampens out. This transient flow phenomenon due to sudden valve closure is known as *water hammer*.

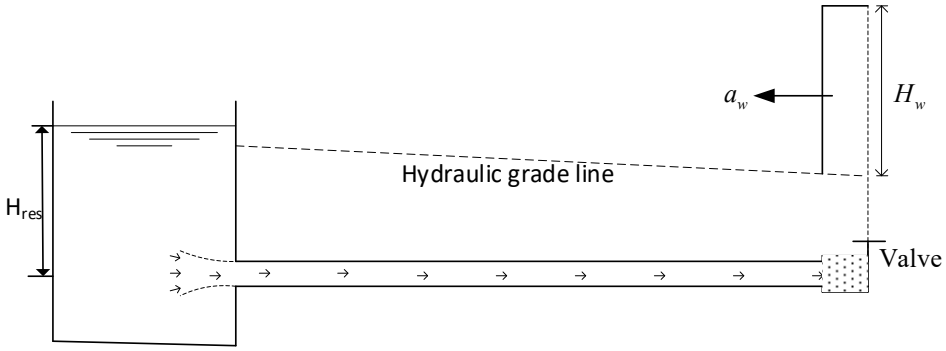

Figure 2.7 Schematic for water hammer in Reservoir-Pipe-Valve (RPV).

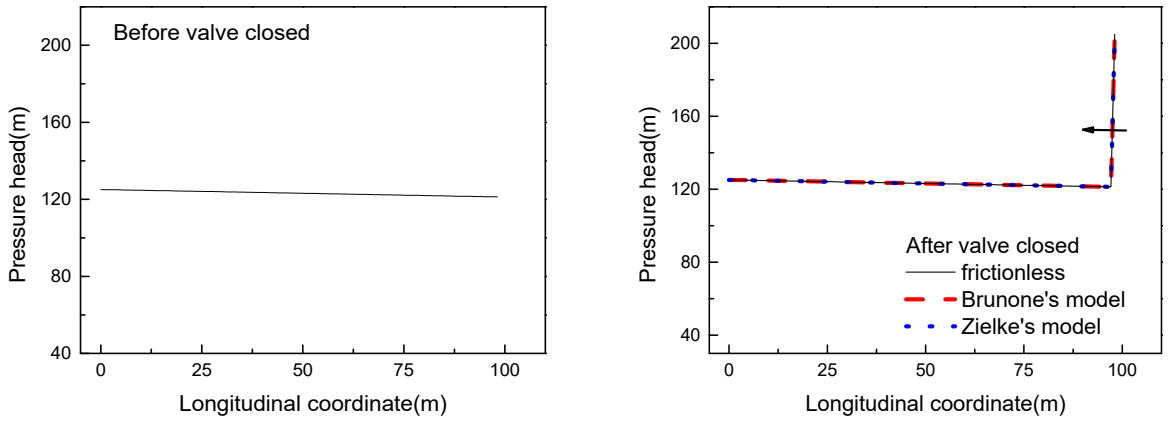

(a) (b)

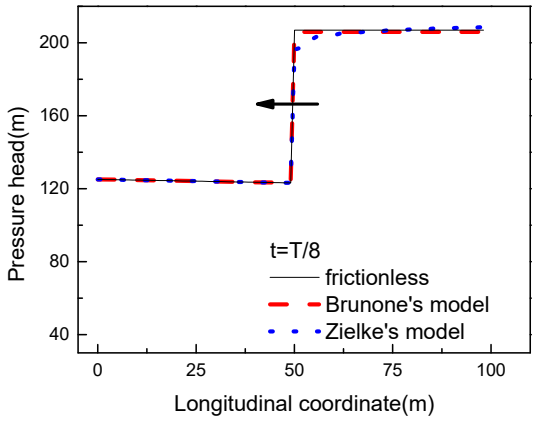
Pressure head(m)
200
160
120
80
40
0
25
50
75
100
Longitudinal coordinate(m)
t=T/8
frictionless
Brunone's model
Zielke's model

(c)

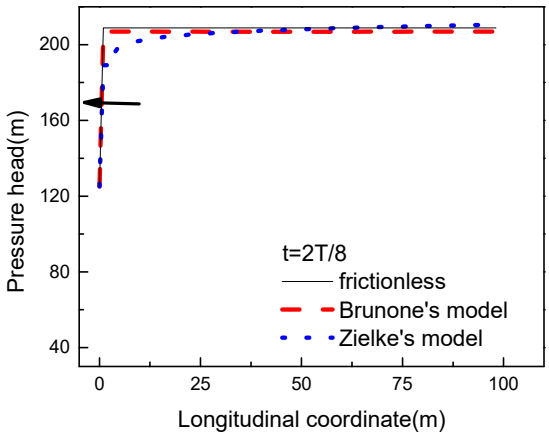
Pressure head(m)
200
160
120
80
40
0
25
50
75
100
Longitudinal coordinate(m)
t=2T/8
frictionless
Brunone's model
Zielke's model

(d)

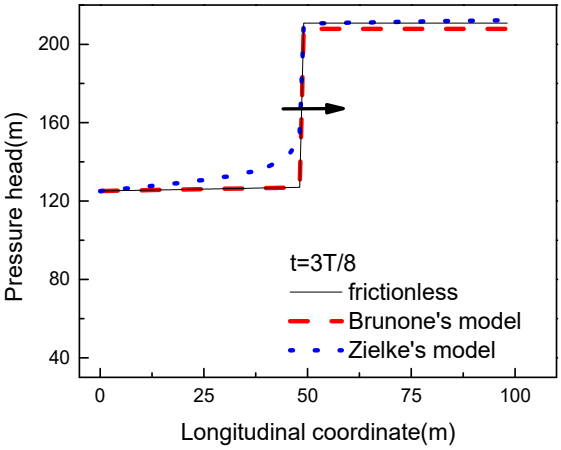
Pressure head(m)
200
160
120
80
40
0
25
50
75
100
Longitudinal coordinate(m)
t=3T/8
frictionless
Brunone's model
Zielke's model

(e)

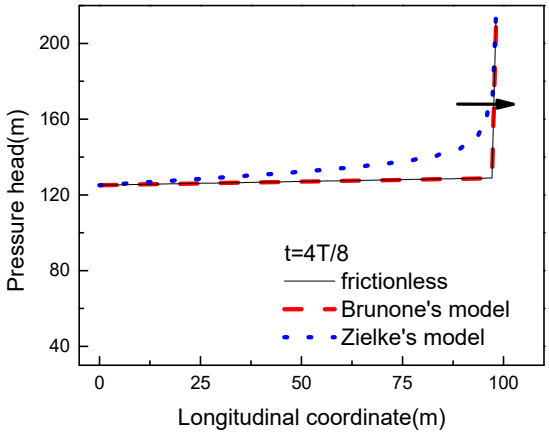
Pressure head(m)
200
160
120
80
40
0
25
50
75
100
Longitudinal coordinate(m)
t=4T/8
frictionless
Brunone's model
Zielke's model

(f)

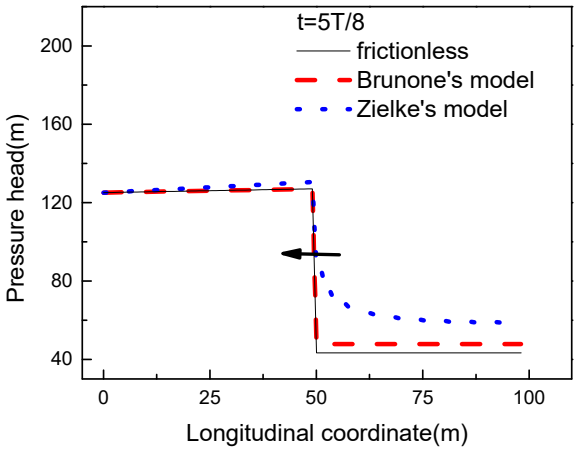
Pressure head(m)
200
160
120
80
40
0
25
50
75
100
Longitudinal coordinate(m)
t=5T/8
frictionless
Brunone's model
Zielke's model

(g)

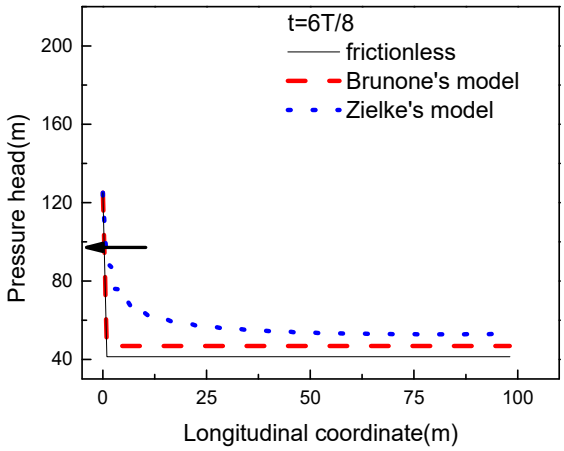
Pressure head(m)
200
160
120
80
40
0
25
50
75
100
Longitudinal coordinate(m)
t=6T/8
frictionless
Brunone's model
Zielke's model

(h)

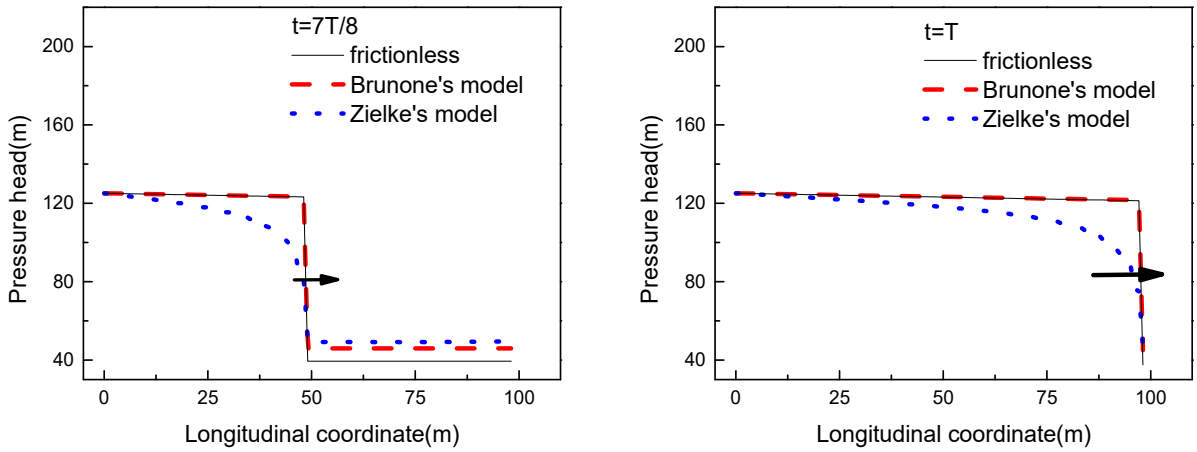

(i) (j)

Figure 2.8 Pressure distribution in one period after sudden valve closure predicted with different friction models. (a) steady flow before valve closure; (b) the moment after valve closure; (c-j) pressure distribution and wave propagation after valve closed. The arrows indicate the wave propagating directions. The experimental system information is obtained from Adamkowski and Lewandowski (2006) with initial velocity 0.94m/s.

Chapter 3 EFFECT OF BOUNDARY ON WATER HAMMER WAVE ATTENUATION AND SHAPE[1]

3.1. Abstract

The present study develops a refined water hammer model by postulating the presence of a water jet within the reservoir as the water hammer wave is reflected at the pipe inlet. The waterjet leads to a new boundary expression that induces a smoothing effect on the pressure wave front by introducing a smoothing factor, which is determined by minimizing the difference between pressure histories predicted numerically and those measured experimentally. The proposed boundary expression is applied in conjunction with the quasi-steady, the Brunone and the Zielke friction water hammer models and is shown to more accurately replicate the peak pressure magnitudes, pressure wave shape, and the phase shifting, when compared to experimental results for a variety of pipe systems and steady flow conditions. Using the quasi-steady and the Brunone models, the study shows that both the friction stresses and the proposed boundary expression attenuate the wave amplitude. However, only the proposed boundary expression smoothens the pressure distribution and delays the wave reflection, in a manner consistent with experimental results. While the conventional Zielke model is shown to attenuate and smoothen the pressure distribution, the proposed boundary expression proved to introduce additional damping and further phase shifting.

3.2. Introduction

Water hammer is a pressure surge or shock wave that oscillates in a pipe system at a speed close to that of sound in water. After rapid valve closure, or after the sudden stop of a pump in a hydraulic system, the pressure in the pipe drastically changes and a pressure wave travels back and forth within the pipe. The traveling pressure wave risks inducing explosion or implosion of the pipe. The pressure wave front distribution and amplitude are affected by the pipe roughness, potential leakages, blockages due to sediment deposition, corrosion, etc. The recorded pressures can be used

---

[1] Cao, H., Nistor, I., Mohareb, M., (2020) "Effect of boundary on water hammer wave attenuation and shape". Journal of Hydraulic Engineering, 146(3): 04020001.

Huade Cao: Conceptualization, Methodology, Software, Validation, Writing - original draft. **Magdi Mohareb:** Conceptualization, Writing - review & editing, Resources, Supervision. **Ioan Nistor:** Conceptualization, Writing - review & editing, Resources, Supervision

to assess the pipe conditions after analyzing the pressure damping patterns. This fluid transient-based methodology is an efficient, convenient and economical way to assess the pipe system conditions, and has recently attracted the attention of several researchers (Duan et al. 2017a, Louati and Ghidaoui 2018, Wang and Ghidaoui 2018, Zhang et al. 2018). Developing an understanding of the water hammer wave damping mechanisms is important for the improvement of transient analysis and hence for pipe safety design.

Wall friction stress is a well-studied mechanism that contributes to water hammer wave damping. This effect is normally captured by adding a friction term to the 1-D water hammer governing equations and represents an improvement in the prediction of pressure wave amplitude damping, when compared to frictionless water hammer models. The simplest friction model is the quasi-steady model (e.g., Watters 1979, Karney and McInnis 1992, Afshar and Rohani 2008, Chaudhry 2014). However, the pressure amplitude decrease predicted by this model has been observed to be slower than that observed in experiments (Wylie 1997, Zielke 1968). Unsteady friction models were then proposed to provide a faster damping representation of the pressure wave. These models are divided into two main classes: (1) convolution-based friction models, and (2) acceleration-based friction models.

Convolution-based models for laminar flows include Zielke's (1968) pioneering work. Aside from being limited to laminar flows, the model is storage-intensive and time-consuming as it requires the velocities for each time step. To overcome these limitations, Trikha (1975) and Suzuki et al. (1991) proposed approximate weighting functions that require the computed velocities only for a few previous time steps. To extend the convolution-based friction model to turbulent flows, approximate-weighting functions were developed for rough-walled pipe (Vardy and Brown 2003) and for smooth pipe (Vardy and Brown 2004), based on idealized radial velocity distribution zones.

Acceleration-based friction models include the work of Brunone et al. (1995) who introduced an empirical unsteady friction coefficient, k_0, to capture the effects of the local instantaneous acceleration and convective acceleration. Vítkovský et al. (2000) reported that Brunone's original model failed to predict the correct sign of the convective acceleration. By analyzing water hammer occurrences in pipes with different flow directions and valve locations, Vítkovský et al. (2006) introduced an additional empirical parameter to increase the accuracy of their model. Other acceleration-based models were applied and verified by several researchers (e.g., Wylie 1997,

Vítkovský et al. 2000, Bergant et al. 2001, Adamkowski and Lewandowski 2006, Tiselj and Gale 2008, Reddy et al. 2012, and Duan et al. 2017b). Compared to convolution-based models, acceleration-based models are easier to implement, computationally efficient, and accurately predict pressure peaks. However, they have two main shortcomings: (1) there is no standard way to determine the value of the unsteady friction coefficient, k_0, and (2) they do not capture the smoothing effect of pressure waves as they travel through the pipe.

Through comparisons to numerical results based on a quasi-2D model, Pezzinga (2000) showed that the unsteady friction coefficient, k_0, depends on the system properties and is a function of location and time. In their discussion of Pezzinga's paper, Brunone et al. (2002) provided an example wherein an increase in the unsteady friction coefficient, k_0, by 35% was found to have little impact on the predicted pressure time-histories at the valve. The unsteady friction stresses were found to be more pronounced in pipe networks than in a single straight pipe (Duan et al. 2009), and to have a smaller effect on pressure wave damping with the increase of the product of the friction coefficient and the Reynolds number of the initial flow (Duan et al. 2012). Commonly, researchers (e.g., Wylie 1997, Brunone et al. 2000, Soares et al. 2013) adopted trial and error procedures to determine the unsteady coefficient, k_0, which provides the best fit. Adamkowski and Lewandowski (2006) quantified the difference between the predicted and measured pressure time-histories at the valve using the difference between the areas enveloped by the pressure histories and the center of the pressure oscillations. Nikpour et al. (2014) and Duan et al. (2017b) used the differences between the predicted and measured peaks of the pressure time-histories at the valve, in order to evaluate the accuracy of their numerical models. Reddy et al. (2012) used the normalized root-mean-square deviation to quantify the difference between the predicted and measured pressure time-histories and determine the unsteady friction coefficient. However, the unsteady friction stresses were found to over-damp the peak pressure values in the first few cycles as their difference minimization method did not capture the effect of peak values. In contrast, the present study proposes an evaluation method that minimizes the areas enclosed by the predicted and measured pressure time-histories at the valve, weighted by the peak pressure value for each cycle.

Experimental studies (e.g., Holmboe and Rouleau 1967, Brunone et al. 2000, Adamkowski and Lewandowski 2006) indicate that pressure waves are smoothened as they propagate into the pipe

and eventually their amplitudes damp out. When using the local balance friction model in (Pezzinga 2009), convolution-based models (e.g., Zielke 1968, Vitkovsky et al. 2004, Szymkiewicz and Mitosek 2013), quasi-2D water hammer models (e.g., Hwang 1991, Pezzinga 1999, Vardy and Zhao and Ghidaoui 2003, and Jang et al. 2016), or 3D-CFD models (Martins et al. 2016, 2017), the first few pressure cycles were found to be initially sharp and gradually become smoother in subsequent cycles. However, pressure waves predicted by quasi-steady and acceleration-based models (e. g, Wylie 1997, Brunone et al. 2000, Soares et al. 2013) exhibit step wave fronts prior to damping out, albeit the model in Pezzinga (2009) was reported to depict a gradual change in the pressure wave. Irrespective of the model used (quasi-steady, acceleration-based, quasi-2D or 3D-CFD), the presence of the friction term does not change the hyperbolic nature of the problem. This fact has been recognized by Szymkiewicz and Mitosek (2007) in their work on quasi-steady and acceleration-based models. Also, the friction in quasi-steady and acceleration-based models do not influence the step wave front, which remains sharp prior to damping out. Hence, the study added a diffusive term to smoothen out the pressure wave front, for cases where the Courant number is less than unity. The above studies suggest the need for introducing an additional energy dissipation mechanism to quasi-steady and acceleration-based models and is the subject of the present study.

Tijsseling et al. (2010) pointed out that the location for pressure wave reflection was inside the reservoir rather than at the pipe entrance. By comparing the pressure wave speeds in pipes with one end closed to those with both ends closed, Mitosek and Szymkiewicz (2016) measured the delay time of the pressure wave reflections from the reservoir. The authors inferred that the delay was due to the occurrence of a water jet when water was pumped into the reservoir by the returning pressure wave, and that the pressure wave was reflected at some interface within the reservoir.

Considering the occurrence of a water jet when the pressure wave reaches the upstream pipe entrance, the authors are herein proposing a boundary expression in order to improve the simplified classical boundary expression. The proposed boundary expression is further employed in the quasi-steady and Brunone's models (Brunone et al. 1995, Bergant et al. 1999), as well as in Zielke's (1968) model, which are solved using the method of characteristics (MOC). The study then introduces a difference minimization method to determine the reservoir smoothing factor associated with the new boundary expression, as well as the unsteady friction coefficient in the

context of the Brunone model. The proposed boundary expression will be shown to introduce an additional energy dissipation mechanism. Specifically, it widens the predicted pressure wave fronts and damps them out in patterns that are identical to experimental observations.

3.3. Problem statement

Consider a reservoir-pipe-valve system with a horizontal pipe of length L with a uniform cross-section, an upstream reservoir of pressure head, H_{res}, and a valve located downstream of the pipe (Figure 3.1). Prior to valve closure, the flow in the pipe has a constant velocity, V_0. Immediately after sudden valve closure, the flow is stopped and the pressure in the vicinity of the valve increases significantly. Subsequently, the increased pressure travels upstream at wave speed, a, and then travels back and forth between the valve and reservoir before it damps out. It is required to develop a water hammer model that accounts for the influence of the upstream reservoir on the pressure wave attenuation and shape.

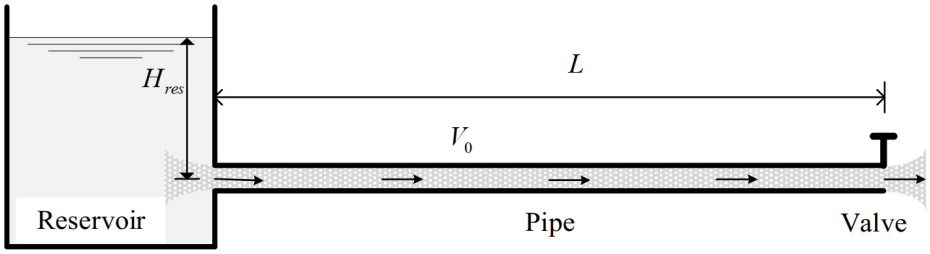

Figure 3.1 Schematic of the Reservoir-Pipe-Valve system.

3.4. Overview of relevant literature

The continuity and momentum equations for water-hammer flow (e.g., Watters 1979, Ghidaoui et al. 2005 and Chaudhry 2014) are

$$\frac{\partial H}{\partial t}+\frac{a^2}{g}\frac{\partial V}{\partial x}=0 \tag{3.1}$$

$$\frac{\partial H}{\partial x}+\frac{1}{g}\frac{\partial V}{\partial t}+J=0 \tag{3.2}$$

where H is the piezometric head, V is the flow velocity, g is the gravitational acceleration, J is the friction head loss, and a is the water hammer wave speed. The friction head loss per unit length J is the summation of quasi-steady head loss, J_q, and unsteady head loss, J_u, i.e.,

$$J = J_q + J_u \tag{3.3}$$

where the quasi-steady friction head loss is $J_q = f_q V|V|/2gD$ and f_q is identical to the friction coefficient for steady flow in the pipe. For a laminar flow with a Reynolds number, $\mathrm{Re} \le 2300$, the friction coefficient is $f_q = 64/\mathrm{Re}$. For a turbulent flow with $\mathrm{Re} > 2300$, the friction coefficient is given by $1/\sqrt{f_q} = -1.8\log\left[6.9/\mathrm{Re} + (\varepsilon/3.7D)^{1.11}\right]$ as proposed by Haaland (1983), where ε is the pipe roughness. The Brunone model (Brunone et al. 1995, Brunone and Morelli 1999) improved by Bergant et al. (1999) in the form $J_u = k_0\left(\partial V/\partial t + a\ \mathrm{sign}(V)|\partial V/\partial x|\right)/g$ is used in the present study, in which *sign* is the sign function. The value of the unsteady friction coefficient, k_0, can be obtained either by using the difference minimization method or by using the Vardy and Brown's equation (1995, 2003), given as

$$k_0 = 2\sqrt{C^*}; \qquad C^* = \min\left(0.00476, 7.41/\mathrm{Re}^{\log(14.3/\mathrm{Re}^{0.05})}\right) \tag{3.4}$$

The Zielke model (1968) is also investigated to determine the unsteady friction head loss. The MOC is used to transform the governing partial differential equations, Eqs.(3.1) and (3.2), into ordinary differential equations along two characteristic lines, $dx/dt = \pm a$. The governing equations can be solved using a rectangular scheme (e.g., Vítkovský et al. 2000, Shimada et al. 2008) with a Courant number $C_r = a\Delta t/\Delta x = 1$, where Δt is the time increment and $\Delta x = L/n$ is the discretization length along the pipe, n being the number of subdivisions between the upstream reservoir and the valve. Each internal node ($i = 2,...,n$) can be solved along two characteristic lines. At the upstream reservoir, $i = 1$, the pressure head, H_{res}, is known, i.e., $H_1^{t+\Delta t} = H_{res}$. Applying the characteristic equation along $C-$ yields

$$V_1^{t+\Delta t} = \frac{g}{a}\left(H_{res} - H_2^t - J_2^t \Delta x\right) + V_2^t \tag{3.5}$$

At the downstream valve, $i = n+1$, the velocity decreases to zero after the valve is closed, i.e., $V_{n+1}^{t+\Delta t} = 0$, and applying the characteristic equation along $C+$ yields

$$H_{n+1}^{t+\Delta t} = H_n^t + \frac{a}{g} V_n^t - J_n^t \Delta x \tag{3.6}$$

The boundary equations (5) and (6) were applied within the finite difference technique (e.g., Chaudhry and Hussaini 1985) and finite volume scheme (e.g., Zhao and Ghidaoui 2004). In the present study, they are applied within the MOC along the characteristic lines.

In the investigation of the energy dissipation of the system, the total internal energy, $U(t)$, and the kinetic energy, $T(t)$, are computed (e.g., Karney 1990), by

$$U(t) = \frac{\rho \pi D^2}{8} \left(\frac{g}{a} \right)^2 \int_{x=0}^{x=L} \left[H(x,t) - H_{res} \right]^2 dx \tag{3.7}$$

$$T(t) = \frac{\rho \pi D^2}{8} \int_{x=0}^{x=L} V(x,t)^2 \, dx \tag{3.8}$$

Duan et al. (2017b) found that unsteady friction models could result in negative dissipation rates. In the present study, in order to ensure that the friction at any instant is always associated with energy dissipation, the absolute value of the local friction dissipation rate $J(x,t)V(x,t)$ is taken as the integrand when computing the portion $D_f(t)$ of the energy dissipated by the friction alone between $t = 0$ to t through

$$D_f(t) = \rho g A \int_0^t \int_{x=0}^{x=L} \left| J(x,t) V(x,t) \right| dx dt \tag{3.9}$$

The total energy of the system at any instant is $U(t) + T(t)$ and the normalized energy dissipated between $t = 0$ to t for the whole system $D^*(t)$ is given by

$$D^*(t) = 1 - \frac{U(t) + T(t)}{U(0) + T(0)} \tag{3.10}$$

Also, the normalized portion $D_f^*(t)$ of the energy dissipated by the friction alone is

$$D_f^*(t) = \frac{D_f(t)}{U(0)+T(0)} \tag{3.11}$$

3.5. Proposed upstream boundary expression and difference evaluation method

3.5.1. Proposed boundary condition at the upstream reservoir

Prior to water hammer, the water near the pipe entrance in the reservoir flows towards the pipe entrance. After water hammer, as the positive pressure wave reaches the pipe entrance, the water attempting to enter the pipe is stopped by the arriving high-pressure wave. Meanwhile, the water near the pipe entrance in the reservoir continues to flow towards the pipe entrance. Thus, the pressure wave propagates upstream into the reservoir to stop the flowing water and reaches the reflection interface (Figure 3.2). After the pressure wave is reflected at the reflection interface, the water in the pipe is expelled into the reservoir and a water jet forms in the vicinity of the pipe entrance. In this case, the influence of the water jet between the reflection interface and pipe entrance is to be investigated.

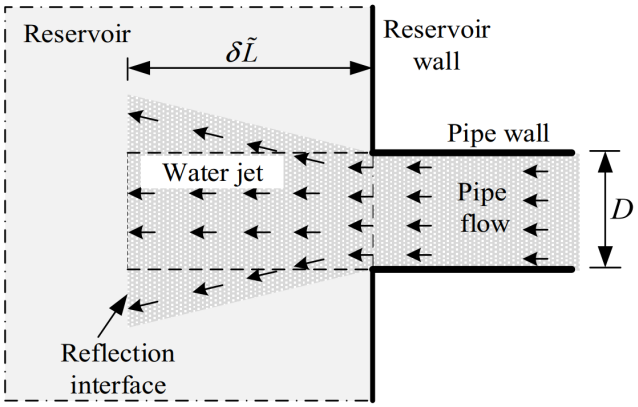

Figure 3.2 Water jet at pipe entrance during the reflection of water hammer pressure wave.

The schematic of the water jet, occurring at the pipe entrance during the water hammer, is shown in Figure 3.2. The length of the water jet is $\delta\tilde{L}$. The cross-sectional area of the water jet at the reflection interface is $\tilde{A}_R$. The dashed line in the water jet area has the same cross-sectional area as the pipe $\tilde{A}_p = \pi D^2/4$. The symbol "~" denotes values in the water jet, and subscripts R and p refer to the reflection interface and the pipe, respectively.

If the water jet is assumed to have a constant cross-section identical to that of the pipe (dashed line shown in Figure 3.2), it can be approximated as an extension of the pipe into the reservoir. Under this assumption, the dynamic behavior of the water jet can be described by the frictionless water hammer equations in the pipe after replacing the water hammer wave speed, a, with the speed of sound in water, $a_f = \sqrt{K_f/\rho}$. Using the MOC, the velocity, $\tilde{V}_p$, at the reflection interface is similar to the classical boundary expression (Eq.(3.5)) and can be expressed in a discretized form as

$$\tilde{V}_p^{t+\Delta t} = \frac{g}{a_f}\left(H_{res} - H_1^t\right) + V_1^t; \quad \Delta\tilde{t} = \frac{\delta\tilde{L}}{a_f} \tag{3.12}$$

where $\Delta\tilde{t}$ is the maximum time increment to investigate the water jet's influence. It is noted however that the cross-sectional area of water jet, $\tilde{A}_R$, will normally differ from that of the pipe cross-section, A_p, and the constant cross-section assumption for the water jet needs to be corrected, as discussed in the following.

Due to the return of the water hammer pressure wave, the flow inside the pipe near the entrance accelerates towards the reservoir and, an inverse flow occurs and forms a water jet. At the same time, entrainment and mixing phenomena occur around the jet (Abani and Ghandhi 2012). These phenomena make it difficult to theoretically and experimentally determine the influenced domain and the cross-sectional area of the reflection interface $\tilde{A}_R$. Thus, the shape of the water jet is assumed to form a circular truncated cone (Figure 3.2). In the water jet, the circular cross-sectional area of the reflection interface, $\tilde{A}_R$, is assumed to be an inverse function of the pressure gradient, $\partial\tilde{H}/\partial\tilde{x}$, between the reflection interface and the pipe entrance. For a higher value of the pressure gradient, the cross-sectional area of the reflection interface, $\tilde{A}_R$, is closer to the pipe's cross-sectional area, A_p. Normally, the cross-sectional area of the reflection interface, $\tilde{A}_R$, is larger than the pipe cross-sectional area, A_p. Thus, the cross-sectional area of the reflection interface, $\tilde{A}_R$, can be assumed as

$$\tilde{A}_R = \left(1 + \frac{k_j}{\left|\partial \tilde{H}/\partial \tilde{x}\right|}\right) A_p \tag{3.13}$$

where $|\bullet|$ denotes the absolute value of the argument function and k_j is the reservoir smoothing factor. Based on mass conservation consideration in the water jet, one has

$$\frac{\partial\left(\tilde{A}_R \tilde{V}_R\right)}{\partial t} = \frac{\partial\left(A_p \tilde{V}_p\right)}{\partial t} \tag{3.14}$$

From Eqs. (3.12) and (3.13), by substituting into the discretized expression of Eq. (3.14) and rearranging, one obtains

$$\tilde{V}_R^{t+\Delta t} = \left(1 - \frac{1}{\tilde{A}^*}\right)\tilde{V}_R^t + \frac{1}{\tilde{A}^*}\left[\frac{g}{a_f}\left(H_{res} - H_1^t\right) + V_1^t\right]; \qquad \Delta\tilde{t} = \frac{\delta\tilde{L}}{a_f} \tag{3.15}$$

where $\tilde{A}^* = 1 + k_j \big/ \left|\partial \tilde{H}/\partial \tilde{x}\right|$ is the ratio of the reflection interface area to the pipe cross-sectional area.

Based on the equation of resonant frequencies influenced by the fluid outside the pipe entrance (Alster 1972), Tijsseling et al. (2010) determined the length of the water jet as $\delta\tilde{L} = 0.24D$, and pointed out that the length, $\delta\tilde{L}$, should be a function of the frequency of pressure wave oscillation. Using the delay times measured by Mitosek and Szymkiewicz (2016) and assuming that the water jet cross-sectional areas is the same as that of the pipe cross-sectional area, the estimated jet lengths, $\delta\tilde{L}$, range from $22.8D$ to $28.2D$. The later estimated jet lengths are two orders of magnitude higher than that estimated by Tijsseling et al. (2010). To the authors' knowledge, there is no certain way to determine the length of the water jet, which should be negligible compared to the pipe length. Since the water jet is located outside the pipe entrance and exhibits different physical properties from those of the main pipe domain, at least one additional segment (prior to the pipe entrance) is required to capture the effect of the water jet in the numerical model. If the water jet length is not a multiple of the pipe segment, Δx, either a time-line or a space-line interpolation technique would be needed for the water jet domain, which would introduce interpolation errors. In the present formulation, the water jet length, $\delta\tilde{L}$, has to be of the same order of the pipe discretization length, Δx. Therefore, based on physical grounds, since the length $\delta\tilde{L}$ is small, it

would necessitate adopting a small value for Δx, thus increasing the computational effort of the model. Thus, the influence of the water jet will be included in the first pipe segment, between nodes 1 and 2, next to the entrance. The velocity at the reflection interface, shown in Eq.(3.15), is interpolated between velocities for two time-steps, $\tilde{V}_R^t$ and $\tilde{V}_P^{t+\Delta t}$. Thus, in the proposed boundary expression, the velocity at the pipe entrance is also interpolated between velocities for two time-steps, V_1^t, and the velocity computed from Eq. (3.5). Using constant reservoir pressure head for the boundary pressure head, $H_1^{t+\Delta t} = H_{res}$, the proposed boundary expression for the velocity is expressed as

$$V_1^{t+\Delta t} = \left(1 - \frac{1}{A^*}\right) V_1^t + \frac{1}{A^*}\left[\frac{g}{a}\left(H_{res} - H_2^t - J_2 \Delta x\right) + V_2^t\right] \tag{3.16}$$

where $A^* = 1 + k_j \Big/ \left|H_{res} - H_2^t\right|$. When A^* equals unity, e.g., $k_j = 0$, the proposed boundary expression is identical to the classical boundary expression for the upstream reservoir (Eq. (3.5)). Since the length of the pipe segment between nodes 1 and 2, $\Delta x = L/n$, is based on the pipe discretization, the value of the reservoir smoothing factor, k_j, is sensitive to the pipe discretization. Both the classical boundary expression (Eq.(3.5)) and the proposed one (Eq. (3.16)) indicate that the velocity change at the pipe entrance is proportional to the pressure gradient at the pipe entrance. The classical boundary expression assumes the pressure at the pipe entrance to be equal to that in the reservoir at that particular depth. This results in a pressure jump at the pipe inlet. In contrast, the proposed waterjet model suggests the presence of a gradual pressure gradient from the reservoir pressure to that of the pressure wave, characterized by a newly defined reservoir smoothing factor. From a physical viewpoint, the authors postulate that the presence of a strong pressure gradient inside of the pipe leads to the formation of a "pulsating" submerged jet expanding into the reservoir with each pressure wave cycle. As a result, while the pressure jump within the classical boundary expression preserves the shape of the reflected wave, the gradual change of pressure in the present model smoothens the reflected wave.

The method of characteristics is a numerical explicit integration scheme. Other explicit schemes include the quasi-2D scheme (e.g., Pezzinga 1999) and the finite volume Godunov-type scheme (e.g., Zhao and Ghidaoui 2004). While the quasi-2D and the finite volume Godunov-type schemes

offer advantages in terms of accuracy, the presently used method is based on the method of characteristics and offer advantages in terms of simplicity, while involving no discretization errors nor numerical energy dissipation when the Courant number is taken $C_r = 1$ (Ghidaoui 1998). The later property ensures that the energy dissipation in the model is induced solely by the friction and the water jet, and thus enables optimizing the pressure wave damping and phase shifting.

3.6. Difference evaluation method

For a precise evaluation of the water hammer model, we adopt the normalized pressure head defined as $H^* = (H - H_{res})g/aV_0$ and the normalized time defined as $t^* = at/L$. As shown in Fig. 3, the normalized pressure time-history line at the valve is divided by the central line for pressure oscillation ($H^* = 0$) into a series (m) of half cycles ($t_i^* \le t^* < t_{i+1}^*, i = 1,...,m$). The percentage difference, E^{n-e}, between the predicted and measured pressure time-histories is computed as

$$\begin{aligned} E^{n-e} &= \frac{1}{t_{m+1}^* - t_1^*} \sum_{i=1}^{m} |W_i| A_i^{n-e} \times 100\%; \\ A_i^{n-e} &= \int_{t_i^*}^{t_{i+1}^*} \left| H_n^* - H_e^* \right| dt^*; \qquad |W_i| = \left| \max \left\langle \left| H_n^* \right| \right\rangle_{t_i^*}^{t_{i+1}^*} - \max \left\langle \left| H_e^* \right| \right\rangle_{t_i^*}^{t_{i+1}^*} \right| \end{aligned} \tag{3.17}$$

where the symbol $\langle \ \rangle_{t_i^*}^{t_{i+1}^*}$ denotes values within the range $t_i^* \le t < t_{i+1}^*$ for the ith half cycle, A_i^{n-e} is the area enclosed between the predicted and measured pressure time-histories in the ith half cycle (the hatched area in Figure 3.3), and $|W_i|$ is the difference between $\max \left\langle \left| H_n^* \right| \right\rangle_{t_i^*}^{t_{i+1}^*}$ and $\max \left\langle \left| H_e^* \right| \right\rangle_{t_i^*}^{t_{i+1}^*}$, which are the peak values of ith half cycle in the predicted and measured pressure time-histories. This difference evaluation method accounts for the prediction accuracy of peak value in $|W_i|$ and the pressure average value in A_i^{n-e} for the ith half cycle.

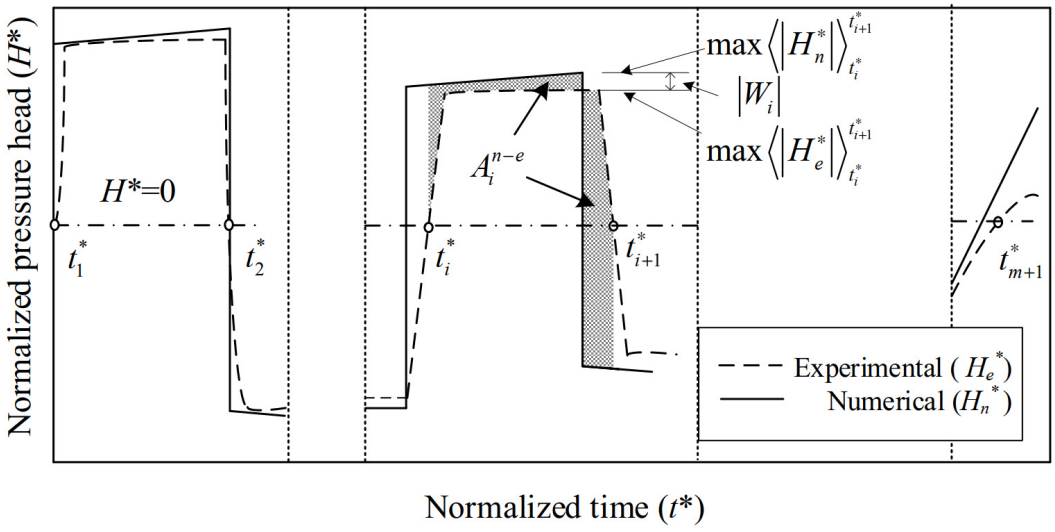

Figure 3.3 Schematic of the definitions introduced to determine the percentage difference.

3.7. Numerical tests and discussion

3.7.1. Description of the experimental system

The experimental results from Adamkowski and Lewandowski (2006) are used to assess the accuracy of the proposed boundary expression in the quasi-steady model and the Brunone (Brunone et al. 1995, Bergant et al. 1999) and the Zielke (Zielke 1968) models. In this experimental work, a high-pressure reservoir connects with a low-pressure reservoir through a copper pipe (Figure 3.4).

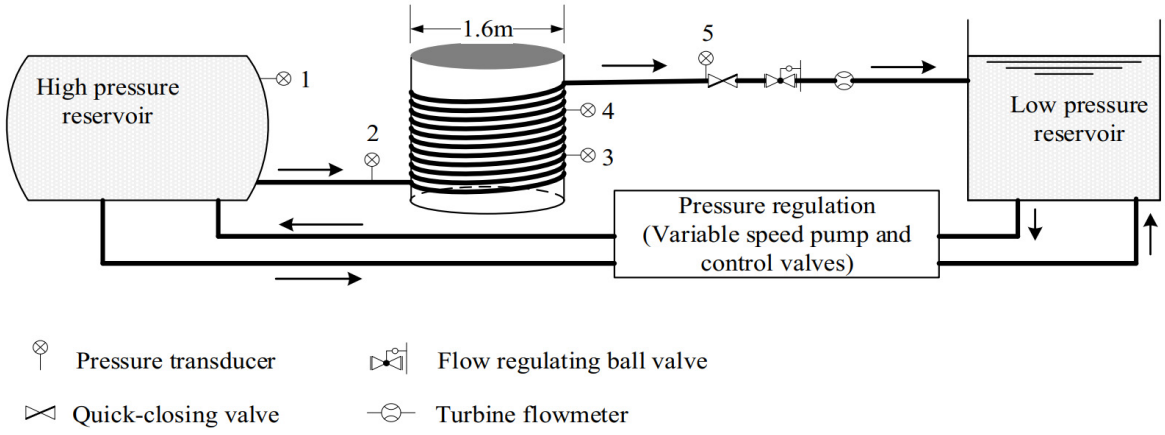

Figure 3.4 Simplified scheme of the experimental system (adapted from Adamkowski and Lewandowski 2006).

As shown in Figure 3.4, the main part of the pipeline is encircled around a steel cylinder with an outside diameter of 1.6m. The effect of pipe inclination, which is less than 0.5 degrees, is

ignored. A turbine flowmeter, located immediately upstream of the low-pressure reservoir, is used to measure the flow velocity. A ball valve is placed upstream next to the flowmeter to control the velocity for steady flow. Upstream, next to the ball valve, is a quick-closing valve with a closure time of less than 3ms which is used to produce the water hammer. Four monitor pressure gauges (2-5) are installed at four locations along the pipe at $0.25L$, $0.5L$, $0.75L$, and L away from the upstream reservoir. Parameters of this pipe system are provided in Table 3-1.

Table 3-1 Parameters of the pipe system.

Parameters	Unit	Symbols	Values
Pipe length	m	L	98.1
Pipe diameter	mm	D	16
Pipe wall thickness	mm	e	1
Pipe roughness [a]	mm	ε	0.01
Reservoir pressure head	m	H_{res}	125
Water density	$\mathrm{kg/m^3}$	ρ	1000
Kinematical viscosity	$\mathrm{m^2/s}$	ν	10^{-6}
Initial velocity	m/s	V_0	0.94
Wave speed	m/s	a	1305
Gravitational acceleration	$\mathrm{m/s^2}$	g	9.81

[a] Pipe roughness was not provided by the authors in their paper (Adamkowski and Lewandowski 2006)

3.7.2. Application of the difference minimization method

Normally, the value of the unsteady friction coefficient, k_0, is determined by trial and error where the numerical results with different values of k_0 are compared to the experimental results to choose the optimal value based on visual inspection. In the present study, the difference minimization method is used to obtain the value of the unsteady friction coefficient, k_0.

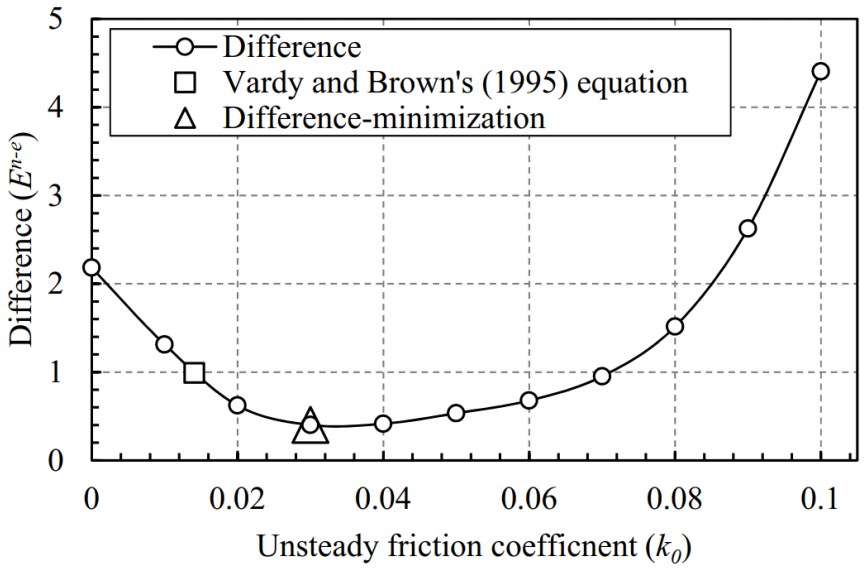

Figure 3.5 Influence of the unsteady friction coefficient, k_0, on the percentage difference, E^{n-e}, with initial velocity V_0=0.94 m/s.

Using the classical boundary expression, the Brunone model is applied to simulate Adamkowski and Lewandowski's (2006) experimental system and solved with the MOC $\left(C_r = 1, n = 100\right)$. The percentage differences between the predicted and measured pressure time-histories at the valve are evaluated by Eq.(3.17) for various values of the unsteady friction coefficient, k_0, and are plotted in Figure 3.5.

As the value of the unsteady coefficient, k_0, increases, the percentage difference decreases rapidly before the minimum difference and increases slowly near the minimum difference, and then rapidly increases. The value of the unsteady friction coefficient, k_0, determined by Vardy and Brown's equation [Eq.(3.4)] is $k_0 = 0.014$, which is smaller than the value $k_0 = 0.030$ obtained using the present difference minimization method. The computed pressure histories at the valve for both values of the unsteady friction coefficient, $k_0 = 0.014$ and 0.030, are plotted against the experimental results in Figure 3.6.

Figure 3.6 shows that the measured pressure history at the valve is smoothed into a curved line along the timeline. However, using the classical boundary expression in the Brunone models, the predicted pressure histories along the timeline behave as square-like waves. Meanwhile, the predicted pressure histories do not have enough phase-shifting compared to the measured pressure

histories, as shown in the zoomed in view (Figure 3.6b). Compared to the measured pressure history, the predicted pressure history with low unsteady friction coefficient, $k_0 = 0.014$, accurately predicts the peak values at the initial cycles (Figure 3.6b) but over-predicts them near the end (Figure 3.6c). The trend reverses for the predicted pressure history with the higher unsteady friction coefficient, $k_0 = 0.030$, which accurately predicts the peak values for the end cycles but over-damps them for the initial cycles. Thus, without quantifying the differences between the predicted and measured pressure time-history, both unsteady friction factor values, $k_0 = 0.014$ and $k_0 = 0.030$ are acceptable to simulate the investigated case based on the Brunone model.

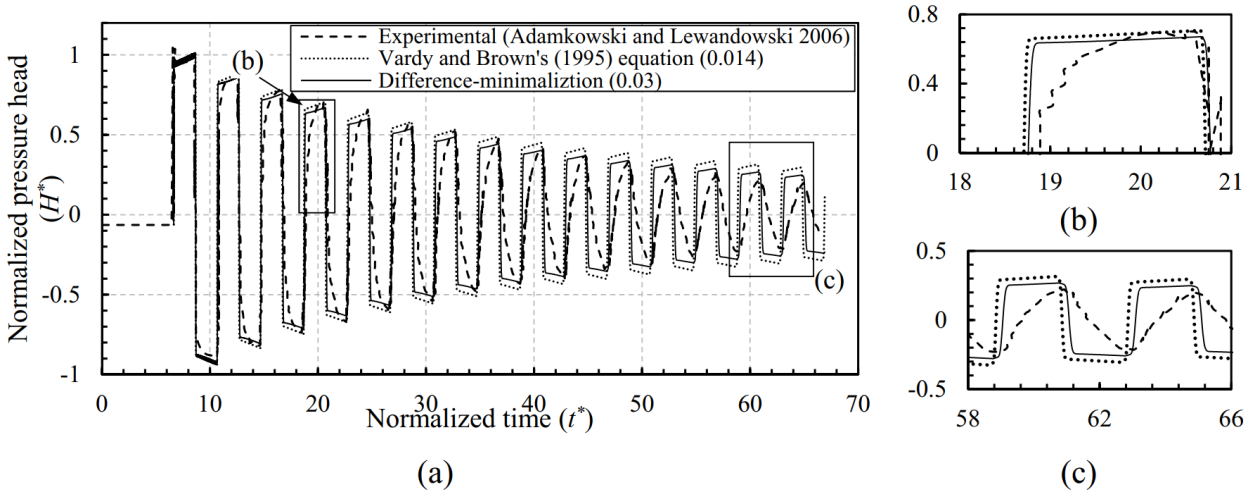

Figure 3.6 (a) Comparison between the measured and predicted pressure time-histories at the valve for both values of the unsteady friction coefficient k_0=0.014 (equation from Vardy and Brown 1995) and k_0=0.030 (difference minimization method) using the classical boundary expression with V_0=0.94 m/s.; (b) and (c) are zoomed-in views of figure (a).

The present difference evaluation method is applied for the 29 half cycles shown in Figure 3.6. For the ith half cycle, $t_i^* \le t^* < t_{i+1}^*$, the peak value difference, $|W_i|$, and the enclosed area, A_i^{n-e}, between the predicted and measured pressure time-histories are plotted in Figure 3.7.

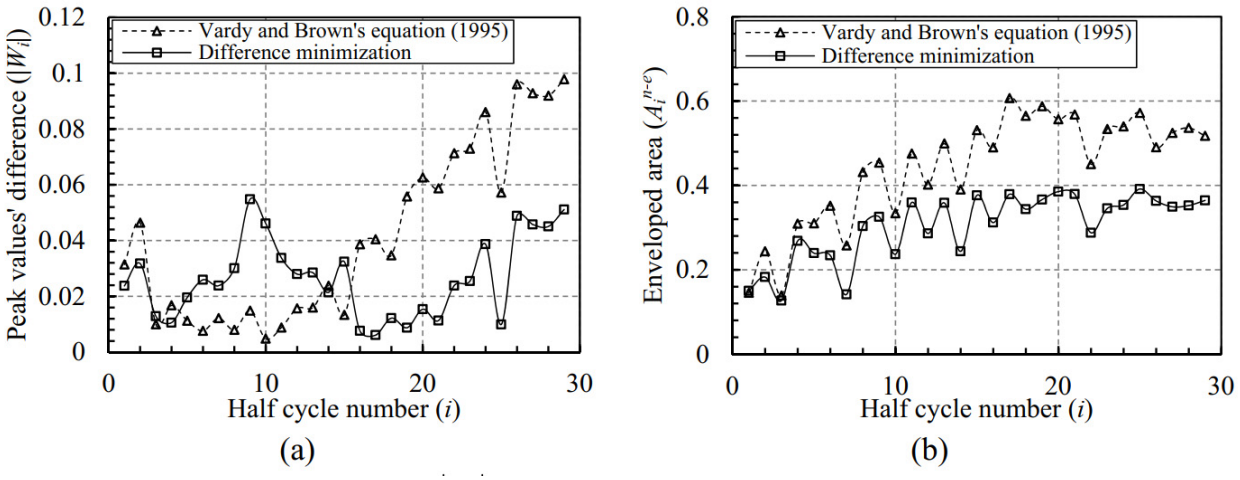

Figure 3.7 (a) Peak values' difference, $|W_i|$, and (b) enveloped area, $A_i^{n\text{-}e}$, of the i th half cycle using different values of unsteady friction coefficient, k_0=0.014 (equation from Vardy and Brown 1995) and k_0=0.030 (difference minimization method) with V_0=0.94 m/s.

Figure 3.7(a) shows that for the first few half cycles, $i \le 15$, the peak value differences, $|W_i|$, between the experimental results and the numerical results for $k_0 = 0.014$, are smaller than the ones based on a higher unsteady friction coefficient, $k_0 = 0.030$. However, the trend reverses for the remaining half cycles $i \ge 16$. Hence, a constant value of unsteady friction coefficient, k_0, in the Brunone model is unable to replicate the peaks of the experimental results over the investigated time domain. As shown in Figure 3.7(b), for all half cycles, the areas, A_i^{n-e}, enclosed between the measured pressure history and that predicted based on $k_0 = 0.030$, are smaller than those obtained when using the low value of the unsteady coefficient, $k_0 = 0.014$. According to the definition of enclosed area, A_i^{n-e}, this means that the predicted pressure time-history with the higher unsteady friction coefficient, $k_0 = 0.030$, replicates the average pressures in each half cycle more accurately than the lower one.

3.7.3. Numerical tests to assess the validity of the proposed boundary expression

The difference minimization method is used to obtain the empirical unsteady friction coefficient, k_0, in the Brunone model and the reservoir smoothing factor, k_j. In order to determine both values, the value of the unsteady friction coefficient was varied from 0 to 0.1 in steps of 0.01. For each value of the coefficient, the reservoir smoothing factor was increased from 0 to 30 in steps of 1.

The percentage differences, E^{n-e}, were computed for all combinations of unsteady friction and reservoir smoothing factors, and the combination that minimizes the percentage difference, E^{n-e}, between the experimental and analytical results was determined. The values for parameters obtained and corresponding percentage differences, E^{n-e}, are provided in Table 3-2. In the case (V_0=0.95 m/s, Adamkowski and Lewandowski 2006), the proposed boundary expression is identical to the classical boundary expression in the Zielke's (1968) model since the difference minimization procedure leads to the condition $k_j = 0.0$.

Table 3-2 Parameters and minimum differences for numerical models (V_0=0.94m/s)

Friction model	Unsteady friction coefficient (k_0)	Reservoir smoothing factor (k_j)	Difference $E^{n-e}(\%)$
Quasi-steady	--	0[a]	2.20
	--	24	0.10
Brunone	0.030	0	0.40
	0.010	16	0.10
Zielke	--	0	0.13

[a] $k_j = 0$: the proposed boundary expression is identical to the classical boundary expression.

Source: Data from Adamkowski and Lewandowski (2006).

The percentage differences, E^{n-e}, both in the quasi-steady and the Brunone models, were found to decrease when adopting the proposed boundary expression, especially for the quasi-steady model. Compared to the Brunone model using the classical boundary expression, the value of the unsteady friction coefficient, k_0, is smaller when using the proposed boundary expression. This indicates that the energy normally dissipated by friction in the conservation models, is now dissipated further by the reservoir. Compared to the unsteady friction stress, the quasi-steady friction stress dissipates less energy. Thus, the reservoir dissipates more energy in the quasi-steady model with a higher value of the reservoir smoothing factor, k_j. Using the parameter values determined by the difference minimization method, the pressure histories are plotted against the experimental results at the valve, $x = L$, in Figure 3.8 and at a quarter of the pipe length, $x = 0.25L$, from the upstream reservoir in Figure 3.9.

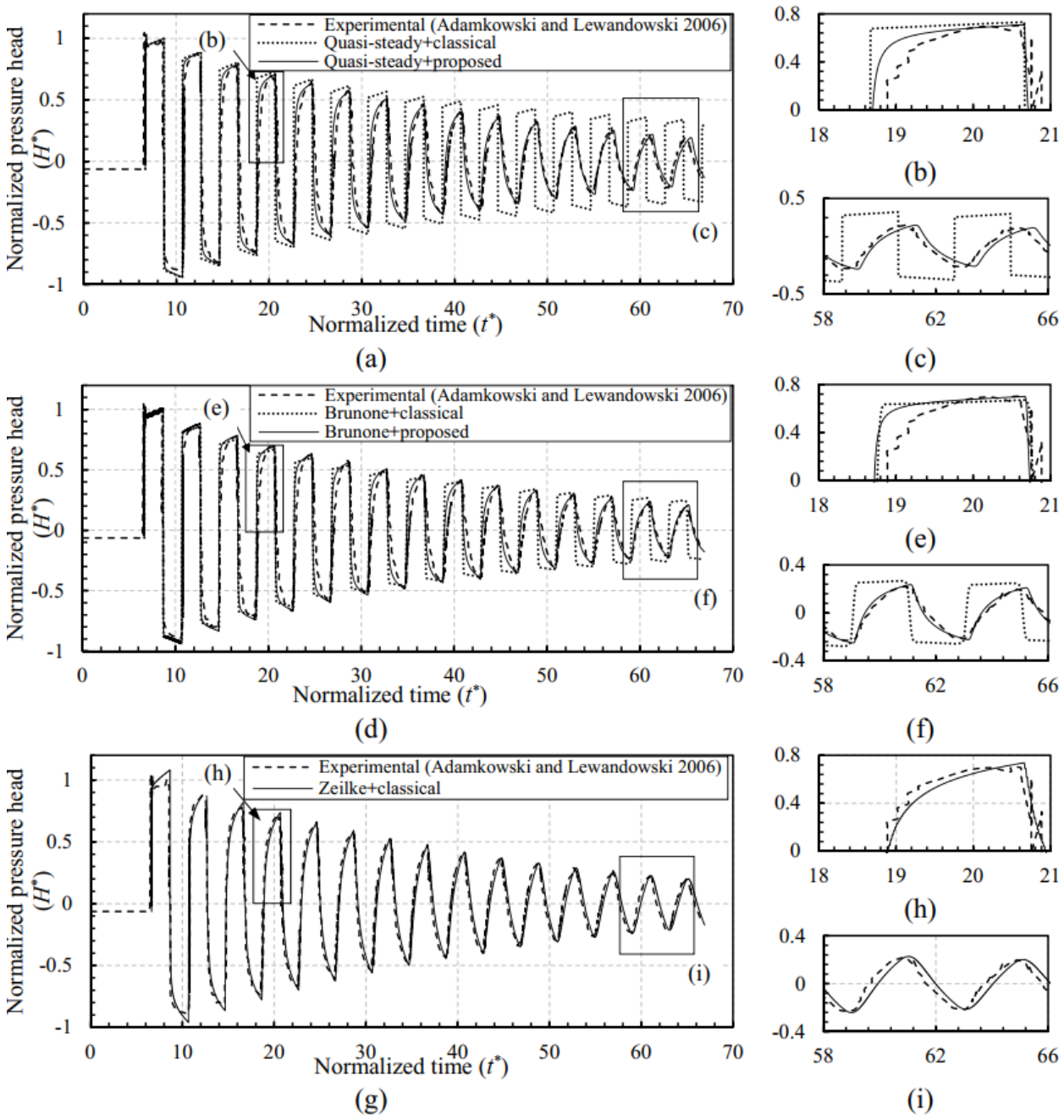

Figure 3.8 Comparison of the measured and predicted pressure histories at the valve using the classical and the proposed boundary expressions in: (a-c) the quasi-steady model; (d-f) the Brunone model (difference minimization method); and (g-i) the Zielke model (classical boundary expression only) with V_0=0.94 m/s.

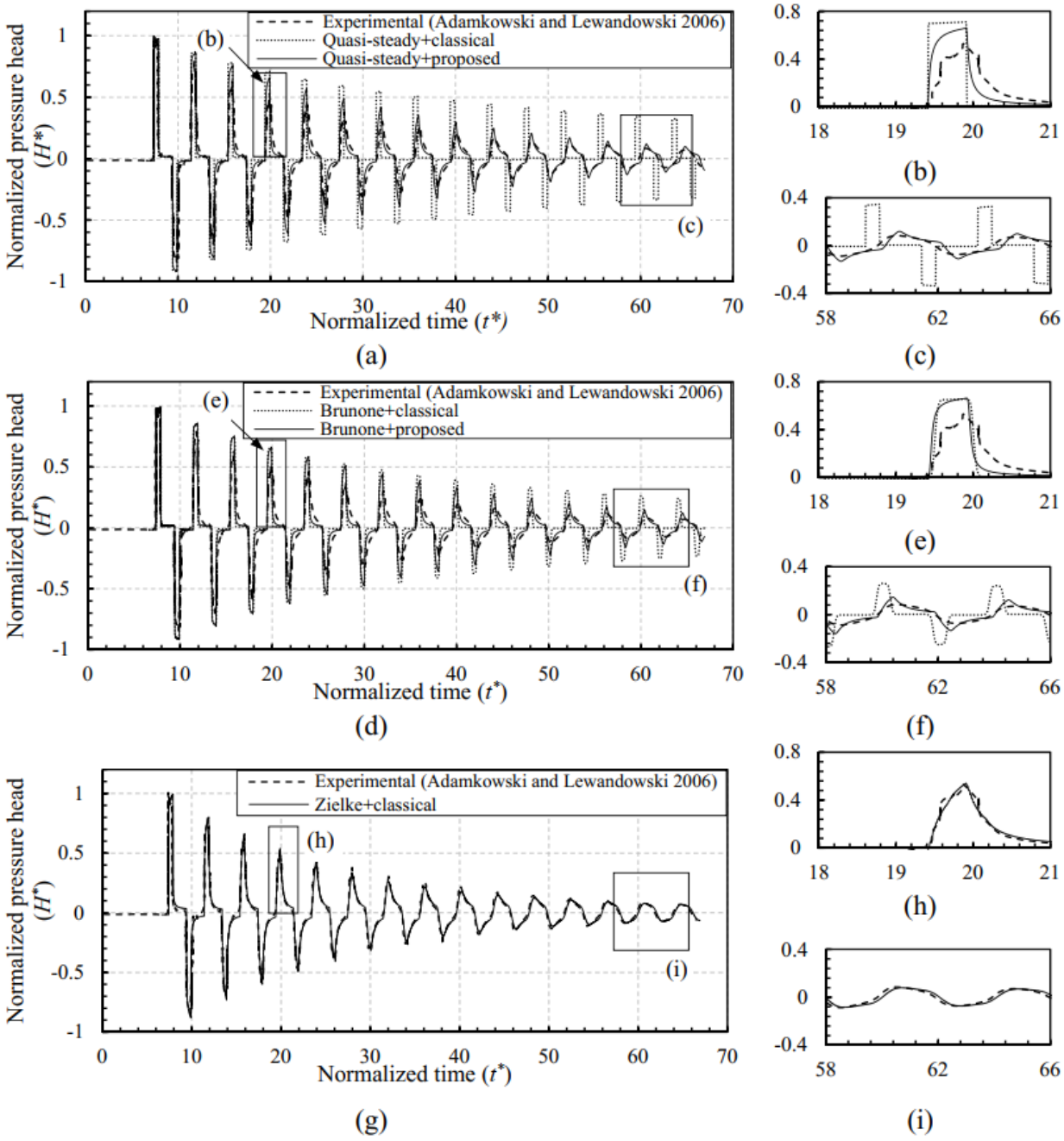

Figure 3.9 Comparison of the measured and the predicted pressure histories at quarter of pipe length from the reservoir using the classical and the proposed boundary expressions in: (a-c) the quasi-steady model; (d-f) the Brunone model (difference minimization method); and (g-i) the Zielke model (classical boundary expression only) with V_0=0.94 m/s.

Prior to valve closure, $t^* < 6.65$, the pressure at the valve remains constant. After rapid valve closure, $t^* > 6.65$, water hammer occurs in the pipe. Compared to the classical expression, the proposed boundary expression improves the accuracy of replicating the experimental results for

both models, in terms of reproducing the pressure peak values, the time-history of their shape, as well as the phase shifting as shown in Figure 3.8(c and f) and Figure 3.9(c and f). These improvements indicate that the proposed boundary expression not only attenuates the pressure amplitude but also smoothens the pressure time-histories. Figure 3.8(a) and Figure 3.9(a) show that the improvements in the quasi-steady model are more significant given that the model is unable to replicate the peak pressures when used with the classical boundary expression. In the quasi-steady model, by applying the new boundary expression, the phases of the pressure histories are found a bit over-shifted compared to the experimental results near the end of the experiment testing time (Figure 3.8c), but are in better agreement with the Brunone model (Figure 3.8f). The reason is that the higher value of the reservoir smoothing factor has a larger lagging effect on the pressure wave reflection. As discussed in the previous section, the unsteady friction coefficient and the reservoir smoothing factor jointly influence the pressure wave damping. Specifically, the unsteady friction coefficient attenuates only the amplitude of the pressure wave, while the reservoir smoothing factor attenuates, smoothens and widens the pressure wave front, leading to a better agreement with experimental pressures. Figure 3.8(g) and Figure 3.9(g) show that the Zielke model exhibit a smoothing of the pressure wave front, and reasonably replicates the pressure peak values and shape of the pressure history at the valve when using the classical boundary expression.

3.7.4. Energy dissipation

Figure 10 depicts the dimensionless dissipated energy time-histories for the whole system as defined in Eq.(3.10), and compares it to the dimensionless energy dissipated by friction alone [Eq.(3.11)] for the quasi-steady model (Figure 3.10a) and for the Brunone model (Figure 3.10b). For the quasi-steady friction model, Figure 3.10a shows that the dimensionless energy dissipated for the whole system based on the proposed boundary expression is higher than that based on the classical boundary equation. However, the corresponding dimensionless energy dissipated by friction alone is lower than that obtained using the classical solution. This finding is consistent, from a physical viewpoint, with the energy loss at the pipe entrance considered in the newly proposed boundary expression. Similar findings are observed for the Brunone model as shown in Figure 3.11b. Based on the classical boundary expression, the energy dissipated by the Brunone friction alone is higher than that dissipated in the whole system. A possible reason is the fact that the energy dissipated by the friction $D_f(t)$ from time 0 to t is defined in the present study as the

integral of the absolute value of the local frictional dissipation rate $\left|J(x,t)V(x,t)\right|$ [Eq. (3.9)], which leads always to positive energy dissipation. This contrasts with the recent findings of Duan et al. (2017b), in which the energy dissipation ratio by friction for the whole system was found to be negative in some instances. Another possible reason stems from the fact that the present water hammer model [Eqs. (3.1) and (3.2)] does not ensure energy conservation. Hence, a portion of the energy dissipated by the Brunone friction model is consumed to reduce the energy flowing into the pipe at the inlet.

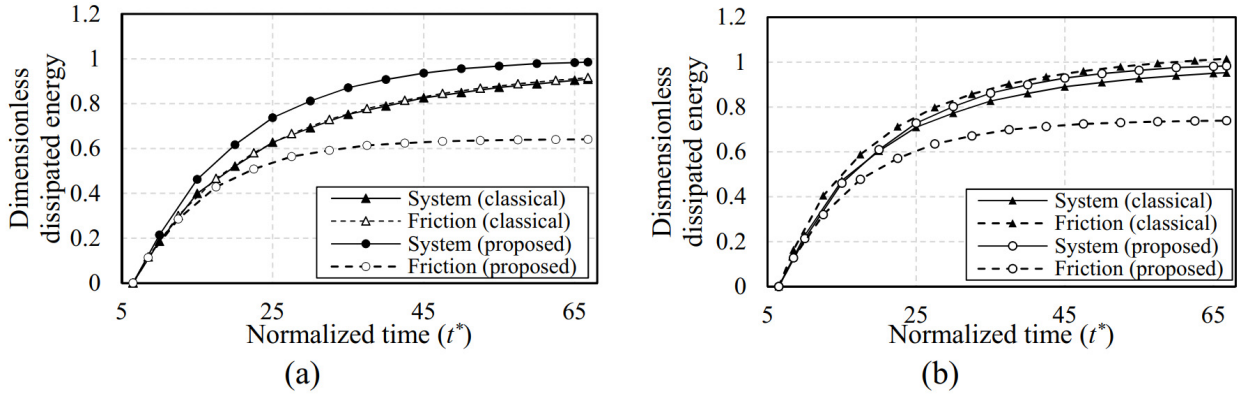

Figure 3.10 Dimensionless dissipated energy history in the whole system and the portion dissipated by the friction in (a) the quasi-steady model and (b) the Brunone model using the classical and proposed boundary expressions with V_0=0.94 m/s.

3.7.5. Smoothing effect of the proposed boundary expression

Using the parameter values in Table 3-2 for the Brunone model with the classical boundary expression and with the proposed boundary expression, the pressure distributions along the pipe are plotted in Figure 3.11 for the first cycle, $t^* = 6.65 \sim 11.65$, and for the last cycle, $t^* = 59.21 \sim 64.21$.

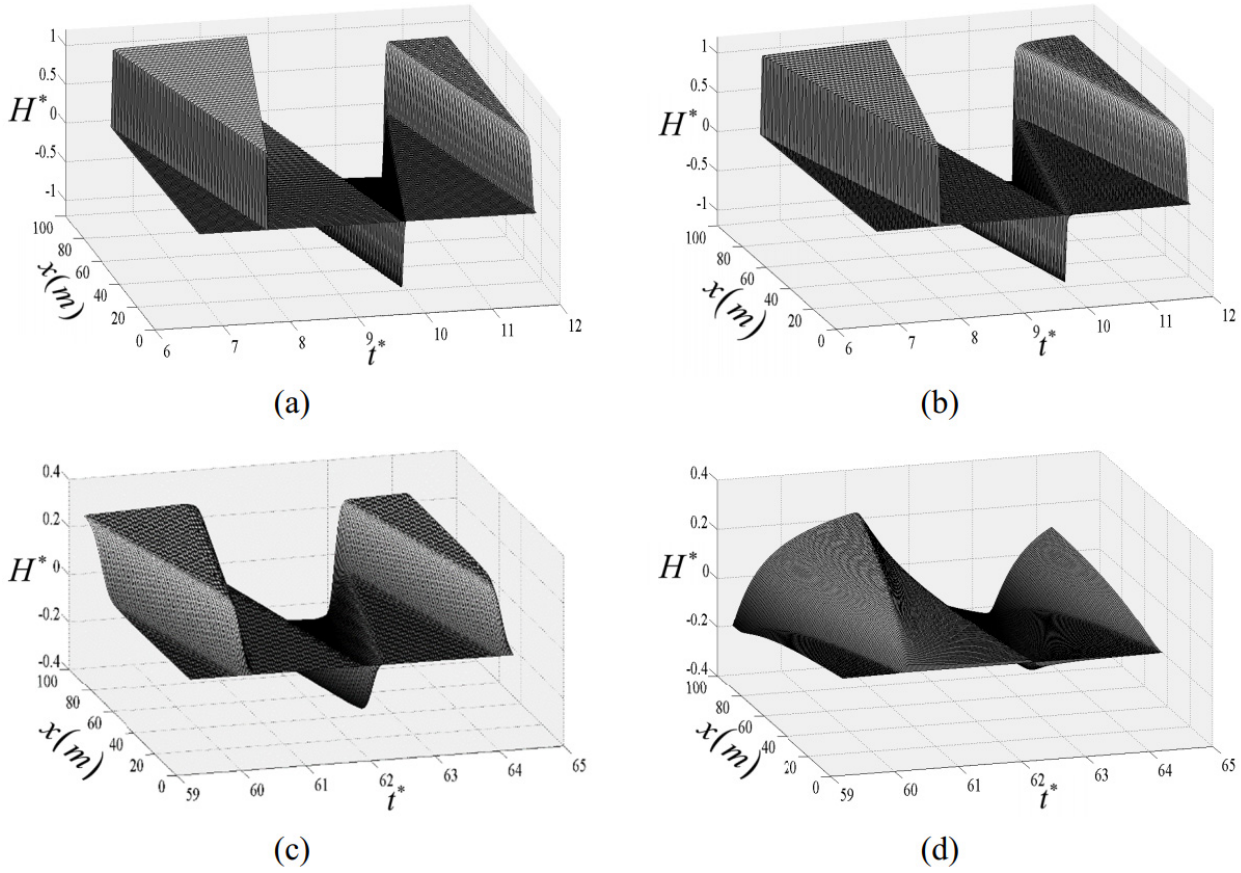

Figure 3.11 Pressure distribution along the pipe predicted by the Brunone model: for the first testing cycle, t^*=6.65~11.65, (a) using the classical boundary expression; (b) using the proposed boundary expression; for the last testing cycle, t^*=59.21~64.21, (c) using the classical boundary expression; and (d) using the proposed boundary expression. The experimental system from Adamkowski and Lewandowski (2006) is simulated with initial velocity V_0=0.94 m/s for all cases.

After rapid valve closure, $t^* > 6.65$, a wave with a stepwise pressure distribution, propagates from the valve at $x = L$, and bounces from the reservoir at $x = 0$. Using either the classical or the proposed boundary expression in the Brunone model, the predicted pressures preserve the stepwise distributions as the pressure waves propagate along the pipe for the first testing cycle, $t^* = 6.65 \sim 11.65$ (Figure 3.11a and b). Using the classical boundary expression, the pressure distributions for the last testing cycle, $t^* = 59.21 \sim 64.21$, are presented in Figure 3.11(c). It is observed that the amplitudes of pressure distributions decrease over the time but preserve the stepwise distributions. When using the newly proposed boundary expression (Figure 3.11d), the pressure amplitudes decrease over time, while the pressure distributions along the pipe are curved lines, without plateaus. Using the proposed boundary expression, the wave front exhibits a high-

pressure gradient at the beginning of the water hammer, which bounces quickly from the reservoir with a tail-like pressure distribution. The tail-like pressure distribution grows each time as the pressure wave bounces from the reservoir. As a result, the surface for the pressure distributions versus time is curved (Figure 3.11d), and the maximum pressures for the different locations in the same cycle decrease from the valve to the reservoir. This trend is observed in the experimental results of Adamkowski and Lewandowski (2006). The predicted and measured maximum pressure values at four locations, $x = 0.25L, 0.5L, 0.75L$ and L, are presented in Figure 3.12 for the last testing cycle.

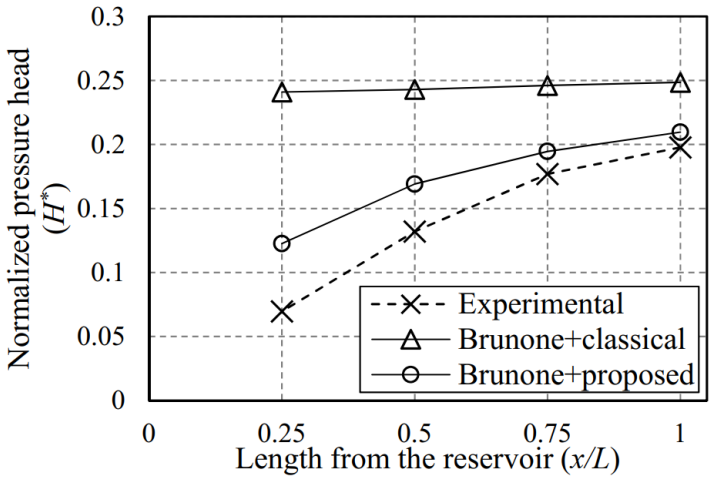

Figure 3.12 Maximum normalized pressure head versus dimensionless longitudinal coordinate from the reservoir for the last investigated cycle.

Due to the reservoir's smoothing effect, the maximum pressure distributions during the last experimental cycle reduces along the pipe from the valve to the reservoir. In contrast, when adopting the classical boundary expression, the maximum pressures do not vary much along the pipe. These observations illustrate that the proposed boundary expression not only improves the ability of the water hammer model to replicate the pressure damping pattern at the valve, but also improves the prediction of the pressure distribution along the pipe over time.

3.7.6. Grid sensitivity analysis for the reservoir smoothing factor k_j

By using a uniform length discretization with $C_r = 1$ in a rectangular discretization scheme, the difference minimization method is used to obtain the reservoir smoothing factor, k_j, in the quasi-steady model and the Brunone model, and the unsteady friction coefficient, k_0, in the Brunone

model. The technique leads to the value $k_0 = 0.03$ when using the classical boundary expression and $k_0 = 0.01$ when using the proposed boundary expression. Figure 3.13(a) shows the pressure time-histories at the valve based on the Brunone model with the proposed boundary expression for three subdivision numbers ($n = 25, 70, 100$). The results indicate that the number of subdivisions has no influence on the predicted pressure time-histories using the Brunone model with the proposed boundary expression. Figure 3.13(b) provides a comparison of the energy dissipation histories in the quasi-steady, the Brunone and the Zielke models based on the classical and proposed boundary expressions. In the initial time intervals, the energy dissipation histories based on the proposed boundary expression are identical to that based on the Brunone model with the classical boundary expression. After the pressure wave is reflected from the upstream reservoir multiple times, the energy dissipation histories in the quasi-steady and the Brunone models with the proposed boundary expression approach the one based on the Zielke model with the classical boundary expression. By varying the number of subdivisions, the energy dissipation histories do not exhibit any change in the two friction models using the proposed boundary expression, indicating that pipe discretization has no influence on energy dissipation, even though the reservoir smoothing factor, k_j, depends on the pipe discretization.

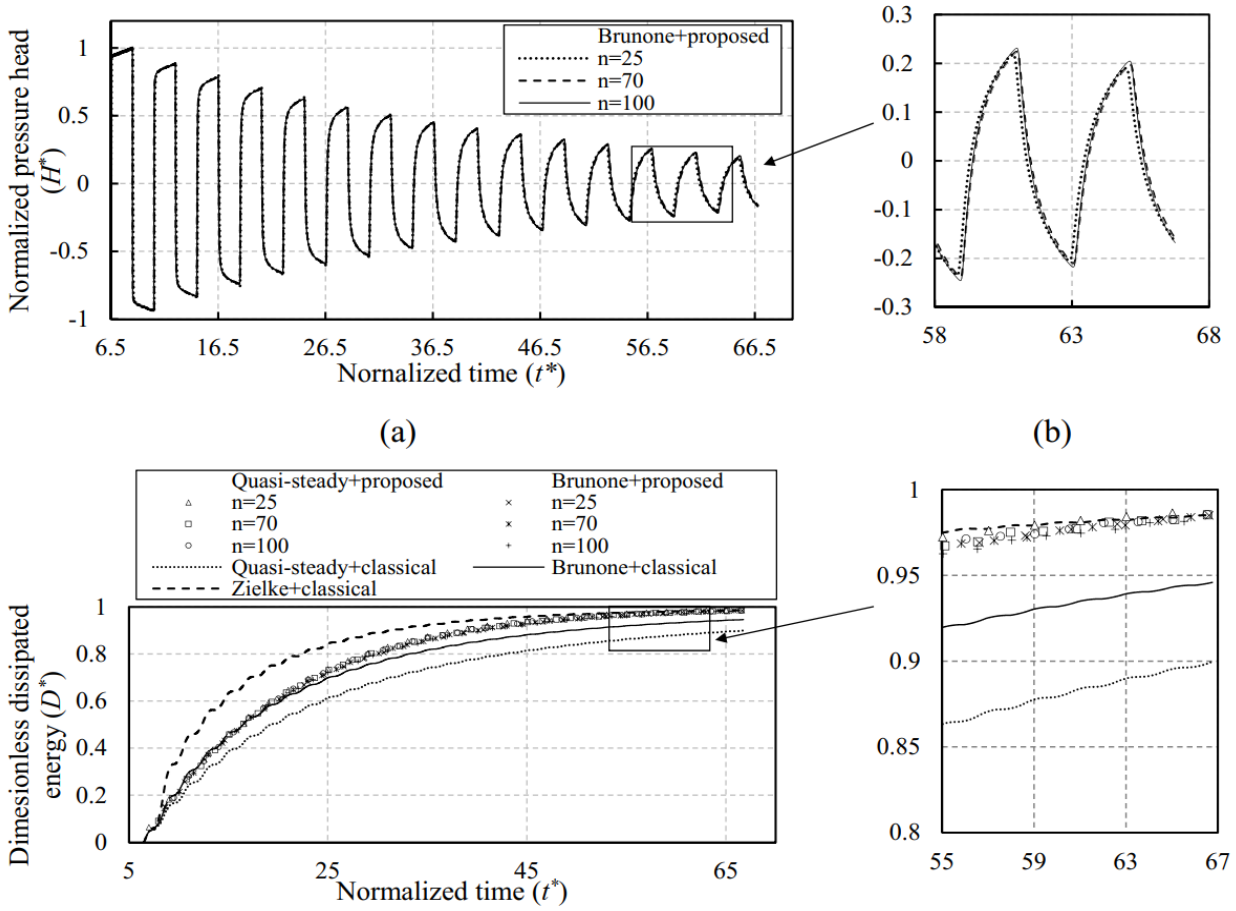

Figure 3.13 (a) Comparison of the pressure time-histories at the valve using the Brunone model with proposed boundary condition for subdivision numbers n=25, 75, 100; (c) Comparison of normalized energy dissipation histories as predicted by various friction models. Figures (b) and (d) are zoomed-in views of figures (a) and (c), respectively, with V_0=0.94 m/s.

Figure 3.14 provides the reservoir smoothing factor, k_j, and the percentage difference, E^{n-e}, for various discretization schemes as determined by the number of subdivisions, n, based on minimum differences for the quasi-steady and Brunone models. As shown in Figure 3.14(a), using the same number of subdivisions, n, the value of the reservoir smoothing factor, k_j, in the Brunone model is lower than that based on the quasi-steady model. Since the unsteady friction stress dissipates more energy than the quasi-steady friction stress, the proposed boundary expression must dissipate less energy in the Brunone model and thus has a lower smoothing factor, k_j. This observation is consistent with the fact that the unsteady friction coefficient, k_0, and the reservoir smoothing factor, k_j, jointly influence the pressure wave damping. A relationship

between the reservoir smoothing factor, k_j, and the number n of subdivisions is obtained by curve fitting as $k_j = 2.47 + 0.21n$ for the quasi-steady model and $k_j = 1.63 + 0.15n$ for the Brunone model. The corresponding friction coefficient as predicted by difference minimization method is $k_0 = 0.01$. The value of the reservoir smoothing factor k_j increases as the number of subdivisions, n, increases. According to the proposed boundary assumption, the water jet energy dissipation effect is now included in the water flow between nodes 1 and 2. The length of the discretized pipe segment $\Delta x = L/n$ decreases as the number of subdivisions n increases. As a result, the intensity of energy dissipation increases in the water flow between nodes 1 and 2, and requires a larger value for the reservoir smoothing factor, k_j. As shown in Figure 3.14(b), for various number of subdivisions, n, the percentage differences are identical in models using the proposed boundary expression. This indicates that pipe discretization has no influence on the numerical results even though the value of the reservoir smoothing factor, k_j, happens to depend on the number of subdivisions. Thus, the number of subdivisions, $n = 100$, and the Courant number, $C_r = 1$, are kept constant.

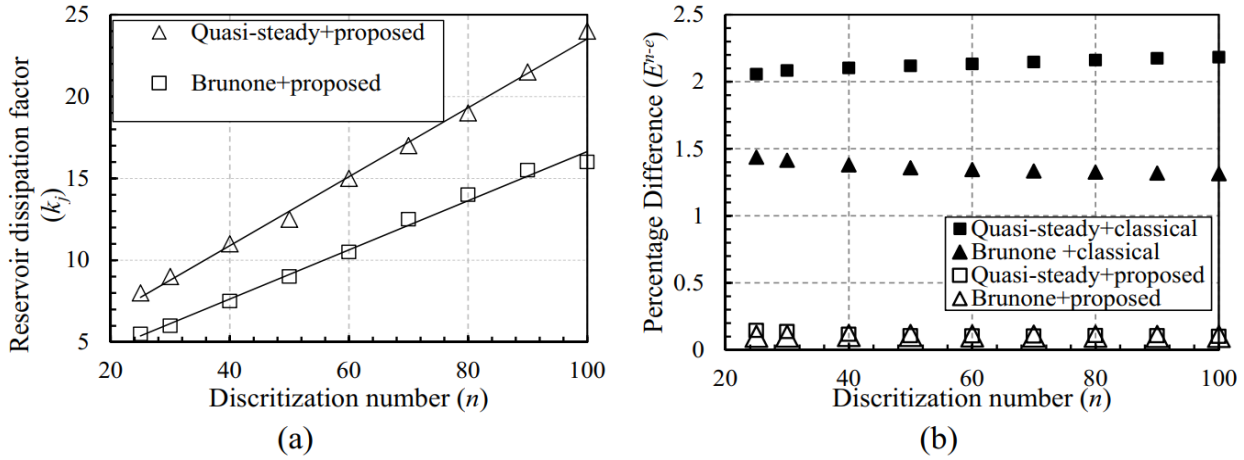

Figure 3.14 Prediction of the difference minimization method using the pipe system information from Adamkowski and Lewandowski (2006) with the initial velocity V_0=0.94 m/s. (a) Reservoir smoothing factor k_j versus number of subdivisions n and (b) Percentage differences E^{n-e} versus number of subdivisions.

3.8. Application of the proposed boundary condition

In this section, the pressure time-histories at the valve, extracted from the quasi-steady, the Brunone and the Zielke models using the newly proposed boundary expression, are compared to

experimental results from Holmboe and Rouleau (1967), Bergant et al. (1999), and Adamkowski and Lewandowski (2006). The information of the experimental systems tested is provided in Table 3-3.

Table 3-3 Experimental data – specific information.

Experiment parameters	Holmboe and Rouleau (1967)		Bergant et al. (1999)			Adamkowski and Lewandowski (2006)			
Case	1[a]	2[a]	3	4	5	6	7	8	9
L(m)	36.08	36.08	37.23	37.23	37.23	98.11	98.11	98.11	98.11
D(mm)	25.40	25.40	22.10	22.10	22.10	16.00	16.00	16.00	16.00
a(m/s)	1439	1435	1319	1319	1319	1305	1305	1305	1305
V_0(m/s)	0.128	0.244	0.10	0.20	0.30	0.066	0.34	0.63	0.94

[a] The fluid used was oil.

In the previous section, using the difference minimization method, the reservoir smoothing factor was found to be $k_j = 0$ in Case 9 of the Zielke model (Figure 3.8c and Figure 3.9c). Figure 3.15 presents the pressure time-histories at the valve in Case 5 as obtained from the Zielke model using the classical and the proposed boundary expressions. The results show that the Zielke model with the classical boundary expression does not exactly replicate the experimentally observed pressure peak values and the phase shifting. By using the proposed boundary expression in conjunction with the Zielke model, the results show an improvement in the ability of the Zielke model to replicate the experimental results.

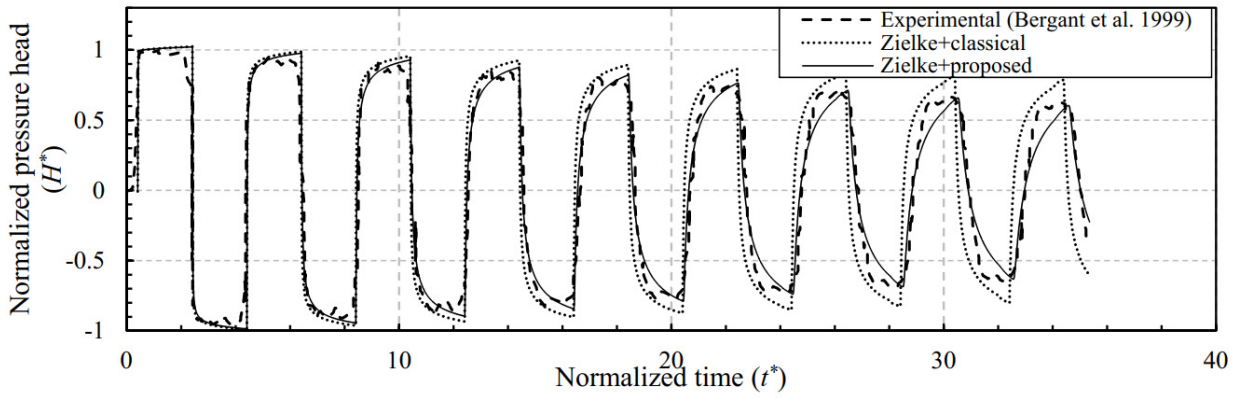

Figure 3.15 Zielke model pressure prediction - Classical versus proposed boundary expressions (Case 5 V_0=0.3m/s of Bergant et al. 1999-at valve location).

Using the difference minimization method, the values of the reservoir smoothing factor, k_j, those of the unsteady friction factor, k_0, and the percentage differences, E^{n-e}, between the predicted and measured pressure time-histories are provided in Table 3-4.

Table 3-4 Parameters for numerical models and percentage differences, E^{n-e}.

	Quasi-steady model				Brunone model					Zielke model		
	classical		proposed		classical		proposed			classical	proposed	
No.	E^{n-e} (%)		k_j	E^{n-e} (%)	k_0	E^{n-e} (%)	k_0	k_j	E^{n-e} (%)	E^{n-e} (%)	k_j	E^{n-e} (%)
1	4.42		36	0.98	0.06	1.47	0.01	32	1.01	1.64	9	1.31
2	1.35		19	0.63	0.03	0.63	0.03	6	0.57	0.70	5	0.53
3	7.10		6	0.12	0.04	0.49	0.02	4	0.14	1.01	1	0.20
4	7.72		14	0.36	0.05	0.24	0.04	2	0.12	1.86	5	0.20
5	6.82		20	0.22	0.04	0.20	0.03	8	0.07	1.7	6	0.15
6	14.6		6	0.97	0.06	0.43	0.05	2	0.35	0.83	1	0.35
7	5.80		22	0.25	0.05	0.33	0.03	10	0.08	0.67	2	0.26
8	2.30		23	0.06	0.03	0.29	0.01	16	0.06	0.43	1	0.27
9	2.18		24	0.10	0.03	0.40	0.01	16	0.10	0.13	0	0.13

In the case of the Brunone model, the values of the unsteady friction coefficient, k_0, using the newly proposed boundary expression, are always lower than those obtained based on the classical boundary formulation. Using the proposed boundary expression, the values of the reservoir smoothing factor, k_j, in the Brunone model, are lower than the ones obtained in the quasi-steady model. These observations are consistent with the previous discussions for the jointly influence of friction stress and the boundary on the pressure wave damping. A comparison of the reservoir smoothing factors based on the three friction models (Table 3-4) shows that the predicted water jet has a higher weight in models with a step pressure front, i.e., the quasi-steady and the Brunone models, than in the Zielke model for which the pressure wave front exhibit a gradual change. Table 3-4 also shows that, compared to the numerical results based on the classical boundary expression, the percentage difference, E^{n-e}, between the predicted and measured pressure time-histories, are lower in the quasi-steady, the Brunone and the Zielke models (except for Case 9) when using the proposed boundary expression. In summary, the proposed boundary was shown to generally improve the ability of quasi-steady and the Brunone models to replicate the pressure wave attenuation and shape. Also, it can be used to introduce extra phase shifting and peak dissipation in the Zielke model. The new boundary expression was successfully applied along the characteristic lines. Its application in conjunction with other schemes, such as the quasi-2D scheme

(Pezzinga 1999) and finite volume Godunov-type scheme (Zhao and Ghidaoui 2004), needs further investigation.

3.9. Conclusions

In the quasi-steady and the Brunone models, the adoption of the classical boundary expression predicts square-wave pressure time-histories at the valve, which differ from the smooth pressure histories observed in experimental measurements. The present investigation showed that the energy dissipated by the friction along the pipe in these models is not sufficient to reproduce the behavior of the real wave front attenuation and smoothing. To improve the ability of these numerical models to predict the pressure wave attenuation and the shape, a newly proposed boundary condition was proposed by postulating the occurrence of an upstream reversing water jet at the pipe entrance during water hammer. The proposed boundary expression introduces a reservoir smoothing factor to simulate the smoothing effect of the reservoir. A difference minimization method was proposed to obtain a reservoir smoothing factor and the unsteady friction coefficient in the Brunone model.

By using the proposed boundary expression, the predicted pressure time-history exhibits a smooth wave front at the upstream reservoir. After a few cycles, the pressure distribution along the pipe takes a smooth shape, with no plateaus. Meanwhile, the maximum pressure distribution in the same cycle was found to reduce along the pipe from the valve to the upstream reservoir. These numerical trends are identical to experimental observations.

When using the proposed boundary expression with the Zielke model, it was found that the pressure wave front becomes smoother than when using the classical boundary expression. As a result, when used with the quasi-steady, the Brunone or the Zielke models, the proposed boundary expression was shown to improve the agreement between the numerical and experimental results in a wide variety of pipe systems and flow conditions. The study suggests that local energy dissipation at the reservoir is non-negligible and needs to be included as an additional damping mechanism in water hammer models.

3.10. List of symbols

The following symbols are used in this paper:

a = water hammer wave speed $(\mathrm{m/s})$;

A = cross-sectional area or enveloped area;

C_r =Courant number;

D = pipe diameter (m);

D^* =normalized dissipated energy;

e = pipe thickness (m);

E^{e-n} = percentage difference between experimental results and numerical results;

f = friction factor;

g = gravitational acceleration $(\mathrm{m/s^2})$;

H = piezometric head (m);

H_{res} = reservoir piezometric head (m);

i , j = integer;

J = friction head loss (m);

k_0 = unsteady friction coefficient;

k_j =reservoir smoothing factor;

L = pipe length (m);

m = number of half cycles;

n = number of subdivisions;

Re = Reynolds number;

t = time (s);

T =kinetic energy (J);

U =internal energy (J);

V = flow velocity $(\mathrm{m/s})$;

W =peak values difference as weight factor;

Δt =time increment(s);

Δx = length between two nodes(m);

$\delta \tilde{L}$ = water jet length (m);

$\delta \tilde{t}$ = relaxation time due to water jet(s);

ε = pipe roughness (mm);

ρ = fluid density $\left(\mathrm{kg/m^3}\right)$;

$+,-$ = along the positive and negative characteristic lines

sign =sign function;

Subscript q and u refer to quasi-steady and unsteady friction part, respectively.

Subscript p and R refer to the cross-sectional area of the pipe and reflection interface.

Superscript $*$ denotes to normalized value.

Superscript n and e refer to numerical results and experimental data.

3.11. References

Abani, N., and Ghandhi, J. B. 2012. "Behavior of unsteady turbulent starting round jets." *J. Fluids Eng.*, 134(6): 061202-061202-8.

Adamkowski, A., and Lewandowski, M. 2006. "Experimental examination of unsteady friction models for transient pipe flow simulation." *J. Fluids Eng.*, 128(6): 1351–1363.

Afshar, M. H., and Rohani, M. 2008. "Water hammer simulation by implicit method of characteristic." *Int. J. Press. Vessel. Pip.*, 85(12): 851–859.

Alster, M. 1972. "Improved calculation of resonant frequencies of Helmholtz resonators." *J. Sound Vib.* 24(1): 63–85.

Bergant, A., Simpson, A. R., and Vítkovský, J. 2001. "Developments in unsteady pipe flow friction modeling." *J. Hydraul. Res.*, 39(3): 249–257.

Bergant, A., Simpson, A. R., and Vitkovsky, J. P. 1999. "Review of unsteady friction models in transient pipe flow." *9th Int. Meet. Behav. Hydraul. Mach. Under Steady Oscil. Cond.*, International Association of Hydraulic Research, Brno, Czech Republic,7-9 Sept.

Brunone, B., Ferrante, M., and Calabresi, F. 2002. "Discussion of 'Evaluation of unsteady flow resistances by Quasi-2D or 1D models' by Giuseppe Pezzinga." *J. Hydraul. Eng.*, 128(6): 646–647.

Brunone, B., Golia, U.M., and Greco, M. 1995. "Effects of two-dimensionality on pipe transients modeling." *J. of Hydraul. Eng.,* 121(12): 906-912.

Brunone, B., Karney, B. W., Mecarelli, M., and Ferrante, M. 2000. "Velocity profiles and unsteady pipe friction in transient flow." *J. Water Resour. Plan. Manag.*, 126:(4): 236–244.

Brunone, B., and Morelli, L. 1999. "Automatic control valve induced transients in an operative pipe system." *J. of Hydraul. Eng.,* 125(5): 534-542.

Chaudhry, M. H. 2014. Applied Hydraulic Transients. *Springer New York*, New York, NY.

Chaudry, M. H., and Hussaini, M.Y. 1985. "Second-order accurate explicit finite-difference schemes for waterhammer analysis." *J. Fluids Eng.,* 107 (4):523-529.

Duan, H. F., Ghidaoui, M. S., Lee, P. J., and Tung, Y. K. 2012. "Relevance of unsteady friction to pipe size and length in pipe fluid transients." *J. Hydraul. Eng.,* 138 (2): 154–166.

Duan, H. F., Ghidaoui, M. S., and Tung, Y. K. 2009. "An efficient quasi-2D simulation of waterhammer in complex pipe systems." *J. Fluids Eng.,* 131(8): 081105-081105-9.

Duan, H. F., Lee, P. J., Che, T. C., Ghidaoui, M. S., Karney, B. W., and Kolyshkin, A. A. 2017a. "The influence of non-uniform blockages on transient wave behavior and blockage detection in pressurized water pipelines." *J. Hydro-Environment Res.*, 17: 1–7.

Duan, H. F., Meniconi, S., Lee, P. J., Brunone, B., and Ghidaoui, M. S. 2017b. "Local and integral energy-based evaluation for the unsteady friction relevance in transient pipe flows." *J. Hydraul. Eng.*, 143(7): 04017015.

Ghidaoui, M. S., Karney, B. W., and Mclnnis, D. A. 1998. "Energy estimates for discretization errors in water hammer problems." *J. Hydraul. Eng.*, 124(4): 384–393.

Ghidaoui, M. S., Zhao, M., Mclnnis, D. A., and Axworthy, D. H. 2005. "A Review of Water Hammer Theory and Practice." *Appl. Mech. Rev.*, 58(1): 49-76.

Haaland, S. E. 1983. "Simple and explicit formulas for the friction factor in turbulent pipe flow." *J. Fluids Eng.*, 105(1): 89-90.

Holmboe, E. L., and Rouleau, W. T. 1967. "The effect of viscous shear on transients in liquid lines." *J. Basic Eng.*, 89(1): 174–180.

Jang, T. U., Wu, Y., Xu, Y., Newman, J., and Sun, Q. 2016. "Efficient quasi-two-dimensional water hammer model on a characteristic grid." *J. Hydraul. Eng.*, 142(12): 06016019.

Karney, W. B. 1990. "Energy relations in transient closed-conduit flow." *J. Hydraul. Eng.*, 116(10): 1180–1196.

Karney, B. W., and Mclnnis, D. 1992. "Efficient calculation of transient flow in simple pipe networks." *J. Hydraul. Eng.*, 118(7): 1014–1030.

Louati, M., and Ghidaoui, M. S. 2018. "Eigenfrequency shift mechanism due to variation in the cross sectional area of a conduit." *J. Hydraul. Res.*, 55(6): 829–846.

Martins, N. M. C., Brunone, B., Meniconi, S., Ramos, H. M., and Covas, D. I. C. 2017. "CFD and 1D approaches for the unsteady friction analysis of low Reynolds number turbulent flows." *J. Hydraul. Eng.*, 143(12): 04017050.

Martins, N. M. C., Soares, A. K., Ramos, H. M., and Covas, D. I. C. 2016. "CFD modeling of transient flow in pressurized pipes." *Comput. Fluids.*, 126: 129–140.

Mitosek, M., and Szymkiewicz, R. 2016. "Reservoir influence on pressure wave propagation in steel pipes." *J. Hydraul. Eng.*, 142(8): 6016007.

Nikpour, M. R., Nazemi, A. H., Dalir, A. H., Shoja, F., and Varjavand, P. 2014. "Experimental and numerical simulation of water hammer." *Arab. J. Sci. Eng.*, 39(4):2669-2675.

Pezzinga, G. 1999. “Quasi-2D model for unsteady flow in pipe networks.” *J. Hydraul. Eng.*, 125(7): 676–685.

Pezzinga, G. 2000. “Evaluation of unsteady flow resistances by quasi-2D or 1D models.” *J. Hydraul. Eng.*, 126(10): 778–785.

Pezzinga, G. 2009. “Local balance unsteady friction model.” *J. Hydraul. Eng.*, 135(1): 45-56.

Reddy, H. P., Silva-Araya, W. F., and Chaudhry, M. H. 2012. “Estimation of decay coefficients for unsteady friction for instantaneous, acceleration-based models.” *J. Hydraul. Eng.*, 138(3): 260–271.

Shimada, M., Brown, J. M., and Vardy, A. E. 2008. “Interpolation errors in rectangular and diamond characteristic grids.” *J. Hydraul. Eng.*,134(10): 1480–1490.

Soares, A. K., Covas, D. I. C., and Ramos, H. M. 2013. “Damping analysis of hydraulic transients in pump-rising main systems.” *J. Hydraul. Eng.*, 139(2), 233–243.

Suzuki, K., Taketomi, T., and Sato, S. 1991. “Improving Zielke’s method of simulating frequency-dependent friction in laminar liquid pipe flow.” *J. Fluids Eng.*, 113(4): 569–573.

Szymkiewicz, R., and Mitosek, M. 2007. “Numerical aspects of improvement of the unsteady pipe flow equations.” *Int. J. Numer. Methods Fluids*., 55: 1039–1058.

Szymkiewicz, R., and Mitosek, M. 2013. “Alternative convolution approach to friction in unsteady pipe flow.” *J. Fluids Eng.*, 136(1): 011202.

Tijsseling, A. S., Hou, Q., Svingen, B., and Bergant, A. 2010. “Acoustic resonance in a reservoir-pipeline-orifice system.” *Proc. ASME 2010 Press. Vessel. Pip. Div. / K-PVP Conf.,* ASME, Bellevue, Washington, USA, PVP2010-25083.

Tiselj, I., and Gale, J. 2008. “Integration of unsteady friction models in pipe flow simulations.” *J. Hydraul. Res*., 46(4): 526–535.

Trikha, A. K. 1975. “An efficient method for simulating frequency-dependent friction in transient liquid flow.” *J. Fluids Eng.*, 97(1): 97–105.

Vardy, A. E., and Brown, J. M. B. 1995. “Transient, turbulent, smooth pipe friction.” *J. Hydraul. Res.*, 33(4): 435–456.

Vardy, A. E., and Brown, J. M. B. 2003. “Transient turbulent friction in smooth pipe flows.” *J. Sound Vib.*, 259(5): 1011–1036.

Vardy, A. E., and Brown, J. M. B. 2004. “Transient turbulent friction in fully rough pipe flows.” *J. Sound Vib.*, 270(1–2): 233–257.

Vardy, A. E., and Hwang, K. L. 1991. “A characteristics model of transient friction in pipes.” *J. Hydraul. Res.*, 29(5): 669–684.

Vítkovský, J. P., Bergant, A., Simpson, A. R., and Lambert, M. F. 2006. “Systematic evaluation of one-dimensional unsteady friction models in simple pipelines.” *J. Hydraul. Eng.*, 132(7): 696–708.

Vítkovský, J., Lambert, M., Simpson, A. R., and Bergant, A. 2000. “Advances in unsteady friction modelling in transient pipe flow.” *8th Int. Conf. Press. Surges*, BHR, The Hague, The Netherlands.

Vitkovsky, J., Stephens, M., Bergant, A., Lambert, M., and Simpson, A. 2004. “Efficient and accurate calculation of Zielke and Vardy-Brown unsteady friction in pipe transients.” *9th Int. Conf. Press. Surges*, BHR, Chester, United Kingdom.

Wang, X., and Ghidaoui, M. S. 2018. “Pipeline leak detection using the matched-field processing method.” *J. Hydraul. Eng.*, 144(6): 04018030.

Watters, G. Z. 1979. “Modern analysis and control of unsteady flow in pipelines.” Ann Arbor Science Publishers, Inc., Michigan.

Wylie, E. B. 1997. “Frictional Effects in Unsteady Turbulent Pipe Flows.” *Appl. Mech. Rev.*, 50(11S): S241–S244.

Zhang, C., Gong, J., Zecchin, A., Lambert, M., and Simpson, A. 2018. “Faster inverse transient analysis with a head-based method of characteristics and a flexible computational grid for pipeline condition assessment.” *J. Hydraul. Eng.*, 144(4): 04018007.

Zhao, M., and Ghidaoui, M. S. 2003. “Efficient quasi-two-dimensional model for water hammer problems.” *J. Hydraul. Eng.*, 129(12) 1007–1013.

Zhao, M., and Ghidaoui, M. 2004. “Godunov-type solutions for water hammer flows.” *J. Hydraul. Eng.*, 130(4): 341–348.

Zielke, W. 1968. “Frequency-dependent friction in transient pipe flow.” *J. Basic Eng.*, 90(1): 109–115.

Chapter 4 FINITE ELEMENT FOR THE DYNAMIC ANALYSIS OF PIPES SUBJECTED TO WATER HAMMER[2]

4.1. Abstract

An axisymmetric finite element is developed for the dynamic analysis of pipes subjected to water hammer. The analysis seamlessly captures the pipe response due to water hammer by solving first the water hammer mass and momentum conservation equations, to recover the spatial-temporal distribution of the internal pressure, and then uses the predicted pressure history to form a time-dependent energy equivalent load vector within a finite element model. The study then determines the pipe response by solving the finite element discretized equations of motion. The formulation of the pipe response is based on Hamilton's principle in conjunction with a thin shell theory formulation, and captures inertial and damping effects. The results predicted by the model are shown to be in agreement with those based on an axisymmetric shell model in ABAQUS for static, free vibration and transient responses for benchmark problems. The water hammer and structural models are seamlessly integrated to enable advancing the transient solution well into the time domain to capture the effect of reflected pressure wave due to water hammer. The results indicate that the radial stress/displacement oscillations approach those of the quasi-steady response when the valve closure time exceeds eight times the period of radial vibrations obtained for the case of instantaneous valve closure.

4.2. Introduction

Pipe systems are vastly used to transport fluids in modern industries, e.g., hazardous chemical liquids, gas, oil, water, etc. In these applications, the safety of pipe systems is frequently challenged by transient phenomena induced by water hammer, which occurs either after sudden opening or closure of valves, or after shut-down of pumps.

One-dimensional water hammer models based on mass and momentum conservation may account for the radial expansion of the pipe as in the classical water hammer model of Ghidaoui

---

[2] Cao, H., Mohareb, M., Nistor, I., (2020) "Finite element for the dynamic analysis of pipes subjected to water hammer". Journal of Fluids and Structures, 93: 102845.

Huade Cao: Conceptualization, Methodology, Software, Validation, Writing - original draft. **Magdi Mohareb:** Conceptualization, Writing - review & editing, Resources, Supervision. **Ioan Nistor:** Conceptualization, Writing - review & editing, Resources, Supervision

et al. (2005) and the extended water hammer model of Wiggert and Tijsseling (2001). Such models consider the pipe as a set of independent rings subjected to circumferential and longitudinal stresses induced by the internal pressure. By applying Hooke's law, the radial displacement of a ring is determined from the circumferential and longitudinal stresses induced in the pipe wall. By omitting the bending rigidity of the pipe wall and the inertial effects of the pipe in the radial direction, the circumferential stress can be considered proportional to the internal pressure. In order to obtain the longitudinal stresses in such one-dimensional models, one of two idealizations can be adopted; either (1) neglecting the longitudinal inertial effect within the pipe, leading to a longitudinal stress that is proportional to the circumferential stress, where the constant of proportionality depends on the anchoring conditions at both ends of the pipe (e.g., Ghidaoui et al., 2005 and Chohan, 1989), or (2) accounting for the longitudinal inertial effects within the pipe, in which case the longitudinal stress can be determined from the equation of motion of the pipe in the longitudinal direction (e.g., Li et al., 2015, Wiggert and Tijsseling, 2001). The above two approaches have been adopted within water hammer models not including fluid structure interaction (e.g., Ghidaoui et al., 2005 and Chohan, 1989) and with fluid structure interaction (e.g., Li et al., 2015; Wiggert and Tijsseling, 2001).

Comparisons of the above water hammer models against experimental results (Ferras et al. 2017, Adamkowski and Lewandowski 2006, Brunone et al. 2004, and Lavooij and Tusseling 1991) showed good agreement in predicting the pressure and velocity fields within the fluid. Regarding the pipe response, however, an abrupt change in pressure near the wave front implies an unrealistically abrupt change in the radial displacement of the pipe wall (if the radial stress is to remain proportional to the internal pressure as implied in classical and the extended water hammer models). In order to rectify this assumption, shell models can be used to predict more realistic responses under abrupt pressure changes, as may be the case near the wave front.

In general, two-way fluid-structure interaction (FSI) schemes are based either on (1) the partitioned approach (Figure 4.1a) or (2) the monolithic approach (Figure 4.1b). The following sections discuss the merits and limitations of both approaches to place the methodology proposed in the present study in the proper context. The partitioned approach (Figure 4.1b) involves two separate systems of governing equations, one for the fluid and another for the structure. The fluid model is based on conservation principles and computes the fluid fields (e.g., fluid pressure and

velocities) as an output for a given set of displacement fields (as input). The structural model is based on the equations of motion and provides the structural fields (e.g., displacements, velocities, and accelerations) for a given pressure distribution (as input). For a given time increment, both systems are solved multiple times until the output variables attain convergence. From a computational viewpoint, the partitioned approach may offer advantages in separating the fluid model from the structural model and adopting solution techniques that are tailored/optimized to each system separately. For instance, one can combine the method of characteristics (MOC) for the fluid model with the finite element analysis (FEA) for the structural model. The partitioned approach has been adopted in fluid-structure applications such as non-reflected wave propagation in elastic tubes (e.g., Haelterman et al. 2016, Mehl et al. 2016 and Degroote et al. 2010) and immersed structures (e.g., Li et al. 2016, Habchi et al. 2013 and Breuer et al. 2012). To the authors' knowledge, the partitioned approach has not been used to date in water hammer problems and is the subject of our present/future investigations.

The monolithic approach (Figure 4.1a) adopts a single system of governing equations simultaneously involving the fluid fields (e.g., pressure and fluid velocity) and structural fields (e.g., longitudinal stress and velocity). Water hammer models (e.g., Ferras et al. 2017, Tijsseling and Vardy 1996 and Wiggert et al. 1986) have largely adopted the monolithic approach (Table 4-1). In contrast to the partitioned approach, the monolithic approach generally does not require iterations, although as an exception, the model of Lavooij and Tijsseling (1991) adopted a MOC-FEA monolithic approach involving an iterative scheme. In general, the monolithic approach typically involves simplifying assumptions. For example, the models of Wiggert et al. (1986) and Tijsseling and Vardy (1996) omit the radial inertial effects in the pipe. Also, the hypothetical case of discontinuity in the water hammer pressure at the wave front along with the adopted assumption of proportionality between the pressure and hoop stresses, would imply an unrealistic discontinuity in the radial displacement in the neighborhood of the wave front, which is not possible based on physical grounds. In summary, while the monolithic approach may not involve iterations, it involves approximations/simplifications compared to the partitioned approach.

Table 4-1 outlines typical simplifications/limitations in two-way FSI solutions in water hammer problems. Some of the models omit the radial inertia of the pipe, while others are limited to specific cases (local dry friction, distributed friction, no friction) or intermediate support conditions

(elastically restrained, fixed, or no supports) and omit the mass of the valve (in all except the study of Ferras et al. 2017). In contrast, the model sought in the present study is able to capture any of these effects.

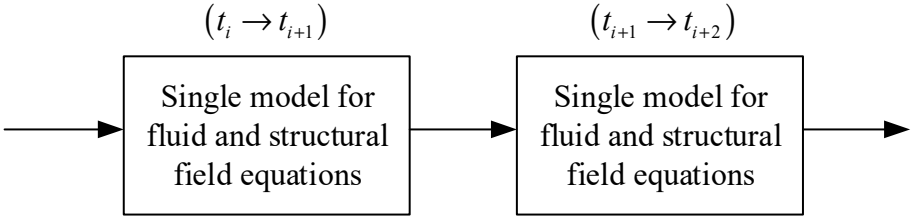

(a) Monolithic approach

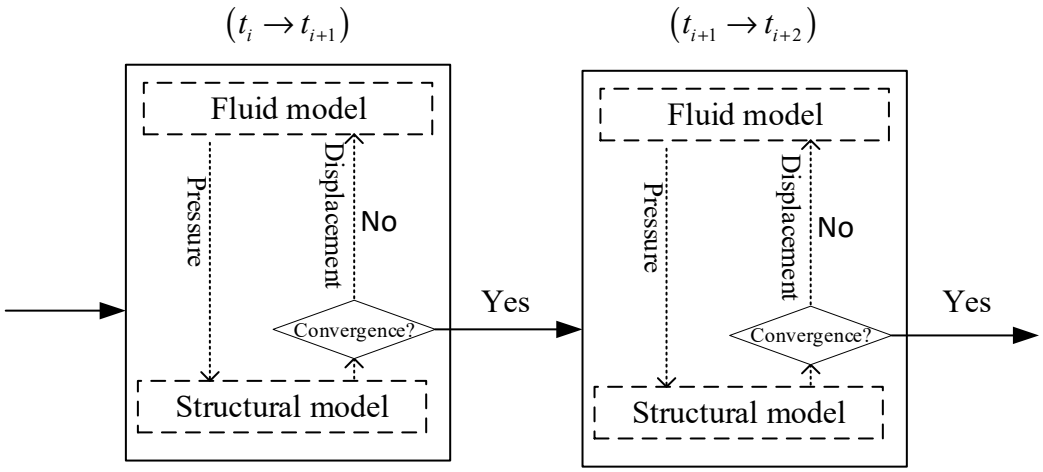

(b) Partitioned approach

Figure 4.1 Schematic representation of (a) monolithic approach and (b) partitioned approach.

Table 4-1 Comparison of the extended water hammer models using monolithic approach for linearly elastic models of straight pipes

		Inertial effect		Bending stiffness of wall	Viscous damping	Dry friction		Internal axial support		Mass of valve
		Axial	Radial			Local	Distributed	Elastically	Fixed	
Walker and Philips (1977)	II	✓	✓							
Wiggert et al (1986)	II	✓								
Budny (1991)	II	✓			✓					
Heinsbroek and Tijsseling (1994)	II	✓						✓		
Tijsseling and Vardy (1996)	II	✓				✓				
Ferras et al (2016)	II	✓					✓			
Ferras et al. (2017)	II	✓					✓		✓	✓
Present	I	✓	✓	✓	✓	☑[1]	☑[1]	☑[1,2]	☑[3]	☑[4]

I: One-way coupling model. II: Two-way coupling model.

☑ Means that the present element implementation is capable of capturing the effect

[1] Dry friction can be treated as an unknown external load.

[2] The axial stiffness of elastically restrained supports can be added to the stiffness matrix.

[3] The anchored condition restrains the related longitudinal displacement.

[4] The mass of the valve can be added to the mass matrix.

4.3. Literature review on finite elements for pipe analysis

Pipe elbow elements were proposed for the pipe analyses. In these elements, Fourier series were used to express the displacement fields around the cross-section and they were combined with beam models, e.g., Melo and Castro (1992,1997), Mackenzie and Boyle (1992). Based on the inextensibility assumption in the circumferential direction, simple elbow elements were proposed to capture the ovalization of pipe cross-section (e.g., Bathe and Almeida 1982, 1980, and Militello and Huespe 1988). To include the pressure stiffening effect in elbow elements, Bathe and Almeida (1982) introduced a pressure stiffness matrix. As the pipe is assumed inextensible in the circumferential direction, the pipe radial expansion was not captured in these elbow elements. In order to incorporate radial expansion into the formulation, the strain-displacement relations based on the thin shell theory were adopted by Ohstubo and Watanabe (1977) to develop a ring element for curved pipes, and by Weicker et al. (2010) for straight pipes. Using shape functions based on closed form solutions Salahifar and Mohareb (2010, 2012) developed an element for the analysis of straight pipe under harmonic loading. By adopting displacement fields that follow a Fourier series distribution around the circumferential direction, solutions for axisymmetric shell elements

were proposed for shells of revolution subjected to unsymmetrical loading by Fan and Luah (1990), Grafton and Strome (1963), To and Wang (1991) and Webster (1967).

Owing to the axisymmetric nature of the water hammer phenomenon and given that a typical pipe thickness is significantly smaller than its radius, axisymmetric thin shell elements are appropriate to investigate the response of pipes under water hammer. Previous axisymmetric formulations for thin shells of revolutions include shells with meridional lines that are linear (Grafton and Strome 1963, Percy et al. 1965 and Cui et al. 2016), quadratic (Stricklin et al. 1966), cubic (Jones and Strome 1966 and Giannini and Miles 1970), following higher order polynomials (Popov and Sharifi 1971), and following B-spline shape functions (Fan and Luah 1989 and Gupta et al. 1991). Axisymmetric shell elements based on the mixed variational principles were also developed by Loula et al. (1989), Kim and Kim (1996) and Toth (2014).

Within the class of axisymmetric solutions for shells of revolution, a number of thick shell formulations were also developed. This includes the work of Zienkiewicz et al. (1977) who resolved shear locking by adopting reduced numerical integration, Mohr (1982) and Tessler and Spiridigliozzi (1988) who adopted a penalty function, Tessler (1982) who adopted an interdependent variable interpolation, and Raveendranath et al. (1999) and Babu and Prathap (1986) who adopted coupled displacement field. Using a 3D ABAQUS model, Leishear (2007) investigated the maximum stresses under water hammer without damping. Due to the extensive computational demand of the 3D model, the study provided the stresses only near the wave front and did not investigate the influence of the reflected pressure and stress waves.

Table 4-2 provides a comparative summary of the studies on the free vibration and transient analyses of circular cylindrical shells for axisymmetric dynamic responses. As shown in the table, the present study aims to develop an axisymmetric shell element to investigate the pipe dynamic response induced by water hammer. The closest studies to the present formulation are possibly the work of Melo et al. (1996) and the ABAQUS elements SAX1 and SAX2. Both formulations differ from the present treatment with respect to the kinematic assumptions and simplifications made in the strain displacement expressions, and hence their underlying variational expressions are different. The interpolation schemes used in ABAQUS are linear for the SAX1 element and quadratic for the SAX2 element, while the present study adopts C-1 continuous Hermitian polynomials.

The finite element sought is based on a thin-shell theory formulation and captures rotary inertia and viscous damping effects while adopting a consistent mass matrix. It is able to capture the static, free vibration responses as well as the transient dynamic response under water hammer for pipes with uniform cross-sections. The seamless one-way coupling of the hydraulic water hammer model and the structural model of the pipe into a single module enables advancing the transient solution well into the time domain to capture the effect of reflected pressure wave due to water hammer. A feature distinguishing the present study from past ones is that it quantifies the effect of dynamic effects induced by water hammer on the stresses in the pipe wall.

Table 4-2 Comparative summary of features in finite element solutions of circular cylindrical shells dynamic axisymmetric response.

	Rotary inertial	Transverse shear	Lumped mass	Consistent mass	Free vibration	Transient vibration	Viscous Damping	Water hammer pressure
Percy et al. (1965)				✓				
Webster (1967)				✓	✓			
Tessler (1982)	✓	✓		✓	✓			
Tessler and Spiridigliozzi (1988)	✓	✓		✓	✓			
Fan and Luah (1989)	✓			✓	✓			
To and Wang (1991)	✓			✓	✓			
Melo et al (1996)	✓	✓	✓			✓		
Raveendranath et al. (1999)	✓	✓		✓	✓			
Cui et al. (2016)				✓	✓	✓	✓	
SAX1 and SAX2 (ABAQUS)	✓	✓	✓	✓	✓	✓	✓	
Present Study	✓			✓	✓	✓	✓	✓

4.4. Statement of the problem

A pipe with circular cross-section with length L, wall thickness h and mid-surface radius R is considered. Pipe material's Young's modulus is E and the Poisson's ratio is ν. Figure 4.2 depicts an elevation view of the un-deformed and deformed pipe middle surface. Given the axisymmetry of the problem, cylindrical coordinate (x,r,ϕ) is adopted such that x is oriented along the pipe axis, r is oriented along the radial direction, and ϕ is an angle along the circumferential direction. The pipe is subjected to axisymmetric body forces $p^i(x,r,t)=\left(p^x,p^r,p^\phi=0\right)$, where p^x is body force along longitudinal direction, and p^r is body force along radial direction. Owing to the axi-symmetry of the pipe geometry and external loading, a generic point $Q(x,t)$ on the middle surface

undergoes a longitudinal displacement $u(x,t)$ and a radial displacement $w(x,t)$. In the absence of tangential tractions, the tangential displacement vanishes, i.e., $v(x,t)=0$. It is required to develop a finite element solution for the dynamic response of the cylinder under water hammer loads.

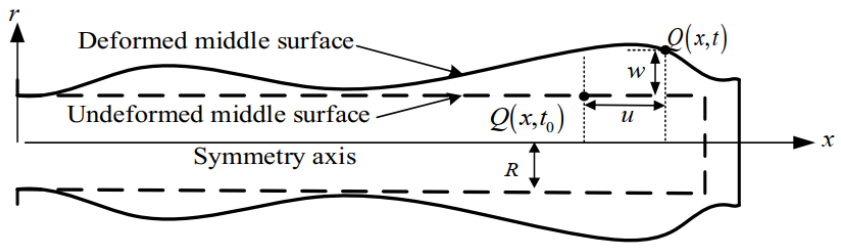

Figure 4.2 Pipe initial configuration at time t_0 and deformed configuration at time t.

4.5. Assumptions

The main assumptions are:

(1) The mid-surface radius and thickness of pipe cross-section are constant.

(2) The shell thickness is small relative to the pipe radius.

(3) The shell thickness remains constant throughout deformation.

(4) A straight fiber normal to the shell mid-surface remains straight and normal to the middle surface throughout deformation.

(5) All displacements are small compared to the radius of pipe.

(6) Material is elastic isotropic.

(7) The pipe response is axisymmetric, i.e., displacements, strains, and stresses are independent of the circumferential coordinate.

4.6. Variational formulation

4.6.1. Overview of relevant past work for thin-shell cylinder

The variational form of the Hamilton's principle (e.g., Townend and Kerr 1982, Salahifar and Mohareb 2012) takes the form

$$\delta \int_{t=t_1}^{t=t_2} \Pi dt = \delta \int_{t=t_1}^{t=t_2} T^* dt - \delta \int_{t=t_1}^{t=t_2} D^* dt - \delta \int_{t=t_1}^{t=t_2} V^* dt + \delta \int_{t=t_1}^{t=t_2} W^* dt = 0 \tag{4.1}$$

where Π is the mechanical energy of the system, T^* is the kinetic energy, V^* is the internal strain energy, and W^* is the external work done by the external loads, D^* is the energy dissipated by non-conservative forces, and the symbol δ denotes the variation of the argument functional. Based on assumptions (1-6), Salahifar (2011) and Salahifar and Mohareb (2012, 2010) expressed the covariant and contravariant components of the displacement fields, and components of the covariant strain tensor in terms of displacement fields at mid-surface. The tensor form of Hamilton's principle was then expanded and integrated along the shell thickness.

4.6.2. Axisymmetric thin-shell cylinder

4.6.2.1. Stress-strain relationship

Based on the assumption (7), the tangential displacement and the terms derivative with respect to the circumferential coordinate vanish in the axisymmetric thin-shell cylinder. The strain-displacement relationships (Salahifar 2011) for axisymmetric thin-shell cylinder are

$$\begin{aligned} \varepsilon_x &= u_{,x} - \frac{r-R}{R} w_{,xx} \\ \varepsilon_\phi &= \frac{w}{r} \end{aligned} \tag{4.2}$$

where all subscripts $,x$ denote differentiation with respect to the longitudinal coordinate. The stress-strain expressions are thus obtained by applying the generalized Hooke's law and given as:

$$\begin{aligned} \sigma_x &= \frac{E}{1-\nu^2}\left(\varepsilon_x + \nu\varepsilon_\phi\right) \\ \sigma_\phi &= \frac{E}{1-\nu^2}\left(\varepsilon_\phi + \nu\varepsilon_x\right) \end{aligned} \tag{4.3}$$

The von Mises σ_v stresses are given by

$$\sigma_v = \sqrt{\sigma_x^{\,2} + \sigma_\phi^{\,2} - \sigma_x\sigma_\phi} \tag{4.4}$$

4.6.2.2. Hamilton's principle for axisymmetric thin-shell cylinder

The variational form of the Hamilton's principle in Eq. (4.1) can be specialized for the axisymmetric case (Assumption 7), leading to:

$$\begin{aligned}
&\int_{t=t_1}^{t=t_2}\delta\Pi dt = 2\pi\rho_s hR\int_{x=0}^{x=L}\left[\left(\dot{u}-\frac{h^2}{12R}\dot{w}_{,x}\right)\delta u+\left(-\frac{h^2}{12R}\dot{u}+\frac{h^2}{12}\dot{w}_{,x}\right)\delta w_{,x}+\dot{w}\delta w\right]_{t_1}^{t_2}dx\\
&-2\pi\rho_s hR\int_{t=t_1}^{t=t_2}\int_{x=0}^{x=L}\left[\left(\ddot{u}-\frac{h^2}{12R}\ddot{w}_{,x}\right)\delta u+\left(-\frac{h^2}{12R}\ddot{u}+\frac{h^2}{12}\ddot{w}_{,x}\right)\delta w_{,x}+\ddot{w}\delta w\right]dxdt\\
&-\delta\int_{t=t_1}^{t=t_2}D^*dt-\frac{2\pi ER}{1-\nu^2}\int_{t=t_1}^{t=t_2}\int_{x=0}^{x=L}\left\{\left(hu_{,x}-\frac{h^3}{12R}w_{,xx}+\nu\frac{h}{R}w\right)\delta u_{,x}\right.\\
&\left.-\left(\frac{h^3}{12R}u_x-\frac{h^3}{12}w_{,xx}\right)\delta w_{,xx}+\left[\frac{\nu h}{R}u_{,x}+\left(\frac{h}{R^2}+\frac{h^3}{12R^4}\right)w\right]\delta w\right\}dxdt\\
&+2\pi R\int_{t=t_1}^{t=t_2}\int_{x=0}^{x=L}\left(\int_{r=R-h/2}^{r=R+h/2}p_x r dr\delta u+\int_{r=R-h/2}^{r=R+h/2}p_x(r-R)rdr\delta w_{,x}+\int_{r=R-h/2}^{r=R+h/2}p_r rdr\delta w\right)dxdt\\
&=0
\end{aligned}\tag{4.5}$$

where p_x and p_r are the body forces along the longitudinal and radial coordinates. In deriving Equation (4.5), the following approximation [resulting from Assumption (2)] has been used (Salahifar, 2011; Salahifar and Mohareb, 2012)

$$\ln\left(\frac{2R+h}{2R-h}\right)\approx\frac{h}{R}+\frac{h^3}{12R^3}\tag{4.6}$$

4.6.3. Natural Frequencies

From the variational expression in Eq.(4.5), by omitting the external work and the damping terms, and performing integration by parts, one obtains the following equations of motion

$$\begin{aligned}
&\frac{\rho_s(1-\nu^2)}{E}\left(\ddot{u}-\frac{h^2}{12R}\ddot{w}_{,x}\right)-u_{,xx}-\frac{\nu}{R}w_{,x}+\frac{h^2}{12R}w_{,xxx}=0\\
&\frac{\rho_s(1-\nu^2)}{E}\left(\frac{h^2}{12R}\ddot{u}_{,x}+\ddot{w}-\frac{h^2}{12}\ddot{w}_{,xx}\right)+\frac{\nu}{R}u_{,x}-\frac{h^2}{12R}u_{,xxx}+\left(\frac{1}{R^2}+\frac{h^2}{12R^4}\right)w+\frac{h^2}{12}w_{,xxxx}=0
\end{aligned}\tag{4.7}$$

and the possible boundary conditions of the problem are:

$$\left\{\left[-\rho_s\left(-\ddot{u}+R\ddot{w}_{,x}\right)-\frac{E}{1-\nu^2}\left(u_{,xx}-Rw_{,xxx}\right)\right]\delta w\right\}_0^L=0$$
$$\left[\left(\frac{u_{,x}}{R}-w_{,xx}\right)\delta w_{,x}\right]_0^L=0, \qquad \left[\left(u_{,x}-\frac{h^2w_{,xx}}{12R}+\nu\frac{w}{R}\right)\delta u\right]_0^L=0 \tag{4.8}$$

4.7. Finite element formulation

4.7.1. Stiffness and mass matrices

The longitudinal and radial displacements are expressed in discretized forms as:

$$u\approx\mathbf{L}^T\mathbf{u}_N;\qquad w\approx\mathbf{H}^T\mathbf{w}_N \tag{4.9}$$

where $\mathbf{u}_N(t)=\langle u_1 \quad u_2\rangle^T$ are nodal longitudinal displacements, and $\mathbf{w}_N(t)=\langle w_1 \quad w_1' \quad w_2 \quad w_2'\rangle^T$ are nodal radial displacements and mid-surface rotation angles, and $\mathbf{L}$ and $\mathbf{H}$ are linear and cubic Hermitian shape functions for displacements in the longitudinal direction, respectively. From Eq.(4.9), by substituting into the Hamilton equation [Eq.(4.5)] and writing in matrix form, the discretized equations of motion are obtained in the form as:

$$\mathbf{M}\ddot{\mathbf{U}}(t)+\mathbf{C}\dot{\mathbf{U}}(t)+\mathbf{K}\mathbf{U}(t)=\mathbf{P}(t) \tag{4.10}$$

where the mass matrix $\mathbf{M}$ is given by

$$\mathbf{M}=\begin{bmatrix}\mathbf{m_{11}} & \mathbf{m_{12}}\\ \mathbf{m_{12}^T} & \mathbf{m_{22}}\end{bmatrix} \tag{4.11}$$

$$\mathbf{m_{11}}=2\pi\rho_sRh\int_{x=0}^{x=L}\mathbf{L}\mathbf{L}^T dx \quad \mathbf{m_{12}}=-\frac{\pi\rho_sh^3}{6}\int_{x=0}^{x=L}\mathbf{L}\mathbf{H}'^T dx \quad \mathbf{m_{22}}=2\pi\rho_sRh\left(\frac{h^2}{12}\int_{x=0}^{x=L}\mathbf{H}'\mathbf{H}'^T dx+\int_{x=0}^{x=L}\mathbf{H}\mathbf{H}^T dx\right)$$

the stiffness matrix $\mathbf{K}$ is given by

$$\mathbf{K}=\begin{bmatrix}\mathbf{k_{11}} & \mathbf{k_{12}}\\ \mathbf{k_{12}^T} & \mathbf{k_{22}}\end{bmatrix} \tag{4.12}$$

$$\mathbf{k}_{11} = \frac{2\pi ERh}{1-\nu^2}\int_{x=0}^{x=L} \mathbf{L}'\mathbf{L}'^{T} dx \qquad \mathbf{k}_{12} = \frac{2\pi E}{1-\nu^2}\left(h\nu \int_{x=0}^{x=L} \mathbf{L}'\mathbf{H}^{T} dx - \frac{h^3}{12}\int_{x=0}^{x=L} \mathbf{L}'\mathbf{H}''^{T} dx \right)$$

$$\mathbf{k}_{22} = \frac{2\pi E}{1-\nu^2}\left[\frac{Rh^3}{12}\int_{x=0}^{x=L} \mathbf{H}''\mathbf{H}''^{T} dx + \left(\frac{h}{R} + \frac{h^3}{12R^3} \right)\int_{x=0}^{x=L} \mathbf{H}\mathbf{H}^{T} dx \right]$$

The stiffness and mass matrices (Appendix A) are obtained by performing explicit integration along the longitudinal direction and $\mathbf{U}^T(t) = \left\langle \mathbf{u}_N{}^T(t) \quad \mathbf{w}_N{}^T(t) \right\rangle$ is the nodal displacement vector. The damping matrix $\mathbf{C}$ and loading vector $\mathbf{P}(t)$ are provided in the following sections.

4.7.2. Viscous damping

Using the Rayleigh damping model, the viscous damping matrix $\mathbf{C}$ is proportional to the mass and stiffness matrices (e.g., Clough and Penzien, 2003), and is given by

$$\mathbf{C} = a_0\mathbf{M} + a_1\mathbf{K} \tag{4.13}$$

where damping parameters a_0, a_1 are related to the damping ratios ξ_m, ξ_n for modes m and n through

$$\begin{Bmatrix} a_0 \\ a_1 \end{Bmatrix} = 2\frac{\omega_m\omega_n}{\omega_n^2 - \omega_m^2}\begin{bmatrix} \omega_n & -\omega_m \\ -1/\omega_n & 1/\omega_m \end{bmatrix}\begin{Bmatrix} \xi_m \\ \xi_n \end{Bmatrix} \tag{4.14}$$

where ω_m, ω_n are the natural frequencies of modes m and n.

4.7.3. Loading vector

The energy equivalent load vector is $\mathbf{P}^T(t) = \left\langle \mathbf{P}_x{}^T(t) \quad \mathbf{P}_r{}^T(t) \right\rangle$, in which

$$\begin{aligned} \left\{\mathbf{P}_x(t)\right\} &= 2\pi \int_{x=0}^{x=L} \mathbf{L} \int_{r=R-h/2}^{r=R+h/2} p_x r dr dx \\ \left\{\mathbf{P}_r(t)\right\} &= 2\pi \int_{x=0}^{x=L} \left\{ \mathbf{H} \int_{r=R-h/2}^{r=R+h/2} p_r r dr + \mathbf{H}' \int_{r=R-h/2}^{r=R+h/2} p_x (r-R) r dr \right\} dx \end{aligned} \tag{4.15}$$

In order to determine the vector load vectors $\left\{\mathbf{P}_x(t)\right\}$, $\left\{\mathbf{P}_r(t)\right\}$ for the presently sought one-way FSI water hammer solution, the body forces $p_x = p_x(x,r,t)$ and $p_r = p_r(x,r,t)$ need to be

determined from a water hammer model. The specifics of the water hammer model are discussed in the following section.

4.7.3.1.Transient pressure induced by water hammer

Consider a reservoir-pipe-valve system with an upstream reservoir at $x=0$ having a hydraulic head H_{res} and a valve located downstream at $x=L$ (Figure 4.3). Under the hydraulic head H_{res}, and with the valve open, the initial velocity of the fluid $V(x,t=0)=V_0$ is known depending on the operating conditions. After instantaneous valve closure, the velocity at the valve becomes $V(L,t)=0$. A pressure wave is initiated (water hammer) that travels longitudinally back and forth along the pipe. It is required to determine the temporal/spatial pressure distribution $P(x,t)$. For a pipe with both ends longitudinally restrained (i.e., $u(0,t)=u(L,t)=0$), the water hammer wave speed a_w (e.g., Ghidaoui et al. 2005) is

$$a_w=\sqrt{\frac{K_f/\rho_f}{1+\left(1-\nu^2\right)\frac{K_f(2R-h)}{Eh}}} \tag{4.16}$$

where K_f is the bulk modulus for the water.

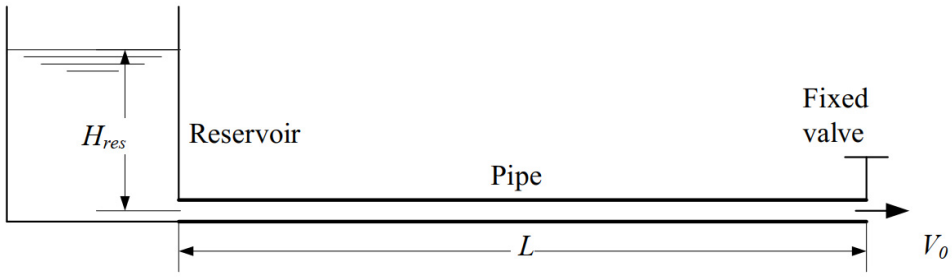

Figure 4.3 Schematic of the reservoir-pipe-valve system.

By adopting a frictionless water hammer model (e.g., Ghidaoui et al. 2005) in the Eulerian scheme, the equations of conservation of mass and momentum in the longitudinal direction are

$$\frac{1}{a_w^2}\frac{\partial P}{\partial t}+\rho_f\frac{\partial V}{\partial x}=0 \tag{4.17}$$

$$\rho_f \frac{\partial V}{\partial t} + \frac{\partial P}{\partial x} = 0 \tag{4.18}$$

where $P = P(x,t)$ is the hydraulic pressure and $V = V(x,t)$ is the fluid velocity, ρ_f is the water density. In the one-dimensional model described by Eqs. (4.17) and (4.18), both the hydraulic pressure and fluid velocity are uniform for a given cross section x. The above equations are solved subject to the initial conditions $V(x,t=0) = V_0$ and $P(x,t=0) = \rho_f g H_{res}$, and subject to the upstream boundary condition $P(0,t) = \rho_f g H_{res}$ and the downstream boundary condition $V(L,t) = 0$, where H_{res} is the pressure head of upstream reservoir and g is the acceleration of gravity. Using the method of characteristics (e.g., Ghidaoui et al. 2005), the governing equations are transformed into ordinary differential equations along characteristic lines. By using a rectangular mesh scheme with a unit Courant number $C_r = a_w \Delta t / \Delta x$, one can numerically determine the unknown velocity $V(x,t)$ and internal pressure $P(x,t)$. The assumption of frictionless water hammer implies that the term p_x appearing in Eq. (4.15) vanishes along the pipe except at the valve, i.e.,

$$p_x(x,r,t) = \begin{cases} 0 & 0 \le x < L \\ \dfrac{P(L,t)(R-0.5h)^2}{2Rh}\,\text{Dirac}(x-L) & x = L \end{cases} \tag{4.19}$$

where Dirac denotes the Dirac delta function. Also, the body force p_r appearing in Eq. (4.15) can be related to the pressure $P(x,t)$ through

$$p_r(x,r,t) = \text{Dirac}\left[r - (R - h/2)\right] P(x,t) \tag{4.20}$$

where $P(x,t)$ has been obtained numerically by solving equations (4.17) and (4.18). For the present problem, given that the pipe end is restrained, the ring force $\left[P(L,t)(R-0.5h)^2\right] / 2Rh$ provided in Eq.(4.19) will not contribute to the work due to external loads, and the work due to external loading then simplifies to

$$\delta W^* = 2\pi R \int_{t=t_1}^{t=t_2} \int_{x=0}^{x=L} F_r(x,t)\,\delta w\,dx\,dt \tag{4.21}$$

where $F_r(x,t) = \int_{r=R-h/2}^{r=R+h/2} \text{Dirac}\left[r-(R-h/2)\right] P(x,t)\,r\,dr = P(x,t)(R-h/2)$.

4.7.3.2. Structural-Hydraulic model Interface

From Eqs. (4.19) and (4.20), by substituting into Eq. (4.15), one can recover the energy equivalent load vectors $\{\mathbf{P}_x(t)\}$, $\{\mathbf{P}_r(t)\}$ for each time step. The stiffness and mass matrices developed in Section 4.7.1. , damping matrix in Section 4.7.2. , load vector in Section 4.7.3. , and water hammer model in Section 4.7.3.1 have been implemented in a MATLAB program featuring a seamless transfer of data between the structural model and water hammer hydraulic model. Both the structural and hydraulic models adopted the same spatial and temporal discretization schemes.

4.7.4. Time integration scheme

The Newmark time integration scheme (Bathe, 2014) is adopted to integrate Eq.(4.10) in time. The velocities $\dot{\mathbf{U}}^{t+\Delta t}$ and displacements $\mathbf{U}^{t+\Delta t}$ at time step $t+\Delta t$ are expressed in terms of the acceleration $\ddot{\mathbf{U}}^{t+\Delta t}$ at $t+\Delta t$, and $\mathbf{U}^t$ $\dot{\mathbf{U}}^t$ $\ddot{\mathbf{U}}^t$ at t as:

$$\dot{\mathbf{U}}^{t+\Delta t} = \dot{\mathbf{U}}^t + \left[(1-\beta)\ddot{\mathbf{U}}^t + \beta\ddot{\mathbf{U}}^{t+\Delta t}\right]\Delta t \tag{4.22}$$

$$\mathbf{U}^{t+\Delta t} = \mathbf{U}^t + \dot{\mathbf{U}}^t\Delta t + \left[\left(\frac{1}{2}-\alpha\right)\ddot{\mathbf{U}}^t + \alpha\ddot{\mathbf{U}}^{t+\Delta t}\right]\Delta t^2 \tag{4.23}$$

The integration scheme is unconditionally stable when $0.5 \le \beta \le 1$ and $0.25(0.5+\beta)^2 \le \alpha \le 1$. The constant-average-acceleration scheme with $\alpha = 1/4, \beta = 1/2$ is adopted in the present study. The displacements for time step $t+\Delta t$ are expressed in terms of force for time step $t+\Delta t$ and displacements $\mathbf{U}^t$, velocities $\dot{\mathbf{U}}^t$ and accelerations $\ddot{\mathbf{U}}^t$ at time step t, one obtains,

$$\begin{aligned}\left(\frac{1}{\alpha\Delta t^2}\mathbf{M} + \frac{\beta}{\alpha\Delta t}\mathbf{C} + \mathbf{K}\right)\mathbf{U}^{t+\Delta t} &= \mathbf{P}^{t+\Delta t} + \left(\frac{1}{\alpha\Delta t^2}\mathbf{M} + \frac{\beta}{\alpha\Delta t}\mathbf{C}\right)\mathbf{U}^t \\ &+ \left[\frac{1}{\alpha\Delta t}\mathbf{M} - \left(1-\frac{\beta}{\alpha}\right)\mathbf{C}\right]\dot{\mathbf{U}}^t + \left[\left(\frac{1}{2\alpha}-1\right)\mathbf{M} - \left(1-\frac{\beta}{2\alpha}\right)\Delta t\mathbf{C}\right]\ddot{\mathbf{U}}^t\end{aligned} \tag{4.24}$$

Eq.(4.24) is solved for the displacement vector $\mathbf{U}^{t+\Delta t}$. Then, the acceleration $\ddot{\mathbf{U}}^{t+\Delta t}$ and the velocity $\dot{\mathbf{U}}^{t+\Delta t}$ are determined from equations (4.22) and (4.23). For static analysis, the mass matrix $\mathbf{M}$ and damping matrix $\mathbf{C}$ vanish in Eq.(4.10) to solve for the displacement vector.

The following differences and similarities exist between the present formulation and the work of Melo et al. (1996): (a) Unlike the mass matrix in Melo et al. (1996) which was based on a lumped mass approximation, Eq.(4.11) develops the consistent mass matrix; (b) The stiffness matrix in Eq.(4.12) is similar, but not identical, to that developed by Melo et al. (1996); (c) Eq.(4.21) provides the energy equivalent load vector based on a water hammer model, a feature not present in Melo et al. (1996); and (d) Unlike the formulation in Melo et al. (1996), which did not capture damping, Eq.(4.13) provides viscous damping matrices.

4.8. Verification

To verify the implementation of the finite element, comparisons were made against finite element models using the SAX1 element in the commercial software ABAQUS. The SAX1 element is a two-node axisymmetric shell element with three degrees of freedom per node; the radial displacement, the longitudinal displacement and the rotation. All three displacement fields are linearly interpolated. The element uses Simpson's rule for integration across the thickness with three integration points by default.

4.8.1. Static analysis

A $1m$ span steel barrel has the boundary conditions $u(0)=w(0)=w_x(0)=0$ and $w(L)=w_x(L)=0$. The steel barrel has a mid-surface radius of 330mm and a thickness of 6 mm. Barrel Young's modulus is 2.1×10^{11}Pa , Poisson's ratio is 0.25. Uniform static loading internal pressure is applied at the internal surface, i.e., $P_r(x,R-h/2)=1(\text{MPa})$. A mesh sensitivity analysis indicated that 256 elements are enough to reach convergence. The longitudinal displacements u, radial displacements w and mid-surface rotation anglers w' along the barrel are shown in Figure 4.4(a-c), in which the deformed configurations predicted by the present solution are in good agreement with those predicted by the SAX1 model. Figure 4.4 (d) and (e) provide the comparison of the strain distributions along the longitudinal coordinates along the inside, mid-surface and outside surfaces as determined from Eq.(4.2). The predictions of the present model are in close agreement with those of the SAX1 model.

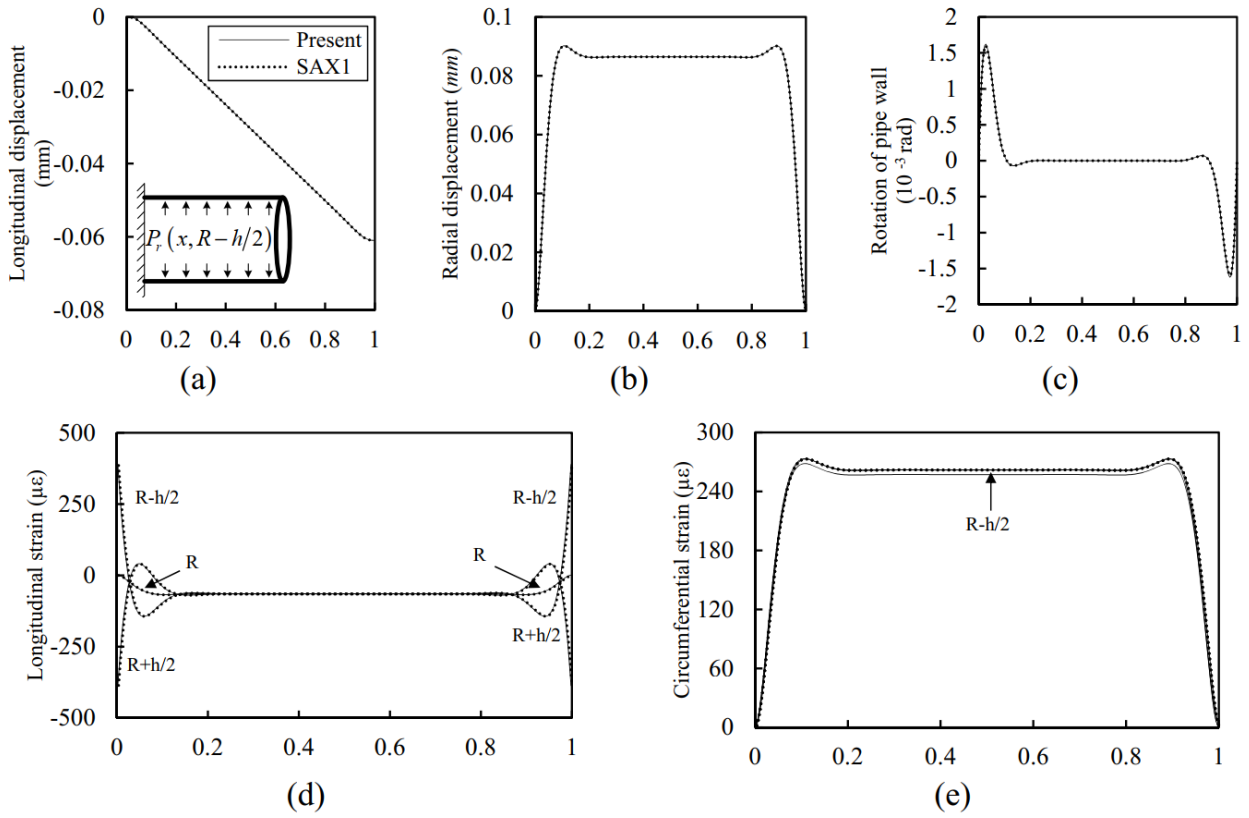

Figure 4.4 Comparison of predicted results for static case using the present finite element solutions and from the ABAQUS model. Horizontal coordinate is the longitudinal coordinate of pipe, vertical coordinates are (a) the longitudinal displacements (mm); (b) the radial displacement (mm); (c) the mid-surface rotation angles (10^{-3} rad); (d) Longitudinal strains (με) and (e) Circumferential strains (με) at the inside (r=R-0.5h), middle (r=R), and outside (r=R+0.5h) surfaces.

4.8.2. Free vibration analysis

A steel pipe with a mid-surface radius of 330mm and a thickness of 6 mm has 30m span. Pipe steel has a Young's modulus of 2.1×10^{11}Pa , a Poisson's ratio of 0.25 and a density of $7980\,\mathrm{kg/m^3}$. Both ends are radially restrained, i.e., $w(0,t)=w(L,t)=0$ and free relative to displacements $u(0,t),u(L,t)$ and rotations $w_x(0,t),w_x(L,t)$. It is required to compare the natural frequencies as predicted by the present model, the SAX1 model, the closed form solution based on the equations of motion (Eq.(4.7)) and the closed form solution reported by Leissa (1993). Three mesh refinements are considered in the present model; 256, 512 and 1024 elements, while two meshes are considered in the SAX1 solution; 2048 and 4096 elements. A closed form solution for the natural frequencies based on the present formulation can be obtained by assuming a solution of the form

$$(u,w)=\sum_{i=1,2,\ldots}^{+\infty}\left[A_i\cos(i\pi x/L),B_i\sin(i\pi x/L)\right]\cos\omega_i t \tag{4.25}$$

in which ω_i is the natural frequency and A_i and B_i are constants related to longitudinal half-wave number for mode i. Equation (4.25) satisfies the essential and the natural boundary conditions of the problem as given in Eq. (4.8). From Eq. (4.25) by substituting into the equations of motion (Eq.(4.7)), one obtains the following expression of the dimensionless frequency $\chi_{i,\pm}=\omega_{i,\pm}R\sqrt{\rho_s\left(1-\nu^2\right)/E}$

$$\chi_{i,\pm}=\sqrt{\frac{b_i\pm\sqrt{b_i^2-4a_ic_i}}{2a_i}} \tag{4.26}$$

where $a_i=1+k(1-k)\lambda_i^2$, $b_i=1+k+(1-2\nu k)\lambda_i^2+2k(1-k)\lambda_i^4$ and $c_i=\left(1+k-\nu^2\right)\lambda_i^2-2k\nu\lambda_i^4+\left(k-k^2\right)\lambda_i^6$, in which $k=h^2/12R^2$ and $\lambda_i=i\pi R/L$. Leissa (1993) provided an expression analogous (but not identical) to the natural frequency expression in Eq.(4.26): $\omega_{i,\pm}=\tilde{\chi}_{i,\pm}\Big/R\sqrt{\rho_s\left(1-\nu^2\right)/E}$ where the Leissa frequency parameter $\tilde{\chi}_{i,\pm}$ was given by

$$\tilde{\chi}_{i,\pm}=\sqrt{\frac{\tilde{b}_i\pm\sqrt{\tilde{b}_i^2-4\tilde{a}_i\tilde{c}_i}}{2\tilde{a}_i}} \tag{4.27}$$

and $\tilde{a}_i=1$, $\tilde{b}_i=1+\lambda_i^2+k\lambda_i^4$ and $\tilde{c}_i=\left(1-\nu^2\right)\lambda_i^2+k\lambda_i^4/2+k\lambda_i^6+k^2\lambda_i^8/4$. A comparison of the natural frequencies for the first 180 vibration modes from all solutions is provided on Figure 4.5(a). The frequencies determined from the closed form solution in Eq. (4.26), are used as reference values against which the frequencies predicted by other solutions are compared (Figure 4.5 b). All four solutions are observed to agree within $\pm1\%$. Compared to the present closed form solution [Eq. (4.26)], Leissa's expression [Eq.(4.27)] and the present finite element solution are found to slightly overestimate the higher natural frequencies, while the SAX1 is found to underestimate them. Both finite element models are found to yield closer results to those predicted by Eq. (4.26) as the number of elements is increased.

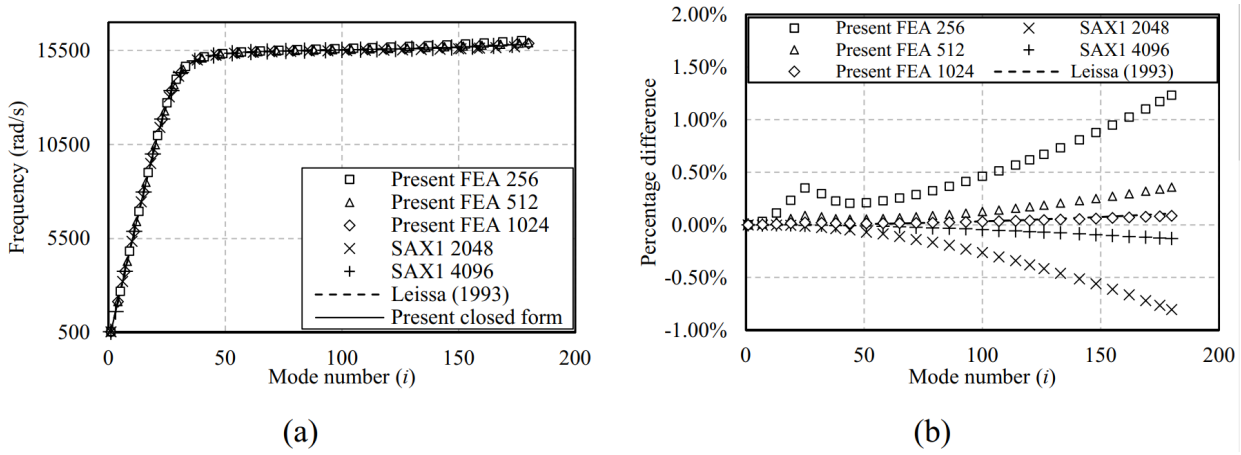

Figure 4.5 Comparison of the natural frequencies determined from the closed form solutions to those based on the finite element solutions. (a) Frequencies for the first 180 modes; (b) Percentage differences from the present closed form solution.

4.9. Pipe subjected to water hammer pressure

4.9.1. Reservoir-pipe-valve system

In the reservoir-pipe-valve system depicted in Figure 4.3, the hydraulic head at the upstream reservoir is $H_{res} = 100\text{m}$. The pipe length is $L = 30\text{m}$ with a mid-surface radius $R = 330\text{m}$ and thickness $h = 6\text{mm}$. Pipe Young's modulus is $E = 210\text{GPa}$, Poisson's ratio is $\nu = 0.25$ and the density is $\rho_s = 7980\,\text{kg}/\text{m}^3$. The water has a bulk modulus $K_f = 2.15\text{GPa}$ and a density $\rho_f = 1000\,\text{kg}/\text{m}^3$. The initial flow velocity is $V_0 = 1.5\,\text{m}/\text{s}$. Both pipe ends are fixed, e.g., $u(0) = w(0) = w'(0) = u(L) = w(L) = w'(L) = 0$. The valve is instantaneously closed. From Eq. (4.16), the water hammer wave speed is $a_w = 1025\,\text{m}/\text{s}$.

4.9.2. Pressure distribution history during water hammer

The water hammer pressure distribution as predicted by the frictionless model in Section 4.3.1, is provided in Figure 4.6. The pressure distributions are then used as input to form the load vector in the structural model, and obtain the dynamic response of the pipe.

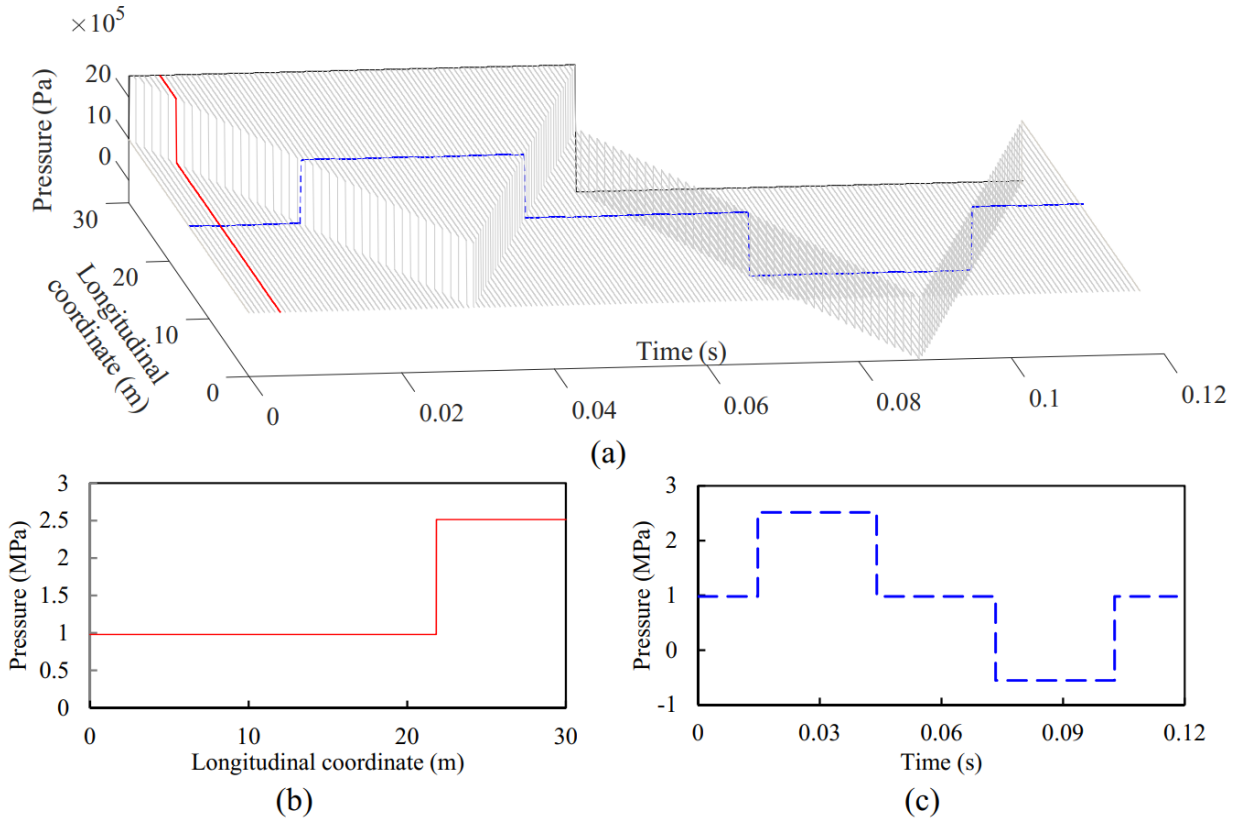

Figure 4.6 Pressure distributions after valve closure for the first cycle. (a) Spatial and temporal pressure distribution; (b) Pressure distribution at time t=8ms;(c) Pressure history at pipe mid-span.

4.9.3. Dynamic response of pipe due to water hammer

The transient response is evaluated using two methods: (a) the present formulation and (b) the SAX1 ABAQUS solution. As shown in the free vibration analysis in Section 4.7.2, a mesh of 2048 elements was found to accurately replicate the pipe mode shapes as predicted by the closed form solution. Therefore, the same mesh is used in the transient analysis based on the present and ABAQUS models. Using a Courant number of 1, and knowing that the water hammer wave speed is $a_w = 1025\,\mathrm{m/s}$, the time increment as determined from $C_r = a_w \Delta t / \Delta x = 1$, is $14.32\,\mu\mathrm{s}$. A total of 8196 steps were taken to model a single pressure cycle, corresponding to a total time of $14.32\,\mu s \times 8196 = 0.12\,\mathrm{sec}$.

In the present implementation, the pressure distributions as predicted by the hydraulic model are seamlessly fed into the structural model which determines the deformation response. In ABAQUS the pressure due to water hammer model is solved first and the pressure at the 8196 time increments were stored for the 2049 nodes and subsequently read by the ABAQUS model.

In the Rayleigh damping model, the damping ratios for the first two modes ($\omega_1 = 537.3 rad/s$ $\omega_2 = 1074.4\,\text{rad/s}$) are taken as $\xi_1 = \xi_2 = 3\%$ and the proportional parameters determined from Eq.(4.14) are $a_0 = 7.16$ and $a_1 = 1.24\times10^{-5}$. The constant-average-acceleration is adopted for the time integration scheme, i.e., $\alpha = 0.25$ and $\beta = 0.5$. On a personal computer [Intel(R) Core(TM) i7-4710MQ CPU @ 2.50GHz, with 8GB RAM, 64bit Win10], the computational time needed to perform the analysis is 24.5sec using the proposed element, which is 138 times faster than the ABAQUS model which takes 3397sec. The longitudinal and radial displacements distributions predicted by the present model are depicted in Figure 4.7 for the first cycle.

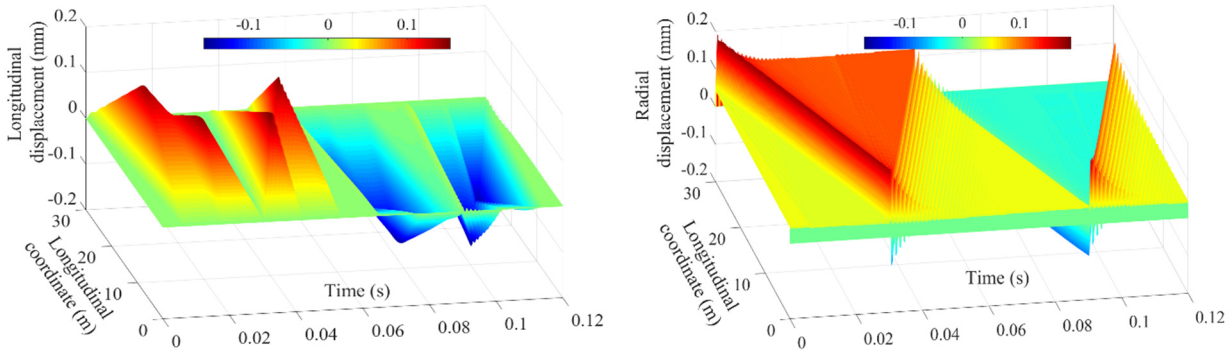

Figure 4.7 Dynamic responses of the pipe subjected to water hammer pressures. (a) Longitudinal displacement (mm) and (b) Radial displacement (mm) distribution histories for the first cycle.

Figure 4.7(a) shows that the history of the longitudinal displacement has multiple peaks in each half-cycle of the pressure wave. These are caused by the combined action of the longitudinal stress wave in the pipe with the pressure wave in the water, as the hoop stress in the pipe wall induced by the water hammer pressure causes a longitudinal stress wave due to the Poisson ratio's effect. The speed of the longitudinal stress wave is that of the sound speed in the pipe $a_s = \sqrt{E/\rho_s} = 5130\,\text{m/s}$, which is nearly four times the pressure wave speed in water. The travelling longitudinal stress wave stretches/shrinks the pipe in the longitudinal direction. Therefore, the longitudinal displacement distribution history shows multiple peaks at each half pressure cycle. Figure 4.6(a) and Figure 4.7(b) show that the radial displacement history has a similar distribution as the pressure history, except for some localized oscillations near the moving pressure wave front. The similarity of the both distributions suggests that the radial displacements are predominately influenced by the water hammer pressure distribution.

The strain-displacement relationships [Eq.(4.2)] are used to determine the longitudinal and circumferential strains, the corresponding stresses are then obtained from [Eq.(4.3)], and the von Mises stresses are recovered from [Eq.(4.4)]. Figure 4.8(a-c) shows close agreement between the predictions of the present model with those of the ABAQUS model for the longitudinal, circumferential and von Mises stresses at the inside, middle and outside surfaces of the pipe at $t = 8\text{ms}$ (the corresponding pressure distribution at $t = 8\text{ms}$ has been provided in Figure 4.6b).

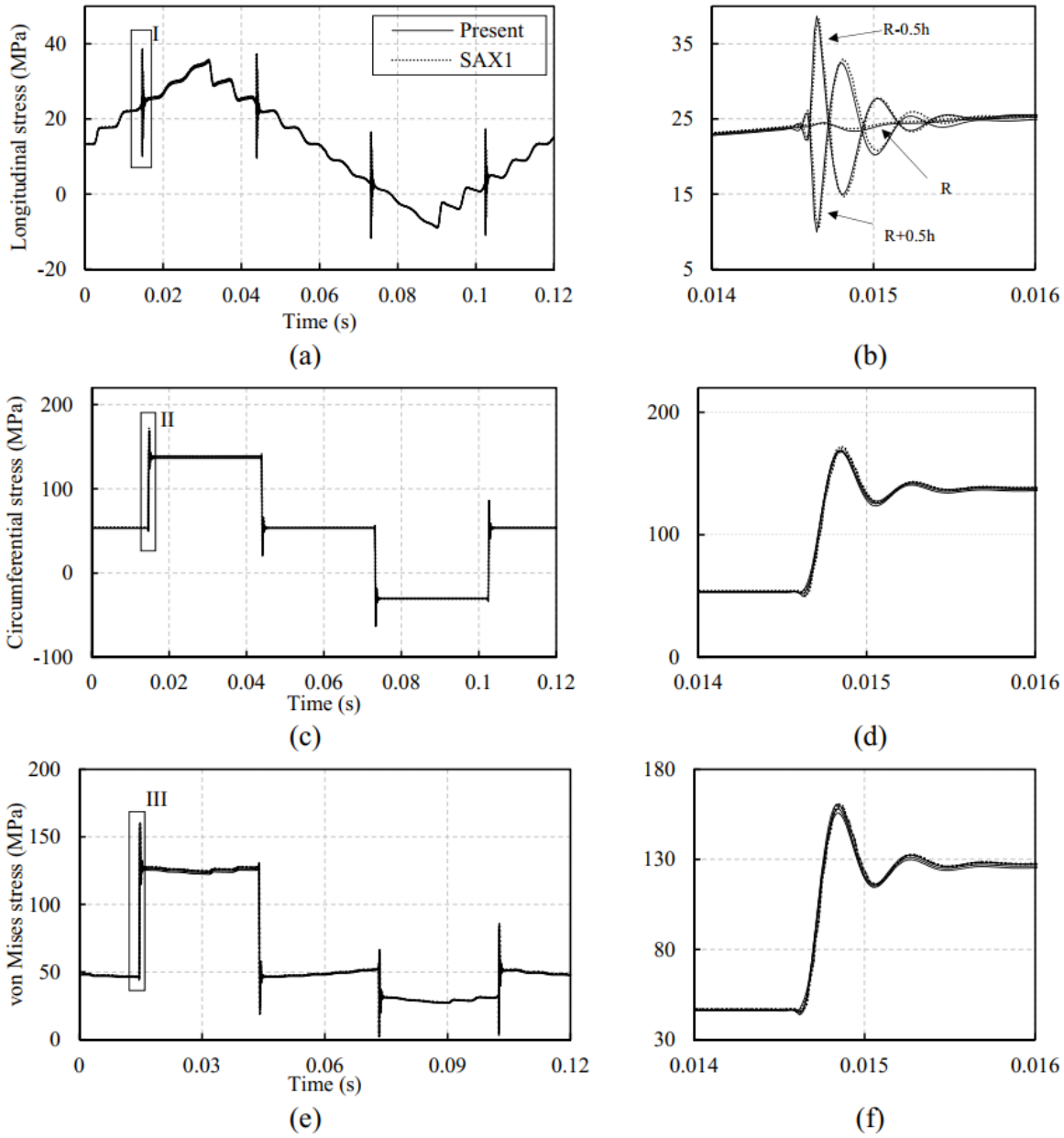

Figure 4.8 Stress distributions along the longitudinal coordinate at t=8ms. (a) Longitudinal stresses; (b) Circumferential stresses; (c) von Mises stresses at the inside R-0.5h, middle R and outside R+0.5h surfaces.

Figure 4.8a shows that at $t = 8\text{ms}$, the pressure wave front (in the fluid) arrives at $x = 21.8\text{m}$ from the reservoir, while the longitudinal stress wave front (in the pipe) arrives near $x = 11\text{m}$. Since the longitudinal stress wave speed is $a_s = 5130\,\text{m/s}$, it travels faster than the pressure wave ($a_w = 1025\,\text{m/s}$). The length travelled by the longitudinal stress wave in 8ms is $a_s t = 41\text{m}$ which is larger than the pipe length of 30m, indicating that the location $x = 11\text{m}$ of the stress wave front at $t = 8\text{ms}$ as predicted by the model represents the reflected stress wave from the upstream reservoir. The observation is consistent with past experimental and numerical observations by Skalak (1953), Williams (1977), and Tijsseling et al. (2008) who reported the occurrence of the longitudinal stress wave prior to the predominant water hammer pressure wave which induces a precursor pressure wave. Figure 4.8(a) and (b) indicate that the magnitudes of the longitudinal stresses are much smaller than those of the circumferential stresses. The maximum von Mises stress is observed to occur at the pressure wave front (Figure 4.8c), which is also the location of the maximum circumferential stresses.

Figure 4.9 shows the histories for the first 0.12s after valve closure for the longitudinal, circumferential and von Mises stresses at the inside, middle surface and outside of the pipes, at the pipe middle cross-section ($x = 15\text{m}$). Excellent agreement is observed between the predictions of the present model and those of the ABAQUS SAX1 model. The longitudinal stress history in Figure 4.9(a) has a similar trend to that predicted by the extended water hammer model of Wiggert et al. (1986) with the exception that the present model predicts oscillations around the pressure wave front (Figure 4.9b) which were not predicted by the model of Wiggert et al. (1986). These oscillations are due to the radial inertial effects in the pipe wall which are captured in the present finite element but not in the extended water hammer model in Wiggert et al. (1986). The radial inertial effects in the pipe wall are also the main reason for the oscillations of the circumferential stresses in Figure 4.9(d).

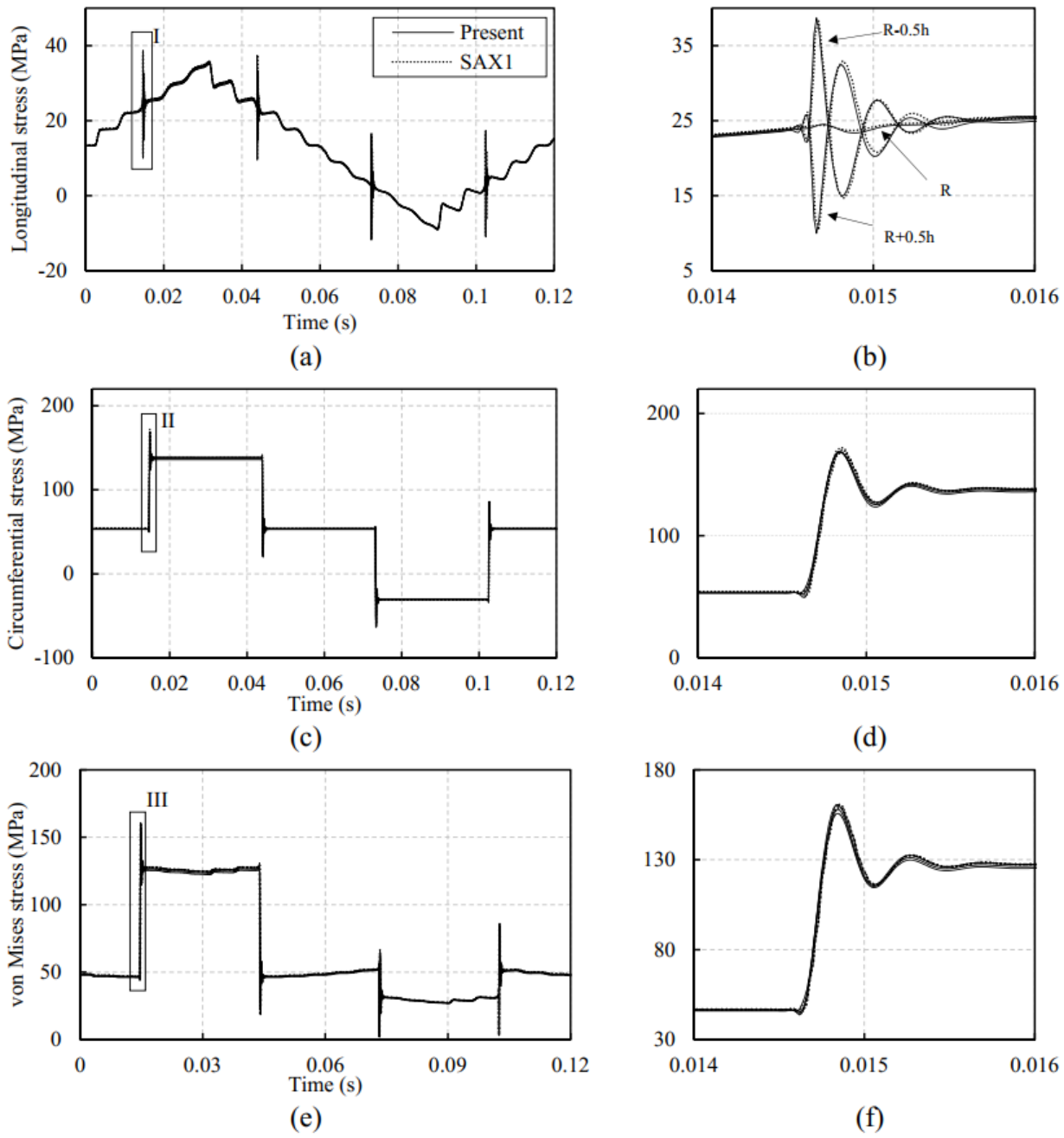

Figure 4.9 Stresses' histories at mid-span along inside R-0.5h, middle R and outside R+0.5h surfaces. (a) Longitudinal stress histories; (b) Zoomed in view of part I in the longitudinal stress histories; (c) Circumferential stress histories; (d) Zoomed in view of part II in the circumferential stress histories; (e) von Mises stress histories; (f) Zoomed in view of part III in the von Mises stress histories.

4.9.4. Effect of damping on the dynamic response

Figure 4.10 shows the stress histories at mid-span as predicted by three solutions: (1) The constant-average-acceleration scheme (i.e., $\alpha = 0.25, \beta = 0.5$) within the Newmark scheme, which

provides no numerical damping to filter the contributions of high frequency modes to the dynamic response according to Chopra (2012) and no viscous damping (i.e., $\xi_1 = \xi_2 = 0$), (2) Using $\alpha = 0.4, \beta = 0.6$ within the Newmark scheme to introduce numerical damping, while applying no viscous damping, i.e., $\xi_1 = \xi_2 = 0$, and (3) Using the constant-average-acceleration scheme, i.e., $\alpha = 0.25, \beta = 0.5$ with no numerical damping, while introducing a viscous damping with $\xi_1 = \xi_2 = 3\%$. Figure 4.10 shows that the stress oscillations are highly dependent on damping. The model with viscous damping damps out the oscillations quickly when compared to the undamped solution, while the model with numerical damping damps out the oscillations slowly. Eventually, numerical damping damps out the oscillations before the arrival of the reflected pressure wave front, as depicted in Figure 4.10(c) for the circumferential stress and Figure 4.10(e) for von Mises stresses. Both the undamped and numerical damping models predicted that stresses oscillate around the steady state values predicted by the model with viscous damping. The undamped model shows that the amplitudes of the circumferential stress oscillations unrealistically increase in each half cycle (Figure 4.10c). The increase in oscillations observed in Figure 4.10c is similar, but not identical, to the beat phenomenon reported in Tijsseling (1997). In the present work, the phenomenon occurs due to interaction between the radial oscillations and the step pressure loading action on the pipe wall. In contrast, the beat phenomenon reported in Tijsseling (1997) is due to the two-way coupling effects between the fluid and the structure. Such effects are not captured in present one-way FSI analysis. The results show that circumferential stress/displacement oscillations after the passage of the pressure wave front are sensitive to numerical and viscous damping. Similar strain oscillations were observed to damp out quickly in shock tubes (Beltman et.al., 1999) and in tubes subjected to internal gaseous detonation (Beltman and Shepherd, 2002). Lavooij and Tijsseling (1991) reported that higher modes were activated by the water hammer front passage. To replicate the stress/strain/displacement oscillations physically observed in experiments, one thus must introduce numerical and viscous damping into the model.

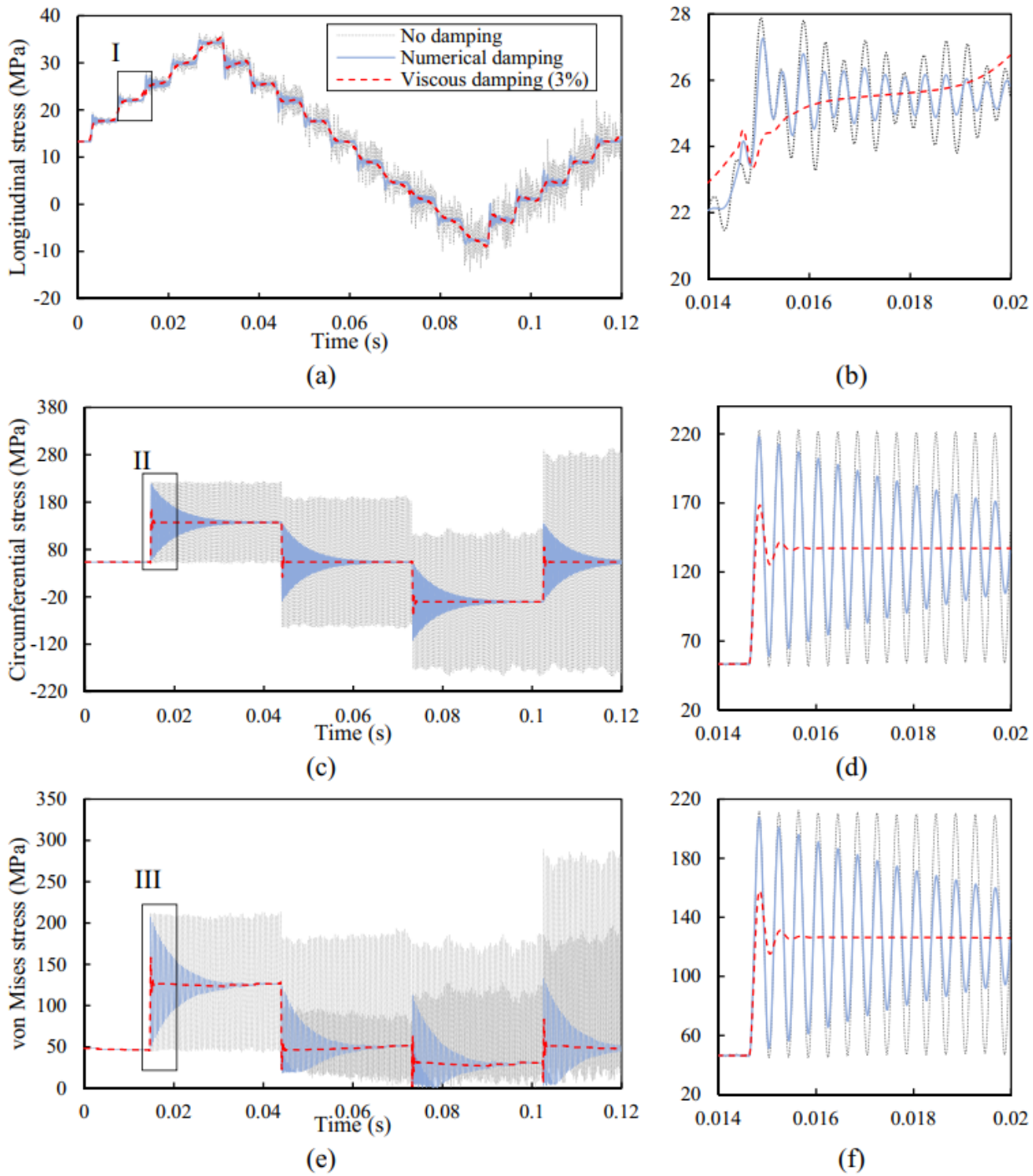

Figure 4.10 Stresses' histories at mid-span along mid-surface obtained from the present finite element analysis. (a) Longitudinal stress histories; (b) Zoomed in view of part I in the longitudinal stress histories; (c) Circumferential stress histories; (d) Zoomed in view of part II in the circumferential stress; (e) von Mises stress histories; (f) Zoomed in view of part III in the von Mises stress history. No damping refers α=0.25, β=0.5 and ξ_1=ξ_2=0 (dot line-black); Numerical damping refers α=0.4, β=0.6 and ξ_1=ξ_2=0 (dash line-red); Viscous damping refers α=0.25, β=0.5 and ξ_1=ξ_2=3% (solid line-blue).

4.9.5. Effect of valve closure time on the pipe dynamic response

4.9.5.1. Valve closure patterns and pressure history during water hammer

The step pressure predicted in conventional water hammer models implies instantaneous valve closure ($t_c = 0$) and is thus a hypothetical scenario. Past studies (e.g., Azoury et al.1986; McInnis et al. 1997) have shown that water hammer pressure is influenced by the valve closure time. The present section investigates the effect of non-zero valve closure times. Numerical damping is taken as ($\alpha = 0.4$, $\beta = 0.6$). Three closure patterns are considered; one linear and two parabolic (Figure 4.11a). The downstream velocities at the valve location during closure ($t \le t_c$) are given by

$$\left.\begin{array}{ll} \text{Pattern 1} & V(t) = (1 - t/t_c) V_0 \\ \text{Pattern 2} & V(t) = (1 - t/t_c)^2 V_0 \\ \text{Pattern 3} & V(t) = \left[1 - (t/t_c)^2\right] V_0 \end{array}\right\} \quad \text{for } t \le t_c; \tag{4.28}$$

The corresponding pressure distributions at the wave front are shown in Figure 4.11b. Comparisons are provided with the theoretical case of instantaneous valve closure ($t_c = 0$). For gradual valve closure $t_c > 0$, the pressure at the valve increases from the steady flow pressure $\rho_f g H_{res}$ to the water hammer pressure $\rho_f g H_{res} + \rho_f a_w V_0$ within closure time t_c. The wave front propagates upstream, such that the distance between points $\mathrm{AB} = a_w t_c$ (Figure 4.11a), and the pressure exhibits a gradual increase from point A to B. The pressure distribution between points A and B is $\rho_f g H_{res} + \rho_f a_w V(\Delta x / a_w)$, where $0 \le \Delta x \le a_w t_c$ is the distance from the wave front, and $V(\Delta x / a_w)$ is the value obtained by substituting $t = \Delta x / a_w$ into Eq. (4.28). For Cases 1 and 2, by taking the Fourier transform for the circumferential stress response right after the pressure passage i.e., $0.0147\,\mathrm{sec} \le t \le 0.03\,\mathrm{sec}$ (Figure 4.10c), it was shown that the radial frequency activated by the step pressure is $f_r = 2490\,\mathrm{Hz}$. It is convenient to normalize the valve closure time t_c by multiplying it with the exciting frequency f_r to yield a dimensionless closure time t_c^* , i.e., $t_c^* = t_c f_r$.($t_c^* \le 10$). Figure 4.11c shows that the pressure time-histories at the valve for various valve closure patterns ($t_c^* = 10$) are almost identical to those of the instantaneous valve closure.

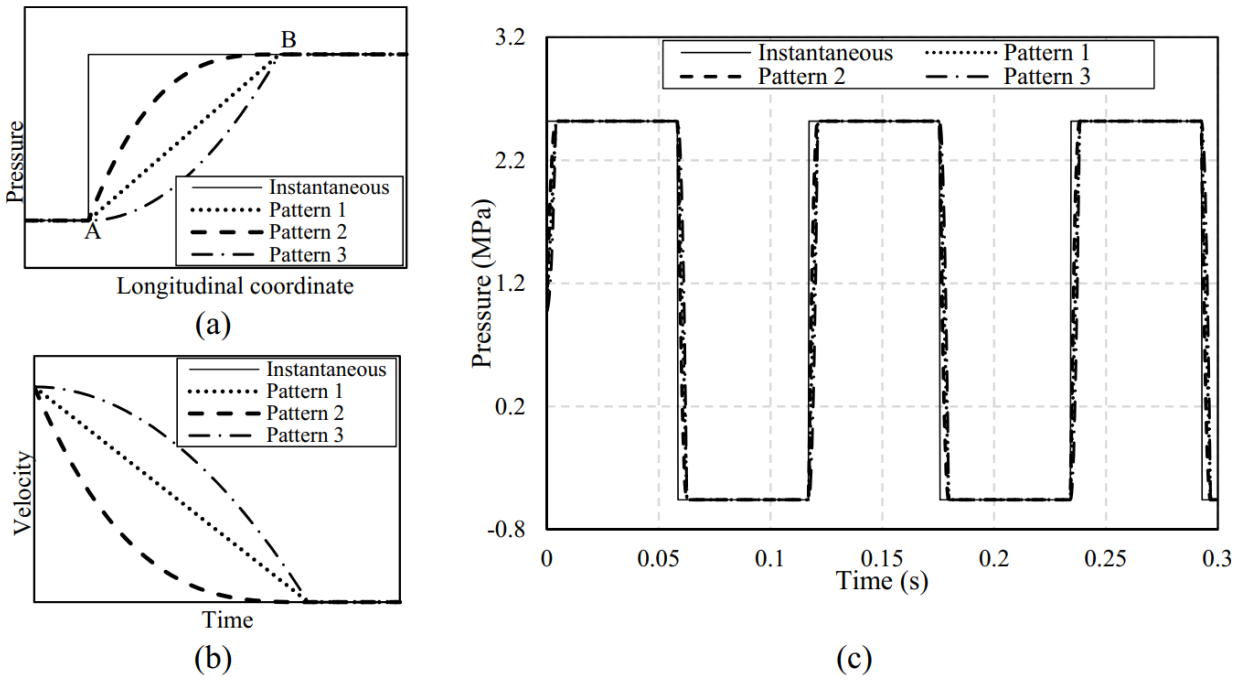

Figure 4.11 (a) Schematic of valve closure patterns and (b) schematic of pressure distributions at wave fronts, (c) Pressure time-histories at the valve for various valve closure patterns (t_c^*=10) in the reference cases.

4.9.5.2. Pipe dynamic response for various valve closure patterns and time

Comparisons of the radial displacement at pipe mid-span after the passage of pressure wave front (AB in Figure 4.11a) are provided in Figure 4.12a for the cases of instantaneous ($t_c^* = 0$) and linearly varying valve closures with $t_c^* = 0.5,\ 1,$ and 1.5. Overlaid on the figure is a preliminary hoop stress value as estimated from the approximate static equation $\sigma_\phi = P(R - 0.5h)/h$, in which the pressure P corresponds to the case of instantaneous pipe closure. As shown in Figure 4.12a, the time corresponding to the peak radial displacement shifts forward as the valve closure time increases. For the linearly varying valve closure with $t_c^* = 1$, the displacement oscillations after the pressure wave passage is identical to that predicted by the preliminary analysis.

A dynamic amplification factor λ_r is defined as the ratio of the maximum circumferential stress increasing after the passage of pressure wave and $\Delta\sigma_\phi = \rho_f a_w V_0 (R - 0.5h)/h$, and is plotted in Figure 4.12b for the three valve closure patterns for various closure times within the interval $0 \le t_c^* \le 10$. For linear valve closure (Pattern 1), as the closure time increases, the dynamic amplification factor λ_r rapidly decreases from 1.97 to 1.00 within $0 \le t_c^* \le 1$. When the

dimensionless closure time has an integer value ($t_c^* = 1, 2, \ldots$), the dynamic amplification factor λ_r corresponds to a local minimum value $\lambda_r = 1.0$. This behavior is analogous to that of a single DOF spring-mass system subjected to a step force with finite rise time (e.g., Chopra 2012). The dynamic amplification factor λ_r is found more sensitive to valve closure time than to the pattern of closure. At the end of the closure time interval investigated in Figure 4.12b, all dynamic amplification factors approach unity, suggesting that inertial effects become negligible when $t_c^* \geq 8$. This finding is consistent with Walker's (1977) observation in that the water hammer wavelength after valve closure exhibits a gradual ramp response, implying that the radial inertial effects are negligible.

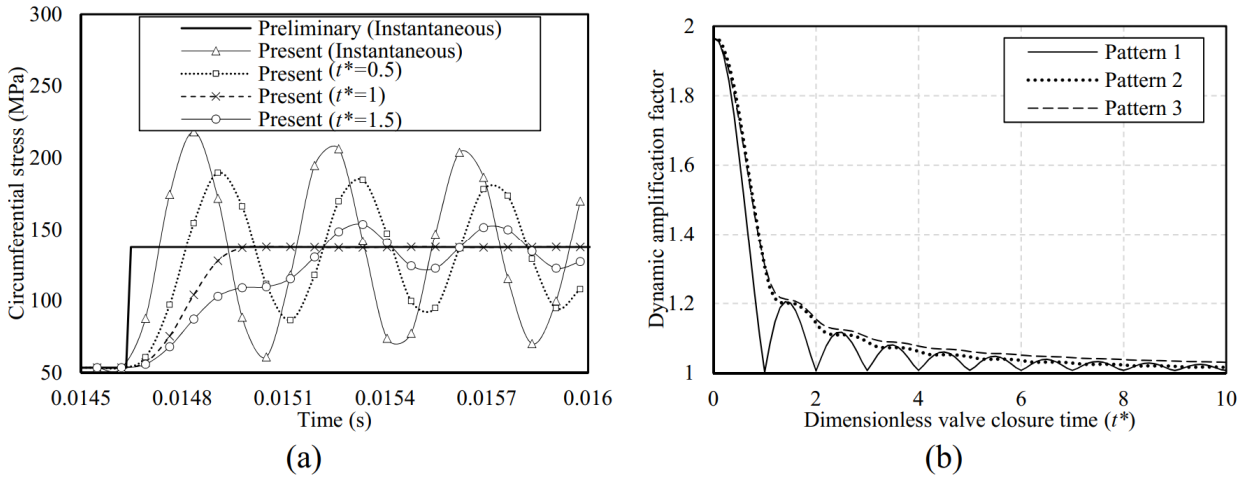

Figure 4.12 Circumferential stress oscillation at pipe mid-span and dynamic amplification factor λ_r for different valve closure patterns. (a) Circumferential stress oscillations for dimensionless valve closure time t_c^*=0, 0.5, 1 and 1.5 in first pattern valve closure and preliminary analysis for instantaneous valve closure (t_c^*=0); (b) Dynamic amplification factor λ_r vs dimensionless valve closure time t_c^* for three valve closure patterns.

4.10. Conclusions

The present study developed a finite element model formulation based on an axisymmetric thin-shell theory. The model was seamlessly integrated with a water hammer model into a single MATLAB program, thus allowing the investigation of the dynamic effects of water hammer on the structural response of the pipe. The validity of the implementation has been verified through comparison with SAX1 model in ABAQUS for static, free vibration, and transient analyses. The main findings of the study are:

(1) The dynamic analysis shows that the circumferential stress distribution in the pipe is predominantly dependent on the distribution of the transient pressure. A secondary effect is

induced due to the Poisson ratio effect, whereby a longitudinal stress wave is induced in the pipe wall, and propagates at sound speed in the pipe wall. Both the longitudinal and circumferential stresses oscillate around the pressure wave front, where they give rise the peak von Mises stresses.

(2) The oscillations in the circumferential and von Mises stresses after the passage of step-pressure were found to be highly dependent on damping. Thus, damping needs to be introduced into models to replicate physically observed phenomena and avoid beat phenomena in water hammer problems.

(3) The present model shows that the circumferential oscillations after the passage of the wave front are sensitive to valve closure time, but insensitive to valve closure patterns. The results indicate that the radial stress/displacement oscillations approach those based on quasi-steady response when the valve closure time exceeds eight times the circumferential mode period obtained for the case of instantaneous valve closure.

4.11. List of symbols

A B =amplitudes of the modes for the longitudinal and radial displacements

a_0 a_1 =constants in the Rayleigh damping model

a_w a_s =wave speed of water hammer pressure and longitudinal stress ($\mathrm{m/s}$)

Dirac =Dirac dealt function

D^* =dissipated energy ($\mathrm{kg \cdot m^2/s^2}$)

f_r =frequency of circumferential stress oscillation (Hz)

i =longitudinal half-wave number

E =Young's modulus (Pa)

H_{res} =Reservoir pressure head (m)

h =pipe thickness (m)

K_f =Bulk modulus for the water (Pa)

L =length of pipe (m)

P =hydraulic pressure (Pa)

p_x =body force component in the longitudinal direction ($\mathrm{N/m^3}$)

p_r =body force component in the radial direction ($\mathrm{N/m^3}$)

R =radius of mid-surface (m)

r =radial coordinate (m)

T^* =kinetic energy ($\mathrm{kg \cdot m^2/s^2}$)

t =time (s)

t^* =dimensionless time

u =longitudinal displacement (mm)

V^* =internal strain energy ($\mathrm{kg \cdot m^2/s^2}$)

V =fluid velocity ($\mathrm{m/s}$)

W^* =external work done by the external loads ($\mathrm{kg \cdot m^2/s^2}$)

w =radial displacement (mm)

x =longitudinal coordinate (m)

α β =constants in the Newmark time integration scheme

δ =variational operator

ε =strain

η_{ij} =component of the strain tensor adjacent to the mid-surface

λ =longitudinal wavelength (m)

λ_r =dynamic amplification factor

ν =Poisson's ratio

ξ =damping ratio

Π =mechanical energy of the system ($\mathrm{kg \cdot m^2/s^2}$)

ρ_f , ρ_s =densities of fluid and solid material ($\mathrm{kg/m^3}$)

σ =stress (Pa)

ϕ =an angle along the circumferential direction (rad)

χ =frequency parameter

Ω =shell volume ($\mathrm{m^3}$)

ω =natural frequency (Hz)

Δt =time increment (s)

Matrices and vectors

C	Damping matrix	**L**	Linear shape function
H	Cubic shape function	**m**	Component of mass matrix
k	Component of stiffness matrix	**M**	Mass matrix
K	Stiffness matrix	**P**	Loading vector

Subscripts and superscripts

c denotes parameters corresponding to the mode with longitudinal half-wave number c .

N denotes nodal values.

m and n denote two mode numbers.

r and x denote derivatives with respect to the longitudinal and radial coordinates.

t and $t + \Delta t$ denote two time-steps.

T refers to the transfer matrix or vector.

$\dot{}$ denotes differentiation with respect to time.

4.12. References

Adamkowski, A., Lewandowski, M., 2006. Experimental Examination of Unsteady Friction Models for Transient Pipe Flow Simulation. *J. Fluids Eng.* 128, 1351.

Azoury, P. H., Baasiri, M., and Najm, H., 1986. Effect of valve-closure schedule on water hammer. *J. Hydraul. Eng.*, 112(10), 890–903.

Babu, C.R., Prathap, G., 1986. A field-consistent two-noded curved axisymmetric shell element. *Int. J. Numer. Methods Eng*. 23, 1245–1261.

Bathe, K.J., 2014. Finite element procedures (2nd), 2nd ed. *Pearson Education,* Inc., Watertown, MA.

Bathe, K.J., Almeida, C. A., 1982. A simple and effective pipe elbow element — interaction effects. *J. Appl. Mech.* 49, 165–171.

Bathe, K J, Almeida, C.A., 1982. A simple and effective pipe elbow element-pressure stiffening effects. *J. Appl. Mech.* 49, 914–916.

Bathe, K.J., Almeida, C.A., 1980. A simple and effective pipe elbow element—linear analysis. *J. Appl. Mech.* 47, 93–100.

Beltman, W. M., Burcsu, E. N., Shepherd, J. E., and Zuhal, L. 1999. The structural response of cylindrical shells to internal shock loading. *J. Press. Vessel Technol*., 121(3), 315–322.

Beltman, W. M., and Shepherd, J. E. 2002. Linear elastic response of tubes to internal detonation loading. *J. Sound Vib*., 252(4), 617–655.

Breuer, M., De Nayer, G., Münsch, M., Gallinger, T., and Wüchner, R. 2012. Fluid–structure interaction using a partitioned semi-implicit predictor–corrector coupling scheme for the application of large-eddy simulation. *J. Fluids Struct.,* 29, 107–130.

Brunone, B., Ferrante, M., Cacciamani, M., 2004. Decay of Pressure and Energy Dissipation in Laminar Transient Flow. *J. Fluids Eng.* 126, 928–934.

Budny, D. D., Wiggert, D. C., and Hatfield, F. J. 1991. The influence of structural damping on internal pressure during a transient pipe flow. *J. Fluids Eng.*, 113(3), 424–429.

Chohan, R.K., 1989. Waves in elastic fluid-filled tubes. *Int. J. Press. Vessel. Pip.* 36, 185–197.

Chopra, A. K., 2012. Dynamics of structures (4th), 4th ed. *Pearson Education*, Inc., Boston, MA.

Clough, R.W., Penzien, J., 2003. Dynamics of structures, 3rd ed. *Computers &Structures*, Inc., Berkeley, CA, USA.

Cui, X.Y., Wang, G., Li, G.Y., 2016. A nodal integration axisymmetric thin shell model using linear interpolation. *Appl. Math. Model.* 40, 2720–2742.

Degroote, J., Haelterman, R., Annerel, S., Bruggeman, P., and Vierendeels, J. 2010. Performance of partitioned procedures in fluid–structure interaction. *Comput. Struct*., 88(7), 446–457.

Fan, S.C., Luah, M.H., 1990. New spline finite element for analysis of shells of revolution. *J. Eng. Mech.* 116, 709–726.

Fan, S.C., Luah, M.H., 1989. Spline finite element for axisymmetric free vibrations of shells of revolution. *J. Sound Vib.* 132, 61–72.

Ferràs, D., Manso, P. A., Schleiss, A. J., and Covas, D. I. C. 2016. Fluid-structure interaction in straight pipelines: Friction coupling mechanisms. *Comput. Struct.,* 175, 74–90.

Ferras, D., Manso, P.A., Schleiss, A.J., Covas, D.I.C., 2017. Fluid-structure interaction in straight pipelines with different anchoring conditions. *J. Sound Vib.* 394, 348–365.

Ghidaoui, M.S., Zhao, M., McInnis, D.A., Axworthy, D.H., 2005. A Review of Water Hammer Theory and Practice. *Appl. Mech. Rev.* 58, 49.

Giannini, M., Miles, G.A., 1970. A curved element approximation in the analysis of axi-symmetric thin shells. *Int. J. Numer. Methods Eng.* 2, 459–476.

Grafton, P.E., Strome, D.R., 1963. Analysis of axisymmetrical shells by the direct stiffness method. *AIAA J.* 1, 2342–2347.

Gupta, A., Kiusalaas, J., Saraph, M., 1991. Cubic B-spline for finite element analysis of axisymmetric shells. *Comput. Struct.* 38, 463–468.

Habchi, C., Russeil, S., Bougeard, D., Harion, J.-L., Lemenand, T., Ghanem, A., Valle, D. Della, and Peerhossaini, H. 2013. Partitioned solver for strongly coupled fluid–structure interaction. *Comput. Fluids*, 71, 306–319.

Haelterman, R., Bogaers, A. E. J., Scheufele, K., Uekermann, B., and Mehl, M. 2016. Improving the performance of the partitioned QN-ILS procedure for fluid–structure interaction problems: filtering. *Comput. Struct.,* 171, 9–17.

Heinsbroek, A.G.T.J and Tijsseling, A.S., 1994. The influence of support rigidity on water hammer pressures and pipe stresses, *Proc of 2nd Int Conf on Water Pipeline Systems*, BHR Group, Edinburgh, UK, 17–30.

Jones, R.E., Strome, D.R., 1966. Direct Stiffness Method Analysis of Shells of Revolution Utilizing Curved Elements. *AIAA J.* 4, 1519–1525.

Kim, Y.Y., Kim, J.G., 1996. A simple and efficient mixed finite element for axisymmetric shell analysis. *Int. J. Numer. Methods Eng.* 39, 1903–1914.

Lavooij, C.S.W., Tijsseling, A.S., 1991. Fluid-structure interaction in liquid-filled piping systems. *J. Fluids Struct.* 5, 573–595.

Leishear, R.A., 2007. Dynamic pipe stresses during water hammer: a finite element approach. *J. Press. Vessel Technol.* 129, 226–233.

Leissa, A.W., 1993. Vibration of Shells. NASA Report SP-288, 1973. Reprinted in book form by the Acoustical Society of America in 1993.

Li, L., Henshaw, W. D., Banks, J. W., Schwendeman, D. W., and Main, A. 2016. A stable partitioned FSI algorithm for incompressible flow and deforming beams. *J. Comput. Phys*., 312, 272–306.

Li, S., Karney, B.W., Liu, G., 2015. FSI research in pipeline systems - A review of the literature. *J. Fluids Struct.* 57, 277–297.

Loula, A.F.D., Miranda, I., Hughes, T.J.R., Franca, L.P., 1989. On mixed finite element methods for axisymmetric shell analysis. *Comput. Methods Appl. Mech. Eng.* 72, 201–231.

Mackenzie, D., Boyle, J.T., 1992. A Simple Pipe Bend Element for Piping Flexibility Analysis. *Int. J. Press. Vessel. Pip.* 51, 85–106.

Mclnnis, D. A., Karney, B. W., and Axworthy, D. H. 1997. Efficient valve representation in fixed-grid characteristics method. *J. Hydraul. Eng.,* 123(8), 709–718.

Mehl, M., Uekermann, B., Bijl, H., Blom, D., Gatzhammer, B., and van Zuijlen, A. 2016. Parallel coupling numerics for partitioned fluid–structure interaction simulations. *Comput. Math. with Appl.*, 71(4), 869–891.

Melo, F.J.M.Q., Castro, P.M.S.T. De, 1997. The linear elastic stress analysis of curved pipes under generalized loads using a reduced integration finite ring element. *J. Strain Anal. Eng. Des*. 32, 47–59.

Melo, F.J.M.Q.D., Castro, P.M.S.T.D., 1992. A reduced integration Mindlin beam element for linear elastic stress analysis of curved pipes under generalized in-plane loading. *Comput. Struct*. 43, 787–794.

Militello, C., Huespe, A.E., 1988. A displacement-based pipe elbow element. *Comput. Struct*. 29, 339–343.

Melo, F.J.M.Q.D., Noronha,J.P., Fernandes,E.A., 1996. The propagation of axisymmetric transverse waves along a thin-walled cylindrical pipe. *Int. J. Pres. Ves. Piping*. 65 (2),109-116.

Mohr, G.A., 1982. Application of penalty functions to a curved isoparametric axisymmetric thick shell element. *Comput. Struct.* 15, 685–690.

Ohstubo, H., Watanabe, O., 1977. Flexibility and stress factors of pipe bends- an analysis by the finite ring method. *J. Press. Vessel Technol*. 99, 281–290.

Percy, J.H., Pian, T.H.H., Klein, S., Navaratna, D.R., 1965. Application of matrix displacement method to linear elastic analysis of shells of revolution. *AIAA J*. 3, 2138–2145.

Popov, E.P., Sharifi, P., 1971. A refined curved element for thin shells of revolution. *Int. J. Numer. Methods Eng.* 3, 495–508.

Raveendranath, P., Singh, G., Pradhan, B., 1999. A two-node curved axisymmetric shell element based on coupled displacement field. *Int. J. Numer. Methods Eng.* 45, 921–935.

Salahifar, R., 2011. Analysis of Pipeline Systems under Harmonic Forces (PhD thesis). University of Ottawa.

Salahifar, R., Mohareb, M., 2012. Finite element for cylindrical thin shells under harmonic forces. *Finite Elem. Anal. Des.* 52, 83–92.

Salahifar, R., Mohareb, M., 2010. Analysis of circular cylindrical shells under harmonic forces. *Thin-Walled Struct.* 48, 528–539.

Skalak, R., 1953. An extension of the theory of water hammer (PhD thesis). Columbia University.

Stricklin, J.A., Navaratna, D.R., Pian, T.H.H., 1966. Improvements on the analysis of shells of revolution by the matrix displacement method. *AIAA J.* 4, 2069–2072.

Tessler, A., 1982. An efficient, conforming axisymmetric shell element including transverse shear and rotary inertia. *Comput. Struct*. 15, 567–574.

Tessler, A., Spiridigliozzi, L., 1988. Resolving Membrane and Shear Locking Phenomena in Curved Shear-Deformable axisymmetric shell elements. *Int. J. Numer. Methods Eng*. 26, 1071–1086.

Tijsseling, A., 1997. Poisson-coupling beat in extended water hammer theory, In Proceedings of the 4th International Symposium on Fluid–Structure Interactions, Aeroelasticity, Flow-Induced Vibration and Noise, Dallas, TX, USA, 53(2): 529–532.

Tijsseling, A.S., Lambert, M.F., Simpson, A.R., Stephens, M.L., Vítkovský, J.P., Bergant, A., 2008. Skalak's extended theory of water hammer. *J. Sound Vib*. 310, 718–728.

Tijsseling, A. & Vardy, A., 1996. Axial modelling and testing of a pipe rack. In:BHR group conference series publication, vol. 19. Mechanical Engineering Publications Limited.

To, C.W.S., Wang, B., 1991. An axisymmetric thin shell finite element for vibration analysis. *Comput. Struct.* 40, 555–568.

Toth, B., 2014. Axisymmetric shell model using a three-field dual-mixed variational principle. *J. Comput. Appl. Mech*. 9, 101–119.

Townend, M.S., Kerr, A.H., 1982. Approximate dynamics using Hamilton's principle, including applications to non-conservative and constrained systems. *Mech. Mach. theory* 17, 213–220.

Walker, J. S., and Phillips, J. W. 1977. Pulse Propagation in Fluid-Filled Tubes. *J. Appl. Mech*., 44(1), 31–35.

Webster, J.J., 1967. Free vibrations of shells of revolution using ring finite elements. *Int. J. Mech. Sci.* 9, 559–570.

Weicker, K., Salahifar, R., Mohareb, M., 2010. Shell analysis of thin-walled pipes. Part II – Finite element formulation. *Int. J. Press. Vessel. Pip.* 87, 414–423.

Wiggert, D.C., Hatfield, F.J., Lesmez, M.W., 1986. Coupled transient flow and structure motion in liquid-filled piping systems, *in: Proceedings of the 5th International Conference on Pressure Surges*. Hannover, Germany, pp. 1–9.

Wiggert, D.C., Tijsseling, A.S., 2001. Fluid transients and fluid-structure interaction in flexible liquid-filled piping. *Appl. Mech. Rev*. 54, 455–481.

Williams, D.J., 1977. Waterhammer in non-rigid pipes: precursor waves and mechanical damping. *J. Mech. Eng. Sci.* 19, 237–242.

Zienkiewicz, O.C., Bauer, J., Morgan, K., Onate, E., 1977. A Simple and Efficient Finite Element for axisymmetric shells. *Int. J. Numer. Methods Eng.* 11, 1529–1543.

4.13. Appendix A: components of the mass and stiffness matrices

$$\mathbf{m}_{11} = 2\pi R\rho_s h\begin{bmatrix} \frac{L}{3} & \frac{L}{6} \\ \frac{L}{6} & \frac{L}{3} \end{bmatrix}; \mathbf{m}_{12} = -\frac{\pi\rho_s h^3}{6}\begin{bmatrix} -\frac{1}{2} & \frac{L}{12} & \frac{1}{2} & -\frac{L}{12} \\ -\frac{1}{2} & -\frac{L}{12} & \frac{1}{2} & \frac{L}{12} \end{bmatrix}$$

$$\mathbf{m}_{22} = \frac{\pi Rh\rho_s}{5}\begin{bmatrix} \frac{h^2}{L}+\frac{26L}{7} & \frac{11L^2}{21}+\frac{h^2}{12} & \frac{9L}{7}-\frac{h^2}{L} & \frac{h^2}{12}-\frac{13L^2}{42} \\ \frac{11L^2}{21}+\frac{h^2}{12} & \frac{2L^3}{21}+\frac{Lh^2}{9} & \frac{13L^2}{42}-\frac{h^2}{12} & -\frac{Lh^2}{36}-\frac{L^3}{14} \\ \frac{9L}{7}-\frac{h^2}{L} & \frac{13L^2}{42}-\frac{h^2}{12} & \frac{h^2}{L}+\frac{26L}{7} & -\frac{h^2}{12}-\frac{11L^2}{21} \\ \frac{h^2}{12}-\frac{13L^2}{42} & -\frac{Lh^2}{36}-\frac{L^3}{14} & -\frac{h^2}{12}-\frac{11L^2}{21} & \frac{2L^3}{21}+\frac{Lh^2}{9} \end{bmatrix}$$

$$\mathbf{k}_{11} = \frac{2\pi ERh}{1-\nu^2}\begin{bmatrix} \frac{1}{L} & -\frac{1}{L} \\ -\frac{1}{L} & \frac{1}{L} \end{bmatrix}; \mathbf{k}_{12} = \frac{\pi Eh\nu}{\nu^2-1}\begin{bmatrix} -1 & -\frac{h^2}{6L\nu}-\frac{L}{6} & -1 & \frac{h^2}{6L\nu}+\frac{L}{6} \\ 1 & \frac{h^2}{6L\nu}+\frac{L}{6} & 1 & -\frac{h^2}{6L\nu}-\frac{L}{6} \end{bmatrix}$$

$$\mathbf{k}_{22} = \frac{\pi E}{1-\nu^2}\begin{bmatrix} \frac{26LA^*}{35}+\frac{2Rh^3}{L^3} & \frac{11L^2A^*}{105}+\frac{Rh^3}{L^2} & \frac{9LA^*}{35}-\frac{2Rh^3}{L^3} & \frac{Rh^3}{L^2}-\frac{13L^2A^*}{210} \\ \frac{11L^2A^*}{105}+\frac{Rh^3}{L^2} & \frac{2L^3A^*}{105}+\frac{2Rh^3}{3L} & \frac{13L^2A^*}{210}-\frac{Rh^3}{L^2} & \frac{Rh^3}{3L}-\frac{L^3A^*}{70} \\ \frac{9LA^*}{35}-\frac{2Rh^3}{L^3} & \frac{13L^2A^*}{210}-\frac{Rh^3}{L^2} & \frac{26LA^*}{35}+\frac{2Rh^3}{L^3} & -\frac{11L^2A^*}{105}-\frac{Rh^3}{L^2} \\ \frac{Rh^3}{L^2}-\frac{13L^2A^*}{210} & \frac{Rh^3}{3L}-\frac{L^3A^*}{70} & -\frac{11L^2A^*}{105}-\frac{Rh^3}{L^2} & \frac{2L^3A^*}{105}+\frac{2Rh^3}{3L} \end{bmatrix}$$

where $A^* = \frac{h}{R}+\frac{h^3}{12R^3}$.

Chapter 5 PARTITIONED WATER HAMMER MODELLING USING THE BLOCK GAUSS-SEIDEL ALGORITHM[3]

5.1. Abstract

The classical and extended monolithic water hammer models are based on the simplified ring hypothesis to characterize the structural radial response of the pipe under pressure. Recent work has shown that this approach predicts an unrealistic discontinuity in the pipe wall in the neighborhood of the step pressure wave front. To remedy this limitation, the present study adopts a partitioned approach which couples a continuous shell-based finite element model with a water hammer fluid model based on the Method of Characteristics, within the context of the partitioned block Gauss-Seidel iterative algorithm. In order to demonstrate the validity of the block Gauss-Seidel implementation, the classical and extended water hammer models, normally solved using a monolithic approach, are solved under the present partitioned model and are shown to predict pressure histories identical to those based on the monolithic solution. Comparisons are then conducted for the pressure histories as predicted by the classical, extended, and shell-based approaches. The study shows that the accuracy is optimized for integer values of the Courant number. By adopting either an optimal constant relaxation factor or the Aitken relaxation factor, the number of iterations needed for convergence was significantly reduced. The accuracy and computational efficiency are shown to highly depend on the number of subdivisions in the fluid model. In contrast, the number of subdivisions in the structural model, while influencing the computational efficiency, is shown not to influence the accuracy of the predictions. When applying the partitioned approach to the classical and shell-based models, the predicted pressure histories are found to be independent of the specified tolerance. In contrast, when applied to the extended model, the tolerance chosen has implications on the stability and accuracy of the solution.

---

[3] Cao, H., Mohareb, M., Nistor, I., "Partitioned water hammer modelling using the block Guass-Seidel algorithm", submitted to peer-revierw journal.

Huade Cao: Conceptualization, Methodology, Software, Validation, Writing - original draft. **Magdi Mohareb:** Conceptualization, Writing - review & editing, Resources, Supervision. **Ioan Nistor:** Conceptualization, Writing - review & editing, Resources, Supervision

5.2. Introduction

Water hammer is pressure wave propagation phenomenon in a fluid-filled-pipe caused by the change in hydraulic conditions, e.g., opening or closure of a valve, start or stopping of a pump, etc. Under the effect of the traveling pressure wave, the pipe wall deforms in the radial direction. The pipe deformation in turn influences the wave speed and the amplitude of the traveling pressure wave. The classical and the extended water hammer models account to various degrees for the influence of the pipe structural response on the water hammer pressure. The classical water hammer theory adopts a correction of the water hammer wave speed which accounts for pipe thickness, Young's modulus, Poisson ratio, and the longitudinal boundary conditions (e.g., Tijsseling and Anderson 2007). However, the theory neglects the inertial effects and the bending stiffness in the pipe wall.

Efforts to improve the representation of the pressure wave damping patterns culminated in developing several unsteady friction models. These include weighting-function based models (e.g., Zielke 1968, Trikha 1975a, Suzuki et al. 1991, and Vardy and Brown 2003, 2004) and instantaneous-acceleration based models (e.g., Brunone et al. 1995, Wylie 1997, Vítkovský et al. 2000, 2006b, Bergant et al. 2001, Adamkowski and Lewandowski 2006b, Tiselj and Gale 2008, Reddy et al. 2012, and Duan et al. 2017). Szymkiewicz and Mitosek (2007) introduced a diffusion term to smooth the pressure wave front. By considering a waterjet to occur at the pipe entrance, Cao et al. (2020a) proposed a boundary expression at the pipe inlet to dampen and smoothen the pressure wave front.

The Method of Characteristics (MOC) is most commonly used in solving the classical water hammer model (e.g., Lai 1988, Sibetheros et al. 1991, Ghidaoui and Karney1994, 1995, and 1997). Other techniques have also been adopted, such as the finite difference method (e.g., Chaudhry and Hussaini 1985, Greyvenstein 2002, Wahba 2006), the finite volume method (e.g., Guinot 2000, Zhao and Ghidaoui 2004, Sohani and Ghidaoui 2019), the finite element method (FEM) (Szymkiewicz 1995, Szymkiewicz and Mitosek 2005), and the wavelet-Galerkin method (Sattar et al. 2009).

An extended water hammer model was proposed based on an axisymmetric thin shell theory (Skalak 1953). The model neglects the flexural rigidity and rotatory inertial terms of the pipe wall. Two additional equations were introduced to the governing equations of the classical water

hammer theory, in order to account for the longitudinal inertial effects in pipe wall. Walker and Phillips (1977) improved the extended water hammer model by incorporating the longitudinal and radial inertial effects. Wiggert et al. (1986) proposed a 14-equation water hammer model that accounts for the longitudinal stress and velocity, in-plane and out-plane shear and bending and torsion in the pipe wall. Budny et al. (1991) investigated the effect of structural damping on the water hammer wave. In a review of Fluid-Structure Interaction (FSI) water hammer models, Wiggert and Tijsseling (2001) indicated that the lateral response of pipe could be captured either using the Bernoulli-Euler or Timoshenko beam theories. Tijsseling (2007) investigated the effect of radial strain in the pipe wall on water hammer for thick-walled pipes. Ferràs et al. (2016) investigated the effects of dry friction on the water hammer pressure wave. The most commonly used method to solve the extended water hammer models is, again, the MOC (e.g., Wiggert et al. 1986, Tijsseling and Lavooij 1990, and Lavooij and Tijsseling 1991). Lavooij and Tijsseling (1991) adopted an iterative scheme to solve the extended water hammer model which solves the fluid equations using the MOC and the structural equations using the FEM. Gale and Tiselj (2008) adopted Godunov's method to solve the extended water hammer model. The extended water hammer models have been employed to investigate the water hammer in L-shaped pipes (Tijsseling et al. 1996) and T-shape pipes (Vardy et al. 1996). The influence of support rigidity was investigated in Heinsbroek and Tijsseling (1994), while the effects of longitudinal restraint conditions and valve mass were investigated in Ferras et al. (2017b).

The previous extended water hammer models are based on a monolithic approach whereby the governing equations for the fluid and pipe domains are solved together. This approach enhances the stability of the solution, but is based on simplified structural representations of the pipe response. Specifically, a common assumption to the previous monolithic models, is that the hoop stresses are proportional to the internal pressure. As a result, such models would predict an unrealistic discontinuity at the pressure wave front (Chapter 2, Appendix A). In order to remedy this inconsistency, a continuous shell model that guarantees displacement continuity of the pipe wall was introduced in Cao et al. (2020b). The model was adopted to model one-way interaction between the structural and fluid models. The continuous shell model lends itself to two-way interaction through the partitioned approach, in which the fluid and structural problems are solved separately and coupled through interfaces for the Fluid-Structure Interaction (FSI). Compared to the monolithic approach, the main advantage of the partitioned approach is the fact that it lends

itself to modularity. While the partitioned approach is widely applied in FSI problems, it has received little attention in the context of water hammer applications. An exception is the recent work of Daude et al. (2018) who adopted the partitioned approach in the context of water hammer with column separation. The model is based on the classical ring assumption for the pipe and a staggered iteration technique in which a single iteration is performed for each time step. In contrast, the present study adopts the partitioned approach by using a shell representation of the pipe along with strong coupling involving on multiple iterations per time step. A review of key aspects related to partitioned FSI models in other applications is provided in the following paragraphs:

In partitioned FSI models, domains are decomposed and coupled by exchanging information at the interface between the fluid and structure domains (e.g., Vierendeels et al. 2007 and Degroote 2013). The FSI model can be solved by adopting either a loose (explicit) coupling scheme, in which each model is solved once per time step (e.g., Burman and Fernández 2009), or a strong (implicit) coupling scheme, in which multiple iterations are performed per time step until convergence is obtained (e.g., von Scheven and Ramm 2011 and Habchi et al. 2013). While strong coupling is computationally more expensive than loose coupling, it leads to more stable solutions (e.g., Causin et al. 2005). Partitioned fluid-structure interaction models can be treated either as a fixed-point problem, which can be solved using the block Gauss-Seidel scheme (e.g., Joosten et al. 2009, Degroote et al. 2010a, and Wood et al. 2010), or as a root-finding problem which can be solved using Newton type schemes (e.g., Gerbeau and Vidrascu 2003, Degroote et al. 2009, Haelterman et al. 2016). Compared to the block Gauss-Seidel scheme, Newton type schemes are more robust with a faster convergence rate in problems in which the added-mass effect is significant. Newton type schemes require the determination of the Jacobian matrix, which can be determined exactly (e.g., Fernández and Moubachir 2003, 2005) or approximately using finite difference (e.g., Matthies and Steindorf 2002, 2003). Gerbeau and Vidrascu (2003) approximated the Jacobian matrix by a simpler operator to avoid its explicit computation. Newton type schemes can be also accelerated by combining them with the Broyden-Fletcher-Goldforb-Shano (BEGS) scheme (Murea 2005), or with the Generalized Minimal RESidual (GMRES) scheme (e.g, Michler et al. 2005 and 2006). Alternatively, the Jacobian can be approximated from reduced order models (Vierendeels et al. 2007).

The iterative procedure can be accelerated by adopting a relaxation technique such as the Aitken relaxation technique (e.g., Küttler and Wall 2008, 2009). Other techniques to improve the convergence rate include either adding artificial compressibility in the fluid around the FSI interface (Degroote et al. 2010b), or introducing fiction-mass and damping (Baek and Karniadakis 2012), or adopting separate parallel solvers for both the fluid and the structure (Mehl et al. 2016). Compared to the above technique, the block Gauss-Seidel scheme with relaxation is the simplest and hence has been adopted in present work. By taking advantage of the modularity in partitioned models, well developed codes have been used as black-box solvers in FSI problems (e.g., Sternel et al. 2008, Kassiotis et al. 2010, Breuer et al. 2012, Habchi et al. 2013). However, adopting general solvers for FSI in water hammer problem is time consuming (Bernard 2013). Hansson and Sandberg (2001) investigated the acoustic wave propagation in pipe filled with static fluid, in which only the pressure filed was accounted for. In blood flow problems (e.g., Formaggia et al. 2001, Colciago et al. 2014, Bukač et al. 2015), the boundaries tend to absorb the waves and hence suppress wave reflection. In such applications, the fluid is assumed incompressible since the sound speed in the fluid is much higher than that in the surrounding arteries. In contrast, in water hammer applications, the pressure wave is reflected at the boundaries and the sound speed in fluid is several times less than that in the structure. In such cases, it becomes important to account for fluid compressibility. The present study focuses on tackling such problems by developing a model with a partitioned scheme that is strongly coupled.

The problem statement is presented in Section 5.3. The assumptions adopted in the classical and extended water hammer models are then reviewed in Section 5.4. A partitioned water hammer scheme is proposed under Section 5.5 and verified in Section 5.6. Section 5.7 investigates the parameters affecting the performance of the water hammer models.

5.3. Description of the problem

Consider a Reservoir-Pipe-Valve (RPV) system with an upstream reservoir (hydraulic head H_{res}) and a valve located downstream at the end of a steel pipe with a length L (Figure 5.1). The pipe has a mid-surface radius R and wall thickness h. Pipe Young's modulus is E, Poisson's ratio is ν and density is ρ_s. The bulk modulus of water is K_f and its density is ρ_f. Water viscosity is ignored. The initial flow velocity is V_0. After the valve is instantaneously closed, a water hammer pressure wave occurs which travels from the valve in the upstream direction and

oscillates between the reservoir and valve at a wave speed close to that of the acoustic speed in water. During the pressure wave oscillation, the pipe wall is deformed by the transient pressure wave. Meanwhile, the deformation of the fluid surface in contact with the pipe wall changes the distribution of pressure and velocity fields in water. It is required to develop a fluid model that simulates the transient inner flow under water hammer and a structural model that captures the pipe dynamic response due to water hammer, and then couple both models to capture the Fluid-Structure Interaction effects between the pipe and the fluid.

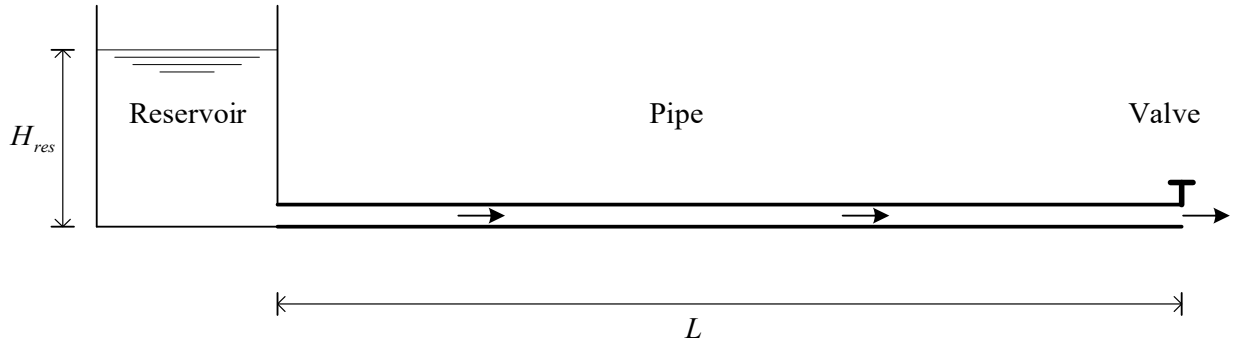

Figure 5.1 Schematic of the Reservoir-Pipe-Valve system.

5.4. Overview of the monolithic water hammer models

5.4.1. Mass and momentum conservation equations for fluid domain

The one-dimensional mass and momentum conservation equations for water hammer in pipes were proposed by Skalak (1953), Walker and Philips (1977) and Budny et al. (1990) as

$$\frac{\partial V}{\partial x}+\frac{1}{K_f}\frac{\partial P}{\partial t}+\frac{2}{R-0.5h}\frac{\partial w}{\partial t}=0 \tag{5.1}$$

$$\frac{\partial V}{\partial t}+\frac{1}{\rho_f}\frac{\partial P}{\partial x}+\frac{2\tau_w}{\rho_f\left(R-0.5h\right)}=0 \tag{5.2}$$

where $V=V\left(x,t\right)$ is the flow velocity, $P=P\left(x,t\right)$ is the pressure which is assumed to be uniform over cross-section, K_f is the bulk modulus of water, $w=w\left(x,t\right)$ is the radial displacement and τ_w is the friction at pipe-fluid interface and x is the longitudinal coordinate, and t denotes time. The unsteady friction can be determined by a weighting-function-based model (e.g., Zielke 1968, Trikha 1975a and Suzuki et al. 1991) or using an instantaneous-acceleration-

based model (e.g., Brunone et al. 2000, Pezzinga 2000, and Vítkovský et al. 2006). The pipe wall radial velocity $\partial w/\partial t$ is determined differently in the classical and extended water hammer models, as is detailed in the following sections.

5.4.2. Structural expressions in classical and extended water hammer models

5.4.2.1.Radial displacement

According to Hooke's law (e.g., Timoshenko and Goodier 1951), the strain-stress relations in a pipe are

$$\varepsilon_\phi = \frac{\sigma_\phi - \nu\sigma_x}{E} \tag{5.3}$$

$$\varepsilon_x = \frac{\sigma_x - \nu\sigma_\phi}{E} \tag{5.4}$$

where ε_ϕ and σ_ϕ are circumferential strain and stress, ε_x and σ_x are longitudinal strain and stress. Both in the classical and the extended water hammer models, the radial inertial effects and wall bending stiffness are neglected, and hence the circumferential stress is proportional to the interner pressure as (e.g., Ghidaoui et al. 2005)

$$\sigma_\phi = \frac{R - 0.5h}{h} P \tag{5.5}$$

From Eqs. (5.3)-(5.5), by substituting into the radial displacement-strain relation for axi-symmetric thin-shell cylinder $\varepsilon_\phi = w/R$, the radial displacement is obtained (e.g., Grafton and Strome 1963) by

$$w = R\varepsilon_\phi = \frac{R}{E}\left(\frac{R - 0.5h}{h} P - \nu\sigma_x\right) \tag{5.6}$$

The difference between the classical and the extended water hammer models lies in the assumptions made in obtaining the longitudinal stress. In the classical water hammer model, the longitudinal inertial effect is neglected (e.g., Brunone et al. 1995, Wylie 1997, Ghidaoui et al. 2005) while it is included in the extended water hammer model (e.g., Tijsseling and Lavooij 1990, Wiggert and Tijsseling 2001, Tijsseling et al. 2008). Additional assumptions to determine the longitudinal stress are detailed in following sections.

5.4.2.2.Incorporating radial velocity of the pipe wall in classical water hammer model (**M1**)

In the classical water hammer model, the assumptions and expressions for the longitudinal stress are: 1) when both pipe ends are longitudinally restrained, the pipe is assumed to be in a plane-strain condition, i.e., $\varepsilon_x = 0$, and the longitudinal stress as obtained from Eq. (5.4) is $\sigma_x = \nu\sigma_\phi$; 2) when both ends are longitudinally unrestrained pipe (anchored by expansion joints), the pipe is assumed to be in a plane-stress condition, i.e., $\sigma_x = 0$; 3) for a pipe with one end longitudinally restrained and the other unrestrained, the longitudinal stress in the pipe wall arising from the action of the internal pressure on the valve end through $\sigma_x = 0.5\sigma_\phi$ (e.g., Tijsseling 1996 and Ghidaoui et al. 2005). From the longitudinal stress expressions, by substituting into Eq.(5.6) and taking derivative with respect to time, the radial velocity $\partial w/\partial t$ of the pipe wall is given by

$$\frac{\partial w}{\partial t} = \frac{cR\left(R - 0.5h\right)}{Eh}\frac{\partial P}{\partial t} \tag{5.7}$$

where $c = 1$ when both ends are restrained from longitudinal movement, $c = 1 - \nu^2$ when both ends are anchored by expansion joints, and $c = 1 - 0.5\nu$ when a pipe is longitudinal restrained at one end (e.g., at the reservoir) and longitudinally free through an expansion joint at the other end (i.e., the valve) (e.g., Tijsseling 1996 and Ghidaoui et al. 2005). From Eq.(5.7), by substituting into Eq.(5.1), one recovers the mass conservation equation for the classical water hammer model as

$$\frac{\partial V}{\partial x} + \frac{1}{a_c^2}\frac{\partial P}{\partial t} = 0 \tag{5.8}$$

where a_c is the wave speed and computed by

$$a_c = \sqrt{\frac{K_f}{\rho_f}\frac{1}{1 + 2cRK_f/Eh}} \tag{5.9}$$

where a_c is the water hammer wave speed and is constant for a given pipe. Equations (5.2) and (5.8) are the governing equations of the monolithic classical water hammer model, and typically they are numerically solved using the MOC (e.g., Lai 1988, Sibetheros et al. 1991, Ghidaoui and Karney 1994 and Cao et al. 2020a)

5.4.2.3.Incorporating pipe wall radial velocity in the extended water hammer model (**M2**)

By neglecting the bending stiffness in the thin-shell cylinder, the longitudinal strain-displacement in the pipe can be expressed as

$$\varepsilon_x = \frac{\partial u}{\partial x} \tag{5.10}$$

where u is the longitudinal displacement of the pipe wall. From Eqs.(5.10) and (5.5), by substituting into Eq.(5.4), one obtains

$$\sigma_x = \nu \frac{P\left(R - 0.5h\right)}{h} + E\frac{\partial u}{\partial x} \tag{5.11}$$

From Eq.(5.11), by substituting into Eq.(5.6), and taking the derivative with respect to time, the radial velocity of pipe wall is given as

$$\frac{\partial w}{\partial t} = R\frac{1-\nu^2}{E}\frac{\left(R - 0.5h\right)}{h}\frac{\partial P}{\partial t} + E\frac{\partial^2 u}{\partial x \partial t} \tag{5.12}$$

From Eq.(5.12), by substituting into the mass conservation equation [Eq.(5.1)], one obtains

$$\frac{\partial V}{\partial x} + \frac{1}{a_e^2}\frac{\partial P}{\partial t} = 2\nu\frac{\partial \dot{u}}{\partial x} \tag{5.13}$$

$$a_e = \sqrt{\frac{K_f}{\rho_f}\frac{1}{1 + 2\left(1-\nu^2\right)RK_f \big/ Eh}} \tag{5.14}$$

where a_e is a constant which differs from the wave propagation wave speed after including the FSI effects (Tijsseling and Lavooij 1990). From Eqs.(5.10) and (5.5), by substituting into Eq.(5.4), and taking the derivative with respect to time, one obtains

$$\frac{\partial^2 u}{\partial x \partial t} - \frac{1}{E}\frac{\partial \sigma_x}{\partial t} = -\frac{\nu R}{Eh}\frac{\partial P}{\partial t} \tag{5.15}$$

Using the force equilibrium equation in the longitudinal direction, the longitudinal stress σ_x is related to the longitudinal displacement u of the pipe wall through

$$\frac{\partial^2 u}{\partial t^2} - \frac{1}{\rho_s}\frac{\partial \sigma_x}{\partial x} = 0 \tag{5.16}$$

Equations (5.2), (5.13), (5.15) and (5.16) are the governing equations for the fluid and structural domains for the extended water hammer model (e.g., Skalak 1953, Tijsseling and Lavooij 1990 and Wiggert and Tijsseling 2001). The extended water hammer model has been solved using the MOC (e.g., Wiggert et al. 1986 and Ferras et al. 2017a) in conjunction with longitudinal restrained valve boundary (i.e., $\dot{u} = 0$) or longitudinal unrestrained valve (i.e., $\sigma_x = \pi\left(R - 0.5h\right)^2 \Delta P \big/ 2h$, in which ΔP is the pressure difference on both sides of the valve).

5.5. Partitioned water hammer models using strong coupling scheme

Both the classical and extended water hammer models are based on the circumferential stress equation in Eq. (5.5) which assumes that the circumferential stress is proportional to the pressure. For a pressure jump as may be the case at the pressure wave front, the circumferential stress field will be discontinuous. In such a case, Eq. (5.6) would lead to a discontinuous radial displacement distribution of the pipe wall, which is unattainable based on physical grounds. The present study remedies this discrepancy by solving the mass and momentum conservation equations Eq.(5.1) and (5.2) under a continuous radial displacement field as determined from a structural model. Towards this goal, a partitioned algorithm is adopted herein to capture the two-way interaction between the fluid and structural models.

5.5.1. Fluid model

From the mass and momentum conservation equations [Eqs.(5.1) and (5.2)] for an inviscid fluid (i.e., $\tau_w = 0$), one obtains the ordinary differential equations along the characteristic lines as

$$\frac{dV}{dt} + \frac{1}{\rho_f a_f}\frac{dP}{dt} + \frac{a_f}{R - 0.5h}\frac{\partial w}{\partial t} = 0; \qquad C+: \ \frac{dx}{dt} = a_f \tag{5.17}$$

$$\frac{dV}{dt} - \frac{1}{\rho_f a_f}\frac{dP}{dt} - \frac{a_f}{R - 0.5h}\frac{\partial w}{\partial t} = 0; \qquad C-: \ \frac{dx}{dt} = -a_f \tag{5.18}$$

where $a_f = \sqrt{K_f / \rho_f}$ is the sound speed in water and the pipe wall radial velocity $\partial w/\partial t$ is determined from the structural model. Equations (5.17) and (5.18) are similar to the equations

along the characteristic lines for the monolithic classical water hammer model used in the past work (Cao et al. 2020a,b). Thus, the classical water hammer model can be modified to develop the fluid solver required in the presently sought partitioned water hammer model.

5.5.2. Possible structural models for the pipe

5.5.2.1.Structural model-1 (**S1**)

By expressing Eq.(5.7), which relates the radial displacement to the pressure within the monolithic classical water hammer model (rather than back-substituting the expression into the mass conservation equation), the nodal radial displacement $w_i^{t+\Delta t}$ at time $t+\Delta t$ is given by

$$w_i^{t+\Delta t} = \frac{cR\left(R-0.5h\right)}{Eh} P_i^{t+\Delta t} \tag{5.19}$$

The radial velocity of the pipe wall is discretized along the time line as

$$\left(\frac{\partial w}{\partial t}\right)_i^{t+\Delta t} = \frac{w_i^{t+\Delta t} - w_i^t}{\Delta t} \tag{5.20}$$

where i is the node number, t is the present time and Δt is the time increment, and the unknown radial displacements ($w_i^{t+\Delta t}$) for time step $t+\Delta t$ is determined from the structural model, e.g., Eq.(5.19).

5.5.2.2.Structural model-2 (**S2**)

Another possible structural model can be developed based on Eqs. (5.15) and (5.16) within an extended water hammer model. Using the Method of Characteristics, the governing equations for the structural model [Eqs.(5.15) and (5.16)] are discretized along the characteristic lines as

$$\frac{d\dot{u}}{dt} - \frac{1}{\rho_s a_s}\frac{d\sigma_x}{dt} = -a_s \frac{\nu R_0}{Eh}\frac{\partial P}{\partial t}; \qquad C+: \frac{dx}{dt} = a_s \tag{5.21}$$

$$\frac{d\dot{u}}{dt} + \frac{1}{\rho_s a_s}\frac{d\sigma_x}{dt} = a_s \frac{\nu R_0}{Eh}\frac{\partial P}{\partial t}; \qquad C-: \frac{dx}{dt} = -a_s \tag{5.22}$$

where $a_s = \sqrt{E/\rho_s}$ is the wave speed of the stress wave in the pipe wall. The pressure is determined from the fluid model [Eqs.(5.17) and (5.18)] in a discretized form as

$$\left(\frac{\partial P}{\partial t}\right)_t^{t+\Delta t} = \frac{P_t^{t+\Delta t} - P_t^t}{\Delta t} \tag{5.23}$$

The structural boundary conditions are identical to those of the monolithic extended water hammer model. The radial displacements are then computed from Eq.(5.6) and the radial velocity at the pipe wall is determined by Eq. (5.20) and sent as input into the fluid model.

5.5.2.3.Structural model-3 (**S3**)

A two-node thin-shell axisymmetric finite element was recently developed in Cao et al. (2020b) to discretize the pipe domain as

$$\mathbf{M}\ddot{\mathbf{U}}(t) + \mathbf{C}\dot{\mathbf{U}}(t) + \mathbf{K}\mathbf{U}(t) = \mathbf{F}(t) \tag{5.24}$$

where $\mathbf{M}$ is the mass matrix, $\mathbf{K}$ is the stiffness matrix and $\mathbf{C}$ is the Rayleigh damping matrix, $\mathbf{U}^T(t) = \langle u_1 \quad w_1 \quad w_1' \quad u_2 \quad w_2 \quad w_2' \rangle$ is the nodal displacement vector at time t, in which u_i is longitudinal displacement, w_i is radial displacement, w_i' is the rotation of the pipe wall due to the change of radial displacement with respect to x, and subscripts $i = 1, 2$ denote the first and second nodes and $\mathbf{F}(t)$ is the energy equivalent load vector resulting from the pressure $P(x,t)$ induced by the fluid. Unlike the solution in Cao et al. (2020b) which was based on one-way coupling, the present study adopts a two-way coupling algorithm.

5.5.3. Partitioned approach algorithm

Table 5-1 provides a summary of the fluid model presented under Section 5.5.1. and the structural models presented in Section 5.5.2. Symbol $\mathbb{F}_{\text{MOC}}$ denotes a fluid solver based on the MOC which computes the fluid velocity field $\mathbf{V}_\mathbf{f}^{t+\Delta t}$ and pressure field $\mathbf{P}_\mathbf{f}^{t+\Delta t}$ at time $t+\Delta t$ given the fluid velocity vector $\mathbf{V}_\mathbf{f}^t$, hydraulic pressure vector $\mathbf{P}_\mathbf{f}^t$, all defined at time t, and the vector of radial displacements at pipe wall $\dot{\mathbf{w}}_\mathbf{f}^{t+\Delta t}$ at time $t+\Delta t$ at the nodes of the fluid solver. Symbol $\mathbb{S}_{\text{MOC}}$ denotes a structural solver using the MOC which computes the longitudinal velocity $\dot{\mathbf{u}}_\mathbf{s}^{t+\Delta t}$ and longitudinal stress $\boldsymbol{\sigma}_{x\mathbf{s}}^{t+\Delta t}$ of the pipe wall at time $t+\Delta t$ given the longitudinal velocity vector $\dot{\mathbf{u}}_\mathbf{s}^t$, longitudinal stress vector $\boldsymbol{\sigma}_{x\mathbf{s}}^t$ of the pipe wall and the pressure vector $\mathbf{P}_\mathbf{s}^t$ (computed in the structural mesh), all defined at time t, as well as the pressure vector $\mathbf{P}_\mathbf{s}^{t+\Delta t}$ at time $t+\Delta t$.

Symbol $\mathbb{S}_{\text{FEM}}$ denotes a structural solver based on FEM which computes wall displacement field $\mathbf{U}^{t+\Delta t}$ of the pipe wall, the velocity field $\dot{\mathbf{U}}^{t+\Delta t}$ and acceleration field $\ddot{\mathbf{U}}^{t+\Delta t}$ at time $t+\Delta t$ given the pipe wall displacement vector $\mathbf{U}^{t}$, velocity vector $\dot{\mathbf{U}}^{t}$ and acceleration vector $\ddot{\mathbf{U}}^{t}$, all defined at time t, as well as the hydraulic pressure vector $\mathbf{P}_{\mathbf{s}}^{t+\Delta t}$ in structural mesh defined at time $t+\Delta t$. In the first two structural models, the radial velocity of the pipe wall is computed from Eq. (5.20) given the radial displacements $\mathbf{w}_{\mathbf{s}}^{t}$ and $\mathbf{w}_{\mathbf{s}}^{t+\Delta t}$.

Table 5-1 Fluid and structural models in the partitioned water hammer models

Fluid model	Structural model
$\left\langle \mathbf{V}_{\mathbf{f}}{}^{t+\Delta t}, \mathbf{P}_{\mathbf{f}}^{t+\Delta t} \right\rangle = \mathbb{F}_{\text{MOC}} \left\langle \mathbf{V}_{\mathbf{f}}{}^{t}, \mathbf{P}_{\mathbf{f}}^{t}, \dot{\mathbf{w}}_{\mathbf{f}}^{t+\Delta t} \right\rangle$	**S1:** $\mathbf{w}_{\mathbf{s}}^{t+\Delta t} = \dfrac{cR\left(R-0.5h\right)}{Eh}\mathbf{P}_{\mathbf{s}}^{t+\Delta t}$
	S2: $\left\langle \dot{\mathbf{u}}_{\mathbf{s}}^{t+\Delta t}, \boldsymbol{\sigma}_{x\,\mathbf{s}}^{t+\Delta t} \right\rangle = \mathbb{S}_{\text{MOC}} \left\langle \dot{\mathbf{u}}_{\mathbf{s}}^{t}, \boldsymbol{\sigma}_{x\,\mathbf{s}}^{t}, \mathbf{P}_{\mathbf{s}}^{t}, \mathbf{P}_{\mathbf{s}}^{t+\Delta t} \right\rangle$
	$\mathbf{w}_{\mathbf{s}}^{t+\Delta t} = \dfrac{R}{E}\left(\dfrac{R-0.5h}{h}\mathbf{P}_{\mathbf{s}}^{t+\Delta t} - \nu\boldsymbol{\sigma}_{x\mathbf{s}}^{t+\Delta t} \right)$
	S3: $\left\langle \mathbf{U}^{t+\Delta t}, \dot{\mathbf{U}}^{t+\Delta t}, \ddot{\mathbf{U}}^{t+\Delta t} \right\rangle = \mathbb{S}_{\text{FEM}} \left\langle \mathbf{U}^{t}, \dot{\mathbf{U}}^{t}, \ddot{\mathbf{U}}^{t}, \mathbf{P}_{\mathbf{s}}^{t+\Delta t} \right\rangle$

The vector of radial velocities in the pipe wall (required as input to the fluid model) $\dot{\mathbf{w}}_{\mathbf{f}\,(n_f+1)\times 1}^{t+\Delta t}$ (n_f being the number of subdivisions in the fluid model) is determined by pre-multiplying vector of radial velocities of the pipe wall from the structural model $\dot{\mathbf{w}}_{\mathbf{s}\,(n_s+1)\times 1}^{t+\Delta t}$ (n_s being the number of subdivisions in the structural model) by the structure-fluid interface matrix $\mathbf{H}_{\mathbf{fs}}$, so that $\dot{\mathbf{w}}_{\mathbf{f}\,(n_f+1)\times 1}^{t+\Delta t} = \mathbf{H}_{\mathbf{fs}}\dot{\mathbf{w}}_{\mathbf{s}\,(n_s+1)\times 1}^{t+\Delta t}$. Also, the pressure $\mathbf{P}_{\mathbf{s}\,(n_s+1)\times 1}^{t+\Delta t}$ required as input to the structural model is obtained by pre-multiplying the vector of pressure $\mathbf{P}_{\mathbf{f}\,(n_f+1)\times 1}^{t+\Delta t}$ as computed from the fluid model by a fluid-structure interface matrix $\mathbf{H}_{\mathbf{sf}}$, so that $\mathbf{P}_{\mathbf{s}\,(n_s+1)\times 1}^{t+\Delta t} = \mathbf{H}_{\mathbf{sf}}\mathbf{P}_{\mathbf{f}\,(n_f+1)\times 1}^{t+\Delta t}$.

Figure 5.2 shows three types of structure-fluid interfaces used to transmit the radial velocity of the pipe wall from the structural model to the fluid model. Interface Γ1 adopts a fixed matched interface (i.e., $n_s = n_f$), Interface Γ2 adopts a fixed non-matched interface ($n_s \neq n_f$), and Interface Γ3 adoptes a moving mesh interface, with $\mathbf{X}_{\mathbf{s}}^{t+\Delta t} = \mathbf{X}_{\mathbf{s}}^{0} + \mathbf{u}_{\mathbf{s}}^{t+\Delta t}$, where $\mathbf{u}_{\mathbf{s}}^{t+\Delta t}$ is vector of nodal

longitudinal displacements at time $t+\Delta t$, $\mathbf{X_s}$ is the vector of nodal coordinates for the structural model and superscript 0 denotes the original configuration.

Using the Interface $\Gamma 1$, the known vector of radial velocity of the pipe wall is assigned to radial velocity vector in fluid model directly through $\dot{\mathbf{w}}^{t+\Delta t}_{\mathbf{f}\,(n_f+1)\times 1} = \dot{\mathbf{w}}^{t+\Delta t}_{\mathbf{s}\,(n_s+1)\times 1}$. Using the Interface $\Gamma 2$, linear interpolation is adopted to obtain the radial velocity vector in the fluid model from the known vector of radial of the pipe wall through $\dot{\mathbf{w}}^{t+\Delta t}_{\mathbf{f}\,(n_f+1)\times 1} = \mathbf{H_{fs}}\dot{\mathbf{w}}^{t+\Delta t}_{\mathbf{s}\,(n_s+1)\times 1}$.

Using the Interface $\Gamma 3$, the updated coordinate vector $\mathbf{X}^{t+\Delta t}_{\mathbf{s}}$ for structural nodes is used to compute the fluid-structure interface matrix. Throughout the pipe longitudinal movement, when an end node of the fluid interface is found outside the structural domain interface, an additional node is added to the end of the structural interface so that its coordinate matches that of the end node of the fluid interface. The radial velocity vector at the additional node is then taken equal to be that of the closest node in the structural domain. Linear interpolation is then used to form the structure-fluid interface matrix, i.e., evaluate $\mathbf{H}^{t+\Delta t}_{\mathbf{fs}} = \mathbf{H}^{t+\Delta t}_{\mathbf{fs}}\left(\mathbf{X}^{t+\Delta t}_{\mathbf{s}}\right)$. In contrast to Interface $\Gamma 2$ in which $\mathbf{H_{fs}}$ is independent of time, the $\mathbf{H}^{t+\Delta t}_{\mathbf{fs}}$ matrix used in Interface $\Gamma 3$ scheme is time dependent.

The radial velocity vector in the fluid model is determined from the known vector of radial of the pipe wall through $\dot{\mathbf{w}}^{t+\Delta t}_{\mathbf{f}\,n_f\times 1} = \mathbf{H}^{t+\Delta t}_{\mathbf{fs}}\dot{\mathbf{w}}^{t+\Delta t}_{\mathbf{s}\,n_s\times 1}$. Similar schemes are developed when transferring the pressure vector from the fluid model into the structural model, except that an additional node will be added to the fluid mesh if necessary in the Interface $\Gamma 3$.

Using schemes described above to exchange radial velocity and pressure between the fluid and structure models, the block Gauss-Seidel algorithm is used to conduct a two-way coupled fluid-structural analysis within each time step as detailed in Table 5-2. The relaxation factor ψ adopted in step 7 can be either (a) set as a constant value in the range of $0 < \psi \le 1$ or (b) determined by the Aitken extrapolation method (e.g., Küttler and Wall 2008, 2009) as

$$\begin{aligned}
\psi_1 &= \max\left(\psi^{t-\Delta t}\Big|_{k=k\max}, \psi_0\right) && k=1 \\
\psi_k &= \psi_{k-1}\frac{\left(-\mathbf{r}\big|_{k-1}\right)^{\mathrm{T}}\left(\mathbf{r}\big|_k - \mathbf{r}\big|_{k-1}\right)}{\left(\mathbf{r}\big|_k - \mathbf{r}\big|_{k-1}\right)^{\mathrm{T}}\left(\mathbf{r}\big|_k - \mathbf{r}\big|_{k-1}\right)} && k=2,3,...
\end{aligned} \tag{5.25}$$

in which $\mathbf{r}$ is the residual vector, k is iteration time, $\psi^{t-\Delta t}\Big|_{k=k\max}$ is the relaxation factor corresponding to the last iteration, i.e., $k = k_{\max}$ attained in the previous time step $t - \Delta t$ and $\psi_{\max}$ is a user specified constant in the range of $0 < \psi_{\max} \le 1$ taken as $\psi_0 = 0.75$ in the present work. All models are programed under the MATLAB platform and were run on a workstation with 24 processors [Intel(R) Xeon(R) CPU E5-2690 v4 @ 2.60GHz, RAM=64G].

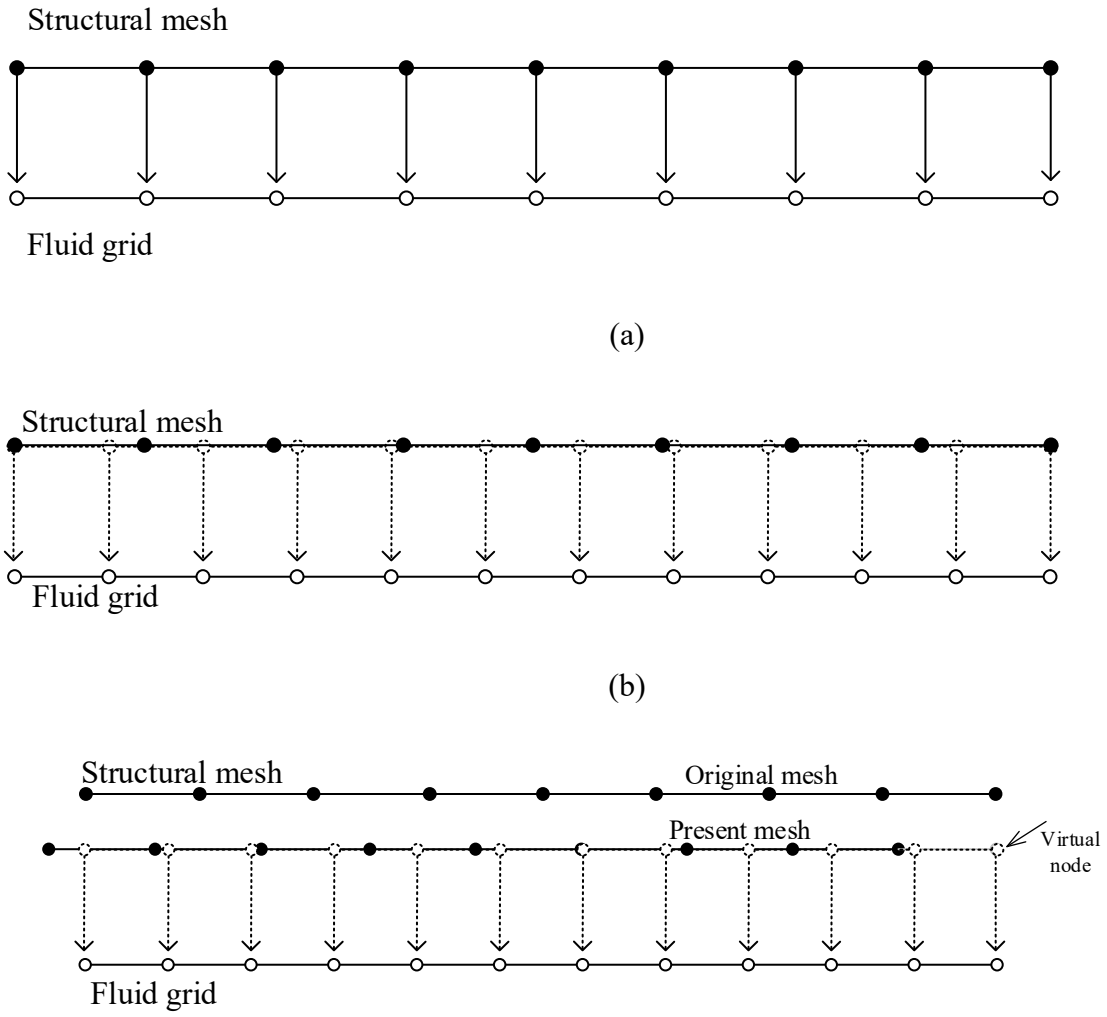

Figure 5.2 Three interfaces for information exchanging between two models. (a) Interface Γ1: matched interface; (b) Interface Γ2: non-matched fixed interface; and (c) Interface Γ3: moving mesh interface.

Table 5-2 Block Gauss-Seidel algorithm for the partitioned water hammer models

	Structural model **S1** and **S2**	Structural model **S3**
1	Increment time step $t = t + \Delta t$ Initialize iteration number $k \to 0$ Update field variables in fluid model velocity vector $\mathbf{V}^t$ pressure vector $\mathbf{P}^t$ For **S2**: Update field variables in structural model longitudinal stress vector $\boldsymbol{\sigma}_x^t$ velocity vector $\dot{\mathbf{u}}_x^t$ in structural model	Increment the time $t = t + \Delta t$ Initialize iteration number $k \to 0$ Update field variables in fluid model velocity vector $\mathbf{V}^t$ pressure vector $\mathbf{P}^t$ Update field variables in structural model displacement vector $\mathbf{U}^t$ velocity vector $\dot{\mathbf{U}}^t$ acceleration vector $\ddot{\mathbf{U}}^t$
2	Increment iteration number $k \to k+1$ Determine radial velocity of pipe wall for iteration k from $\dot{\mathbf{w}}_{\mathbf{f}}^{t+\Delta t}\Big\|_k = \begin{cases} \mathbf{0} & k = 1 \\ \mathbf{H}_{\mathbf{fs}}\Big\|_k \dot{\mathbf{w}}_{\mathbf{s}}^{t+\Delta t}\Big\|_k & k = 2,3,.. \end{cases}$	
3	Solve the fluid model for the velocity $\mathbf{V}_{\mathbf{f}}^{t+\Delta t}\Big\|_k$ and pressure $\mathbf{P}_{\mathbf{f}}^{t+\Delta t}\Big\|_k$.	
4	Transfer the pressure vector to the structural model though $\mathbf{P}_{\mathbf{s}}^{t+\Delta t}\Big\|_k = \mathbf{H}_{\mathbf{sf}}\Big\|_k \mathbf{P}_{\mathbf{f}}^{t+\Delta t}\Big\|_k$	
5	Calculate the rate of pressure change $\left(\mathbf{P}_{\mathbf{s}}^{t+\Delta t}\Big\|_k - \mathbf{P}_{\mathbf{s}}^{t}\right)\Big/\Delta t$	Calculate the energy equivalent load vector $\mathbf{F}^{t+\Delta t}\Big\|_k = \mathbf{H}_{\mathbf{L}}\, \mathbf{P}_{\mathbf{s}}^{t+\Delta t}\Big\|_k$ (1)
6	From the structural model obtain the longitudinal velocity at the valve location (2) $\dot{u}^{t+\Delta t}\left(x = L\right)\Big\|_k$ and	
	Determine radial displacement of the pipe wall $\mathbf{w}_{\mathbf{s}}^{t+\Delta t}\Big\|_k$.	Determine radial velocity of the pipe wall $\dot{\mathbf{U}}^{t+\Delta t}\Big\|_k$.

7	Compute the residual of radial displacement of the pipe wall, e.g., $\mathbf{r}\big\vert_k = \begin{cases} \left(\mathbf{w}_\mathbf{s}^{t+\Delta t}\big\vert_k - \mathbf{w}_\mathbf{s}^{t}\right) & k=1 \\ \left(\mathbf{w}_\mathbf{s}^{t+\Delta t}\big\vert_k - \mathbf{w}_\mathbf{s}^{t+\Delta t}\big\vert_{k-1}\right) & k=2,3,.. \end{cases}$	Compute the residual of displacement filed of the pipe wall, e.g., $\mathbf{r}\big\vert_k = \begin{cases} \left(\mathbf{U}^{t+\Delta t}\big\vert_k - \mathbf{U}^{t}\right) & k=1 \\ \left(\mathbf{U}^{t+\Delta t}\big\vert_k - \mathbf{U}^{t+\Delta t}\big\vert_{k-1}\right) & k=2,3,.. \end{cases}$
8	Compute the estimated radial displacement of pipe wall: $\mathbf{w}_\mathbf{s}^{t+\Delta t}\big\vert_k = \mathbf{w}_\mathbf{s}^{t+\Delta t}\big\vert_k + \psi\,\mathbf{r}\big\vert_k$ (3)	Compute estimated fields of pipe wall: $\mathbf{U}^{t+\Delta t}\big\vert_k = \mathbf{U}^{t+\Delta t}\big\vert_k + \psi\,\mathbf{r}\big\vert_k$ $\dot{\mathbf{U}}^{t+\Delta t}\big\vert_k = \dot{\mathbf{U}}^{t+\Delta t}\big\vert_k + \psi\left(\dot{\mathbf{U}}^{t+\Delta t}\big\vert_k - \dot{\mathbf{U}}^{t+\Delta t}\big\vert_{k-1}\right)$ $\ddot{\mathbf{U}}^{t+\Delta t}\big\vert_k = \ddot{\mathbf{U}}^{t+\Delta t}\big\vert_k + \psi\left(\ddot{\mathbf{U}}^{t+\Delta t}\big\vert_k - \ddot{\mathbf{U}}^{t+\Delta t}\big\vert_{k-1}\right)$
9	Check convergence (4), i.e., $\left\Vert\mathbf{r}\big\vert_k\right\Vert_2 \Big/ \left\Vert\mathbf{w}_\mathbf{s}^{t+\Delta t}\big\vert_k\right\Vert_2 \le \varepsilon_{cr}$ If satisfied: Go to Step 1 for new time step. Otherwise: Compute radial velocity of pipe wall through $\dot{\mathbf{w}}_\mathbf{s}^{t+\Delta t}\big\vert_k = \left(\mathbf{w}_\mathbf{s}^{t+\Delta t}\big\vert_k - \mathbf{w}_\mathbf{s}^{t}\right)\Big/\Delta t$, Go to step 2 for next iteration	Check convergence (4), i.e., $\left\Vert\mathbf{r}\big\vert_k\right\Vert_2 \Big/ \left\Vert\mathbf{U}^{t+\Delta t}\big\vert_k\right\Vert_2 \le \varepsilon_{cr}$ If satisfied: Go to Step 1 for new time step. Otherwise: Go to step 2 for next iteration

(1) the transfer matrix $\mathbf{H}_\mathbf{L}$ is determined such that it relates the energy equivalent load vector $\mathbf{F}^{t+\Delta t}\big\vert_k$ based on Cao et al. (2020b) to the pressure vector $\mathbf{P}_\mathbf{s}^{\,t+\Delta t}\big\vert_k$

(2) The velocity at the valve end is set to zero when using the structural model **S1**.

(3) ψ is a relaxation factor.

(4) Symbol $\left\Vert\bullet\right\Vert_2$ denotes the Euclidean norm of the argument vector and ε_{cr} is a user-specified tolerance.

5.6. Verification of partitioned water hammer models

5.6.1. Reference case

To assess the validity of the partitioned water hammer schemes proposed herein, the problem reported in Lavooij and Tijsseling (1991) is considered as a reference case. In the Reservoir-Pipe-Valve system (Figure 5.1), the pipe has a length $L = 20\text{m}$, mid-surface diameter $D = 805\text{mm}$ and a thickness $h = 8\text{mm}$. Young's modulus of pipe is $E = 2.1\times10^{11}\,\text{N/m}$ and Poisson's ratio is $\nu = 0.3$. The pipe wall density is $\rho_s = 7900\,\text{kg/m}^3$ and the water density is $\rho_f = 1000\,\text{kg/m}^3$. The bulk modulus of water is $K_f = 2.1\times10^9\,\text{N/m}$. The water is assumed inviscid, i.e., $\tau_w = 0$. The datum level is set at the inlet of pipe, i.e., $H_{res} = 0$, and the pressure behand the valve is zero. The initial velocity is $V_0 = 1\text{m/s}$ and the valve is assumed to close instantaneously. The above problem will be analyzed using five different model types. These are:

M1: monolithic classical water hammer model;

M2: monolithic extended water hammer model;

P1: partitioned classical water hammer model based on structural model **S1**;

P2: partitioned extended water hammer model using the structural model **S2**: and

P3: partitioned shell-based water hammer model using the structural model **S3**.

The pressure wave speed as determined by Eq. (5.9) is $a_c = 1064\,\text{m/s}$ for the monolithic classical water hammer model **M1**. Equation (5.14) provides the wave speed $a_e = 1047\,\text{m/s}$ for the monolithic extended water hammer model **M2**. For the partitioned water hammer models **P1**-**P3**, the sound wave speed in the water is $a_f = \sqrt{K_f/\rho_f} = 1449\,\text{m/s}$ and stress wave speed in the pipe wall is $a_s = \sqrt{E/\rho_s} = 5156\,\text{m/s}$. Unlike the wave speed a_c associated with the monolithic classical water hammer model, the wave speeds a_f and are a_s associated with fluid-structure interaction models do not represent the physical propagation wave speeds. In the fluid model, the boundary conditions are $P(0,t) = 0$ at the upstream reservoir and $V(L,t) = \dot{u}(L,t)$ at the valve end. In models **M1** and **P1**, the longitudinal velocity of the valve is neglected, e.g., $\dot{u}(L,t) \approx 0$. In

the **P3** model based on the **S3** structural model, the boundary conditions at the valve are taken as $u(L,t) \neq 0,$ i.e., is considered longitudinally free and $w(L,t) = w'(L,t) = 0$. At the reservoir, the boundary conditions are $u(0,t) = w(0,t) = w'(0,t) = 0$.

5.6.2. Designations

Each of models used to analyze the reference problem depends on various parameters. As a notation convention, each model is assigned a designation of the form ' Model-Interface-n_f-n_s-C_r ', in which

"Model' identifies the type model and takes one of the values **P1**, **P2**, **P3**, **M1**, or **M2**.

'Interface' denotes the interface type and takes the values $\Gamma 1$, $\Gamma 2$ or $\Gamma 3$.

' n_f ' denotes the numbers of subdivisions taken for the fluid model and ' n_s ' denotes the numbers of subdivisions for the structural model and take the values 64, 512, 1024, 2048, or 4096,

' C_r ' denotes the Courant number $C_r = a_0 \Delta t / \Delta x$, and takes a value between 0.1 to 4.0, and $\Delta x = L / n_f$ is the subdivision length, $a_0 = a_c$ in Model **M1**, $a_0 = a_e$ in Model **M2**, and $a_0 = a_f$ in Models **P1, P2, P3.**

For example, **M1**-$\Gamma 1$-2048-2048-1.0 represents Model **M1** with Interface $\Gamma 1$, with 2048 subdivisions for the fluid and structural models, and a Courant Number of 1.0.

5.6.3. Selection of benchmark solutions

The present section presents the results for all five models M1, M2, P1, P2, and P3 while fixing the Interface Type to $\Gamma 1$, and the Courant number to $C_r = 1$. The number of subdivisions in the fluid and structural domains is taken to be equal. Two subdivision values are used, namely $n_f = n_s = 64$ and $n_f = n_s = 2048$. All the runs take the generic designation.

The time increment in each model is determined based on the Courant number and the number of subdivisions taken, e.g., $\Delta t = C_r \Delta x / a_0$. A natural frequency analysis based on the **S3** model was conducted to extract the predominant longitudinal natural frequency ($\omega_1 = 405 \, \text{rad/s}$) and the predominant radial natural frequency ($\omega_{16} = 11123 \, \text{rad/s}$). The corresponding damping ratios were

taken as $\xi_1 = 2\%$ and $\xi_{16} = 5\%$, respectively. The Aitken relaxation technique is used in the block Gauss-Seidel algorithm with a convergence tolerance $\varepsilon_{cr} = 10^{-7}$. The pressure histories at the valve are extracted from all five models. By increasing the number of subdivisions from 64 to 2048, the predictions of the partitioned models were shown to approach to those predicted by the corresponding monolithic models as depicted in Figure 5.3 (a) and (b). These results suggest the correctness of the implementation of the partitioned water hammer models.

Figure 5.3b shows that the predictions of the extended water hammer, which captures the fluid-structure interaction effects, differ from those based on the classical water hammer model, which omits interaction. The results are consistent with past work (e.g., Tijsseling and Lavooij 1990 and Ferràs et al. 2016). The present partitioned implementation **P2** model is able replicate results of the monolithic implementation **M2** of the extended water hammer when enough subdivisions are taken.

Figure 5.3c shows that model **P3** predicts results similar to those of the extended water hammer models (**M2** and **P2**), except for the presence of some spikes. This suggests that, for the present problem, apart from the pressure spikes observed, the radial inertial effects and the bending stiffness in pipe wall have a negligible effect on the water hammer pressure predictions. The partitioned implementation herein illustrates the advantages in terms of modularity whereby a given solver can be reused in different Fluid-Structure Interaction models, e.g., the same fluid model can be re-used to capture coupling effects with different structural models.

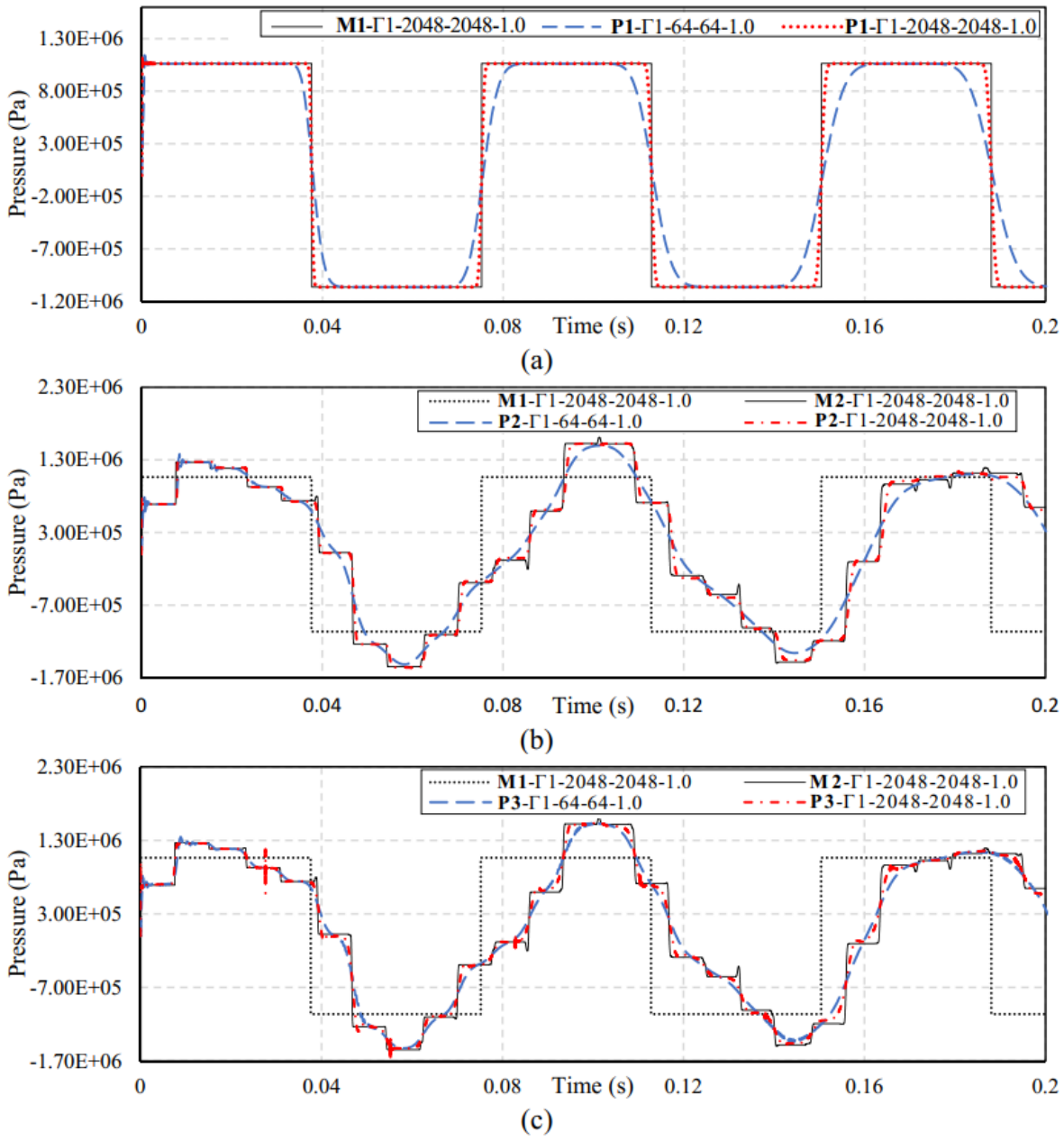

Figure 5.3 Pressure histories at the valve in the benchmark problem using the monolithic and partitioned water hammer models.

As shown in Figure 5.3, all the partitioned water hammer models predict approximate pressure histories at the valve, when compared to those predicted by the monolithic water hammer models. By selecting Interface Γ1 with $n_s = n_f = 2048$ subdivisions and a Courant number $C_r = 1$, the pressure histories $P_b(t)$ at the valve based on the monolithic model are extracted within the interval $0s \le t \le 0.2s$ to serve as benchmark solutions for the corresponding partitioned water

hammer models $P_a(t)$, i.e., **M1** for **P1**, **M2** for **P2** and **P3**. The percentage difference $\eta(a,b)$ of the pressure between $P_a(t)$ based on the model of interest and that of the benchmark solution $P_b(t)$ is defined as

$$\eta(a,b) = \frac{\int_{t=0}^{t=0.2s} \left| P_a(t) - P_b(t) \right| dt}{\int_{t=0}^{t=0.2s} \left| P_b(t) \right| dt} \times 100\% \tag{5.26}$$

The percentage differences $\eta(a,b)$ of the pressure for various solutions are presented in Table 5-3. The percentage difference decreases as the number of subdivisions $n_s = n_f$ increases. The monolithic model predictions approach those of the well-known classical/extended pressure with a lower number of subdivisions than the partitioned model. In subsequent sections, the benchmark models (b) provided in Column 2 of Table 3 are adopted for comparison of results of all models investigated.

Table 5-3 Percentage difference *η(a,b)* between the benchmark pressure history $P_b(t)$ and pressure history $P_a(t)$ based on various solutions/number of subdivisions

Model Examined (a)	Benchmark Model (b)	% pressure difference $\eta(a,b)$
M1-Γ1-64-64-1.0	**M1**-Γ1-2048-2048-1.0	2.28
M2-Γ1-64-64-1.0	**M2**-Γ1-2048-2048-1.0	3.99
P1-Γ1-64-64-1.0	**M1**-Γ1-2048-2048-1.0	12.7
P1-Γ1-2048-2048-1.0	**M1**-Γ1-2048-2048-1.0	2.20
P2-Γ1-64-64-1.0	**M2**-Γ1-2048-2048-1.0	13.3
P2-Γ1-2048-2048-1.0	**M2**-Γ1-2048-2048-1.0	2.88
P3-Γ1-64-64-1.0	**M2**-Γ1-2048-2048-1.0	11.4
P3-Γ1-2048-2048-1.0	**M2**-Γ1-2048-2048-1.0	5.95

5.7. Characteristics of the partitioned approach

The accuracy and efficiency of the partitioned water hammer models are influenced by the tolerance, the Courant number chosen, the relaxation factor, and the type of interface adopted. The following sections will vary one of the above four parameters at a time along with the number of subdivisions, while keeping the remaining parameters identical to those used in section 5.6.3.

($C_r = 1$, $\xi_{cr} = 10^{-7}$, the Aitken relaxation factor, Interface $\Gamma 1$, and for model **P3**, the damping ratios $\xi_1 = 2\%$, $\xi_{16} = 5\%$).

5.7.1. Effect of tolerance

Figure 5.4 provides the percentage difference $\eta(a,b)$ in pressure history as determined by Eq. (5.26) for models **P1**, **P2**, **P3** while varying the number of subdivisions $n_f = n_s$ for various tolerances ranging from 10^{-5} to 10^{-8}. For Model **P1**, Figure 5.4a shows that $\eta(a,b)$ decreases from about 12% at $n_f = n_s = 64$ down essentially zero at $n_f = n_s = 4096$. For Model **P2** (Figure 5.4b), $\eta(a,b)$ decreases with the number of subdivisions for relatively coarse meshes of up to 512 subdivisions. For finer meshes, the convergence behaviour depends on the tolerance chosen. For the relatively coarse tolerances $\varepsilon_{cr} = 10^{-5}, 10^{-6}$, $\eta(a,b)$ was found to increase with the number of subdivisions when $n_f = n_s \geq 1024$. For the relatively finer tolerance $\varepsilon_{cr} = 10^{-7}$, $\eta(a,b)$ decreases with the number of subdivisions up to $n_s = n_f = 2048$, where it reaches a minimal value, after which it mildly increases at $n_s = n_f = 4096$. At the very low tolerance value of $\varepsilon_{cr} = 10^{-8}$, convergence was not attainable for meshes finer than $n_f = n_s = 1024$ flagging instability. For Model **P3** (Figure 5.4c), $\eta(a,b)$ is found to decrease with the number of subdivisions for relatively coarse meshes and then reach a plateau at $n_f = n_s = 1024$

In Models **P1** and **P2** (Figure 5.4a-b), the pressure percentage difference $\eta(a,b)$ (Figure 5.4b) attained are smaller value than that of Model **P3** (Figure 5.4c) since Models **P1** and **P2** adopt governing equations identical to those of the chosen benchmark solutions (**M1, M2,** respectively) while adopting a partitioned approach. In contrast, Model **P3** based on shell analysis captures additional structural features (material damping, radial inertial effect of the pipe, bending stiffness of the pipe wall, etc.) that are not captured in the chosen benchmark solution **M2** and hence is not expected to coincide with the predictions of the **M2** model, irrespective of the number of subdivisions taken.

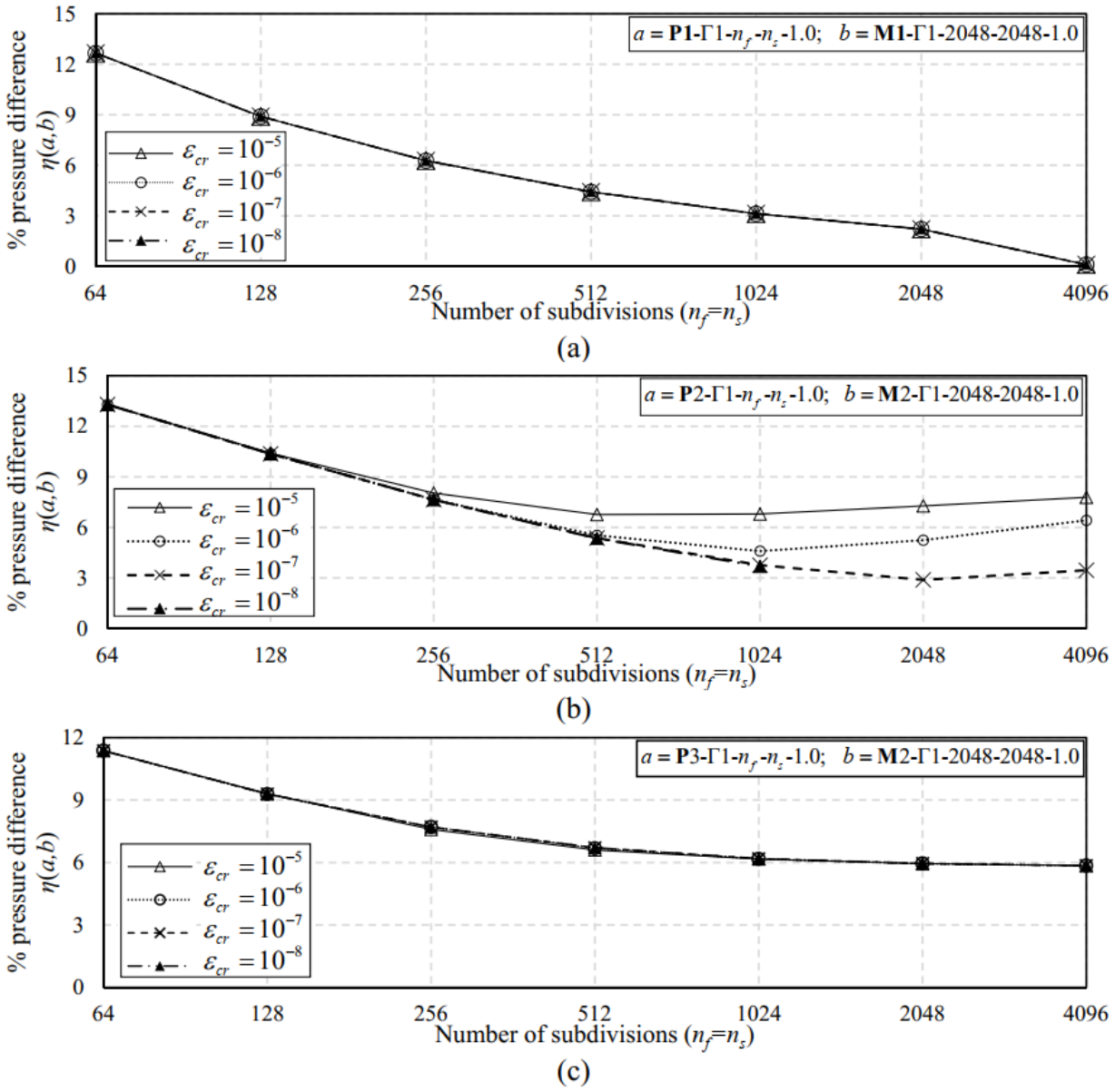

Figure 5.4 Effect of tolerance on pressure percentage difference based on Partitioned models (a) Model **P1** (classical); (b) Model **P2** (extended); and (c) Model **P3** (shell-based).

5.7.2. Effect of the Courant number

Figure 5.5 depicts the percentage difference $\eta(a,b)$ of the pressure versus the Courant number C_r for various values of subdivisions $n_s = n_f$ for all five models. A common feature in all five models is that $\eta(a,b)$ is decreased as $n_s = n_f$ increases. In Model **M1** (Figure 5.5a) and Model **M2** (Figure 5.5b), $\eta(a,b)$ approaches zero when Courant number is an integer and peaks in

between integer Courant values. Further it is observed that the peak $\eta(a,b)$ value decays as the Courant number increases.

Since an increase in Courant number corresponds to a larger time step, a smaller number of time-steps (involving spatial interpolations) is needed to simulate a given period, leading to smaller $\eta(a,b)$ values. The above observations are similar to those reported by Shimada et.al. (2008b) for Model **M1**. The present study extends the observations for model **M2.** The results suggest that higher integer Courant numbers may be selected for models **M1** and **M2** to increase the computational efficiency without scarifying the accuracy of the predictions.

In Models **P1** (Figure 5.5c) and **P3** (Figure 5.5e), by increasing the Courant number from zero to unity, $\eta(a,b)$ is observed to decrease and attains a minimum value at $C_r = 1$, albeit the value does not approach zero. In contrast to the **M1** and **M2** models, by increasing the Courant number past unity $\eta(a,b)$ is found to increase, although it exhibits local minima at higher integer Courant numbers. For the **P3** model, the smallest $\eta(a,b)$ value is observed to correspond to $C_r = 1$ higher integer values $C_r = 2$ or 3 would not result in a larger percentage difference and such values may be taken to increase computational efficiency.

In Model **P2** (Figure 5.5d), $\eta(a,b)$ decreases as the Courant number increases from zero to unity. However, unlike for the other models, it becomes unstable when the Courant number exceeds unity, suggesting that $C_r = 1$ is the optimum choice for model **P2.**

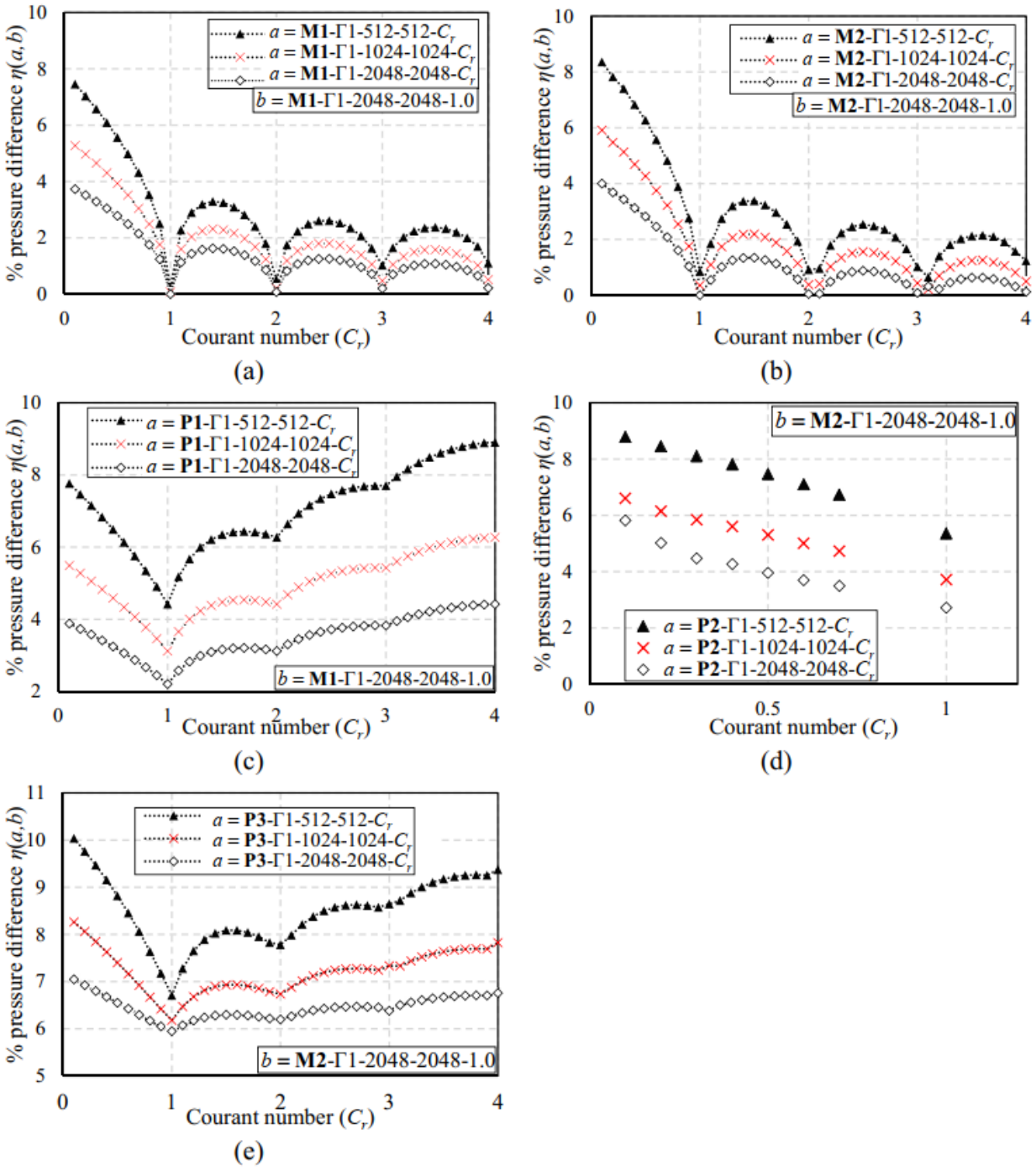

Figure 5.5 Effects of the Courant number C_r on the percentage difference of the pressure η^*_{ab} adopting Interface 1 in five models. (a) Model **M1** (classical); (b) Model **M2** (extended); (3) Model **P1** (classical); (d) Model **P2** (extended); and (e) Model **P3** (shell-based).

5.7.3. Effect of relaxation factor

The convergence of the block Gauss-Seidel algorithm can be accelerated by adopting an appropriate relaxation factor, taken either as a constant or as a dynamic value, e.g., by the Aitken

method (e.g., Küttler and Wall 2008). Figure 5.6 (a-c) depicts the average number of iterations versus the relaxation factor in the range $0 < \psi \leq 1$ for partitioned models **P1**, **P2**, and **P3.** Overlaid on the figures are the number of iterations based on Aitken method for comparison. Figure 5.6 shows that by adopting a constant relaxation factor, one can reduce the average number of iterations. Using 2048 subdivisions in fluid and structural models, the optimal values for the relaxation factor is 0.5 for Model **P1**, 0.5 for Model **P2**, and 1.0 for Model **P3**. The average number of iterations needed for convergence using the Aitken relaxation factor is always smaller than those using a constant relaxation factor in all three partitioned models (**P1**, **P2**, **P3**).

Using a constant relaxation factor, the average number of iterations is found to slightly decrease with the number of subdivisions. By increasing the number of subdivisions from 64 to 2048 with while using Aitken relaxation factor was found not to influence the average number of iterations in Model **P1**, but to decrease them from 7.6 to 5.3 for Model **P2**, and from 4.4 to 2.2 for Model **P3**. Figure 5.6(b) shows that, irrespective of the number of subdivisions taken, Model **P2** becomes unstable when no relaxation is applied (i.e., $\psi = 1$). Figure 5.6(b) shows that by adopting $n_s = n_f = 2048$ in **P2**, the model becomes unstable when taking a constant relaxation factor exceeding 0.6.

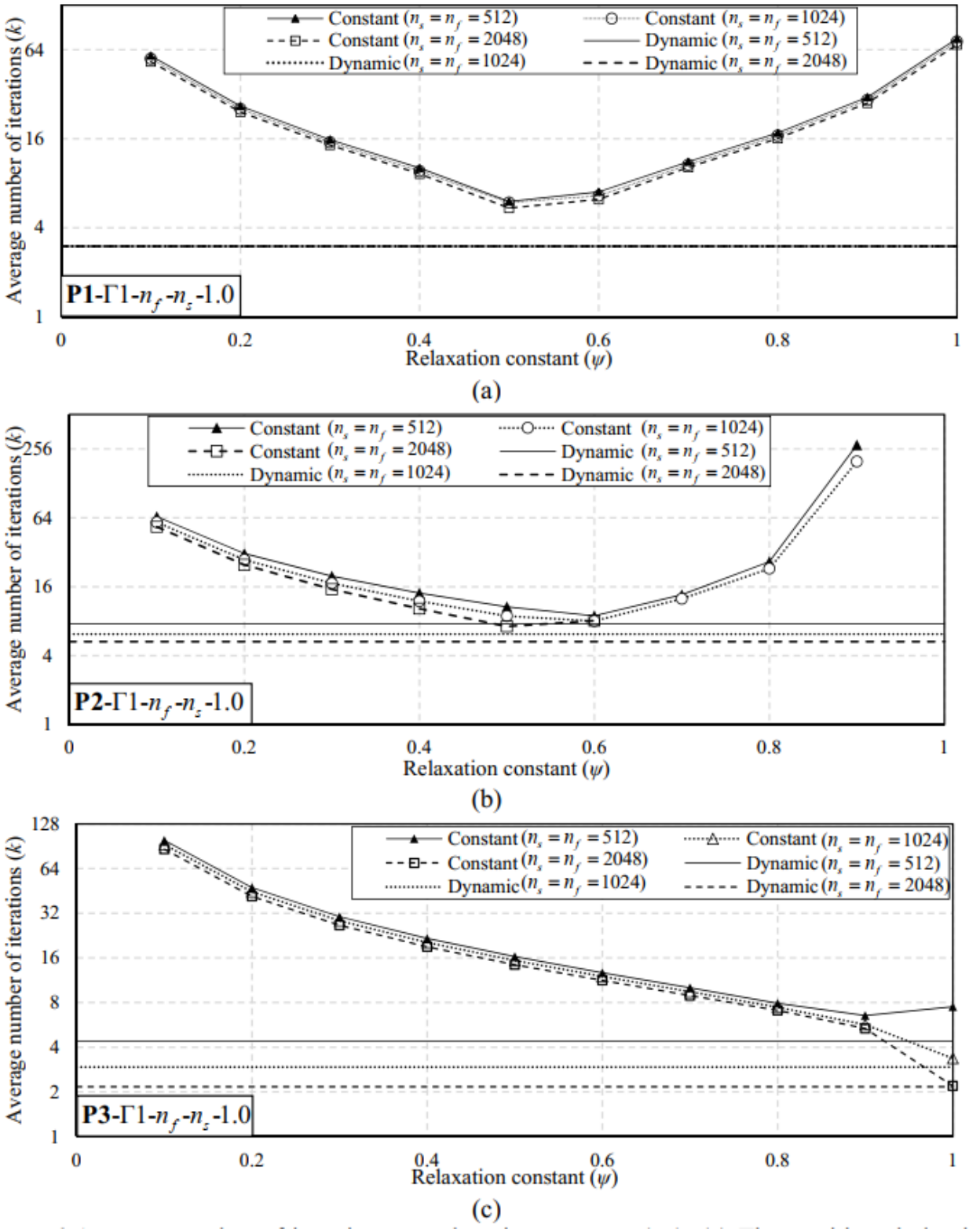

Figure 5.6 Average number of iterations versus relaxation factor ψ for partitioned models (a) **P1** (classical), (b) **P2** (extended), and (c) **P3** (shell-based).

Using the optimal constant relaxation factor or the dynamic relaxation factor, Figure 5.7 depicts the history of number of iterations k for each time step in Models **P1**-Γ1-2048-2048-1.0, **P2**-Γ1-2048-2048-1.0, **P3**-Γ1-2048-2048-1.0. For Model **P1**, Figure 5.7(a) shows that the number of iterations is constant at three iterations, when adopting a dynamic relaxation factor. In contrast, when using a constant relaxation factor $\psi = 0.5$, the number of iterations oscillates between 5 and 6 iterations with occasional spikes. The time interval Δt_s between two consecutive spikes is equal to the time interval needed for the pressure wave to propagate from one end of the pipe to the other end, e.g., $\Delta t_s = L/a_c = 18.8ms$. When using a constant relaxation factor in Model **P1**, Figure 5.7a shows that the occurrences and magnitudes of the repeating spikes indicate that fewer iterations are needed when the pressure wave bounces back at the reservoir while more iterations are required as the pressure wave bounces back from the valve.

In Model **P2**, the number of iterations is found to oscillate along the timeline when using a constant relaxation factor $\psi = 0.5$ (Figure 5.7b) and when using a dynamic relaxation factor (Figure 5.7(c)). The histories of the number of iterations for Model **P2** in [Figure 5.7 (b) and (c)] are transferred to the frequency domain in Figure 5.8 to further investigate the oscillations in the iterations. Figure 5.8 shows that, by using constant or dynamic relaxation factors, the first three peaks correspond are found to correspond to equal frequencies; 25Hz (Peak I), 130Hz (Peak II) and 255Hz (Peak III). The frequency at Peak I is approximately equal to that at which the pressure wave travels back to the valve, e.g., $a_e/2L = 26.2\text{Hz}$. The frequencies of Peaks II and III are dominated by the reflections of the longitudinal stress wave, i.e., $a_s/2L = 129\text{Hz}$ and $a_s/L = 257.8\text{Hz}$. When either the pressure wave or the stress wave bounce back at pipe ends, the number of iterations differs from the average number of iterations, with either fewer or more iterations.

For Model **P3**, Figure 5.7d shows that the numbers of iterations when using a constant relaxation factor $\psi = 1$ is comparable to that when using a dynamic relaxation factor (Figure 5.6c).

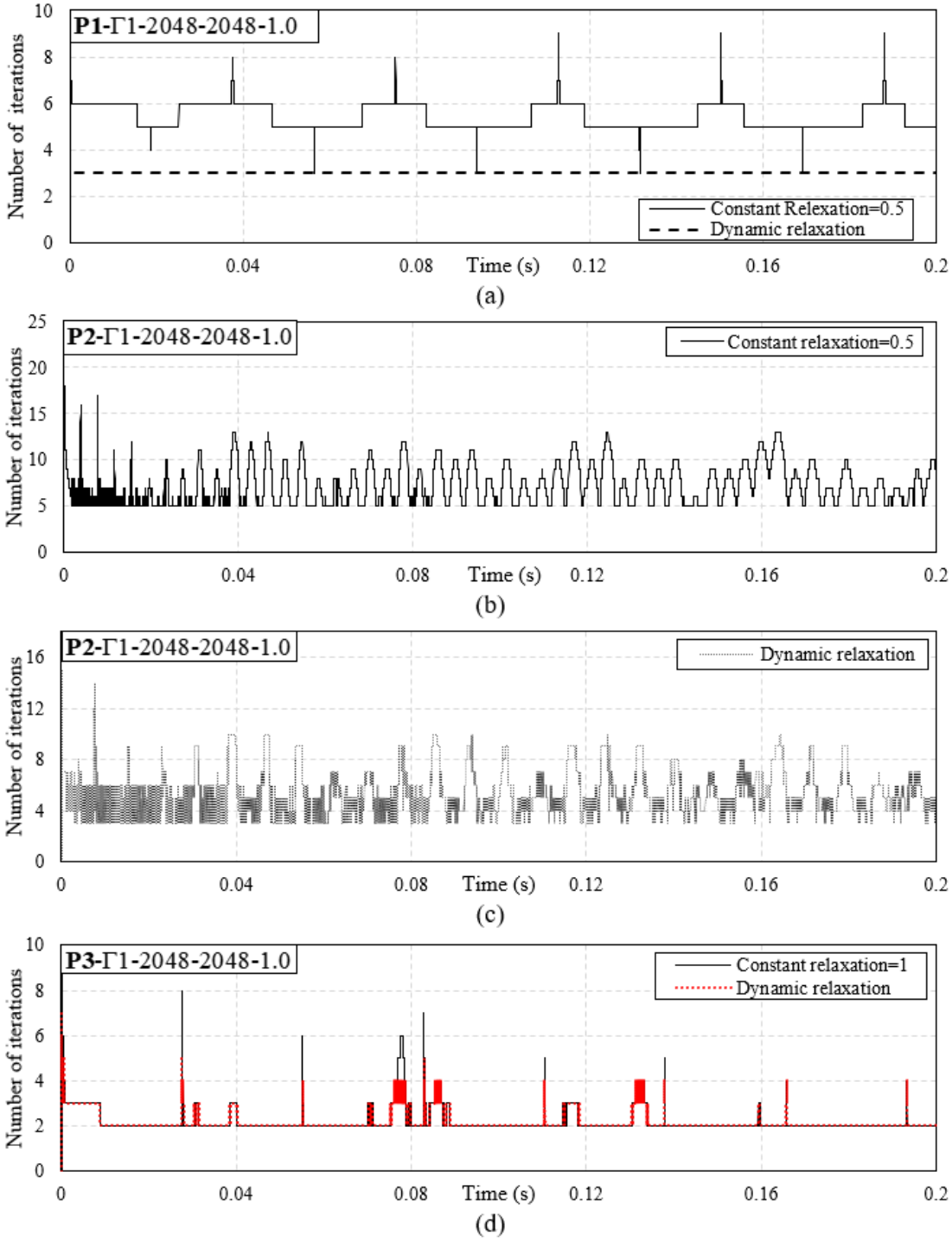

Figure 5.7 History of number of iterations for partitioned models with 2048 subdivisions. (a) **P1** (classical) using constant relaxation factor (ψ=0.5) and dynamic relaxation factor; **P2** (extended) using (b) constant relaxation factor (ψ=0.5) and (c) dynamic relaxation factor; (d) **P3** (shell-based) using constant relation factor (ψ=1) and dynamic relaxation factors.

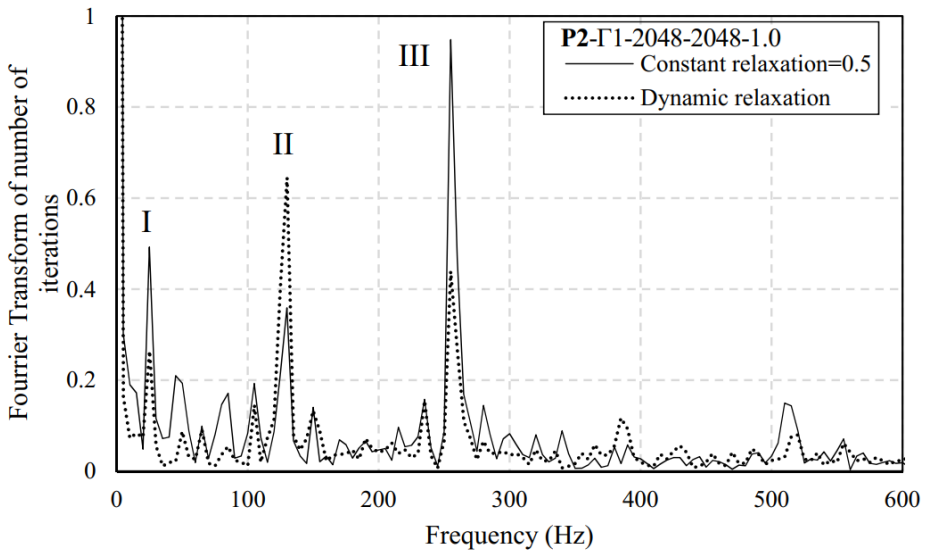

Figure 5.8 Frequency of the number of iterations for each time step using Model **P2** (extended).

5.7.4. Effect of interface type

Using the partitioned approach, the fluid and structural models can have a different number of subdivisions, i.e., $n_s \neq n_f$. Since the stability of Model **P2** using Interface II depends on the ratio n_s/n_f, it will be excluded from the discussion in this section. The Interface Type and the number of subdivisions n_s and n_f are varied in Runs **P1**-Interface-n_f-n_s-1.0 and **P3**-Interface-n_f-n_s-1.0. The percentage difference in the pressure $\eta(a,b)$ is depicted in Figure 5.9(a) and (b) and the corresponding computational time is presented in Figure 5.9 (c) and (d). It is observed that $\eta(a,b)$ is primarily dominated by the number of subdivisions n_f in the fluid model, and is independent from (1) the number n_s of subdivisions in the structural model and (2) from the type of interface adopted. Figure 5.9(b) and (d) show that, for a given number of fluid model subdivisions n_f, the computational time increases with n_s. For example, in Runs **P3**-Γ2-4096-n_s-1.0 (Figure 5.9d), the computational time is 49.2s when adopting $n_s = 512$, and increases to 96.0s when adopting $n_s = 2048$. In Model **P3**, the computational time decreases when adopting Interface Type Γ2 compared to that adopting Interface Γ3. For example, in Runs **P3**-Interface-4096-2048-1.0, the computational time is 96.0s when adopting Interface Γ2, and is 138.4s when adopting Interface Γ3. The difference is attributed to the fact that in Interface Γ2, transfer matrices $\mathbf{H}_{\mathbf{sf}}, \mathbf{H}_{\mathbf{fs}}$ are

constant since they are independent of displacement field. In contrast, the transfer matrixes $\mathbf{H_{sf}}^{t+\Delta t}\big|_k$, $\mathbf{H_{fs}}^{t+\Delta t}\big|_k$ for Interface Γ3 depend on the pipe longitudinal displacement $\mathbf{u}^{t+\Delta t}\big|_k$ and hence need updating for each iteration k based on the searching technique. As long as the partitioned models **P1**, **P3** remain stable, the above observations suggest the merit of adopting Interface Γ2 to increase the computational efficiency, while using a number of subdivisions n_f in the fluid model that is larger than number of subdivisions n_s in the structural model.

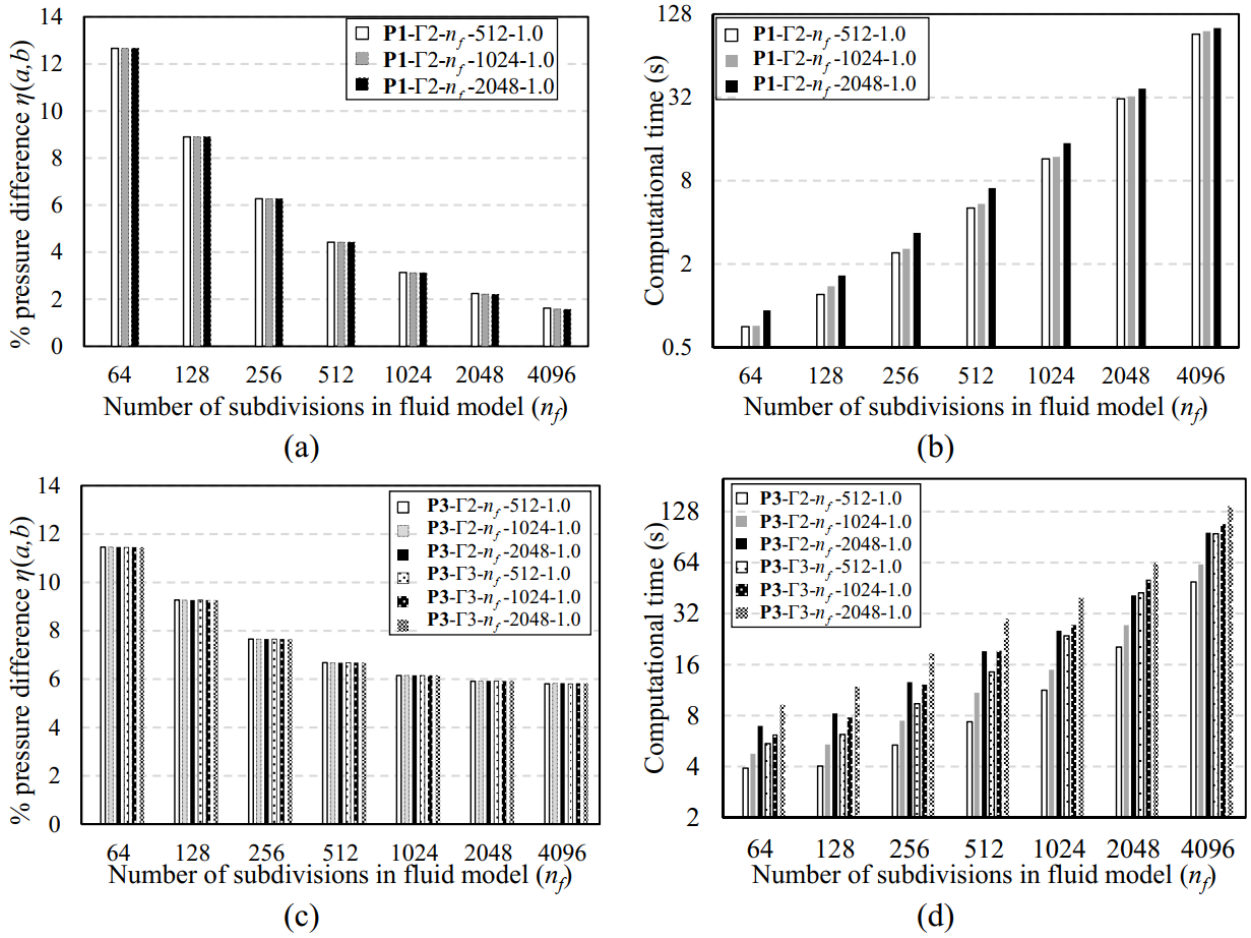

Figure 5.9 Effect of the interface adopted on percentage difference of pressure and computing time in partitioned models (a-b) **P1** (classical) and (c-d) **P3** (shell-based).

5.8. Summary conclusions

The present study developed a series of water hammer models by using the partitioned methodology. The solutions capture two-way FSI effects. Three representations for the structural model were implemented within the partitioned scheme: (1) a model analogous to that used under

monolithic classical water hammer, (2) a model analogous to that used under monolithic extended water hammer, and (3) a finite element shell-based model that captures radial inertial effects and ensures the continuity of the displacements along the pipe length.

Two-way coupling between the fluid solver and each of the structural solvers was ensured by using the Block Gauss-Seidel iterative algorithm in conjunction with relaxation factors to accelerate the convergence. Results based on the monolithic models were used as benchmarks to investigate the effects of the selected convergence criterion, the relaxation factor, the type of interface and the time increment on the predicted pressure history.

The conclusions are summarized as:

(1) The results from the partitioned implementation of the classical and extended water hammer models are in close agreement with results predicted from the monolithic models, suggesting the correctness of the implementation of the Block Gauss-Seidel iterative algorithm.

(2) The results predicted from the partitioned models approach the benchmark solutions as the specified convergence criterion becomes more stringent and/or as the number of subdivisions increases. An exception was observed for the partitioned extended water hammer model, in which the solution may diverge in some cases.

(3) The Aitken dynamic relaxation was observed to significantly decrease the number of iterations compared to the constant relaxation, and is recommended for computational efficiency.

(4) Compared to the monolithic classical and extended water hammer models, the pressure difference of the extended implementation of the models show local minimum values when the Courant number approaches an integer value. A similar observation is observed in the partitioned implementation of the classical and shell-based water hammer models. However, since the shell-based model captures effects not included in the benchmark comparison runs (based on the extended water hammer), the percentage pressure difference does not approach a zero value.

(5) Apart from the partitioned extended water hammer model, all monolithic and partitioned models are found to be stable when using large time increments.

(6) Using non-matched fluid and structure interfaces, the partitioned solution for the extended water hammer model was found to diverge in some cases. Thus, only the partitioned classical and

shell-based water hammer models were investigated. For both models, the percentage difference of the predicted pressure history decreases with the number of subdivisions in the fluid model, but is found independent of the interface type and the number of subdivisions in the structural model.

5.9. Notations

a_c =wave speed for the monolithic classical water hammer model (m/s)

a_e =wave speed for the monolithic extended water hammer model (m/s)

a_f =sound speed in water (m/s)

c =constant in the classical wave speed equation

C_r =Courant number

E =Young modulus (Pa)

h =pipe thickness (m)

H_{res} =reservoir hydraulic head (m)

K_f =bulk modulus of water (Pa)

L =pipe length (m)

n_f =number of subdivisions in fluid model

n_s =number of subdivisions in structural model

P =pressure (Pa)

R =pipe mid-surface radius (m)

t =time (s)

u =longitudinal displacement (m)

V =flow velocity (m/s)

V_0 =initial flow velocity (m/s)

w =radial displacement (m)

x =the longitudinal coordinate (m)

Δt =time increment (s)

Δx =length subdivision (m)

ε_{cr} =convergence tolerance

ε_x =longitudinal strain

ε_ϕ =circumferential strain

η^*_{ab} =percentage difference between two solutions

ν =Poisson's ratio

ρ_f =fluid density ($\mathrm{kg/m^3}$)

ρ_s =pipe material density ($\mathrm{kg/m^3}$)

σ_x =longitudinal stress (Pa)

σ_ϕ =circumferential stress (Pa)

τ_w =friction at pipe-fluid interface (Pa)

ψ =relaxation factor

ω =natural frequency (Hz)

Matrices and vectors

M =mass matrix

C =Rayleigh damping matrix

K =stiffness matrix

U =nodal displacement vector

F =energy equivalent load vector

$\mathbf{V_f}$ =fluid velocity vector

$\mathbf{P_f}$ =hydraulic pressure vector

X =nodal coordinate vector

w =nodal radial displacement vector

u =nodal longitudinal displacement vector

$\mathbf{H_{fs}}$ =structure-fluid interface matrix

$\mathbf{H_L}$ =transfer matrix for energy equivalent load

$\mathbf{H_{sf}}$ =fluid-structure interface matrix

r =residual vector

Subscripts and superscripts

Subscript **f** denotes fluid model.

Subscript **s** denotes structural model.

Subscript k denotes iteration time.

Superscript $\bullet$ denotes derivative with respect to time.

Superscript $'$ denotes derivative with respect to longitudinal coordinate.

Superscript t denotes values at time t.

Superscript $t + \Delta t$ denotes values at time t.

5.10. References

Adamkowski, A., and Lewandowski, M. (2006). "Experimental examination of unsteady friction models for transient pipe flow simulation." *J. Fluids Eng.,* 128(6), 1351–1363.

Baek, H., and Karniadakis, G. E. (2012). "A convergence study of a new partitioned fluid–structure interaction algorithm based on fictitious mass and damping." *J. Comput. Phys.*, 231(2), 629–652.

Bergant, A., Simpson, A. R., and Vítkovský, J. (2001). "Developments in unsteady pipe flow friction modelling." *J. Hydraul. Res.*, 39(3), 249–257.

Bernard, D. (2013). "Numerical modelling of water hammer effects in penstocks." Master thesis, University of Ottawa.

Breuer, M., De Nayer, G., Münsch, M., Gallinger, T., and Wüchner, R. (2012). "Fluid–structure interaction using a partitioned semi-implicit predictor–corrector coupling scheme for the application of large-eddy simulation." *J. Fluids Struct.*, 29, 107–130.

Brunone, B., Golia, U. M., and Greco, M. (1995). "Effects of two-dimensionality on pipe transients modeling." *J. Hydraul. Eng.*, 121(12), 906–912.

Brunone, B., Karney, B. W., Mecarelli, M., and Ferrante, M. (2000). "Velocity Profiles and Unsteady Pipe Friction in Transient Flow." *J. Water Resour. Plan. Manag.*, 126:4(236), 236–244.

Budny, D. D., Wiggert, D. C., and Hatfield, F. (1990). "Energy Dissipation in the axially-coupled model for transient flow." *Proc. 6th Int. Conf. Press. Surges*, A. R. D. Thorley, ed., BHRA, Cambridge, UK, 15–26.

Budny, D. D., Wiggert, D. C., and Hatfield, F. J. (1991). "The Influence of Structural Damping on Internal Pressure During a Transient Pipe Flow." *J. Fluids Eng.*, 113(3), 424–429.

Bukač, M., Čanić, S., and Muha, B. (2015). "A partitioned scheme for fluid–composite structure interaction problems." *J. Comput. Phys.*, 281, 493–517.

Burman, E., and Fernández, M. A. (2009). "Stabilization of explicit coupling in fluid–structure interaction involving fluid incompressibility." *Comput. Methods Appl. Mech. Eng.*, 198(5), 766–784.

Cao, H., Nistor, I., and Mohareb, M. (2020a). "Effect of Boundary on Water Hammer Wave Attenuation and Shape." *J. Hydraul. Eng.*, 146(3), 4020001.

Cao, H., Mohareb, M., and Nistor, I. (2020b). “Finite element for the dynamic analysis of pipes subjected to water hammer.” *J. Fluids Struct.*, 93, 102845.

Causin, P., Gerbeau, J. F., and Nobile, F. (2005). “Added-mass effect in the design of partitioned algorithms for fluid–structure problems.” *Comput. Methods Appl. Mech. Eng.*, 194(42), 4506–4527.

Chaudhry, M. H., and Hussaini, M. Y. (1985). “Second-Order Accurate Explicit Finite-Difference Schemes for Waterhammer Analysis.” *J. Fluids Eng.*, 107(4), 523–529.

Colciago, C. M., Deparis, S., and Quarteroni, A. (2014). “Comparisons between reduced order models and full 3D models for fluid–structure interaction problems in haemodynamics.” *J. Comput. Appl. Math.*, 265, 120–138.

Daude, F., Tijsseling, A. S., and Galon, P. (2018). “Numerical investigations of water-hammer with column-separation induced by vaporous cavitation using a one-dimensional Finite-Volume approach.” *J. Fluids Struct.*, 83, 91–118.

Degroote, J. (2013). “Partitioned Simulation of Fluid-Structure Interaction.” *Arch. Comput. Methods Eng.*, 20(3), 185–238.

Degroote, J., Annerel, S., and Vierendeels, J. (2010a). “Stability analysis of Gauss–Seidel iterations in a partitioned simulation of fluid–structure interaction.” *Comput. Struct.*, 88(5), 263–271.

Degroote, J., Bathe, K.-J., and Vierendeels, J. (2009). “Performance of a new partitioned procedure versus a monolithic procedure in fluid–structure interaction.” *Comput. Struct.*, 87(11), 793–801.

Degroote, J., Swillens, A., Bruggeman, P., Haelterman, R., Segers, P., and Vierendeels, J. (2010b). “Simulation of fluid–structure interaction with the interface artificial compressibility method.” *Int. j. numer. method. biomed. eng.*, 26(3-4), 276–289.

Duan, H. F., Meniconi, S., Lee, P. J., Brunone, B., and Ghidaoui, M. S. (2017). “Local and integral energy-based evaluation for the unsteady friction relevance in transient pipe flows.” *J. Hydraul. Eng.*, 143(7), 04017015.

Fernández, M. A., and Moubachir, M. (2003). “An exact Block-Newton algorithm for the solution of implicit time discretized coupled systems involved in fluid-structure interaction problems.” Bathe,K.J., ed., Elsevier Science Ltd, Oxford, 1337–1341.

Fernández, M. Á., and Moubachir, M. (2005). “A Newton method using exact jacobians for solving fluid–structure coupling.” *Comput. Struct.*, 83(2), 127–142.

Ferras, D., Manso, P. A., Covas, D. I. C., and Schleiss, A. J. (2017a). “Fluid–structure interaction in pipe coils during hydraulic transients.” *J. Hydraul. Res.*, 55(4), 491–505.

Ferras, D., Manso, P. A., Schleiss, A. J., and Covas, D. I. C. (2017b). “Fluid-structure interaction in straight pipelines with different anchoring conditions.” *J. Sound Vib.*, 394, 348–365.

Ferràs, D., Manso, P. A., Schleiss, A. J., and Covas, D. I. C. (2016). “Fluid-structure interaction in straight pipelines: Friction coupling mechanisms.” *Comput. Struct.*, 175, 74–90.

Formaggia, L., Gerbeau, J. F., Nobile, F., and Quarteroni, A. (2001). “On the coupling of 3D and 1D Navier–Stokes equations for flow problems in compliant vessels.” *Comput. Methods Appl. Mech. Eng.*, 191(6), 561–582.

Gale, J., and Tiselj, I. (2008). “Godunov’s Method for Simulatinons of Fluid-Structure Interaction in Piping Systems.” *J. Press. Vessel Technol.*, 130(3).

Gerbeau, J.-F., and Vidrascu, M. (2003). “A Quasi-Newton Algorithm Based on a Reduced Model for Fluid-Structure Interaction Problems in Blood Flows.” *ESAIM Math. Model. Numer. Anal.*, 37(4), 631–647.

Ghidaoui, M. S., and Karney, B. W. (1994). “Equivalent Differential Equations in Fixed-Grid Characteristics Method.” *J. Hydraul. Eng.*, 120:10(1159), 1159–1175.

Ghidaoui, M. S., and Karney, B. W. (1995). “Modified transformation and integration of 1D wave equations.” *J. Hydraul. Eng.*, 121:10(758), 758–760.

Ghidaoui, M. S., Zhao, M., McInnis, D. A., and Axworthy, D. H. (2005). “A review of water hammer theory and practice.” *Appl. Mech. Rev.*, 58(1), 49.

Grafton, P. E., and Strome, D. R. (1963). “Analysis of axisymmetrical shells by the direct stiffness method.” *AIAA J.*, 1(10), 2342–2347.

Greyvenstein, G. P. (2002). “An implicit method for the analysis of transient flows in pipe networks.” *Int. J. Numer. Methods Eng.*, 53(5), 1127–1143.

Guinot, V. (2000). “Riemann solvers for water hammer simulations by Godunov method.” *Int. J. Numer. Methods Eng.*, 49(7), 851–870.

Habchi, C., Russeil, S., Bougeard, D., Harion, J.-L., Lemenand, T., Ghanem, A., Valle, D. Della, and Peerhossaini, H. (2013). “Partitioned solver for strongly coupled fluid–structure interaction.” *Comput. Fluids*, 71, 306–319.

Haelterman, R., Bogaers, A. E. J., Scheufele, K., Uekermann, B., and Mehl, M. (2016). “Improving the performance of the partitioned QN-ILS procedure for fluid–structure interaction problems: Filtering.” *Comput. Struct.*, 171, 9–17.

Hansson, P.-A., and Sandberg, G. (2001). “Dynamic finite element analysis of fluid-filled pipes.” *Comput. Methods Appl. Mech. Eng.*, 190(24), 3111–3120.

Heinsbroek, A. G. T. J., and Tijsseling, A. S. (1994). “The influence of support rigidity on waterhammer pressures and pipe stresses.” *BHR Group,Proc.of Second Int.Conf.on Water Pipeline Syst.*, D. S. Miller, ed., London,UK:Mechanical Engineering Publications, Edinburgh, Scotland.

Joosten, M. M., Dettmer, W. G., and Perić, D. (2009). “Analysis of the block Gauss–Seidel solution procedure for a strongly coupled model problem with reference to fluid–structure interaction.” *Int. J. Numer. Methods Eng.*, 78(7), 757–778.

Karney, B. W., and Ghidaoui, M. S. (1997). “Flexible discretization algorithm for fixed-grid MOC in pipelines.” *J. Hydraul. Eng.*, 123:11(1004), 1004–1011.

Kassiotis, C., Ibrahimbegovic, A., and Matthies, H. (2010). “Partitioned solution to fluid–structure interaction problem in application to free-surface flows.” *Eur. J. Mech. - B/Fluids*, 29(6), 510–521.

Küttler, U., and Wall, W. A. (2008). “Fixed-point fluid–structure interaction solvers with dynamic relaxation.” *Comput. Mech.*, 43(1), 61–72.

Küttler, U., and Wall, W. A. (2009). “Vector Extrapolation for Strong Coupling Fluid-Structure Interaction Solvers.” *J. Appl. Mech.*, 76(2).

Lai, C. (1988). “Comprehensive Method of Characteristics Models for Flow Simulation.” *J. Hydraul. Eng.*, 114:9(1074), 1074–1097.

Lavooij, C. S. W., and Tijsseling, A. S. (1991). “Fluid-structure interaction in liquid-filled piping systems.” *J. Fluids Struct.*, 5(5), 573–595.

Matthies, H. G., and Steindorf, J. (2002). “Partitioned but strongly coupled iteration schemes for nonlinear fluid–structure interaction.” *Comput. Struct.*, 80(27), 1991–1999.

Matthies, H. G., and Steindorf, J. (2003). “Partitioned strong coupling algorithms for fluid–structure interaction.” *Comput. Struct.*, 81(8), 805–812.

Mehl, M., Uekermann, B., Bijl, H., Blom, D., Gatzhammer, B., and van Zuijlen, A. (2016). "Parallel coupling numerics for partitioned fluid–structure interaction simulations." *Comput. Math. with Appl.*, 71(4), 869–891.

Michler, C., van Brummelen, E. H., and de Borst, R. (2005). "An interface Newton–Krylov solver for fluid–structure interaction." *Int. J. Numer. Methods Fluids*, 47(10-11), 1189–1195.

Michler, C., van Brummelen, E. H., and de Borst, R. (2006). "Error-amplification analysis of subiteration-preconditioned GMRES for fluid–structure interaction." *Comput. Methods Appl. Mech. Eng.*, 195(17), 2124–2148.

Murea, C. M. (2005). "The BFGS algorithm for a nonlinear least squares problem arising from blood flow in arteries." *Comput. Math. with Appl.*, 49(2), 171–186.

Pezzinga, G. (2000). "Evaluation of unsteady flow resistances by quasi-2D or 1D models." *J. Hydraul. Eng.*, 126:10(778), 778–785.

Reddy, H. P., Silva-Araya, W. F., and Chaudhry, M. H. (2012). "Estimation of decay coefficients for unsteady friction for instantaneous, acceleration-based models." *J. Hydraul. Eng.*, 138(3), 260–271.

Sattar, A. M., Dickerson, J. R., and Chaudhry, M. H. (2009). "Wavelet-Galerkin Solution to the Water Hammer Equations." *J. Hydraul. Eng.*, 135(4), 283–295.

von Scheven, M., and Ramm, E. (2011). "Strong coupling schemes for interaction of thin-walled structures and incompressible flows." *Int. J. Numer. Methods Eng.*, 87(1-5), 214–231.

Shimada, M., Brown, M. B. J., and Vardy, A. E. (2008). "Interpolation errors in rectangular and diamond characteristic grids." *J. Hydraul. Eng.*, 134:10(1480), 1480–1490.

Sibetheros, A. I., Holley, R. E., and Branski, M. J. (1991). "Spline Interpolations for Water Hammer Analysis." *J. Hydraul. Eng.*, 117:10(1332), 1332–1351.

Skalak, R. (1953). "An extension of the theory of water hammer.", Ph.D thesis, Columbia University.

Sohani, S. M., and Ghidaoui, M. S. (2019). "Mesoscopic-based finite volume solutions for waterhammer flows." *J. Hydraul. Res.*, 57(3), 337–352.

Sternel, D. C., Schäfer, M., Heck, M., and Yigit, S. (2008). "Efficiency and accuracy of fluid-structure interaction simulations using an implicit partitioned approach." *Comput. Mech.*, 43(1), 103–113.

Suzuki, K., Taketomi, T., and Sato, S. (1991). “Improving Zielke’s method of simulating frequency-dependent friction in laminar liquid pipe flow.” *J. Fluids Eng.*, 113(4), 569–573.

Szymkiewicz, R. (1995). “Method to solve 1D unsteady transport and flow equations.” *J. Hydraul. Eng.*, 121(5), 396–403.

Szymkiewicz, R., and Mitosek, M. (2005). “Analysis of unsteady pipe flow using the modified finite element method.” *Commun. Numer. Methods Eng.,* 21(4), 183–199.

Szymkiewicz, R., and Mitosek, M. (2007). “Numerical aspects of improvement of the unsteady pipe flow equations Romuald.” *Int. J. Numer. Methods Fluids,* 55, 1039–1058.

Tijsseling, A. S. (1996). “Fluid-structure interaction in liquid-filled pipe systems: a review.” *J. Fluids Struct.*, 10(2), 109–146.

Tijsseling, A. S. (2007). “Water hammer with fluid–structure interaction in thick-walled pipes.” *Comput. Struct.*, 85(11), 844–851.

Tijsseling, A. S., and Anderson, A. (2007). “Johannes von Kries and the History of Water Hammer.” *J. Hydraul. Eng.*, 133(1), 1–8.

Tijsseling, A. S., Lambert, M. F., Simpson, A. R., Stephens, M. L., Vítkovský, J. P., and Bergant, A. (2008). “Skalak’s extended theory of water hammer.” *J. Sound Vib.*, 310(3), 718–728.

Tijsseling, A. S., and Lavooij, C. S. W. (1990). “Waterhammer with fluid-structure interaction.” *Appl. Sci. Res.*, 47(3), 273–285.

Tijsseling, A. S., Vardy, A. E., and Fan, D. (1996). “Fluid-structure interaction and cavitation in a single-elbow pipe system.” *J. Fluids Struct.*, 10(4), 395–420.

Timoshenko, S., and Goodier, J. N. (1951). “Theory of elasticity”. McGraw-Hill International Book Co., New York, NY.

Tiselj, I., and Gale, J. (2008). “Integration of unsteady friction models in pipe flow simulations.” *J. Hydraul. Res.*, 46(4), 526–535.

Trikha, A. K. (1975). “An Efficient Method for Simulating Frequency-Dependent Friction in Transient Liquid Flow.” *J. Fluids Eng.*, (3), 97–105.

Vardy, A. E., and Brown, J. M. B. (2003). “Transient turbulent friction in smooth pipe flows.” *J. Sound Vib.*, 259(5), 1011–1036.

Vardy, A. E., and Brown, J. M. B. (2004). “Transient turbulent friction in fully rough pipe flows.” *J. Sound Vib.*, 270(1–2), 233–257.

Vardy, A. E., Fan, D., and Tijsseling, A. S. (1996). “Fluid-structure interaction in a T-piece pipe.” *J. Fluids Struct.*, 10(7), 763–786.

Vierendeels, J., Lanoye, L., Degroote, J., and Verdonck, P. (2007). “Implicit coupling of partitioned fluid–structure interaction problems with reduced order models.” *Comput. Struct.*, 85(11), 970–976.

Vítkovský, J., Lambert, M., Simpson, A. R., and Bergant, A. (2000). “Advances in unsteady friction modelling in transient pipe flow.” *8th Int. Conf. Preessure Surges*, BHR, The Hague, The Netherlands.

Vítkovský, P. J., Bergant, A., Simpson, R. A., and Lambert, F. M. (2006). “Systematic evaluation of one-dimensional unsteady friction models in simple pipelines.” *J. Hydraul. Eng.*, 10.1061/(ASCE)0733-9429(2006)132:7(696), 696–708.

Wahba, E. M. (2006). “Runge–Kutta time-stepping schemes with TVD central differencing for the water hammer equations.” *Int. J. Numer. Methods Fluids*, John Wiley & Sons, Ltd, 52(5), 571–590.

Walker, J. S., and Phillips, J. W. (1977). “Pulse Propagation in Fluid-Filled Tubes.” *J. Appl. Mech.*, ASME, 44(1), 31–35.

Wiggert, D. C., Hatfield, F. J., and Lesmez, M. W. (1986). “Coupled transient flow and structure motion in liquid-filled piping systems.” *Proc. 5th Internaltional Conf. Press. surges*, Hannover, Gernany, 1–9.

Wiggert, D. C., and Tijsseling, A. S. (2001). “Fluid transients and fluid-structure interaction in flexible liquid-filled piping.” *Appl. Mech. Rev.*, 54(5), 455–481.

Wood, C., Gil, A. J., Hassan, O., and Bonet, J. (2010). “Partitioned block-Gauss–Seidel coupling for dynamic fluid–structure interaction.” *Comput. Struct.*, 88(23), 1367–1382.

Wylie, E. B. (1997). “Frictional Effects in Unsteady Turbulent Pipe Flows.” *Appl. Mech. Rev.*, ASME, 50(11), S241–S244.

Zhao, M., and Ghidaoui, M. S. (2004). “Godunov-Type Solutions for Water Hammer Flows.” *J. Hydraul. Eng.*, 130(4), 341–348.

Zielke, W. (1968). “Frequency-dependent friction in transient pipe flow.” *J. Basic Eng.,* ASME, 90(1), 109–115.

Chapter 6 SUMMARY, CONCLUSIONS AND RECOMMENDATIONS

6.1. Summary

The present study contributed to water hammer analysis of pipes in three aspects. These are summarized as follows;

1. When adopting the classical water hammer model with the classical boundary expressions, the pressure wave is dissipated only by the friction stresses at the pipe wall or artificially by introducing numerical dissipation. In such a case, even though the pressure wave eventually damps out, the damping pattern (in terms of phase shifting and wave front smoothing) differs from that observed in experimental results. The present study attributed the cause to the fact that the classical boundary expressions do not account for the energy dissipation at the pipe inlet. In order to improve the classical water hammer model, the influence of the waterjet occurring at the pipe inlet was considered in the proposed boundary expression, which accounts for the energy dissipation at the pipe inlet. A newly proposed boundary expression at the reservoir was proposed and applied in conjunction with the quasi-steady friction model, and in unsteady friction models based on instantaneous acceleration and the weighting functions. The pressure histories at the valve and the system energy were determined from three friction water hammer solvers using various discretization schemes.

2. Both the classical and extended water hammer models are based on the assumption that the hoop stresses are proportional to the pressure in the pipe. This assumption leads to an unrealistic discontinuity of the radial displacement field in the pipe wall at the abrupt pressure wave front. In order to simulate the continuous displacement fields, an axisymmetric shell finite element was developed based on the variational form of the Hamilton principle. The finite element implementation was validated for static, natural vibration, and transient analyses through comparison of the predicted results to those based on ABAQUS. The model was then adopted to conduct one-way coupled water hammer analysis in order to investigate the influence of the valve closure times and patterns on the structural dynamic response of the pipe.

3. In order to capture two-way coupling effects in water hammer analysis, the structural model developed under the second contribution was coupled to the fluid model by using the block Gauss-

Seidel algorithm in a partitioned scheme. To assess the correctness of implementation of the partitioned scheme, both the monolithic classical and extended water hammer models were implemented into the partitioned schemes. Comparisons of pressure histories as predicted by the monolithic and partitioned classical and extended water hammer models demonstrate the correctness of the implementation. The two-way coupled models thus developed are adopted to characterize the influence of the tolerance, the Courant number, the relaxation factor, and the interface type on the performance of the partitioned water hammer models.

6.2. Conclusions

The following conclusions can be summarized from Chapter 3:

1. Adopting the proposed boundary expression was shown to improve the predicted pressure histories when compared to damping patterns observed in experiments, with respect to wave smoothing, phase shifting, and wave peak damping.

2. Since the proposed boundary expression accounts for the energy dissipated at the waterjet in the first computational cell attached to reservior, the empirical constant introduced within the proposed boundary expression depends on the discretization scheme adopted. However, the numerical results were shown to be independent of the discretization scheme when using the proposed boundary expression.

3. Using the minimum difference method to determine the constant introduced within the proposed boundary expression, the energy dissipation due to the friction and waterjet effects was shown to be independent of the discretization scheme. The investigation has shown that the energy dissipated at the pipe inlet is important to replicate the experimentally observed pressure damping patterns.

The following conclusions can be summarized from Chapter 4:

4. The proposed pipe finite element was shown to accurately predict the static, natural vibration, and time history responses for the pipe.

5. In the frictionless classical water hammer model, the length of the pressure gradient in the neighbourhood of wave front is proportional to the valve closure time. Using the one-way coupling water hammer model, the oscillation of pipe radial displacement was observed to depend on the

length of pressure gradient. It was found that the radial inertial effects become negligible when the valve closure time is longer than eight times the period of radial displacement vibration.

The following conclusions can be summarized from Chapter 5:

6. In the two-way partitioned coupling model, when using non-matched fluid-structure interfaces, the difference between the predicted pressure histories was found to depend on the number of subdivisions in the fluid and to be independent of the number of subdivisions in structural model.

7. By using the space-line interpolation scheme in the fluid model and the finite element structural model developed herein, the partitioned water hammer model was found to be stable for large Courant numbers corresponding to large time steps. It was also found that local minimum values of the pressure difference percentage are obtained when the Courant number is an integer value.

8. By using either an optimal constant relaxation or the Aitken relaxation, it was found that the number of iterations needed for convergence reduces, thus increasing the computational speed of the program. The Aitken relaxation is recommended as there is no standard way to determine the optimal constant relaxation.

6.3. Recommendations

Since the present work developed a partitioned model for single-phase water hammer in straight pipes, the proposed partitioned water hammer model can be improved in four respects: the energy dissipation, the solvers for each domain, the iterative scheme adopted and the fluid-structure interface, as follows:

1) In the proposed partitioned water hammer model, the system energy is dissipated only through material damping in the structural model. Other sources of energy dissipation can be included into the model to more realistically account for the energy dissipation, such as the friction at the fluid-structure interface (in quasi-steady or unsteady friction models), the Coulomb friction between the outer surface of the pipe and surrounding soil, and the waterjet occurring at the pipe entrance (using the boundary expression proposed in Chapter 3).

2) Both the fluid and the structural models can be replaced by other numerical models that account for additional features. For the fluid model, possible improvements include:

a) The convective term has been ignored in present fluid model and could be added in future studies. Once included in the fluid model, the wave speeds will differ along the positive and negative characteristic lines. Hence, either the time-line or space-line interpolation schemes can be adopted, which will introduce numerical damping. To reduce the artificial numerical damping introduced, either high-order finite difference schemes or finite volume schemes can be adopted to develop the fluid model.

b) The present fluid model assumes uniform pressure and velocity over the cross-section. In reality, the fluid velocity is lower near to the pipe wall and higher at the core of the flow. To account for the variation in pressure and velocity over the cross-section, a quasi-2D fluid solver could be adopted.

c) The present fluid model is valid for a single-phase flow. During water hammer, column separation may be associated with a low-pressure wave which releases air and vapours near the valve. In this case, a two-phase fluid model would be required to realistically simulate the compressibility of the air in such water hammer phenomena.

Possible improvements of the structural model include:

a) The structural finite element developed in the present study was intended for steel pipes. As such it is based on a linearly elastic material representation. By incorporating viscoelastic effects into the model, one could extend its use to polyethylene (PE) and polyvinylchloride (PVC) pipes.

b) The finite element developed in the present study is intended for horizontal pipes. As such, it is based on an axisymmetric idealization. For inclined pipes, non axi-symmetric loading conditions will arise. For such cases, it would be beneficial to extend the capabilities of the present model to non axi-symmetric loading.

c) Also, the present structural model is limited to straight pipe segments. It would be of interest to extend its applicability to curved elbow elements to enable the model to analyze complex non-straight pipe networks. In such cases, the fluid model would also have to be modified to account for the centrifugal forces arising due to the deviation of the flow direction.

3) The block Gauss-Seidel iterative algorithm used in the present work is computationally expensive. It would be interesting to investigate whether other iterative methods such as the Newton-type iterative algorithm. can lead to a reduction in computational effort.

4) Linear interpolation was used for information exchange at the fluid-structure interfaces in the present study. Other interpolation techniques such as spline interpolation can be adopted to improve the efficiency and accuracy of information exchange. Also, the radial-function-based interpolation can be adopted in models of 2D or 3D models.